Novel Topology of Saturated-core Fault Current Limiter

Dalibor Čvorić

Novel Topology of Saturated-core Fault Current Limiter

PROEFSCHRIFT

ter verkrijging van de graad van doctor
aan de Technische Universiteit Delft,
op gezag van de Rector Magnificus prof.ir. K.C.A.M. Luyben,
voorzitter van het College voor Promoties,
in het openbaar te verdedigen op woensdag 15 december 2010 om 10.00 uur
door

Dalibor ČVORIĆ

Graduate Electrical and Computer Science Engineer,
University of Novi Sad, Serbia
geboren te Zvornik, Bosnië-Herzegovina

Dit proefschrift is goedgekeurd door de promotor:
Prof.dr. J.A. Ferreira

Samenstelling promotiecommissie:

Rector Magnificus, voorzitter
Prof.dr. J.A. Ferreira, Technische Universiteit Delft, promotor
Ir. S.W.H. de Haan, Technische Universiteit Delft, copromotor
Prof.dr. E.H. Brück, Technische Universiteit Delft
Prof.dr. E. Lomonova, Technische Universiteit Eindhoven
Prof.dr. T.A. Meynard, LEEI Instituut, Toulouse
Prof.dr. M. Zeman, Technische Universiteit Delft
Prof.dr. J. Jäger, Technische Universiteit Erlangen-Nürnberg

To my family

ACKNOWLEDGEMENTS

This PhD research has been done at Delft University of Technology in the group for Electrical Power Processing (EPP). Hereby, I would like to express my appreciation for people who supported me and contributed, in one way or the other, to the successful completion of my work.

I would like to thank my promotor Professor Braham Ferreira for believing in me and giving me the opportunity to join EPP group at TU Delft and do my PhD. I highly appreciate his support, guidance and advice in the last four years, which were very important and helpful in fulfilling the goals of this research. I enjoyed our meetings and discussions.

I would like to express my great appreciation for my co-promotor ir. Sjoerd de Haan for his guidance and contribution to this work. The numerous discussions and suggestions from his side helped in keeping this research on the right track. His efforts and dedication contributed greatly to the value of this PhD regarding research and writing of publications and thesis.

This work is partially funded by the Energy Research Program EOS of the Ministry of Economic Affairs - SenterNovem. Thank you.

I am very grateful to Maarten van Riet and Jan Bozelie from Alliander B. V. for their contribution to the practical side of this PhD work. The development and building of the full-scale FCL prototype would not have been possible without their help. The results of our collaboration have increased the quality of this thesis.

I would like to thank Dr. Domenico Lahaye from the department of Applied Mathematics for his contribution to the Finite Element model development. His dedication and persistence have contributed positively to this thesis.

I highly appreciate the help of Rob Schoevaars. His suggestions and assistance regarding the practical work in the lab were very helpful and irreplaceable at many times. Thanks to him for making the time I have spent in the lab much more productive and enjoyable. Also, thanks for the help with translating the propositions into Dutch.

I appreciate the help of Bart Roodenburg in making my first lab-setup and translating the summary into Dutch. Thank you.

I want to express my appreciation for everything that Suzy Sirks-Bong has done for me during my PhD. Thank you for being there whenever I needed it and thanks for being patient to talk in Dutch to me. I am also grateful to EPP secretary Laura Bruns for helping me with all administrative issues.

I would like to thank Professor Lou van der Sluis from Electrical Power System group for proofreading one of the chapters of this thesis.

I am grateful to the phd defense committee members for reading and evaluating the thesis and for giving me the feedback which further improved the thesis.

I would like to thank Humanitarni Fond 'Privrednik' from Novi Sad, especially Mrs. Jelena Tabak and Mrs. Nena Mrdjenović, for the financial support when I was starting the PhD. Thank you also for giving me a chance to attend your school of foreign languages, which greatly helped me in pursuing my dream. It was my honor to be pitomac of 'Privrednik'.

I am grateful to my friends and officemates Zhihui Yuan and Marcelo Gutierrez, who contributed to my PhD work through many whiteboard-discussions, which usually were an irreplaceable part of a problem-solving procedure. It was lots of fun playing tennis with Zhihui and Anoop Jassal. They have made my out-of-office life more interesting and pleasant. I would like to thank Anoop for being a good friend and, of course, my first tennis coach. I appreciate his contribution to proofreading of this thesis. I would like to thank other colleagues from EPP group: Miloš Ačanski, Ivan Josifović, Deok-Je Bang, Aleksandar Borisavljević, Balazs Czech, Ghanshyam Shrestha, Yi Wang, Xun Gong, Jianing Wang, Vasileios Karapanos, Sam Ani, Hung Vu Xuan, Jinku Hu, Rodrigo Teixeira Pinto, Frank van der Pijl, Yeh Ting and Dongsheng Zhao.

I have enjoyed being in The Netherlands for the last four years. I would like to convey huge thanks to my friends who made my every-day life pleasant and also helped me go smoothly through difficulties in my PhD work. I am grateful to Miloš Ačanski, Ivan Josifović and Sanja Petrović. I enjoyed the time we spent together. Thanks Miloš for the help with making the cover for the thesis. I liked our regular going-out to enjoy 'Kebab met patat'. Ivan and Sanja, after spending five years together in Novi Sad, it was really pleasant for me to spend these four years together with you in Delft. It helped me feel as if I was not that far away from home. I also would like to thank my friends Jelena, Mark and Una Gerber for many enjoyable moments. Thanks Jelena for supporting me when I was applying for a PhD position. I appreciate very much the numerous emails you have sent back to me, answering on perhaps endless number of my questions and worries. I would also like to thank Stevan and Maja Rudinac for making my time in Delft more enjoyable. I am grateful to many friends from Delft, Rijswijk and Rotterdam for many great moments that we have spent together.

I would like to express my gratitude to my professor of mathematics from Grammar high school Saveta Mojsilović. Her dedication and support helped me develop interest in mathematics and technical sciences and led me to continue my education in the field of electrotechnics.

I would like to express my great appreciation for my family. Želim da se zahvalim mojoj majci Miladi i braći Darku i Dragi za njihovu bezrezervnu podršku i ljubav kroz sve prethodne godine i sve teške trenutke. Uvijek ste bili tu kad je to bilo potrebno. Bez vas sigurno ne bih došao ovako daleko. Hvala vam.

Dalibor Čvorić
Delft, December 2010

SUMMARY

It is determined that, based on the applied technology, the numerous types of Fault Current Limiters (FCLs) can be classified into three main groups: non-semiconductor-based, solid-state and hybrid FCLs. On the other hand, based on one of the most important operating characteristics, namely fault-reaction delay, FCLs can be classified into two groups: FCLs with inherent reaction to a fault and those with a fault-reaction delay. The performed analyses have shown that saturated-core FCLs, belonging to non-semiconductor-based FCLs, have significant operational advantages over other FCL types. However, the saturated-core FCL topologies require a large volume of magnetic material resulting in high initial cost and large size of the device.

To solve the problem of large mass and high cost, a novel three-leg configuration of a magnetic core is proposed. The volume of magnetic material required by this core topology is reduced by applying the principle of an air gap insertion in a core. This principle is typically used for non-linear inductors. It is not possible to use a gap with state-of-the-art FCL core configurations because the gap would be a part not only of an ac but also of a dc magnetic circuit. In such a case, it is very difficult to saturate the core and reduce the FCL's normal impedance. In this novel design, the core has three legs and the arrangement of ac and dc windings in such a way that the dc flux does not flow through the middle leg of the core. Therefore, a gap can be inserted in the middle leg without having to increase the dc mmf to saturate a core. This gap ensures smaller core size for the same voltage level.

Based on the new core design, two novel FCL topologies are proposed: a single-phase single-core and a three-phase single-core FCL. The proposed single-phase topology uses only one three-leg magnetic core per phase. The arrangement of the ac and dc windings provides that in each half cycle during a fault one of the two outer legs is driven out of saturation and limits fault current. By employing the new structure, the total

weight of the FCL is reduced by approximately 70% compared to a typical inductive FCL design. Three single-phase units are needed for the protection of a three phase system. The principle of operation of the novel FCL topology is proved by means of simulations and lab-scale testing. The results agree very well. The volume of required material is further decreased by using novel three-phase single-core topology. The windings from all three phases are wound on a common three-leg core, which reduces the volume of magnetic material by nearly 66%. Since the fluxes from three-phase windings cancel each other out under normal operation, the number of dc turns which is needed to drive the core into saturation, is considerably decreased. The dc windings are used only to compensate for a possible asymmetric current of a system. Therefore, the number of the required dc turns is reduced. The associated value of the induced voltage across the dc windings is proportionally diminished. A novel trifilar arrangement of the phase windings is proposed to reduce the impedance during normal operation. The simulations and experimental testing showed that trifilar arrangement improves magnetic coupling between the phases and reduces FCL normal impedance by a factor of approximately 8. To improve the inter-turn insulation, the windings are made of MV cables. The drawback of the three-phase topology is that it is only capable of limiting single-phase to ground faults. Due to magnetic coupling between phase windings, the current in the faulted phase is increased to a higher level by the currents from the two healthy phases. Thus, due to the coupling between phases, the FCL limiting impedance appears to be lower than the designed value. The 'effective' fault impedance is equal to the ratio between the phase voltage of the faulted phase and the total fault current. Faults involving more than one phase are invisible to the FCL due to the cancellation of fluxes produced by the different phase windings and the core remains in saturation even during a fault. The operation of the proposed topology is validated by simulations and testing of lab-scale demonstrators, where the results match very well.

A novel three-step modeling procedure for the design of saturated-core FCLs is introduced. The following three models are developed and used in the corresponding modeling steps:

i. An analytical first-order model,
ii. A transient model in Saber simulator,
iii. A 3D Finite Element (FE) transient FCL model.

The initial estimate of the FCL design parameters is obtained using an analytical model in Mathcad. The model does not take into account leakage fluxes and it does not accurately account for the fringing flux in a gap. A first FCL design is obtained using a transient model in Saber simulator. The model produces the waveforms of the signals and makes it easier to assess the operation of an FCL during both normal and fault regimes. The accuracy of the results of the Saber model is however dependent on the gap length. More specifically, this model does not fully account for leakage and fringing fluxes, which can have considerable influence on the results. Finally, as the last modeling stage, a transient 3D FE model is developed in Ansys. This model takes into account both leakage and fringing flux effects and gives very accurate results. The proposed three-step design procedure for saturated-core FCLs is very effective and accurate.

In addition to the FE model in Ansys, a model of saturated-core FCLs is built in Comsol Multiphysics as well. The development of the FE model in Comsol provides insight in the mathematical background of FE modeling and allows a better understanding of how these models work. FCL modeling on two software platforms has advantages and disadvantages. It is more difficult to create 3D geometry of windings with multiple turns in Ansys than in Comsol. In Ansys, each turn must be drawn separately, and in the case that the windings have many turns it is nearly impossible to draw them all. A modeling procedure where the number of modeled turns is lower than in reality is proposed; the electrical circuit is modified to account for this difference. Also, Ansys requires that the time integrated value of voltage to be applied to an FCL model as an input variable instead of its real value. The modeling of an electrical circuit in this case requires the resistive load to be replaced by a capacitive load. Ansys offers the possibility of modeling a full electrical circuit. Comsol is more 'mathematically oriented' software and requires equations to be inserted for calculation of both winding inductance and electrical circuit parameters. All modeling issues are solved in both 2D and 3D domains and guidelines for development of both FE models are presented.

Using FE model in Ansys, the design of the proposed FCL topologies is further improved from the point of view of the required volume of magnetic material. The obtained results from the analytical and Saber models showed that the cross-section of core's middle leg must be two times larger than that of the outer leg. However, FE simulations showed that the cross-section of the middle leg can be reduced by a factor of five without significantly impairing an FCL's fault limiting ability. In the analysis performed on three-phase single-core design, the volume of magnetic material was reduced by 30.4% while the fault current was increased by 40% (from 4.4 p.u. to 6.1 p.u.). Such an increase of the fault current is insignificant while the FCL weight is considerably reduced.

On the initiative of industry partners, a full-scale 10 kV prototype of a three-phase single-core FCL has been designed and tested to prove that the FCL is able to protect real power grids. Testing of the prototype was done in two steps. In the first, low-voltage stage, the FCL was tested for all fault scenarios at 400 V. The obtained results showed that the FCL limits single-phase to ground faults and that it does not react to faults involving more than one phase. The agreement with 3D FE results was very good. During a fault period, induced voltage in the dc windings resulted in the large value of the induced current in the dc circuit. The dc electrical circuit was modified to interrupt the induced current, which would otherwise reduce the FCL limiting factor at 10 kV operation. As the next step, a full-voltage 10 kV testing is performed. The testing is done in four stages, corresponding to four different levels of the prospective fault current, namely, 10, 20, 30 and 40 kA. For all cases, the FCL has successfully limited single-phase to ground faults. The agreement between measurements and simulation results was very good. Faults involving multiple phases were not limited, as it was expected from the simulations. The full-voltage testing proved that the FCL is capable of protecting real grids from single-phase fault currents. It also validated the 3D FE model in Ansys Classic.

The issues regarding the installation of FCLs in power systems are addressed in the end of the thesis where the following topics are considered:

i. The positioning of FCLs in power systems,
ii. The interaction between FCLs and existing protective schemes,
iii. The interaction between FCLs and circuit breakers (CBs),
iv. The influence of FCLs on power quality and system stability.

Some of these aspects have been extensively investigated in literature in the last decade and an overview of the available results and conclusions is provided. In the analyses, two principal types of FCLs are considered, namely, reactive and resistive.

The influence of FCLs installation on four protection schemes (over-current, differential, distance and directional protection) is also analyzed in this thesis. It is pointed out in which situations the operation of the given protective scheme could be compromised and what could be done to address the arising problems.

While determining the cost-effectiveness as a power system protection solution, the positive effects that FCLs have on power quality and system stability should be included.

SAMENVATTING

Op basis van de toegepaste technologie is vastgesteld dat kortsluitstroombegrenzers (Fault Current Limiters, FCLs) in drie hoofdgroepen kunnen worden geclassificeerd, te weten niet-halfgeleider gebaseerde types, halfgeleider gebaseerde types (solid-state) en hybride FCLs. Echter FCLs kunnen ook worden geclassificeerd in twee groepen gebaseerd op n van de belangrijkste karakteristieken, namelijk de vertragingsreactie op een fout. Deze groepen zijn: FCLs met inherente reactie op een kortsluitstroom en FCLs met een vertraagde reactie op een kortsluitstroom. De uitgevoerde analyses in dit proefschrift hebben aangetoond dat FCLs met een verzadigde kern, die tot de inherente niet-halfgeleider gebaseerde FCLs behoren, significante operationele voordelen hebben in vergelijking met de andere FCL types. Het resterende ontwerp probleem van deze state-of-the-art FCLs is het reduceren van het te grote volume van het magnetisch materiaal. Dit grote volume resulteert in hoge initile kosten, een excessief gewicht en grote afmetingen van het apparaat.

Om het probleem van het excessieve gewicht en de hoge kosten op te lossen, is voor de FCL een nieuwe magnetische kern met drie poten gentroduceerd. De hoeveelheid magnetisch materiaal gebruikt in deze configuratie, wordt verminderd door toepassing van het ontwerpprincipe dat typisch is voor niet-lineaire spoelen, te weten het toepassen van een luchtspleet in de kern. Bij state-of-the-art FCL kernconfiguraties is het niet mogelijk om een luchtspleet te gebruiken. De luchtspleet maakt niet alleen deel uit van het AC magnetisch circuit, maar ook van het DC magnetisch circuit. In een dergelijk geval is het zeer moeilijk om de kern te verzadigen en om de normale impedantie van de FCL te verminderen. In dit nieuwe ontwerp heeft de kern van de FCL drie poten en de plaatsing van de AC en de DC windingen is zodanig dat de DC flux niet door de middelste poot van een kern loopt. Daarom kan een luchtspleet nu wel in de middelste poot worden ingepast zonder dat het noodzakelijk wordt om het aantal DC amprewindingen te verhogen om de kern te verzadigen. Met de introductie van deze luchtspleet kunnen kleinere kernen worden gebruikt voor hetzelfde spanningsniveau.

Gebaseerd op dit nieuwe kernontwerp zijn twee nieuwe FCL topologien voorgesteld, te weten een enkelfasige en een driefasige FCL, beide met enkele kern. De voorgestelde topologie van de enkelfasige FCL maakt gebruik van een magnetische kern met drie poten per fase. De ordening van de AC en DC windingen is zodanig dat tijdens een fout in elke halve periode n van de twee buitenste poten van de kern uit verzadiging genomen wordt. Dit leidt tot begrenzing van de kortsluitstroom. Door gebruik te maken van de nieuwe FCL structuur is het totale gewicht van de FCL, vergeleken met de standaard inductieve FCL, met 70% gereduceerd. Drie enkelfasige FCLs moeten worden ingezet voor de bescherming van een driefasig systeem. Het werkingsprincipe van de nieuwe FCL topologie is aangetoond door middel van simulaties en laboratoriumtesten. De overeenstemming tussen meet- en simulatieresultaten is erg goed.

De hoeveelheid kernmateriaal voor de FCL is verder gereduceerd door gebruik te maken van een nieuwe driefasige FCL topologie met enkele kern. Die verdere verlaging van het magnetisch materiaal, tot ongeveer 66%, is gerealiseerd door de windingen van alle drie de fasen op een kern met drie poten te plaatsen. Omdat de magnetische flux van de drie fase windingen elkaar tijdens normaal bedrijf compenseren, is het aantal DC windingen dat nodig is om de kern te verzadigen flink verminderd. De DC windingen worden alleen gebruikt ter compensatie van een mogelijke asymmetrische stroom. De bijbehorende genduceerde spanning over de DC windingen is proportioneel verminderd. Om in normaal bedrijf de impedantie van de FCL te verminderen, is een nieuwe tri-filaire wikkelmethode van de fasewindingen voorgesteld. Simulaties en experimentele testen hebben aangetoond dat door de tri-filaire wikkelmethode de magnetische koppeling tussen de fasen is verbeterd en de impedantie in normaal bedrijf met ongeveer een factor acht is verminderd. Om het isolatieprobleem tussen de wikkelingen op te lossen, is gebruik gemaakt van Medium Voltage (MV) kabels. Het nadeel van de driefasige FCL topologie is dat deze alleen een enkelfasige foutstroom naar aarde kan beperken. Ten gevolge van de magnetische koppeling tussen de fasewindingen neemt de totale foutstroom in deze foute fase toe. Dit wordt veroorzaakt door de invloed van de stromen in de andere twee fasen. Dus vanwege deze koppeling tussen de fasen lijkt de stroombeperkende impedantie van de FCL lager te zijn dan de ontwerpwaarde. De term 'effectieve' stroombeperkende impedantie is gedefinieerd als de verhouding tussen de fasespanning van de foute fase en een totale stroom in deze fase. Kortsluitingen die meer dan n fase omvatten worden niet begrensd door de FCL. Dit is ten gevolge van het compenseren van de fluxen die door de verschillende fasen windingen geproduceerd worden. Het werkingsprincipe van de voorgestelde FCL topologie is door middel van simulaties en laboratoriumtesten gevalideerd. De verkregen simulatie-en meetresultaten zijn zeer goed in overeenstemming met elkaar.

Een nieuwe modelleringsprocedure voor het ontwerpen van een FCL met een verzadigde kern is in 3 stappen gentroduceerd. De volgende drie FCL modellen zijn ontwikkeld en toegepast:

i. Analytisch eerste orde model,
ii. Dynamisch simulatie model uitgevoerd in Saber,
iii. 3D eindig elementen model (FE model).

Als eerste wordt door middel van een analytisch model, dat in Mathcad is ontwikkeld, een schatting van de FCL ontwerpparameters gemaakt. Een dergelijk model houdt geen rekening met spreidingsfluxen en het houdt niet nauwkeurig rekening met het uitbloezen (fringing) van de flux in de luchtspleet. Als tweede is het initile ontwerp van de FCL verkregen met behulp van een transint simulatie model in Saber. Dit model produceert golfvormen als functie van de tijd en dit maakt het, zowel tijdens normale- als tijdens foutsituaties, makkelijker om de werking van de FCL te beoordelen. De nauwkeurigheid van de resultaten van het FCL model uit Saber is afhankelijk van de luchtweglengte omdat de spreidingsflux en fringingsflux niet volledig berekend worden door het model. Ten slotte in de laatste fase van de modellering, is een 3D FE model van de FCL in Ansys ontwikkeld. Dit model houdt rekening met zowel de spreidings- als fringingsflux en geeft zeer nauwkeurige resultaten. De voorgestelde procedure om in drie stappen een FCLs met verzadigde kern te ontwerpen is zeer effectief en accuraat. Naast modellering in Ansys, is het FE model van de FCL met verzadigde kern ook opgebouwd in Comsol Multiphysics. Ontwikkeling van een FE model voor een FCL in Comsol biedt meer inzicht in de wiskundige achtergrond van FE modellering en helpt om de werking ervan beter te begrijpen. FCL modellering heeft in beide software pakketten voor- en nadelen. In Ansys is het moeilijker om een 3D geometrie van de spoelen met meerdere windingen te creren dan in Comsol. In Ansys moet elke winding apart worden opgesteld en in het geval dat de spoelen vele windingen hebben, is het lastiger die te maken. Daarom is tijdens de modelleringsprocedure voorgesteld het aantal gemodelleerde windingen lager gehouden dan het werkelijke windingaantal. Het elektrisch circuit is hierop aangepast om rekening te houden met dit verschil. Bovendien, vereist Ansys dat de gentegreerde waarde van de spanning naar de tijd wordt toegepast in plaats van de werkelijke waarde. In dit geval, vereist het modelleren van een elektrisch circuit dat een ohmse belasting is, wordt vervangen door een capacitieve belasting. Ansys biedt de mogelijkheid om het volledige elektrische circuit te modelleren. Comsol is echter meer 'wiskundig georinteerde' software en vereist dat de vergelijkingen van zowel zelfinductie als het elektrische circuit worden opgegeven. Alle modellen zijn zowel in het 2D als 3D domein opgelost en richtlijnen voor de ontwikkeling ervan zijn gepresenteerd.

Met behulp van het FE model zijn in Ansys de voorgestelde FCL topologien verbeterd. De basis voor deze verbetering is het benodigde volume van magnetisch materiaal. Gebaseerd op de resultaten uit de analytische en de Saber modellen, moet de doorsnede van de middelste poot van de kern twee keer groter zijn dan die van de buitenste poot. Met FE simulaties is aangetoond dat de doorsnede van de middelste poot verminderd kan worden met een factor vijf, zonder significante aantasting van de stroombeperkende werking. In de uitgevoerde optimalisatie van een driefase FCL met enkele kern, werd het volume van het magnetisch materiaal met $30,4\%$ verminderd terwijl de kortsluitingstroom met 40% werd verhoogd (van $4,4$ p.u. naar $6,1$ p.u.). Een dergelijke verhoging van de kortsluitstroom kan als onbeduidend worden beschouwd, terwijl het gewicht van de FCL aanzienlijk verminderd is.

Op initiatief van de industrile partners is op ware grootte een 10 kV prototype ontworpen en gebouwd. Dit prototype betreft een driefasige FCL met enkele kern en is getest om de toepasbaarheid in werkelijke netten te bewijzen. Het testen van de FCL gebeurde in twee fasen. In de eerste fase is de FCL voor alle fout scenario's op 400 V laagspanning getest. Uit de verkregen resultaten bleek dat de FCL enkelfasige foutstromen naar aarde kon begrenzen maar dat bij fouten waarbij meer dan n fase was betrokken de FCL niet functioneerde. De experimenteel verkregen meetdata is erg goed in overeenstemming met de resultaten van het 3D FE model. Tijdens de foutsituatie veroorzaakte een genduceerde spanning in de DC winding een grote stroom in het DC circuit. Het DC circuit werd aangepast om de stroom te onderbreken, omdat dit anders het stroombeperkend effect bij 10 kV-bedrijf zou kunnen verminderen. In de tweede fase zijn testen bij de volledige spanning van 10 kV uitgevoerd. Deze testen zijn uitgevoerd in vier stappen, corresponderend met vier foutstroom niveaus, te weten 10, 20, 30 en 40 kA. In alle gevallen zijn enkelfasige kortsluitstromen door de FCL succesvol beperkt. De experimenteel verkregen data is erg goed in overeenstemming met de simulaties. Zoals voorspeld in de simulaties werden kortsluitingen waarbij meerdere fasen waren betrokken niet in stroom beperkt. Testen bij volledige spanning bewijzen dat de FCL in staat is elektriciteitsnetten te beschermen tegen kortsluitstromen. Het in Ansys Classic ontwikkelde 3D FE model van de FCL met verzadigde kern is aan de hand van deze metingen gevalideerd.

Aan het einde van het proefschrift zijn onderwerpen met betrekking tot de installatie van FCLs in elektriciteitsnetten besproken. De volgende onderwerpen zijn beschouwd:

i. Positie van FCLs in het net,

ii. Interactie tussen FCLs en de bestaande (net)beveiligingstechnieken,

iii. Interactie tussen FCLs en vermogensschakelaars,
iv. Invloed van FCLs op de kwaliteit en de stabiliteit van het net.

Verscheidene van deze aspecten zijn het afgelopen decennium in de literatuur uitvoerig bestudeerd. Voor deze gevallen wordt een overzicht van de beschikbare resultaten en conclusies gegeven. In de analyses worden twee FCL principes onderzocht. Dit zijn de reactieve en de resistieve FCL.

De benvloeding van de FCL op de werking van de vier standaard beveiligingstechnieken in het elektriciteitsnet (overstroom-, verschilstroom-, afstands- en richtingsbeveiliging) worden in dit proefschrift geanalyseerd. In welke situaties het werkingsprincipe van de gebruikte beveiligingstechnieken kan worden verstoord wordt aangegeven. Tevens wordt besproken hoe deze problemen aangepakt kunnen worden.

Bij de bepaling van de kosten-baten analyse van een FCL, en de keuze deze wel of niet toe te passen, moet er rekening gehouden worden met het positieve effect dat een FCL heeft op de netkwaliteit en netstabiliteit.

Contents

Chapter 1

INTRODUCTION

1.1 Introduction

THE electrical power system is a complex composition of components and circuits for generating, transmitting, transforming, and distributing electrical energy [Wiki]. The invention of ac polyphase system of generators, transformers and motors by Nikola Tesla in the 19^{th} century made it possible to produce, use and transport electrical energy over large distances.

Ac electrical systems became the basis for the development of the modern world. Nowadays, ac power system infrastructures supply electrical energy to consumers worldwide. Power systems are composed of a relatively small number of centralized generators which produce and supply electrical energy via high (HV), medium (MV) and low (LV) voltage grids to a large number of loads, see Figure 1-1. Such an organization of the power system is recognized as vertical. Power flows from the 'top' of the system, where generators are installed, to the 'bottom' of the system comprising loads.

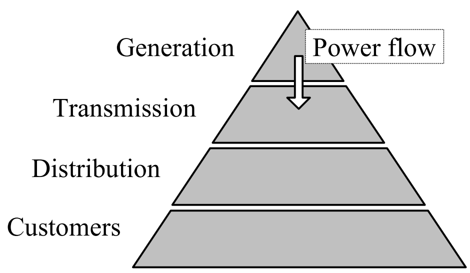

Figure 1-1: Power flow - vertical organization of power system.

The demand for electrical power grows continuously. Abrupt technological advances in the last two decades, such as development of computer digital technology, are the reasons of the increased power consumption. The large number of devices is designed with the goal to improve comfort of living. As an example, the number of every-day-used electrical accessories and pieces of equipment in households increases every year. Consequently, the amount of electrical energy used by each person enlarges. In addition, the number of people that use electrical energy grows. More electrical energy is required not only inside the households but also at work or outside in the public places.

In the developing world, several technological trends, such as electrical cars and renewable generators, may cause that the electrical energy consumption will increase substantially. Electrical cars are expected to replace cars with combustion engine in the near future aiming at reduction of emission of greenhouse gasses. The demand for electrical energy would significantly rise.

Electrical energy is an indispensable part of each aspect of modern life. Power systems are and will be required to meet the energy demands. A number of measures are necessary to achieve a balance between power generation and consumption: the power systems' generation, transmission and distribution capacities have to be increased. These measures are addressed in the following pages in the given order. The generation capacity is increased by:

i. Installing new centralized generators,
ii. Installing renewable sources of electrical energy (wind, solar,...),
iii. Installing Combined Heat and Power (CHP) generators.

Apart from installing new centralized generators (thermo- and hydro-generators), the application of renewable sources of electrical energy is growing fast. They reduce the usage of fossil fuels and do not pollute the environment. The extensively conducted research in this field shows that renewables are expected to be an important source of energy for the future. The penetration level of the Distributed Generators (DGs) in the existing power systems increased progressively in the last decade. Two types of renewable sources are mainly used today: wind turbines and solar panels, while development of other types such as wave and tidal energy is still in progress. Wind energy plays the dominant role, with an energy production of 56 GW in Europe in 2007. The current goal of the EU is to obtain 20% of electrical energy from wind farms by 2020. Wind farms do not have to be placed near rivers or coal mines like traditional power plants, but can rather be placed at any location with sufficient wind energy. From there they can be connected to either transmission or distribution power systems. Up to now, solar panels are always installed in the distribution system.

In addition to the types of DGs already listed, another type should also be mentioned: combined heat-power (CHP) generators. These generators deliver both electrical energy and heat, which is used usually for supplying hot water to households or greenhouses. Mostly, CHPs are integrated in MV grids. These local small-scale electrical sources, which range from several kW to several MW, can be distributed throughout the whole power system.

Electrical power required by loads is not only delivered by the centralized generators, but also by the DGs which can be installed in neighboring parts of the system at the same voltage level. As a consequence, the organization of the system has gradually changed from vertical to horizontal where the electrical power is supplied from different voltage levels, see Figure 1-2.

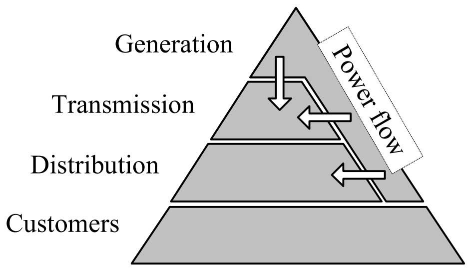

Figure 1-2: Power flow - organization of power system gradually changed to horizontal.

The increased power generation has two effects on the operation of the distribution and transmission systems:

i. Risk of steady-state overload - the amount of power generated and transmitted through the power system may exceed the ratings of the system's components, such as lines and transformers.
ii. Increased short-circuit currents - in case of a fault, the amount of power captured by a short-circuit is increased, which results in higher levels of the short-circuit currents.

The transmission and distribution capacities of the power system also have to be increased since the amount of power that has to be transmitted through the system during nominal regime increases. In the first place, new transformers and new power lines have to be installed. In this way the effective impedance of the system is decreased which makes it possible to transmit a larger amount of power. These measures can be costly. The problem of steady-state overload of the system can also be solved by installing power flow controllers (PFC) [Yuan 07]. They can divert the power from the overloaded part of the system to another part in which power capacity is not exceeded.

Increased power generation and increased transmission and distribution power capacities also lead to increased short-circuit currents. It is of the utmost importance to protect the power systems from being thermally and mechanically over-stressed, which can be caused by fault over-currents. Faults in power systems are inevitable. They can occur, for example, as a result of lightning strikes, falling tree branches or equipment failure. The faulted part of the system must be disconnected from the rest of the system as soon as possible. In Figure 1-3 a part of a typical distribution system is shown, consisting of one bus A, one incoming feeder and three outgoing feeders with connected loads. Each of the feeders is equipped with Circuit Breakers (CB). In this system a fault occurs in feeder 2. Feeder 2 should be disconnected by opening the circuit breaker 2. The power supply to other feeders should not be disrupted. The fault currents can cause instability of the synchronous generators and of the whole system if not cleared on time. In the traditional organization of power systems a relatively small number of centralized generators supply a large number of loads, see Figure 1-1. The disconnection of the unstable generator in such a system could leave many customers without a power supply, which is unacceptable. Loss of generator G in Figure 1-3 would leave unfaulted loads in feeders 1 and 3 without a supply. On the other hand, fault currents can cause the most severe voltage dips. The voltage of the bus which is in the fault current path can be very low. In the given example, bus A will experience a severe drop in voltage affecting the loads connected to that bus. A fast fault clearance must be performed in order to restore the voltage and normal power supply. Nowadays, when the number of sensitive loads is increasing continuously, the issue of fast fault clearance becomes very important.

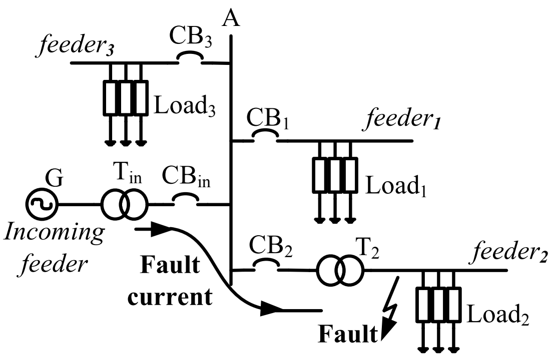

Figure 1-3: A fault in one of the feeders causes a drop in voltage on the common bus and could cause generator instability.

Protective relays are used in power systems for the detection of fault currents and fault locations. Several relay protective schemes are employed: over-current protection, differential protection, distance (impedance) protection and directional protection. In essence, they all utilize two operational principles to distinguish between the normal and the fault states of the system: the measured line current or line impedance is compared to a predefined reference value. When this threshold value is exceeded an appropriate switching action is taken. The threshold levels of the relays are adjusted in such a way that the relay closest to the fault source operates first. Such discrimination (coordination) between the relays can be time- or current-based. In any case, it is of the utmost importance that the fault location is detected and isolated from the system fast enough to preserve or restore the stability and voltage quality of the system. In this way, the supply disturbances seen by the loads are minimized.

After a relay detects a fault within its operating zone, it generates a tripping signal for the appropriate circuit breaker. The CB is a device used to open or close an electrical power circuit either during normal power system operation or during abnormal conditions. During abnormal conditions, when excessive current develops, the CB opens to protect equipment and surroundings from possible damage due to excessive current, to avoid instability of the generators and support the reliability of the power supply [Cred 03]. The CB disconnects the faulted feeder or the larger part of the system from the rest of the system. The coordination between the protective relays has to ensure that only a minimal part of the system is isolated and it must be avoided that customers connected to the unfaulted sections of the system are disconnected. Since the CBs are the only protective units used for line breaking, it must be ensured that they have sufficient short-circuit capacity, meaning they should be able to handle the maximum expected fault current. Their failure to operate, due to over-loading, could result in severe mechanical and thermal over-stresses of different system components.

The breaking capacity of the CBs in the MV grids may need to be increased to cope with the increased fault current levels. The maximum rating of a nowadays CB is limited by the physics of the applied dielectric medium and is around 80 kA. On the basis of the type of dielectric media used, the CBs can be classified into four groups: air, oil, SF6 and vacuum CBs. In some places, short-circuit currents of 70 kA have been measured. It is expected that they will exceed the mentioned maximum CB ratings in the near future. Breaking such large currents presents a challenge for e.g. air-based CBs technology. The size of such devices would become too large and unacceptably expensive. On the other hand, even if CBs are upgraded, the underlying problem would not be solved. The levels of fault currents would continue to grow with the increase in power demand, requiring continuous upgrades.

A more effective way to protect the power system from over-currents could be to limit the currents before they reach too large values. This would eliminate the need for constant, expensive system upgrades.

1.2 Problem definition and thesis objective

Apart from interrupting the fault currents with CBs, measures can be taken to limit their magnitude. On one hand, topological measures can be applied: splitting of grids and busbars. On the other hand, installations of new or upgraded components in the power system, i.e. apparatus measures, are an option: installations of transformers with increased short-circuit impedance, air-core reactors and high-voltage fuses. Splitting grids and busbars prevents one section of the system contributing to a fault in a neighboring section. In Figure 1-4, for the fault incepted in grid A, a contribution from grid B is prevented. In principle, this avoids multiple generators contributing to the same fault.

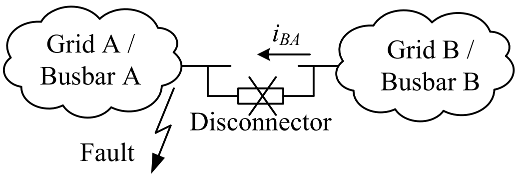

Figure 1-4: Separation of grids or busbars.

Another solution is to increase the short-circuit impedance of the transformers or to install air-core reactors, see Figure 1-5. This directly results in the lower levels of the fault currents.

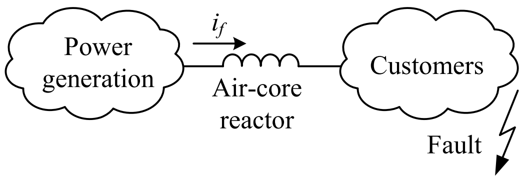

Figure 1-5: Installation of air-core inductors to increase short-circuit impedance of power system.

All of the mentioned measures lead to increased system impedance during nominal regime. Splitting the grids and busbars reduces the availability of the power supply; the number of available generators for the unfaulted feeders is decreased during a fault. However, as stated earlier, the increased load demands require opposite measure: the installation of additional interconnections between the grids and installations of the new generating units. Thus, splitting the grids cannot be considered as an effective solution.

An increase in the transformers' impedance or the insertion of air-core inductors can affect the transient stability of a system because the critical fault-clearing time, required by the generators, is decreased. Consequently, the system could become transiently unstable. Such measures would also introduce a significant voltage drop and power losses in normal operation. In addition, the replacement of existing transformers can be expensive.

In addition to CBs, high-voltage fuses are also used for the interruption of fault currents. However, the manual replacement of fuses is required after each fault operation.

The reconnection of the disconnected loads is, therefore, delayed, reducing the effectiveness of this solution.

Thus, it is required to find a more effective way to limit fault currents in power systems which fulfills the following criteria: the normal impedance of the system should not be increased, availability of the power supply should not be affected and the fault current should be limited to an acceptable value.

Fault Current Limiters (FCLs) are expected to provide the required protection for power systems from excessive short-circuit currents. A Fault Current Limiter can be defined as:

... a device which imposes negligible impedance in the line during normal operation of power system, but limits fault current to a predetermined level in case of a fault.

An FCL is installed in series with a line, as shown in Figure 1-6. It can be integrated in both HV and MV grids. FCL impedance is low during nominal operation of the system, causing an insignificant voltage drop, and it increases after a fault inception. The FCL fault impedance limits fault currents to an acceptable level, which depends on the system requirements.

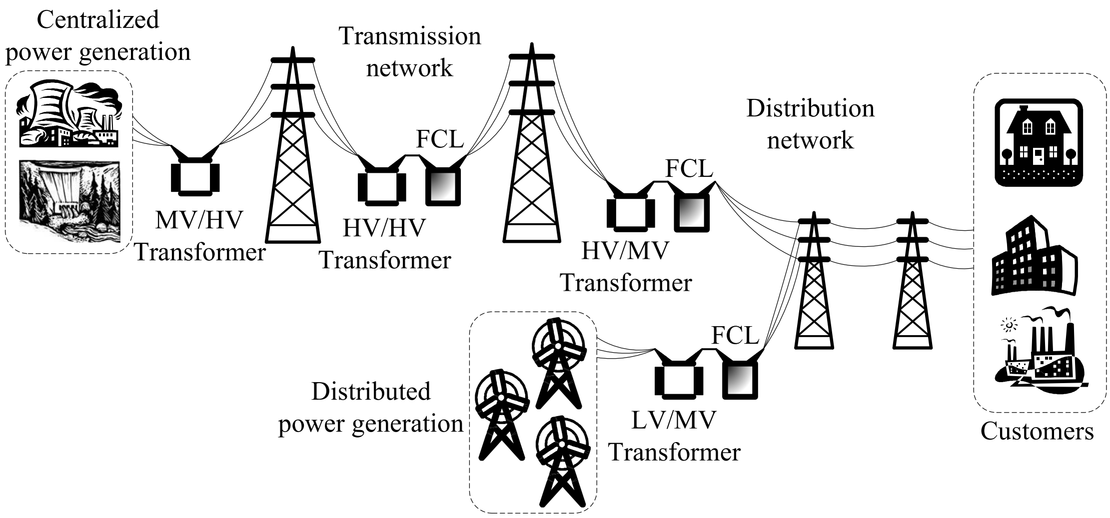

Figure 1-6: FCL installations in electrical power system. Other power system components, such as circuit breakers, are not shown to maintain the simplicity of the figure.

Figure 1-7 presents the typical waveform of a fault current with and without an FCL [CIGR 03]. The prospective fault current comprises a decaying dc component due to the presence of the system reactance L_L. Consequently, the first peak of the fault current has a higher value than its steady-state value. It causes severe mechanical stresses to the system equipment. The FCL should react fast enough (within 5 ms from the fault inception) to limit the first fault peak. The limited fault current can either be interrupted by the FCL or allowed to flow until it is cleared by other protection units, e.g. CBs. In the first case, the FCL should incorporate a current breaking mechanism.

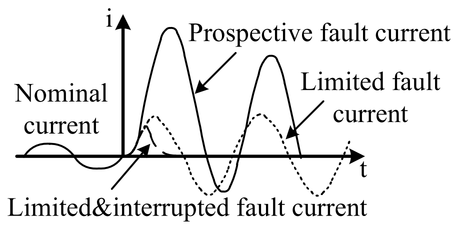

Figure 1-7: Typical waveform of a fault current with and without an FCL [CIGR 03].

Ideally, an FCL should fulfill the following requirements before its operation is considered acceptable:

i. Low impedance during normal operation of the power system - an FCL should not cause a significant voltage drop,
ii. Rapid, fail-safe and adequate current limiting performance - the FCL should react fast to limit the first fault current peak,
iii. Automatic recovery within a short recovery time - after the fault is cleared the FCL should return to a low-impedance state,
iv. No deterioration of the limiting behavior during the FCL's useful life,
v. High reliability,
vi. Low initial cost and low losses (low operational cost),
vii. Small size and low weight,
viii. No risk for operational personnel,
ix. Environmentally friendly - it should not use substances that can have a detrimental influence on the environment, such as greenhouse gasses,
x. No action due to system transient phenomena (motor startup, transformer magnetization etc.),
xi. Integration into existing protective schemes,
xii. Low maintenance requirements.

The FCL must be able to limit the first peak of the fault current and must become 'invisible' for the power system as fast as possible after the fault is cleared. The fault-reaction delay and post-fault-recovery delay are among the most important functional characteristics of the FCL. Figure 1-8 shows the classification of the FCL types in three groups based on the used technology. From the aspect of fault-reaction delay, FCLs can be classified into two groups (see Figure 1-8): FCLs with inherent reaction and FCLs with a fault-reaction delay.

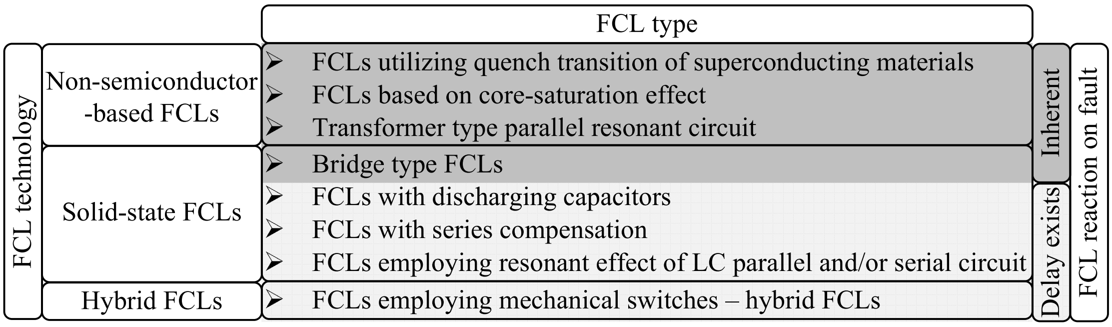

Figure 1-8: FCLs classification based on used technology and fault-reaction delay.

Non-semiconductor-based FCLs do not require fault-detection control. They inherently react to a fault because of the properties of the applied materials. FCLs utilizing the quench transition of a superconducting material, however, experience significant post-fault recovery delay because time is needed to remove the dissipated heat from the superconductor. FCLs based on the core saturation effect utilize two states of their magnetic core to produce low and high impedance states. They satisfy both of the given operational conditions: they provide zero-delay insertion of fault impedance and, after the fault is cleared, the FCL impedance immediately returns to a low state. Despite these significant operational advantages, saturated-core FCLs are still seen as a costly solution. Their high cost is associated with the large amount of magnetic and winding materials.

Solid-state FCLs utilize power semiconductors to provide a path for the nominal current of the system. Most of them must be activated (tripped) by an external fault-detection circuit when a fault is incepted or cleared. So, they will inevitably have fault-reaction and post-fault recovery delays. Bridge-type solid-state FCLs do not have fault-reaction delay. Their topology is such that the fault current itself, when crossing a preset threshold, trips the FCLs and initiates the limiting action.

Hybrid FCLs use both power semiconductors and mechanical switches, bringing the advantage of a negligible voltage drop during nominal operation. Their principle of operation is the same as that of solid-state FCLs. Due to the presence of mechanical switches both delays are prolonged in comparison to those of solid-state FCLs.

Research in the field of FCLs has been intensified in the last two decades with the aim of overcoming the disadvantages of existing FCL technologies. Despite the numerous publications proving the ability of different FCL technologies to protect power systems from over-currents, FCLs have still not been commercialized. Two problems remain:

i. Existing FCL technologies have to be improved, namely, the fault-reaction and post-fault-recovery delays and power losses during nominal operation of the system have to be improved,

ii. The initial cost of FCLs should be lowered.

This gives an inspiration for the following objective of this thesis:

- ◇ Find a new fault-current limiting concept or improve the existing one in order to increase its applicability for MV power systems. The improvements that should be considered are: reduced fault-reaction and post-fault-recovery delays, reduced losses during nominal operation (operation cost) and reduced initial cost.

1.3 Research approach

To achieve the objective the following tasks are defined:

i. Identify the fundamental methods of limiting current from a physical point of view.

ii. Investigate the topologies and configurations of existing FCLs. The topologies will be classified into groups based on established criteria.

iii. Identify which topology (concept) is the most promising. Identify the setbacks of the topology which need improvement.

iv. Propose the new FCL configuration (concept) which solves defined drawbacks.

The performed analysis shows that the FCL fault-reaction delays are the most critical design requirements. From this aspect, FCLs based on the core-saturation effect are the most advantageous. Their reactions to fault inception and clearance are inherent, i.e. they do not have any delay. However, the required amount of magnetic and winding material is considered too large. It will be shown that a saturated-core FCL topology, as proposed in this thesis, substantially decreases FCL weight and cost.

Two different concepts are analyzed and proposed: single-core per phase and single-core for all three phases. To prove the concept, the following four-step procedure is followed.

In the first stage, a first-order mathematical FCL model is developed in Mathcad. The model does not take much computational time. As the accuracy of the result is not sufficient, further design validation is required.

As the next step, the obtained results are used in a transient FCL model in Saber simulator. The created model has the following advantages:

i. The model is simple and the parameters are easy to modify,
ii. It incorporates the non-linear BH curve of the core,
iii. The accuracy of the results is better than the accuracy achieved through the analytical model,
iv. It consumes little computation time - enables optimizations (tuning) of the analytical results.

Although Saber is very suitable for the initial design step, it has key shortcomings. The surrounding air cannot be modeled and the leakage and fringing fluxes are not accounted for. Because large air gaps are included in the proposed FCL topology, these setbacks have a considerable influence on the results.

Therefore, as a final modeling step, the transient non-linear Finite Element (FE) FCL models are developed in both Ansys Classic and Comsol Multiphysics. Having models in both software platforms made it possible to compare and validate the results. The models are excellent tools for verification and optimization of saturated-core FCLs. They take into account all flux effects and the accuracy of the results can be adjusted. The accuracy is a function of the mesh size and the dimensions of the surrounding air. The FE simulations consume much more time and therefore are used only for the final design validation.

The fourth design step is an experimental verification of the designed models. In the first stage, the lab-scale prototypes are built and tested. This is done for both single-phase and three-phase FCL topologies. After proving the FCL principle and verifying the FE FCL model, a full-scale 10 kV prototype is designed and tested.

1.4 Thesis layout

Figure 1-9 shows the main content of the chapters and the relationship between the chapters.

Chapter 2 presents the overview and classification of the existing FCL topologies. The main FCL types are compared with respect to the most important operational requirements. The results show which FCL configuration is the most promising for further development as well as what challenges have to be addressed.

Chapter 3 describes the process of deriving the improved FCL and introduces the new saturated-core FCL topology with an air gap. By using an air gap, the required

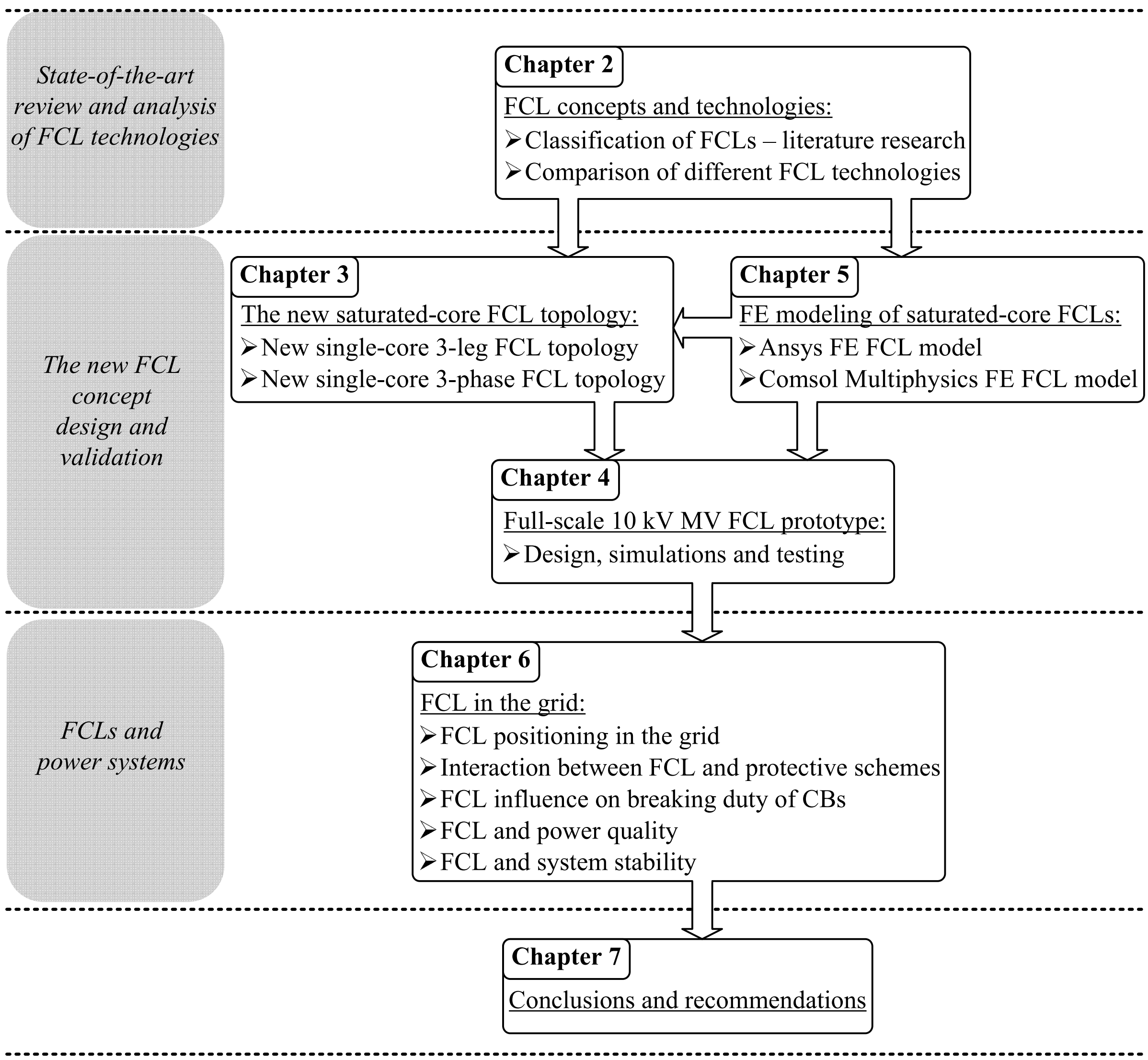

Figure 1-9: Organization and relationship between chapters in the thesis.

amount of magnetic material is considerably reduced. Two configurations are presented: single-phase and three-phase FCLs. The principle of operation is proved through both simulations and experimental testing. Three FCL models are used for this purpose: the first-order analytical model, an FCL transient model in Saber and a Finite Element (FE) transient FCL model in Ansys Classic.

Chapter 4 presents the design and testing results of a full-scale 10 kV MV FCL prototype. The construction of a full-scale FCL prototype was initiated and carried out by Alliander. For this purpose, a single-core three-phase FCL topology is used. The prototype demonstrates the ability of the proposed FCL topology to successfully limit single-phase fault currents in the live grid.

The FE models of saturated-core FCLs are developed in both Ansys Classic and Comsol Multiphysics. Because building these models is not a straightforward process, guidelines on how to make these models are given in Chapter 5. They present the main modeling challenges and steps. The models assure a high level of accuracy of the results by taking into account all flux effects, such as leakage and fringing effects, as well as the nonlinear characteristics of the used materials. The FE modeling results are used in Chapters 3 and 4.

Chapter 6 gives an analysis of different aspects of the interaction between the FCLs and the grid. The following issues are considered the most important: the influence of the FCLs on grid protection and the breaking duty of CBs, the FCLs and power quality and the FCLs and system stability.

Chapter 7 gives the conclusions of the presented work and recommendations for future work.

Chapter 2

FAULT CURRENT LIMITING TECHNOLOGIES

2.1 Introduction

THE previous chapter explained the need for limitation of fault currents in power systems. FCLs are expected to restrain the fault currents to the levels which are low enough not to damage any part of the system and high enough to be detectable by existing protection schemes. A number of different FCL technologies have been introduced in literature. This chapter gives an overview of existing FCL configurations and their operational advantages and drawbacks.

Section 2.2 presents the main fault current limiting principles. Section 2.3 gives an overview of existing FCL topologies, belonging to one of three main FCL groups. The FCL classification in these three groups was introduced in the previous chapter.

Section 2.4 of the chapter gives an analysis of non-semiconductor-based FCLs, where two FCL subtypes are addressed: superconducting and saturated-core FCLs. The analysis firstly includes an overview of the historical background of superconductivity, state-of-the-art review and expectations for new development in the years to come. Secondly, analysis of the operation of saturated-core FCLs in the grid is presented. The goal is to determine the topology which is the most suitable and promising for integration into power systems.

The development status of semiconductor technology is addressed in section 2.5. Power switches present the basis of the design of solid-state and hybrid FCLs.

The last section of the chapter, section 2.6, presents an analysis of the operation of different types of FCLs in power systems. The FCLs are distinguished on the basis of fault-reaction delay and the employed limiting principle. The addressed issues are:

i. The dependency of the first fault current peak on the FCL's fault-reaction delay and the moment of fault inception,

ii. The amount of dissipated energy during the fault in the FCL, as a function of the moment of fault inception, the FCL fault-reaction delay and the duration of the limiting period,

iii. The amount of dissipated energy in CBs as a function of the used type of the FCL.

The most promising technology will be further investigated in order to propose an FCL with improved characteristics, which will be more suitable for installation in power systems.

2.2 Fault current limiting principles

Fault current limiters have extensively been investigated in the past two decades, resulting in a large number of different topologies presented in literature. Two fault-limiting principles can be distinguished:

i. Insertion of resistive impedance,

ii. Insertion of reactive impedance (an inductor, with or without a capacitor).

In essence, an FCL is installed in series with a line as shown in Figure 2-1. The FCL limits the current to an acceptable level, which depends on the system requirements. The limited fault current is also referred to as the 'follow current'.

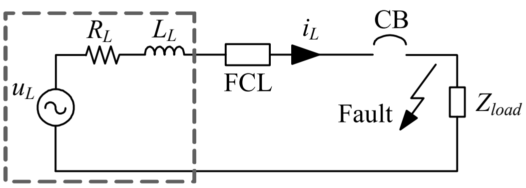

Figure 2-1: Single-phase equivalent circuit with an FCL.

The fault current of the system, in the case of a single-phase to ground fault (see Figure 2-1), is described with the following equation:

$$i_{L,f}(t) = \frac{U_L \sin(\omega t - \varphi_L)}{|Z_L|} + \left(I_{L,t_f} - \frac{U_L \sin(\omega t_f - \varphi_L)}{|Z_L|} \right) e^{-\frac{t-t_f}{\tau_L}}, \tag{2.1}$$

where $i_{L,f}(t)$ is the fault current, $u_L(t)$ the line voltage, φ_L the phase angle of the line impedance, Z_L the line impedance, $I_{L,tf}$ the line current value at the moment of fault inception, t_f the moment of fault inception and τ_L the time constant of the line.

When using a resistive (reactive) FCL, the FCL in Figure 2-1 is replaced by a resistor (an inductor), see Figure 2-2.

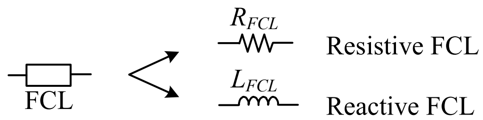

Figure 2-2: A resistive and an inductive FCL.

The difference in the fault operation of the system, when a resistive or an inductive FCL is employed, is that the value of the time constant of the system is different, resulting in a different value of the decaying dc component of the fault current. For the same total impedance of the FCL, the time constant of the faulted line is smaller when a resistive FCL is installed (2.2) than that when an inductive FCL is present (2.3):

$$\tau_{L,RFCL} = \frac{L_L}{R_L + R_{FCL}}, \tag{2.2}$$

$$\tau_{L,XFCL} = \frac{L_L + L_{FCL}}{R_L}, \tag{2.3}$$

where $\tau_{L,RFCL}$ and $\tau_{L,XFCL}$ are the time constants of the faulted system with an inserted resistive or inductive FCL, respectively, L_L is the stray inductance of the line, R_L is the stray resistance of the line and R_{FCL} and L_{FCL} the resistive and inductive impedances of the FCL, respectively.

Thus, for the same total FCL impedance, the first peak of the fault current is lower for a resistive limiting impedance than for an inductive one.

Another difference is that resistive FCLs dissipate energy during a fault, whereas inductive FCLs store the energy in the magnetic field and returns it to a system at the end of each cycle during a fault. Therefore, if the normal operation of the system is restored without interrupting the current flow, inductive FCLs do not introduce power losses to a system (inductor resistance is neglected here). In the case that a line is interrupted, only the energy that is stored in the last cycle is dissipated in the CB.

A reactive FCL can utilize both an inductor and a capacitor to limit a fault current. The FCL is, in this case, typically replaced by a parallel connection of the capacitor and the inductor, which are tuned to resonate at the grid frequency, see Figure 2-3.

The capacitor C_{FCL} is inserted in series with a line and its value is set to compensate the stray inductance L_L of the line. In the case of a fault, the inductor L_{FCL} is placed

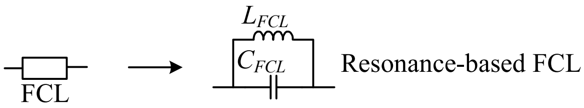

Figure 2-3: A resonance-based FCL.

in parallel to the capacitor C_{FCL} and the resonant impedance of the parallel LC circuit limits the fault current:

$$Z_{FCL,res} = j\frac{\omega L_{FCL}}{1-\omega^2 L_{FCL} C_{FCL}}. \tag{2.4}$$

The following section gives an overview of existing FCL topologies and their operational characteristics. Each of these topologies uses one of the two described limiting principles.

2.3 Overview of FCL technologies

The classification of the FCL technologies is given in Chapter 1. As stated, three main groups are distinguished: non-semiconductor-based, solid-state and hybrid FCLs. This classification of FCLs will be used for further considerations in this chapter. The rest of this section summarizes the main features of each of the three main groups.

Table 2-1 shows which limiting principle is used by each of the FCL technologies. As can be seen, hybrid FCLs utilize only the principle of resistive impedance, whereas other FCL technologies use both limiting principles.

Table 2-1: FCL technologies and utilized fault limiting principles.

		Limiting principle		
		Resistive	Reactive	
			L	LC
FCL Technology	Non-semiconductor-based FCLs	√	√	√
	Solid-state FCLs	√	√	√
	Hybrid FCLs	√		

Very important feature of non-semiconductor based FCLs is that they inherently react to a fault when the fault current crosses a preset threshold value. There is no reaction-delay since no fault-detection circuit is required for the FCL activation. After the fault is cleared, they automatically return to the pre-fault state, i.e. their limiting impedance becomes sufficiently low.

Solid-state FCLs employ power semiconductor switches. The switches conduct during normal operation of the system and provide a low impedance path for the normal current.

In the case of a fault, the switches are turned off, diverting the fault current onto the parallel path comprising the limiting impedance. As stated in Chapter 1, solid-state FCLs can be with or without a fault-reaction delay. The FCLs belonging to the first group must be triggered by a fault-detection circuit, which results in a fault-reaction delay. As will be shown later, some topologies of solid-state FCLs can be designed to inherently react to a fault. The drawback of these FCLs in comparison to the non-semiconductor-based FCLs is that their reliability is lower since semiconductors are employed.

To avoid power losses (voltage drop) in the semiconductors during normal regime, mechanical switches can be added to solid-state FCLs. They provide a primary path for the normal current. Such a device, comprising both mechanical and electrical parts, is recognized as a hybrid FCL. The drawback of employing a mechanical switch is that the fault-reaction delay of an FCL is increased. It is equal to the sum of the fault-detection delay and the time needed for the mechanical switch to fully open and regain its dielectric strength. The delay of the mechanical switch is determined by its size, i.e. by the value of the normal current and the breaking voltage that it has to provide to force the fault current onto the auxiliary parallel path comprising power semiconductors. This delay considerably extends the fault-reaction delay of an FCL, by a factor of 2 or more with respect to solid-state FCLs.

An overview of the existing FCL topologies is given in the rest of the section. They are presented according to the introduced classification of FCLs in three groups, based on the applied technology (see Table 2-1).

2.3.1 Non-semiconductor-based FCLs topologies

Three types of non-semiconductor-based FCLs can be distinguished:

i. FCLs based on Superconducting/Normal (S/N) transition of superconducting materials,
ii. FCLs based on the core-saturation effect,
iii. Transformer-type FCLs with parallel resonant circuit.

i. FCLs based on S/N transition of superconducting materials

Superconductivity (SC), the state when a conductor experiences zero-resistance for the current flowing through it, was discovered in 1911 by Dutch physicist Heike Kamerlingh Onnes. He observed that the resistance of mercury, when cooled to a temperature of 4.2 K, practically disappears [Onne 11]. The temperature dependency of SC resistance is

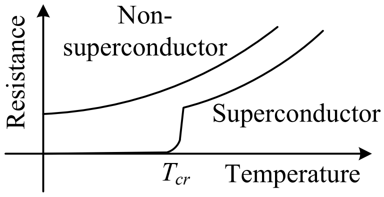

Figure 2-4: Change of SC resistance with temperature.

shown in Figure 2-4. When the temperature of the superconducting material reaches the critical temperature T_{cr}, its resistance suddenly drops to a very low (negligible) value.

When used as an FCL, an SC device is connected in series with a line and conducts the line current, see Figure 2-5 [Noe 07b]. A refrigeration system ensures that power losses, dissipated in the SC during normal operation of the system, are removed so that the temperature of the SC stays below its critical temperature T_{cr}. In this state, the superconductive FCL (SFCL) imposes no impedance on the power system. In the case of a fault, the increased current density in the SC triggers its transition, called quenching, from the superconducting to normal state. The increased resistance of the SC restrains the fault current.

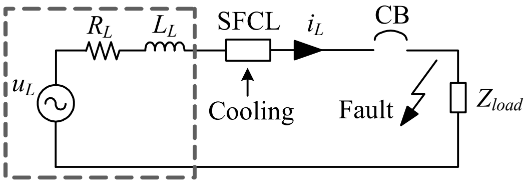

Figure 2-5: Installation of SFCL in series with a line.

After the fault is cleared, the SFCL is cooled again to the temperature below its critical temperature T_{cr}, i.e. it regains its low-resistance state and again becomes 'invisible' for the power system. The reaction of an SFCL to a fault is fast enough to restrain the first peak of the short-circuit current.

The quenching of an SC can be triggered not only by its current density but also by the value of its temperature and by the value of magnetic field to which the SC is exposed. A superconducting operating area is defined by critical levels of these three parameters, see Figure 2-6 [Busc 01]. If any of them exceeds its critical level, the SC will experience superconducting-normal (S/N) transition.

A number of SC materials (compounds) have been discovered since 1911. Research on SC for fault current limiting applications has been intensified with the discovery of High Temperature Superconductors (HTS) in 1986 by Karl Muller and Johannes Bednorz. High-temperature superconductors have a critical temperature T_{cr} above 30 K and they are cooled by liquid nitrogen.

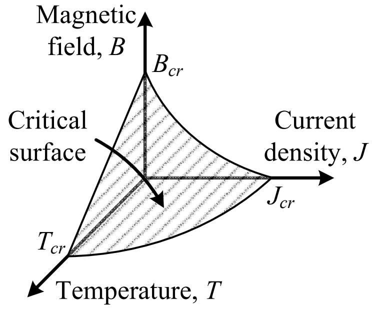

Figure 2-6: An SC critical surface as a function of magnetic field intensity B, current density J and temperature T.

The SFCLs can utilize two limiting principles: insertion of resistive or reactive impedance. A resistive SFCL is connected in series with a line and quenches when a fault current exceeds its critical current density (see Figure 2-6). The SFCL exhibits a rapid quench, shorter than 1 ms, and successfully limits the first fault-current peak [Chen 02; Xie 07]. The duration of a fault-limiting period is proportional to the available thermal capacity of the refrigerator and the amount of dissipated heat. The longer the fault-operation of the SFCL is, the more time is required for the recovery (N/S transition) of the SC.

Magnetic-shield SFCLs insert reactive impedance in a line [Ichi 03a; Ichi 95]. The typical topology uses one magnetic core, one ac and one superconductive winding, see Figure 2-7.

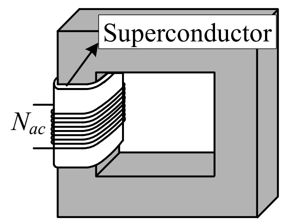

Figure 2-7: Magnetic-shield superconducting FCL topology.

The ac winding is connected in series with a line. During normal operation, the superconductive winding cancels the flux generated by the main winding. The resulting inductance of the ac winding is, consequently, very low. Upon fault inception, the induced currents in the superconducting winding exceed the threshold level and cause a quench of the superconductor. Since the flux generated by the ac winding is not cancelled out any more, the inductance of the ac winding increases and limits the fault current. In this topology, the superconductor is not directly limiting the fault current as is the case with resistive SFCLs.

ii. FCLs based on the core-saturation effect

The impedance of a non-linear inductor (see Figure 2-8) is a function of the mean length of the flux path l_{mean}, the cross-section of a core A_{core}, the number of winding turns N_{ind} and the relative permeability of the core μ_r (2.5). By driving the magnetic core into saturation, the inductance of the inductor decreases in comparison to when the BH working point is outside the saturation region (see Figure 2-9) [Raju 82].

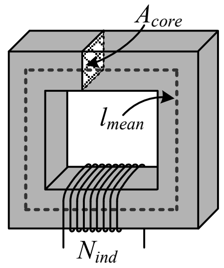

Figure 2-8: Non-linear inductor.

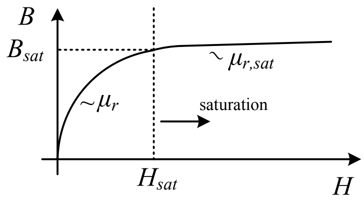

Figure 2-9: Non-linear BH curve of the magnetic core.

The approximate inductances for the unsaturated and saturated case are given by:

$$L_{wind,lin} = \mu_0 \mu_r \frac{N_{ind}^2 A_{core}}{l_{mean}}; \quad L_{wind,sat} = \mu_0 \mu_{r,sat} \frac{N_{ind}^2 A_{core}}{l_{mean}}, \tag{2.5}$$

where $L_{wind,lin}$ and $L_{wind,sat}$ are the impedances of the FCL during fault and normal regimes respectively, μ_0 the permeability of air and $\mu_{r,sat}$ the relative permeability of the core in saturation.

Since the inductance can take two values, such an inductor can be used as an FCL. The cores must be saturated during normal operation of the system and driven out of saturation in the case of a fault. The core can be saturated by an additional winding conducting a dc current that is supplied from an auxiliary source or by using a permanent magnet, as presented in Figure 2-10. The inductor winding is connected in series with a line and conducts the phase ac current. During normal regime, the saturation must be deep enough that the maximum expected normal current cannot drive the core out of saturation (2.6). Upon fault inception, the rising mmf $N_{ac} i_{L,f}$ desaturates the core and increases the FCL inductance considerably.

$$N_{dc} I_{dc} - N_{ac} I_{L,max} > H_{sat} l_{mean}, \tag{2.6}$$

where N_{dc} is the number of dc turns, I_{dc} the dc current, $I_{L,max}$ the maximum normal magnitude of the line current and H_{sat} the saturation value of the magnetic field.

The FCL cores in Figure 2-10 only limit the current for one polarity of the fault current. Two configurations of the FCLs based on the core-saturation effect exist to deal

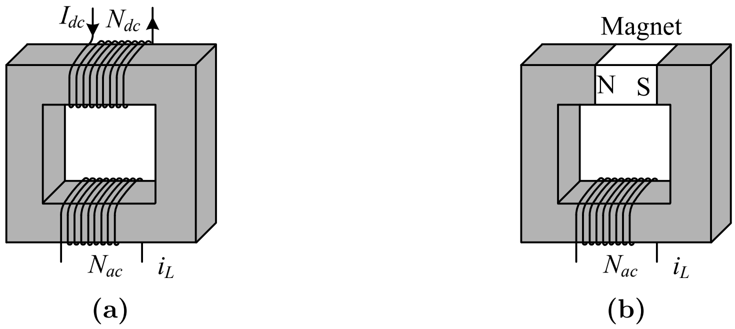

Figure 2-10: Means of saturation of FCL core: (a) Using a dc current; (b) Using a permanent magnet.

with the bipolar nature of ac current: namely an FCL with two cores per phase (see Figure 2-11a) and an FCL with one core and one bridge rectifier per phase (see Figure 2-11b). If only a single-core FCL is used, the core would be desaturated in one half-cycle by the fault current and driven even deeper to saturation in the following half-cycle. Thus, the fault current would not be restrained during the whole cycle. By employing two cores saturated in opposite directions [Raju 82] or by rectifying the line current [Muta 04] the proper limiting effect for both polarities of the fault current is obtained.

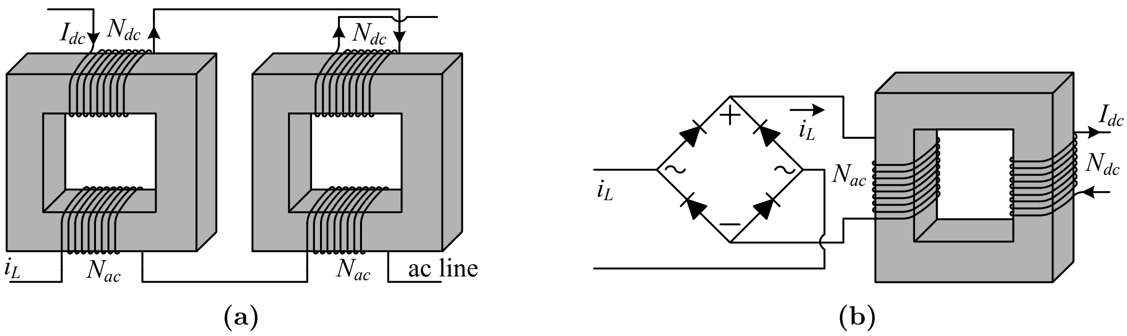

Figure 2-11: Two topologies of saturated-core FCLs: (a) FCL with two cores per phase; (b) FCL with one rectifier and one core per phase.

Saturated-core FCLs thus employ the limiting principle of the insertion of reactive impedance.

iii. Transformer-type parallel resonant circuit

The schematic of a resonant FCL with a parallel connected transformer is given in Figure 2-12 [Xiao 05]. It comprises a capacitor and transformer with a discharging gap on the secondary side. During normal operation, the secondary side of the transformer operates as an open circuit since the voltage drop across the FCL is not sufficiently large to cause a breakdown of the discharging gap. Consequently, the transformer impedance from the primary side is almost equal to the magnetizing reactance, which is much larger than the capacitive reactance of the capacitor C_{FCL}. The FCL is seen by the system as the series capacitor and it compensates for the stray reactance of the system.

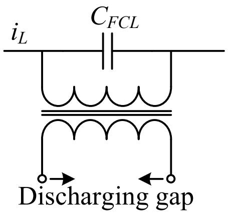

Figure 2-12: FCL topology with a parallel resonant circuit and discharging gap.

During fault regime, the discharging gap is exposed to the much higher voltage. It breaks down and the inductance seen from the primary side becomes very low. The inductance resonates with the parallel capacitance C_{FCL} and increases the limiting impedance of the FCL.

This FCL type employs, thus, principle of insertion of reactive impedance, where both inductor and capacitors are used.

2.3.2 Solid-state FCL topologies

A number of different FCL topologies utilizing power semiconductors are proposed. They can be classified in four subgroups on the basis of employed operational principle:

i. Bridge-type FCLs,
ii. FCLs with discharging capacitors,
iii. FCLs with series compensation,
iv. FCLs employing resonant LC parallel and/or serial circuits.

They will be considered below.

i. Bridge-type FCLs

The principal schematic of bridge-type FCLs is presented in Figure 2-13 [Hosh 01]. During normal operation of the system, all four semiconductors are forwardly biased by an installed dc voltage source. Provided that the value of dc current is larger than the normal line current, all diodes will be conducting during normal operation. This implies that the limiting impedance of an FCL is not inserted in the system, see Figure 2-13. As can be seen, bridge-type FCLs employ reactive impedance.

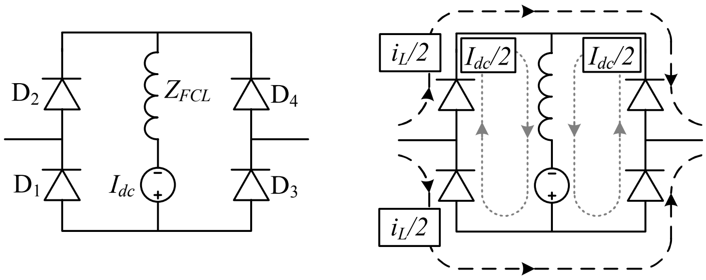

Figure 2-13: A bridge-type FCL with a dc current source: schematic and current distribution.

In the fault regime, the fault current exceeds the level of the biasing dc current and turns off a pair of diodes D_1-D_4 or D_2-D_3 respectively, from one half-cycle to the other. The path of the fault current is, therefore, diverted to the limiting impedance Z_{FCL}. Since the fault current itself triggers the limiting operation, there is no fault-reaction delay. The fault-triggering level can be adjusted by tuning the value of the dc current.

To reduce the losses of an FCL, a dc reactor can be fabricated from the superconducting material [Min 04; Seun 04]. Since SC material does not quench on fault, there is no recovery delay after the fault clearance. Still, losses in this type of FCL are not negligible since semiconductors are placed in series with a line.

The performance of bridge-type FCLs is dependent on the reliability of the utilized semiconductors. This is a drawback of this FCL type in comparison to non-semiconductor-based FCLs. Other bridge-type FCL topologies can be found in Appendix A.

ii. FCLs with discharging capacitors

An FCL with two discharging capacitors - Two main thyristors Th_1 and Th_2 are used to conduct the normal current, see Figure 2-14. At a fault, the main thyristors cannot be turned off before the next natural zero-crossing of the line current, which would allow too much time for the fault current to rise. An artificial (induced) zero-crossing of the current through the main thyristors is obtained by triggering the auxiliary thyristors Th_{1A} and Th_{2A} and discharging the precharged capacitors C_1 and C_2. The fault current is diverted to the limiting impedances R_1 and R_2 and limited [Noe 07b]. FCLs with discharging capacitor employ therefore a principle of insertion of resistive impedance.

The magnitude of the follow current can be controlled by adjusting the phase angle of the main thyristors. An FCL topology with one discharging capacitor instead of two is presented in Appendix A.

iii. FCLs with series compensation

Figure 2-15 shows the typical topology of an FCL with series compensation [Junz 99]. The FCL utilizes both an inductive L_{FCL} and a capacitive C_{FCL} impedance, which are

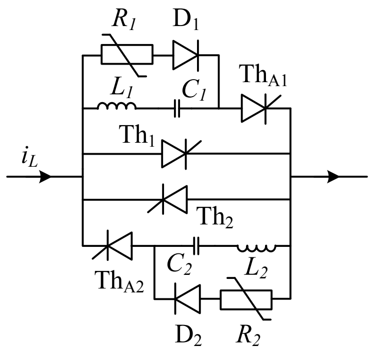

Figure 2-14: FCL with two discharging capacitors.

inserted in series with a line. They compensate each other during normal operation (2.7) so that the FCL does not insert impedance in the line.

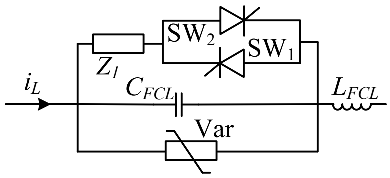

Figure 2-15: FCL with series compensation [Junz 99].

$$\omega L_{FCL} = \frac{1}{\omega C_{FCL}} \tag{2.7}$$

The semiconductors are turned on when a fault is detected. They bypass the capacitors C_{FCL} and leave only the inductor L_{FCL} in the line. The impedance Z_1 prevents an inrush current through the semiconductors. The switches and capacitor are protected from voltage peaks by the varistor Var.

The value of the capacitor C_{FCL} can be adjusted to compensate not only the FCL inductance L_{FCL} but also the inductance of the system L_L (not shown in Figure 2-15). In this way the power capacity of the power system can be enlarged. However, readjustment of the capacitance is required since the parameters of the power system change with time.

Other topologies of an FCL with series compensation are given in [Xing 02; Zou 02].

iv. FCLs using the resonant effect of an LC parallel and/or serial circuit

Resonant type FCLs are based on a specific property of parallel and/or series connected inductors and capacitors - a very high or a very low impedance at their eigenfrequency:

$$\omega^2 = \frac{1}{L_{FCL} C_{FCL}}. \tag{2.8}$$

For an FCL this frequency is selected to be equal to the frequency of the power grid. A typical resonance-based FCL topology is presented in Figure 2-16 [Chan 00]. During normal regime, the switches are not gated allowing the line current i_L to flow through the capacitor. The capacitor is tuned to compensate the stray inductance L_L of the system. After fault inception, the switches are turned on and the parallel connection of the inductor L_{FCL} and the capacitor C_{FCL} resonates and introduces reactive limiting impedance in the line.

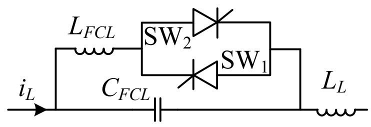

Figure 2-16: FCL resonant topology with a parallel resonant circuit.

2.3.3 Hybrid FCL topologies

Hybrid FCLs employ both power semiconductors and mechanical switches to enable controllability of the fault current value and provide low power losses during normal operation.

A typical hybrid FCL topology is presented in Figure 2-17. The normal conducting path comprises only mechanical switch S_2. Thus, the FCL has no losses during normal operation. Upon fault inception, the switch S_2 opens and transfers the fault current onto the branch with IGCTs and mechanical switch S_1. After a certain time delay, during which the dielectric capability of the switch S_2 is recovered, the IGCTs are turned off and the fault current is shunted onto the limiting impedance Z_{FCL}. In principle, hybrid FCLs insert resistive impedance in the line. The function of the switch S_1 is to interrupt the branch after the IGCTs are gated off and to protect the IGCTs from an over-voltage [Noe 07b]. Other hybrid FCL topologies are presented in Appendix A.

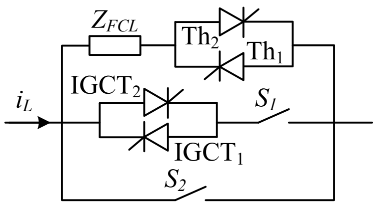

Figure 2-17: Hybrid FCL topology [Noe 07b].

2.3.4 FCLs - Past experience and on-going projects

Appendix B gives an overview of worldwide experience regarding the development and testing of FCL prototypes based on some of the presented technologies. The overview includes project specifications, achieved results, remaining challenges and plans for the future.

2.4 Non-semiconductor-based FCLs - state-of-the-art and operational analysis

2.4.1 Introduction

This section gives a detailed analysis of the operational advantages and disadvantages of non-semiconductor-based FCLs, where two subtypes are considered: superconductive and saturated-core FCLs.

The analysis firstly includes an overview of the historical background of superconductivity, its state-of-the-art status and expectations for further development and new possibilities. Secondly, an analysis of the operation of saturated-core FCLs in a grid is presented. The goal is to determine which topology is most suitable and promising for integration in power systems. This topology will be further analyzed in order to solve its operational disadvantages.

2.4.2 Superconductive FCLs

The detailed and extensive research on superconductive FCLs (SFCLs) has been performed in the last decade. Superconducting technology is investigated more than any other fault current limiting technology, resulting in a large number of publications. The experience and running projects about SFCLs can be found in appendix B.

The analysis of the SFCLs presented in this section is given in the form of an overview of the results available in literature.

Material types - Research into the application of superconductivity for fault current limiting purposes has increased since the discovery of high-temperature superconductive (HTS) materials in 1980s. These HTS materials are also known as second generation (2G) superconductors. HTS are characterized by their relatively high critical temperature, above 30 K. They are cooled using liquid nitrogen LN_2 instead of liquid helium, whose temperature is 4.2 K. Low-temperature superconductive FCLs usually operate very close to their critical temperature and are therefore very sensitive to temperature changes. The refrigeration system must have a higher capacity than that of HTS FCLs, which significantly increases investment costs. Refrigeration costs can be decreased by using HTS instead of LTS, even by a factor of 10 [Supe]. The most used HTS materials for FCL applications are:

i. $YBa_2Cu_3O_7$ (yttrium barium copper oxide - typically referred to as YBCO),
ii. $Bi_2Sr_2Ca_1Cu_2O_8$ (bismuth strontium calcium copper oxide - typically referred

to as BSCCO 2212),

iii. $Bi_2Sr_2Ca_2Cu_3O_{10}$ - typically referred to as BSCCO 2223.

The YBCO superconductor was discovered in 1987 [Wu 87] and its critical temperature is equal to T_{cr}=93 K. The BSCCO HTS material was discovered in 1988 [Maed 88]. The critical temperature of the BSSCO-2212 is T_{cr}=95 K and that of the BSCCO-2223 is T_{cr}=107 K. An FCL made of these materials would be cooled by liquid nitrogen and would operate, thus, below 77 K.

FCL design challenges - The challenges of SFCL technology are:

i. Post-fault recovery time is too long - especially if Recovery Under Load (RUL) operation is required,

ii. The post-fault recovery time is a function of the duration of the limiting period. If the limiting period is shortened, the operation of protective relays can be affected,

iii. Hot-spot effect, i.e. the problem of uneven quench of SC, occurs during quench,

iv. Scaling up for higher-voltage applications is challenging,

v. SFCLs are considered as costly.

These challenges are addressed below in the listed order.

An SFCL with quench has to be cooled below its critical temperature using cryogenic system to regain its superconductive state and again become 'invisible' for the power system. This transition usually requires a considerably long time interval, in the range of several seconds [Min 07; Tekl 99; Xie 07]. The recovery interval is further extended if the superconductor has to recover while conducting the normal current of the system - RUL requirement. The RUL requirement can even prevent the SFCL from achieving full recovery [Supe 08]. The duration of the fault limiting period is directly related to the amount of dissipated heat in the SFCL. Since SC material can be damaged by overheating [Bock 05; Hass 04], the fault must be cleared fast enough to prevent a too high rise in SC temperature. The imposed constraint can affect the coordination of protective relays which need a certain amount of time to detect and localize the fault source.

Recovery delay can be reduced if YBCO Coated Conductor (YBCO CC) is employed [Xie 07]. Namely, this conductor has a larger cooling area and therefore enables easier and faster heat removal in comparison to that of a bulk superconducting material [Min 06]. Fast post-fault recovery is a strict operational constraint, and has to be improved before integration of SFCLs in the electrical grid can be realized.

The YBCO CC (2^{nd} generation of HTSC) superconductor is the most promising material for the FCL applications. It features the following merits in comparison with the other SC materials (YBCO thin film, BSCCO-2212 bulk tube, BSCCO-2212 thick film etc.) [Ho M 04; Min 06]:

i. It is made by a coating process - making it relatively easy to control the thickness of material and stabilizer part,
ii. It has large critical current density,
iii. It has good cryo-stability.

Localized (non-uniform) power dissipation in the superconductor during a fault operation is caused by electrical inhomogeneities [Park 03]. It leads to the occurrence of 'hot spots' [Noe 07b]. In the case of a slow quench, which is typical for bulk material with low current density and large thermal capacity, the hot spots are not likely to occur. However, YBCO CC has high current density and low thermal capacity. In this case, S/N transition is very fast and the development of hot spots is very likely [Ok B 03]. Localized power dissipation can lead to severe damage of the SC material. Two techniques are proposed in literature to provide a uniform quench of the SC:

i. Deposition of a shunt resistive layer (metallic bypass) along the superconductor,
ii. Magnetic-assisted quench.

The resistive shunt layer has to be deposited along the whole length of the SC material and electrically connected to it [Noe 07b]. Occurrence of hot spots in the SC will divert the fault current onto the resistive shunt layer. As a result, the voltage is uniformly distributed along the SC length, which leads to a uniform quench [Ok B 03]. It is particularly important to apply a shunt-assisted quench when connecting a larger number of SC elements in series for higher-voltage applications. Uneven quenching could damage one of them. This technique is demonstrated in live-grid testing [Bock 05]. However, due to the lower resistance of the shunt layer, very large lengths of the superconductor are required for higher-voltage applications. This is an impractical solution.

Quenching of the superconductor can be induced by applying an external magnetic field, see Figure 2-6. The magnetic-assisted quenching technique utilizes this principle [Elsc 06]. A coil is wound around the SC module for this purpose. If hot spots occur, a part of the fault current is diverted onto the coil. The produced magnetic field induces a rapid and simultaneous magnetic quenching of the SC. Since the fault current is limited by the normal impedance of the SC, a much shorter length of SC is needed than with the shunt-layer technique. A conceptual design of an HV 110 kV SFCL shows the feasibility of the magnetic-assisted quenching technique [Noe 07a].

A large drawback of SFCLs is the high price of the SC materials and cryogenic cooling systems [Lee 08]. The price-performance ratio (electrical performance versus production cost) of SC material has to be significantly lowered to compete with that of copper. The price of copper presently ranges from 25 euro/kAm to 50 euro/kAm in typical cable applications. The cost of SC material is determined by three factors: the cost of the raw material, production (labor) costs and equipment costs [Fles 09]. Improvements regarding raw material utilization in the production process, automation of the production process and development of equipment with higher production rates of SC material could lower the price of SFCLs. Presently, the price of first generation (1G) SC wire is 150 euro/kAm (a long term decrease to 50 euro/kAm is expected), while 2G wire has a higher price of 200-300 euro/kAm (long term $<$ 10 euro/kAm) [Noe 08]. The reduction of ac losses in the SC material would result in a smaller and more compact cryogenic system and, therefore, a lower overall price of SFCLs.

The superconductivity of magnesium diboride (MgB_2) at temperatures below 39 K was discovered in 2001 [Yuji 01]. The price of raw MgB_2 is significantly lower than that of other SC materials [Brac 07; Gras 05]. On the other hand, its operating cost is higher since its normal operation temperature, being much lower than that of other HTSs, requires more powerful cooling systems. The applicability of MgB_2 for fault current limiting purposes is demonstrated [Nard 07]. This material has to be further investigated and characterized before it could be used for the protection of real grid.

Recently, a hybrid superconductive FCL concept has been introduced [Lee 08] with the goal of reducing the overall cost of FCLs, see in Figure 2-18. A superconductor is used as the main conducting path for the normal current. After fault inception, the SC quenches and transfers the current onto a parallel path with a so-called drive coil that actuates a contact. An interrupter (mechanical switch) is consequently opened and the fault current is limited by the coil. Thus, the SC material is only used for the initial fault-operation. The post-fault recovery time is reduced because less heat is dissipated in the SC part. It is said that the cost of FCL is reduced by a factor of 10 [Lee 08]. The concept requires further investigation before it can be applied to real grid.

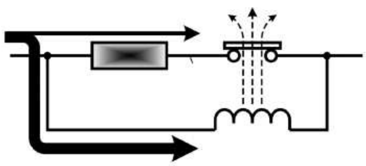

Figure 2-18: Hybrid SFCL topology [Lee 08].

In general, superconductivity is a promising technology for fault current limiting applications. It does not introduce a voltage drop in a line during normal regime and it reacts automatically in case of a fault. However, drawbacks such as slow post-fault recovery time, problems with scalability and high cost have to be resolved before SFCLs can be applied to power systems.

2.4.3 Saturated-core FCLs

Introduction

The principle of operation of an FCL based on the core saturation effect was explained in the subsection 2.3.1. The first saturated-core FCL prototype, rated at U_L=3 kV$_{rms}$ and I_L=556 A$_{rms}$, was designed and tested in 1982 by Raju B. P. [Raju 82], proving that this type of FCL can successfully limit a fault current.
The analysis presented in this section includes the following points:

i. An overview of the principal advantages and drawbacks of saturated-core FCLs in comparison with other types of FCL,
ii. Double-core versus single-core FCL design,
iii. An analysis of existing double-core FCL topologies.

i. Advantages and drawbacks of saturated-core FCLs

The operational advantages of FCLs based on the core saturation effect are:

a. There is no fault-reaction delay,
b. There is no recovery delay after a fault is cleared,
c. The duration of the fault limiting period is unrestricted,
d. There is no operational deterioration when limiting consecutive faults,
e. Power dissipation during normal regime is negligible.

The FCL's magnetic cores are saturated deep enough so that flux change due to the normal current cannot drive them back to a linear regime, see Figure 2-19. In the case of a fault, the BH working point is driven out of saturation which results in increased FCL impedance. The level of the fault current at which the FCL will begin its limiting action is a function of the width of the safety margin, see Figure 2-19. In respect to the peak of the limited fault current, the width of the safety margin is negligible and the reaction of the FCL can be considered instantaneous.

The number of required ac turns N_{ac} is determined using the equation (2.5). The relation between the dc current I_{dc}, the line current i_L and the magnetic field in the core

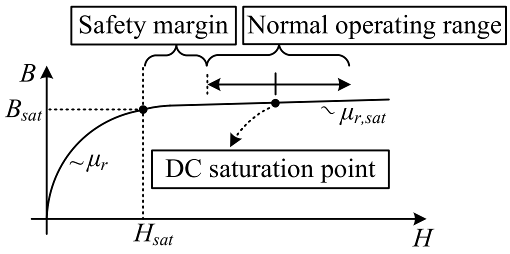

Figure 2-19: FCL operation during normal regime - a flux variation.

H is given by (2.6). To account for the width of the safety margin H_{saf}, the equation (2.6) can be rewritten as:

$$N_{dc}I_{dc} - N_{ac}I_{L,max} = (H_{sat} + H_{saf})\, l_{mean}. \tag{2.9}$$

The cores instantaneously return to the saturation state after the fault clearance. Thus, as the value of the line current is decreased, the impedance of the ac windings drops without post-fault recovery delay. This enables the inductive FCL to restrain any number of consecutive faults.

In principle, there is no energy dissipation (Joule's losses) during the limiting period due to the inductive nature of FCL impedance. There are losses due to the windings resistance. They can be removed by means of liquid oil. The dissipated power is rather small in comparison to the nominal line power. The duration of the limiting period is not restricted by the amount of acceptable heat dissipation in the limiting impedance, as it was the case with resistive FCLs. The limited fault current can continuously flow as long as is required by the present protective schemes. Inductive FCLs cannot operate as a current interrupter. The fault current has to be cleared by other protective equipment, such as CBs.

In spite of the listed advantages of inductive FCLs over other FCL types, they have not been commercialized due to the following design challenges:

a. Large size and cost of materials,
b. Induced over-voltage across a dc current source during fault operation.

A number of the FCL topologies have been proposed with the goal of solving some of the listed challenges. Still, a better solution is awaited. The following section investigates the saturated-core FCLs in more detail. The operation of the two main topologies, the single-core and double-core topologies, are compared in order to determine the one which is more advantageous.

ii. Comparison of single-core and double-core FCL topologies

The size and cost of a saturated-core FCL can be reduced if one magnetic core with a bridge rectifier is used per phase, instead of two magnetic cores (see Figure 2-11a and Figure 2-11b). With one core the total amount of material is reduced by 50%.

Models of both topologies have been made in Saber simulator (Figure 2-20) in order to compare them with respect to the amount of required material and the operational characteristics during a fault regime. Saber can be used as a simulator for mixed electro-magnetic circuits. The ac electrical circuits, see Figure 2-20a, consists of a voltage source, the inductance and resistance of the line, a diode rectifier, the ac windings of the FCL and load resistance. The dc electrical circuit comprises two elements: a dc current source and the dc FCL winding.

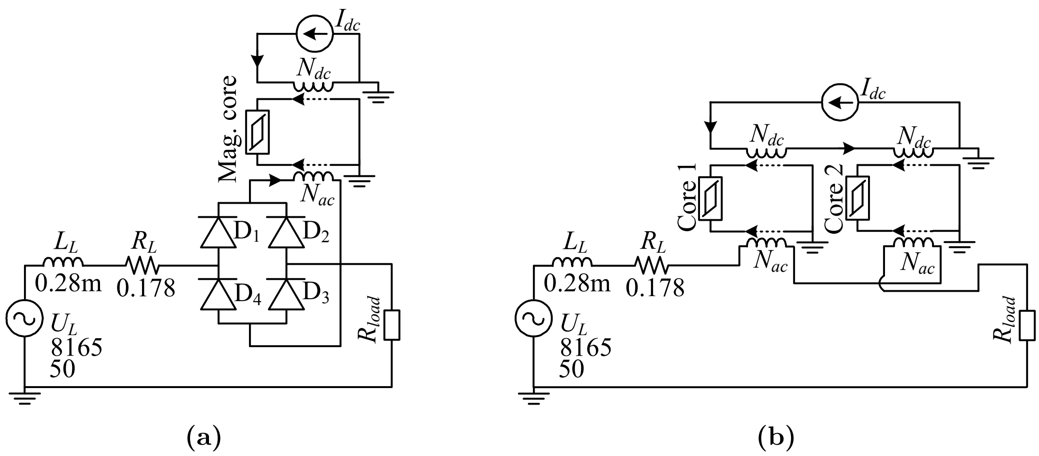

Figure 2-20: FCL models in Saber: (a) A single-core FCL topology; (b) A double-core FCL topology.

The magnetic circuit is modeled using magnetic elements. Each magnetic element represents one leg of a magnetic core. A closed magnetic path is created by connecting the ends of the magnetic elements to each other. Two examples are given in Figure 2-21. If the magnetic core has a single closed path, one magnetic element is sufficient, see Figure 2-21a. In the case that the core has more than one closed path, the number of required magnetic elements is equal to the number of the core's legs, see Figure 2-21b. One node of the core must be grounded in order to define a reference point for simulated signals. An option set of a magnetic element offers the possibility of defining a non-linear BH curve and, if needed, an air gap.

In the created FCL models, the magnetic core is modeled using one non-linear magnetic element, see Figure 2-20.

Simulations showed large differences in operation during fault and post-fault periods

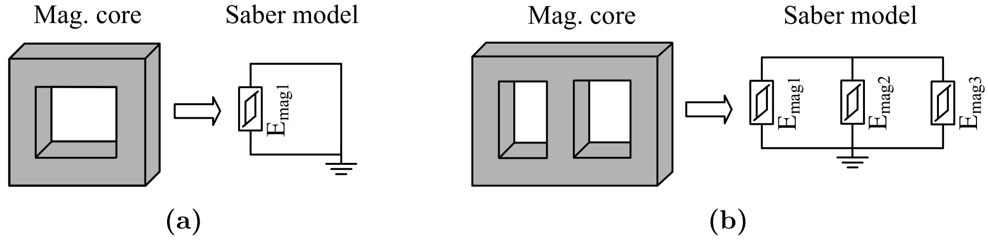

Figure 2-21: The model of a magnetic core in Saber: (a) A core with a single closed magnetic path; (b) A core with multiple closed magnetic paths.

of these two FCL configurations. Namely, when the single-core FCL topology is used, attention has to be paid to the following drawbacks:

a. The duration of the fault-limiting period is restricted,

b. A post-fault recovery delay actually exists.

With a single-core FCL, the peak of the fault current increases from cycle to cycle because its ac winding conducts a dc current, see Figure 2-22a. The core will gradually be driven to the opposite saturation region and, consequently, will stop limiting the fault current after a certain number of cycles (see Figure 2-22b). The duration of the limiting period is proportional to the size of the core. However, if the size of the core is enlarged to prolong the limiting-period, the single-core FCL would lose its advantage over the other FCL topology: a lower amount of magnetic material.

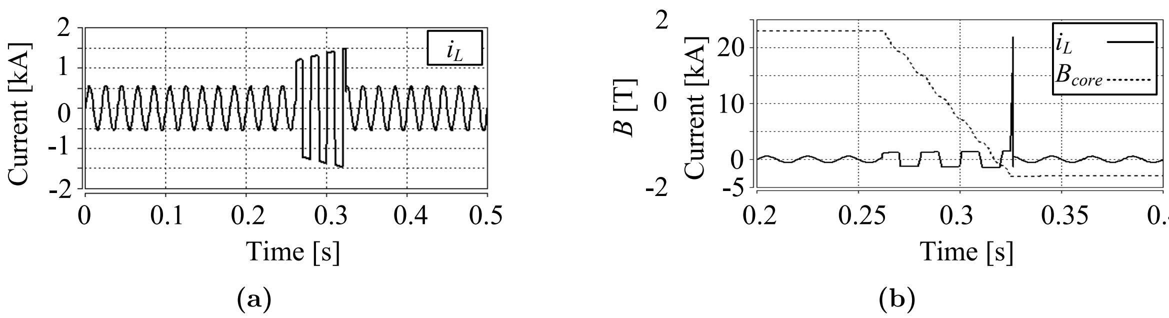

Figure 2-22: The simulation results of a single-core FCL model in Saber: (a) The fault current; (b) The fault current gradually drives the core toward the opposite saturation region.

Another disadvantage of the single-core FCL topology is that it has a post-fault recovery delay. Namely, even though the fault is cleared and the system enters its nominal regime, the large current inside the bridge rectifier continues to flow for a considerable interval of time. This interval is proportional to the time constant L_{FCL}/R_D (see Figure

2-23a), where R_D is the resistance of the bridge diode. Since the bridge current is much larger than the nominal current of the system, all four bridge diodes continue to conduct. The path of the line current is presented in Figure 2-23b. As long as the bridge current is different from zero, the FCL is not capable of restraining the following fault. Its BH operating point remains in the position determined by the peak of the previous fault current. In the case of a following fault, the core can be driven to the opposite saturation region, see Figure 2-24. The fault current is not limited in this case.

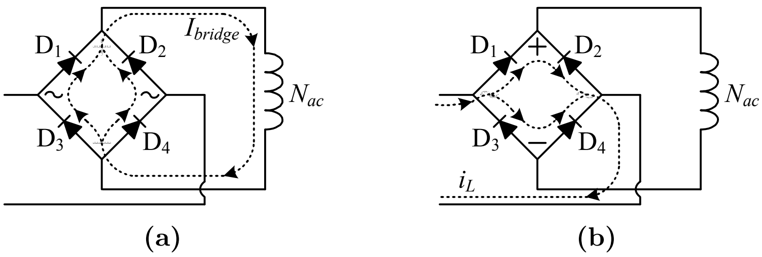

Figure 2-23: Post-fault current flow: (a) The bridge dc current; (b) The line current.

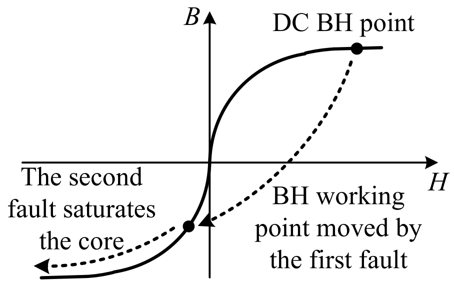

Figure 2-24: Core is driven to the opposite saturation region by the second fault if the bridge current is not cleared after the first fault.

For the single-core topology, the simulation results presented in Figure 2-25a and Figure 2-25b show the current of the ac winding and the current of bridge diodes D_1 and D_2, respectively. The fault is incepted at t_f=0.262 s. After the fault is cleared at t_{cl}=0.324 s, the current of the ac winding decays gradually toward the value of the nominal line current. Due to the large time constant, which is in the range of several seconds, the decay of the current cannot be seen in Figure 2-25a. It appears to have a constant value. Figure 2-25b shows that, after the fault is cleared, each of the diodes conducts half of the winding current i_{wind} and half of the line current.

The simulation result of the FCL reaction to two consecutive faults is shown in Figure 2-26. The faults are incepted with a time difference of 0.438 s, at t_{f1}=0.262 s and t_{f2}=0.762 s. Clearly, the FCL did not limit the second fault.

It is necessary to clear the bridge post-fault current by some other means if the FCL is to limit consecutive faults. Controllable power semiconductors could be used instead of

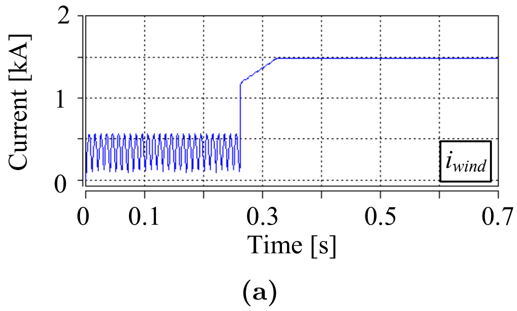

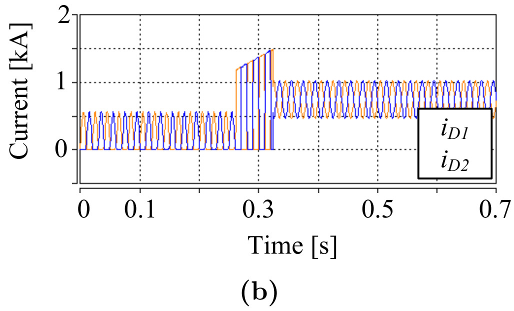

Figure 2-25: The current waveforms during pre-fault, fault and post-fault periods: (a) The current in the ac winding; (b) The currents in diodes D_1 and D_2.

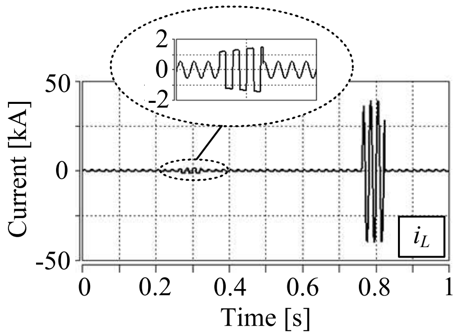

Figure 2-26: The second fault is not restrained by the FCL.

the diodes. By turning off semiconductors, a limiting resistance could be inserted in the current path. This would reduce the time constant and restrain the dc current. However, a control system would be required for switching off the power semiconductors, which does not align with the crucial advantage of the inductive FCLs over the other FCL types: they react inherently to a fault and do not require control.

Thus, even though a single-core FCL with a bridge rectifier uses 50% less material than is used in a topology with two cores, its operation in the system cannot be considered satisfactory. It is recommended to use the two-core FCL because this configuration preserves the main advantages of inductive FCLs: no fault-reaction or post-fault recovery delay and an unlimited duration of the fault-limiting period.

Several double-core FCL topologies are proposed in literature. They aim to solve some of the design challenges listed in the previous section. The goal of the analysis presented in the following section is to compare these topologies and assess how the design of saturated-core FCLs could be further improved.

iii. Double-core FCL topologies utilizing the core saturation effect

A number of different double-core topologies of the FCL with the core saturation effect have been proposed in literature. They aim at reducing the amount of necessary material and the value of the induced over-voltage. The proposed concepts are:

a. An FCL with total magnetic decoupling of the ac and dc magnetic circuits [Geor 79],
b. A three-phase FCL with a single dc coil [Darm 04],
c. An open-core FCL topology [Shuk 07].

An FCL with total magnetic decoupling of the ac and dc magnetic circuits

During normal operation of a power system, a voltage drop across the ac winding of a typical saturated-core FCL (see Figure 2-11a) is a few percent of the nominal grid voltage $u_L(t)$. On the other hand, during fault operation a full phase voltage $u_L(t)$ is applied to an ac winding. Due to the transformer coupling between the ac and the dc windings, an over-voltage $u_{FCL,dc,wind}(t)$ is induced across the dc current source:

$$u_{FCL,dc,wind}(t) = \frac{N_{dc}}{N_{ac}} u_L(t), \tag{2.10}$$

where N_{ac} and N_{dc} are the number of turns of the ac and dc windings, respectively.

The magnetic decoupling of ac and dc windings would solve the problem of the induced over-voltage. Figure 2-27 shows the existing topology that employs this principle.

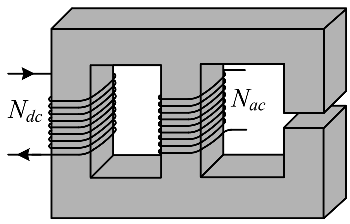

Figure 2-27: The FCL topology with total decoupling of the ac and dc magnetic circuits.

The dc winding is placed on the left leg of the core. The dc flux flows through and saturates only the left and middle legs of the core. The large reluctance of the gapped leg diverts the dc flux from this leg:

$$\Re_{mid} = \frac{l_{mean,mid}}{\mu_0 \mu_r A_{core,mid}} << \frac{l_{mean,right} + \mu_r l_{gap}}{\mu_0 \mu_r A_{core,right}} = \Re_{right}, \tag{2.11}$$

where $\Re$, l and A are the reluctance, length and cross-section of the corresponding leg, respectively, l_{gap} the gap length and μ_0 and μ_r the permeability of air and the relative permeability of the core, respectively.

During a fault, the ac flux, which is induced by the fault current, flows only through the middle and right legs; the reluctance of the left leg is higher than that of the gapped leg due to saturation:

$$\Re_{left} = \frac{l_{mean,left}}{\mu_0 \mu_r A_{core,left}} >> \frac{l_{mean,right} + \mu_r l_{gap}}{\mu_0 \mu_r A_{core,right}} = \Re_{right}. \tag{2.12}$$

In this way the dc winding does not 'see' the ac flux, i.e. does not sense any flux variation. As a result, there is no induced over-voltage. The resulting flux distribution is presented in Figure 2-28. Two cores are used per phase, one for each polarity of the line current.

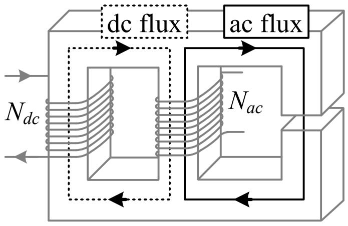

Figure 2-28: The flux distribution in the FCL with total magnetic decoupling.

However, it is found that the concept of total magnetic decoupling brings another design problem: the impedance of the ac winding during normal operation is too large [Cvor 08b]. The large normal impedance is a consequence of a non-deep saturation of the middle leg. Since the dc winding is placed in another leg of the core, it is able to drive only that leg to deep saturation. Suppose the dc current is gradually increased starting from zero. Once the H field in the middle leg reaches the knee (the saturation point) of the hysteresis curve, the reluctance $\Re_{mid,sat}$ of that leg increases significantly (2.13). The remaining dc flux is diverted through the gapped leg, see Figure 2-29.

$$\Re_{mid,sat} = \frac{l_{mean,mid}}{\mu_0 \mu_{r,sat} A_{core,mid}} >> \frac{l_{mean,right} + \mu_r l_{gap}}{\mu_0 \mu_r A_{core,right}} = \Re_{right} \tag{2.13}$$

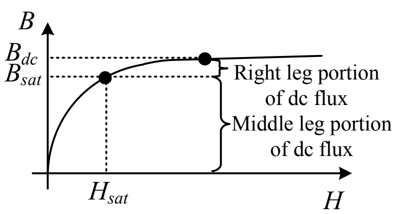

Figure 2-29: Distribution of dc flux in the middle and right legs of the core.

As a consequence of the non-deep saturation of the middle leg, where the ac winding is placed, even the nominal line current can take the core back to the linear regime and increase the FCL impedance. The simulation results, obtained from the FCL model in

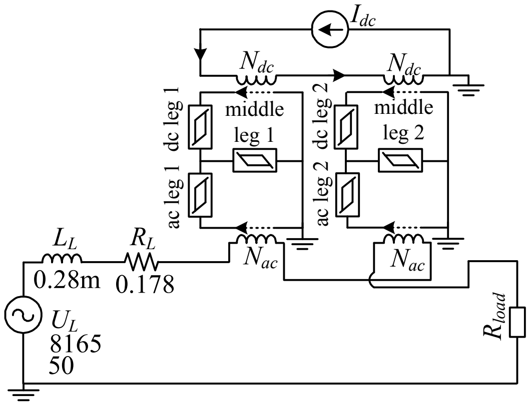

Figure 2-30: Developed Saber model of the FCL with the total magnetic decoupling.

Table 2-2: The parameters of the FCL model in Saber.

Electrical circuit		**FCL**	
Parameter	**Value**	**Parameter**	**Value**
Voltage	10 kV	Number of ac turns	30 turns
Load resistance	14.2 Ω	Number of dc turns	500 turns
Normal current	400 A_{rms}	DC current	450 A
Limited fault current	1.6 kA_{rms}	Cross-section of ac leg	0.2 m^2
Fault current	28 kA_{rms}	Cross-section of middle leg	0.4 m^2
Line stray resistance	0.178 Ω	Cross-section of dc leg	0.2 m^2
Line stray inductnace	0.28 mH	Gap length	0.5 m

the Saber simulator (see Figure 2-30), prove this. The parameters of the model are given in Table 2-2.

The variation of the magnetic flux density B_{mid} in the middle leg is shown in Figure 2-31a for both the normal and fault regimes. During normal operation ($t < 0.065$ s), the core is driven out of saturation. As can be seen in Figure 2-31a, the minimal flux density value in the core is 1.17 T. Since the core is driven out of saturation, the FCL normal impedance increases. The effect of the increased FCL impedance on the system can be seen in Figure 2-31b. The normal line current is equal to 386 A_{rms}. As stated in Table 2-2, the value of the normal current, before the FCL installation, is I_L=400 A_{rms}. The drop of the normal system voltage seen by the load is proportional to that of the line current. It can be concluded that the FCL inserts impedance into the system even during the normal operation.

Equation (2.14), representing Ampere's law, shows that the variation of the magnetic flux density B_{var} during the normal regime can be diminished if the ac mmf is reduced,

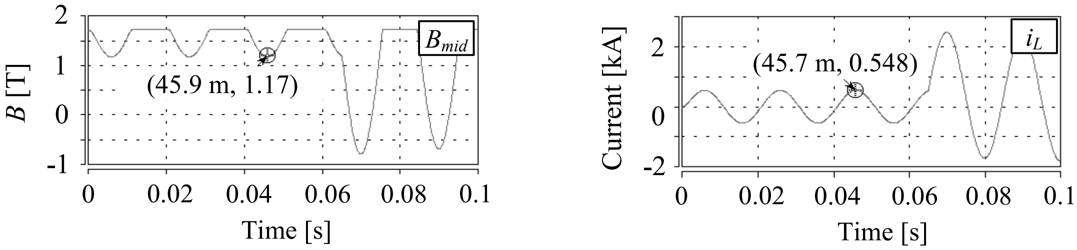

(a) (b)

Figure 2-31: The simulation results for the FCL with total magnetic decoupling: (a) The B field in the middle leg; (b) The line current.

i.e. if the number of ac turns N_{ac} is reduced:

$$B_{var} = \mu_0\mu_r\frac{N_{ac}i_L}{l_{mean,ac} + \mu_r l_{gap}}, \tag{2.14}$$

where $l_{mean,ac}$=$l_{mean,mid}$+$l_{mean,right}$ is the mean-length of the ac flux path.

The reduction of the number of ac turns N_{ac} reduces the FCL fault impedance as well (2.15). To avoid the larger fault current resaturating the core during the fault period a larger cross-sectional area of the core is required.

$$L_{FCL} = \mu_0\mu_r\frac{N_{ac}^2 A_{core,mid}}{l_{mean,ac} + \mu_r l_{gap}} \tag{2.15}$$

The parameters of an FCL model with the applied changes are given in Table 2-3.

Table 2-3: The parameters of an FCL model in Saber.

FCL	
Parameter	**Value**
Number of ac turns	30 turns
Number of dc turns	500 turns
DC current	450 A
Cross-section of ac leg	0.4 m^2
Cross-section of middle leg	0.8 m^2
Cross-section of dc leg	0.4 m^2
Gap length	0.5 m

The waveforms of the magnetic flux density in the core and the line current are shown in Figure 2-32. The core is driven significantly less out of saturation during normal operation. As a result, the normal impedance of the FCL is reduced; the peak of the normal current is equal to 399.5 A_{peak}. Since the FCL does not introduce impedance in the line, the load voltage is equal to the system voltage.

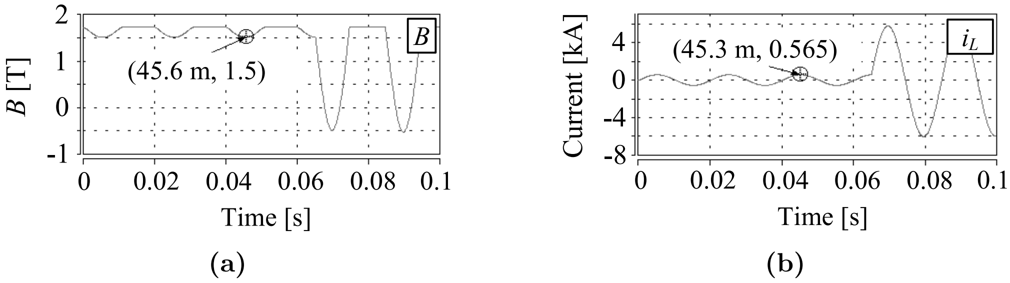

Figure 2-32: The simulation results of the changed FCL with total magnetic decoupling: (a) The B field in the middle leg; (b) The normal line current.

As said, by reducing the number of ac turns, the inductance of the FCL is reduced during both the normal and fault regimes. Thus, the value of the limited fault current is also increased, see Figure 2-32b. Instead of 1.6 kA (Figure 2-31b), it is equal to 4.2 kA. It can be concluded that the FCL with total magnetic decoupling does not offer the possibility of independently adjusting both the normal and fault FCL impedances; the peak of the limited fault current is dependent on the acceptable value of the FCL normal impedance.

Thus, the FCL with total magnetic decoupling brings the advantage of zero induced over-voltage across the dc current source, but it has serious drawbacks [Cvor 08b]:

a. The cross-section of the core is too large,
b. The normal and fault impedances of the FCL cannot be adjusted independently from each other.

A three-phase FCL with a single dc coil

A three-phase FCL uses six cores, two for each phase. To reduce the amount of dc winding material, all six magnetic cores are placed in such a way that a single dc coil can be used [Darm 04], see Figure 2-33. Its operation is equivalent to that of a typical FCL topology since the cores are magnetically isolated from each other.

There is no reduction of the amount of magnetic material, which represents the dominant part of an FCL's weight and size. The induced over-voltage is not diminished. The coupling between the ac and dc windings still exists and the ratio of the number of turns is not altered in comparison to that of a typical FCL design.

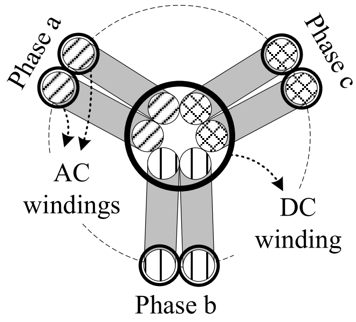

Figure 2-33: A cross-section, through the cores' legs, of a three-phase FCL configuration with a single dc winding - top view.

Open-core FCL topology

The open-core FCL topology comprises only one core per phase, see Figure 2-34a [Shuk 07]. The arrangement of the windings enables the FCL to limit the fault current in both half cycles. In each half cycle the ac and dc flux align in one leg and counteract each other in another leg. Thus, one of the legs is driven out of saturation leading to the increased fault impedance of the FCL. The ac flux closes its path through the surrounding air; the desaturated leg therefore operates as a solenoid, see Figure 2-34b.

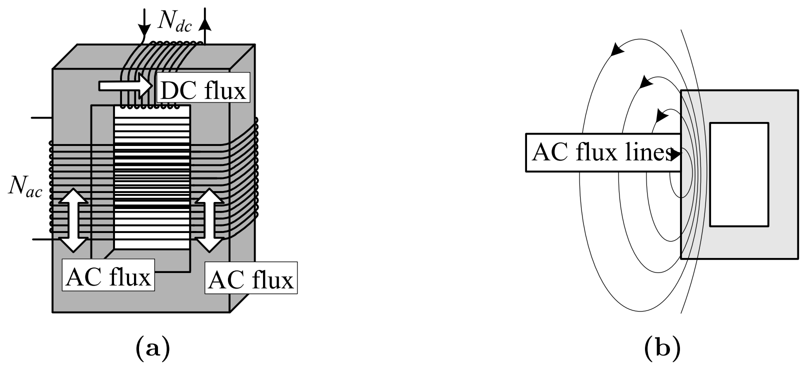

Figure 2-34: Open-core FCL: (a) Topology; (b) Distribution of the ac flux.

Since only one core per phase is used, the amount of magnetic material is significantly lower than in other FCL topologies. The over-voltage across the dc current source is reduced because the dc winding is only partially exposed to the ac flux [Roze 07], see Figure 2-34b.

However, for the same number of turns N_{ac} and the same cross-section of the core A_{core}, the open-core FCL has a lower fault inductance than that of a typical FCL. The inductance during the fault regime is lower because the open-core FCL operates as a solenoid, i.e. the path of the ac flux is closed partially through surrounding air, as shown in Figure 2-34b. On the other hand, the path of the ac flux in a typical FCL, or an FCL with total magnetic decoupling, is completely closed through magnetic material. To show the difference in the inductance value, static Finite Element (FE) models of both the open-core and typical FCLs are created. These lab-scale models were created in Ansys Workbench (WB), see in Figure 2-35. The cores of both FCLs are identical and the windings have an equal number of turns (see Table 2-4).

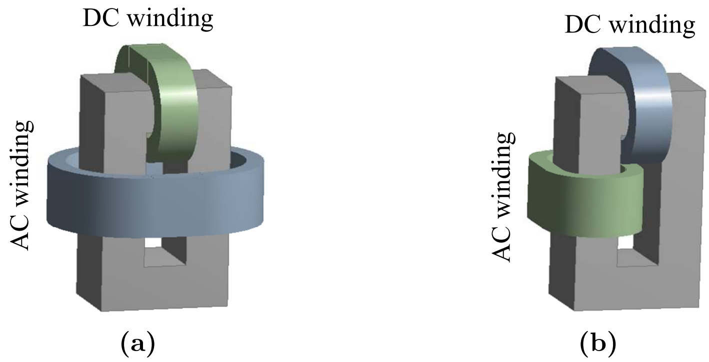

Figure 2-35: FE FCL geometry: (a) Open-core FCL topology; (b) Typical FCL topology.

Table 2-4: Parameters of the developed FE FCL models.

Parameter	Value	Parameter	Value
Core width	7.5 cm	Core depth	5 cm
Core height	12.6 cm	Core's cross-section	12.65 cm^2
Window width	2.5 cm	Number of dc turns	250 turns
Window height	7.8 cm		

The obtained results for the inductance of both FCLs are presented in Figure 2-36. It can be seen that inductance of the typical FCL (i.e. the FCL with the closed-magnetic flux path) is significantly larger, by 70%. The open-core FCL requires 30% more ac winding material to achieve the same inductance value. Thus, the amount of magnetic material is reduced when the open-core FCL is used, but the amount of the ac winding material is increased.

A lab experiment with the open-core topology is performed to verify the simulation results. The experimental FCL is shown in Figure 2-37, with the designated ac and dc windings. The size of the core is the same as the one used in simulations, the cross-section A_{core}=12.65 cm^2 and the number of ac and dc turns are N_{ac}=200 and N_{dc}=250 respectively. The BH curve of the experimental silicon-steel core is similar to that used in the FE simulations. The measured value of the ac winding inductance is L_{FCL}= 12 mH, whereas in the simulation it was L_{FCL}=9.5 mH (see Figure 2-36). Since the experimental

BH curve is not equal to the one used in the simulation, the difference between the results can be considered acceptable. It can be concluded that the FE FCL model is validated.

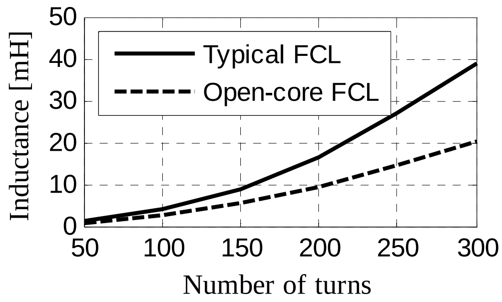

Figure 2-36: The comparison of the inductance values of the two FCL topologies.

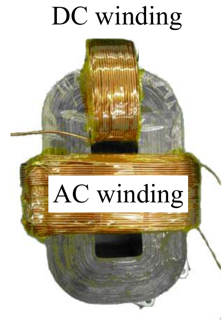

Figure 2-37: Experimental open-core FCL.

2.5 Solid-state and hybrid FCLs - state-of-the-art of semiconductor technology

Solid-state and hybrid FCLs are based on semiconductor technology. An overview of the existing semiconductor switches and their characteristics is given in this section.

Advances in semiconductor technology enabled power electronics switches to be used in fault-current limiting applications. Currently, semiconductors are capable of continuous conducting of currents in the range of several kA and blocking voltages as high as several kV. The conduction voltage drop (power losses) is several volts and turn-on and turn-off times are in the range of several μs.

Thyristor-based power semiconductors that are used in FCL applications are: Gate Turn-off Thyristor (GTO), Hard-Driven Transparent Gate Turn-off Thyristor (HD-TGTO), Gate-Commutated Thyristor (GCT), Integrated Gate-Commutated Thyristor (IGCT) and Emitter Turn-off Thyristor (ETO or sometimes referred to as Self-Powered ETO - SPETO). In addition, Insulated-Gate Bipolar Transistors (IGBTs), which are transistor-based, can be employed.

The applicability of different power switches for FCL applications can be compared on the basis of four factors: on-state power losses, requirement of auxiliary circuits (e.g. turn-off snubber), blocking voltage and breaking current capabilities. Switching losses and switching times are not of such importance as in converter applications because the switches operate at the grid frequency when used in FCLs [Meye 04a].

When used for low-voltage applications (lower than 1.5 kV) IGBTs have the advantage that on-state losses are lower than those of thyristor-based semiconductors [Ahme 06]. Thyristor-based semiconductors (GTO, IGCT and ETO) have lower losses in higher-voltage applications [Bin 06; Meye 04b], see Figure 2-38. The figure shows that the on-state losses of thyristor-based switches are significantly lower than those of IGBTs. Switching losses are less important because of the low operating frequency (power-grid frequency).

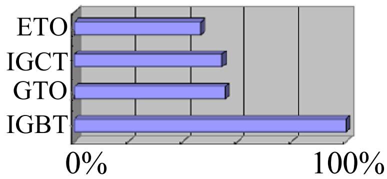

Figure 2-38: Relative on-state losses.

Presently, the maximum available rating of IGBT modules is 6.6 kV/600 A. The losses of 6.6 kV modules are two times higher than those of 3.3 kV IGBTs [Huan 99]. IGBTs do not require a turn-off snubber circuit.

For many years, GTO switches were the dominant high-power semiconductors since they are fully controllable and have large current and voltage capabilities [Ahme 06]. The development of IGCT switches (see Figure 2-39a) brought further operational advantages of power semiconductors: snubberless turn-off transition and lower on-state losses (see Figure 2-38). Since a snubber comprises capacitors, the reliability of the system without a snubber is increased. Snubberless operation is achieved by driving a negative gate current which is equal to the anode current during commutation. This condition is referred to as a unity-gain or hard-driven switching. The hard-driven TGTO is an improved version of the standard GTO. It has improved anode design, where the added buffer layer stops the electric field before it can reach the anode layer. As a result, the thickness and losses of the device can be decreased substantially [Eich 96]. The on-state voltage drop is reduced from 3.2 V to 1.9 V when modules rated at 4.5 kV/3 kA are compared [Grun 96]. The TGTO switches can operate without a turn-off snubber circuit. The ETO (SPETO) switches, an another improved version of the standard GTO, (see Figure 2-39b) have lower conduction losses than those of the IGCTs [Chen 05], see in Figure 2.38 and Figure 2.40. The ETOs utilize advantages of both GTOs and IGBTs: high voltage and current ratings and voltage gate control. They feature snubberless turn-off capability, demonstrated for 2.8 kV/$4-5$ kA rating of the device [Bin 06; Zhan 04]. The additional benefits offered by this power module are: a built-in current and built-in voltage sensors and the self-power generation for a gate drive. This allows for a simplified design of the FCL and lowered total cost.

Table 2-5 summarizes the list of power semiconductors with maximum available rat-

(a) (b)

Figure 2-39: Semiconductor modules: (a) IGCT module; (b) SPETO module.

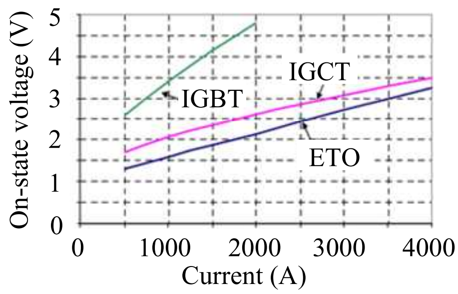

Figure 2-40: Comparison of the on-state losses of IGBT, IGCT and ETO switches. '5SHY 35L4511' IGCT, 'CM900HB-90H' IGBT and 4.5 kV/4 kA ETO modules are compared [Chen 05].

ings. A more extensive overview of available power semiconductors can be found in [Bern 03; Bhal 08].

The reliability of semiconductors must be considered. The operation of a system must not be disrupted in the case of failure of the solid-state or hybrid FCLs. This means that the flow of normal current must not be interrupted. The probability of FCL failure increases when more semiconductors are placed in series in the design of FCLs for higher-voltage applications. It is preferred that the switch in the failure mode operates as a short-circuit instead of as an open-circuit. Such functionality is provided by the press-pack housing of the semiconductors [Sati 02], which guarantees the low-impedance failure condition (short-circuit failure mode - SCFM) until the system is serviced. Metal, which has contact with the electrodes of the semiconductor, melts in the case of a switch failure and forms a short-circuit path between the electrodes [Lang 02]. This way of fault tolerance is usually also applied in HVDC systems.

Emerging SiC (Silicon-Carbide) technology is expected to enhance the listed operational characteristics of power semiconductors due to better physical and electrical properties of SiC in comparison to Si (Silicon). The development of GCT modules with a 12.7 kV blocking-voltage capability and an on-state voltage drop of only 6.6 V demonstrates the feasibility of SiC technology [Suga 04]. Nowadays, 99% of all commercially available SiC devices are used in low-voltage application range (< 1.2 kV) [Deve 09]. A 10-year prediction of the SiC market share, with the market divided into voltage ranges, is presented in Figure 2-41. As can be seen, the expected penetration of SiC devices in HV range (2.5-6.5 kV+) is very low. Although they offer superior operational advantages, the

Table 2-5: Ratings of currently available power semiconductors.

Module	Ref.	Repetitive peak off-state voltage	Max. controllable turn-off current	Max. RMS on-state	On-state voltage
IGCT	[ABB 05]	4.5 kV	4 kA	3.3 kA	1.8 V
	[ABB 07]	5.5 kV	1.8 kA	1.3 kA	2.95 V
	[ABB 08]	6.5 kV	4.2 kA	2 kA	3.8 V
	[Bern 03] [Bhal 08]	10 kV	3 kA		6.5 V
GTO	[Grun 96]	4.5 kV	3 kA	1.8 kA	3.2 V
	[Boon 08] [Naka 95]	6 kV	6 kA	2 kA	4 V
HD GTO	[Grun 96]	4.5 kV	$3-6$ kA	2.4 kA	1.9 V
ETO	[Bin 03a] [Chen 05]	4.5 kV	4 kA		3.25 V
	[Chen 05] [Mott 00]	6 kV	4 kA		5.4 V
IGBT	[Wake 05]	4.5 kV	4.2 kA	1.7 kA	4.1 V
	[Powe]	6.5 kV	1.2 kA	0.6 A	5.1 V

cost of SiC devices has to be reduced if they are to penetrate the market [maga 09; Ener]:

i. SiC substrate euro/mm^2 cost,

ii. SiC device manufacturing cost, with particular emphasis on the epitaxial process.

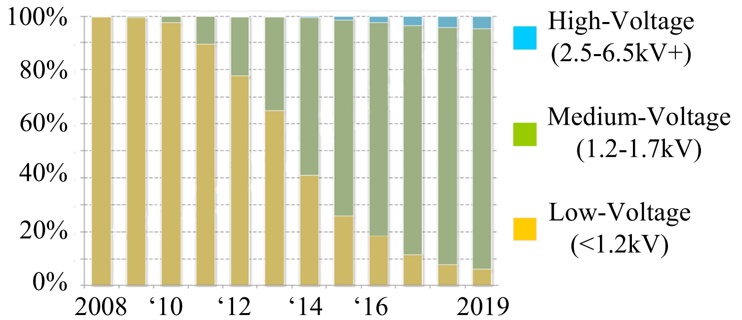

Figure 2-41: SiC device market share by percentage, split by voltage range, until 2019 [Deve 09].

2.6 FCL operation in power systems - principal considerations

2.6.1 Introduction

The analysis that will be presented in this section distinguishes FCL types on the basis of the applied limiting principle and the fault-reaction delay. The operation of FCLs in the system is investigated by considering the following points:

i. The dependency of the first fault-current peak on the FCL fault-reaction delay and the moment of fault inception - it is necessary to determine how fast the FCLs have to react in order to successfully limit the first fault current peak. The results of this analysis do not apply to the FCL types without a fault-reaction delay: non-semiconductor-based and bridge-type solid-state FCLs,

ii. The amount of dissipated energy in the FCL during a fault, as a function of the moment of fault inception, the FCL fault-reaction delay and duration of the limiting period - the amount of dissipated heat in the FCL indicates the required value of the thermal capacities of the limiting impedance and the applied cooling system. The contribution to the dissipated energy from the first fault current peak and the follow current is distinguished and the dependency between the duration of the limiting period and the thermal capacity of the FCL is pointed out. This analysis, therefore, considers the FCLs with resistive impedance and gives the possibility to assess their applicability to the power systems,

iii. The amount of dissipated energy in a CB as a function of the used type of the FCL - the amount of dissipated energy in the CB should be reduced by inserting the FCL in the line. However, as shown in the analysis, the reduction factor depends on the applied limiting principle: the insertion of resistive or reactive impedance.

2.6.2 Acceptable duration of an FCL fault-reaction delay

A fault-reaction delay is the principal difference between the operation of solid-state and hybrid FCLs. Due to the slowness of the mechanical switch, the hybrid FCLs have a longer delay. The analysis presented in this subsection determines the maximum acceptable FCL fault-reaction delay.

Having defined that $u_L(t)$ is the nominal line voltage, R_L and X_L the short-circuit impedances of the line and R_{load} the resistance of a load (see Figure 2-42), the nominal line current can be expressed as:

$$i_L(t) = \frac{U_L}{|Z_{nom}|}\sin(\omega t - \varphi_{nom}), \tag{2.16}$$

where $\varphi_{nom} = \arctan\left(\frac{X_L}{R_L+R_{load}}\right)$ is the phase angle and $|Z_{nom}| = \sqrt{(R_L+R_{load})^2+X_L^2}$ the nominal impedance of the line.

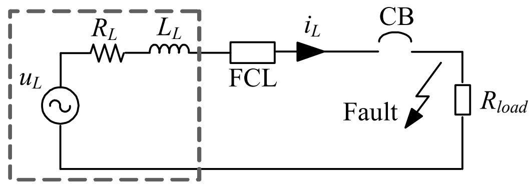

Figure 2-42: Single-phase equivalent circuit.

Upon the fault inception at moment t_f, the parameters of the system are changed (R_{load}=0 Ω) and behavior of the fault current $i_{L,f}(t)$ can be described as given in (2.1).

The parameters of the system are changed once more when a fault-limiting resistance R_{FCL} is inserted in the line. Change of the limited fault current $i_{L,lim}(t)$ with time can be expressed as:

$$i_{L,\lim}(t) = \frac{U_L\sin(\omega t - \varphi_{L,\lim})}{|Z_{L,\lim}|} + \left(I_{L,f,t_{\lim}} - \frac{U_L\sin(-\varphi_{L,\lim})}{|Z_{L,\lim}|}\right)\cdot e^{-\frac{t-t_{\lim}}{\tau_{L,\lim}}}, \tag{2.17}$$

where $\varphi_{L,\lim} = \arctan\left(\frac{X_L}{R_L+R_{FCL}}\right)$, $|Z_{L,\lim}| = \sqrt{(R_L+R_{FCL})^2+X_L^2}$, $I_{L,f,t_{\lim}}$ is the value of the fault current at moment t_{lim} when the FCL incepts the limiting action. The fault-reaction delay of the FCL can be found as $t_{lim} - t_f$.

The waveforms of normal, fault and limited-fault currents are presented in Figure 2-43. The moments of fault inception t_f and the inception of the FCL limiting action t_{lim} are designated.

The analysis is done for the typical parameters of an MV power system: $U_{L,L} = 10\,kV$, $I_L = 400\,A_{rms}$, $R_L = 0.178\,\Omega$, $X_L = 0.089\,\Omega$ and $\frac{R_L}{X_L} = 2$.

The first peak of the fault current is a function of the moment of fault inception t_f and the FCL fault-reaction delay. This delay comprises the fault-detection time and the insertion delay of the FCL impedance. It has been assumed, for this analysis, that the reaction-delay of the solid-state FCL is 0.1 ms and of the hybrid FCL 3 ms, where the difference comes from the slowness of the mechanical switch employed by the hybrid FCL. It has been further assumed that the current pick-up value (the fault-triggering value) is equal to $1.25I_L$. Figure 2-44 presents the value of the first fault current peak versus the moment of fault inception for both FCLs. The results are obtained by running the

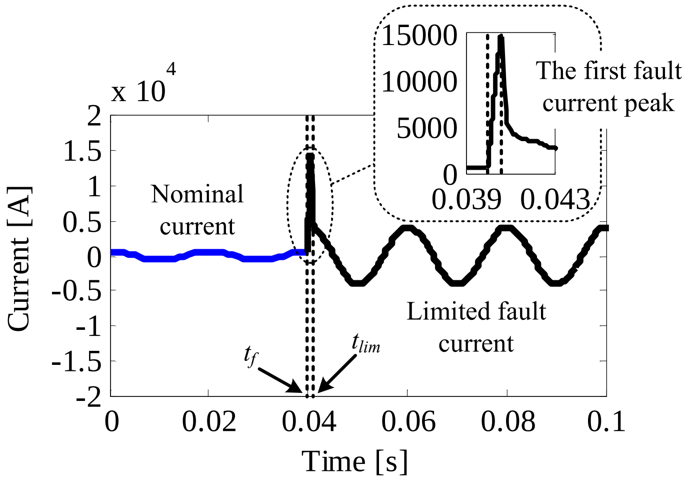

Figure 2-43: The waveforms of the nominal, fault and limited-fault currents.

introduced analytical model of the single-phase equivalent circuit in Matlab. As can be seen, the value of the first peak is a function of the moment of fault inception. The peaks are much lower with the solid-state FCL since the fault-reaction delay is considerably shorter [Cvor 08a].

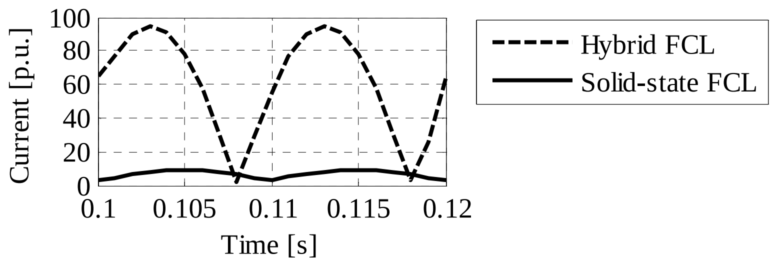

Figure 2-44: First fault current peak versus moment of the fault inception: hybrid and solid-state FCL.

The maximum allowable fault current peak for the analyzed power system is 25 p.u.. The conclusion is that the fault-reaction delay of 3 ms of the hybrid FCL is unacceptably long. If a hybrid FCL is going to be used it has to insert the limiting impedance within 1 ms of fault inception. Such a delay will ensure that, at worst, the fault current remains below 25 p.u..

The results presented above are obtained, as already stated, based on the parameters of a typical MV power system. However, a requirement of containing the limited fault current within the range of $3I_L - 4I_L$ can be a realistic case. In this case, the maximum allowable fault-reaction delay would be significantly shorter than 1 ms. Such fast fault detection and clearance can be very difficult to achieve in both solid-state and hybrid FCLs. This is particularly the case in today's complex electrical networks that are characterized by the many interconnections and installations of distributed generators [Cost 08].

2.6.3 Energy dissipation in an FCL impedance

The amount of energy dissipated during limiting action determines the size and cost of resistive solid-state and hybrid FCLs. The thermal capacity of the limiting impedance R_{FCL} has to be large enough to accommodate all of the dissipated heat, since the heating can be considered an adiabatic process. The amount of dissipated heat $E_{FCL,diss}$ can be calculated as follows:

$$E_{FCL,diss} = R_{FCL} \cdot \int_{t_1}^{t_2} i_{L,\lim}^2(t)\,dt, \tag{2.18}$$

where $i_{L,\lim}(t)$ is given in (2.17).

Total dissipated energy $E_{FCL,diss}$ after the first three cycles is shown in Figure 2-45a. The difference between the two curves is due to the difference in the first fault-current peak, which is smaller for the solid-state FCL. Since dissipation is a function of $i_{L,lim}^2$, it diminishes with the increase of FCL resistance, i.e. with the decrease of $i_{L,lim}$ value.

The contribution of the first fault current peak to total energy dissipation can be significant [Cvor 08a], see Figure 2-45b. The initial jump in dissipated heat, with the hybrid FCL inserted in the line, is a result of the large value of the first fault current peak. After three cycles, the differences in energy dissipation, for resistive and inductive FCLs, is around 30%. This means the size (cost) of the hybrid FCL has to be significantly increased in comparison to that of the solid-state FCL in order to be able to absorb the heat. The resistance of the FCL, used in this case, is 4.8 Ω.

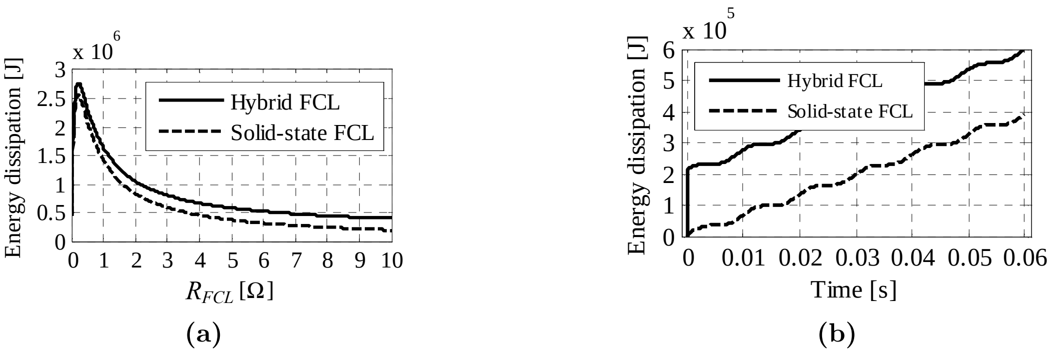

Figure 2-45: Energy dissipation in hybrid and solid-state FCLs for the worst moment of fault inception: (a) after the first three cycles; (b) during the first three cycles.

The varistors (variable resistors) are placed in parallel with both solid-state and hybrid FCLs as voltage surge protection. Their resistance rapidly drops when the voltage is higher than the knee threshold U_{knee}. The varistor forms a low-resistance shunt path for the line current [EPCO 02].

Since the varistor conducts a part of the fault current, it dissipates a certain amount of energy that would otherwise be dissipated in the FCL resistance R_{FCL}. The ratio of the heat-dissipation share is illustrated using a Matlab model of a solid-state FCL. The parameters of the varistor are U_{knee}=9 kV and I_{knee}=750 A. The clamping voltage is 10 kV. The full model is presented in Figure 2-46. Two semiconductors conduct the normal line current. A fault is initiated by closing the switch.

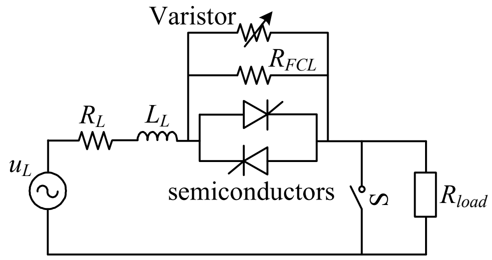

Figure 2-46: Model of a single-phase electrical circuit with an FCL.

Figure 2-47a shows a voltage surge across the FCL in the case when a varistor is not used. The waveform of the line current during both normal and fault periods is presented in Figure 2-47b. Energy dissipation, due to the fault current, takes place in the resistor. However, a part of the first fault current peak goes through the snubber circuit ($R = 1\ \Omega$ and $C = 10\ \mu$F). The waveform of the resistor current is shown in Figure 2-47c.

The varistor limits the voltage surge to 10 kV, see Figure 2-47d. The distribution of the fault current between the varistor and R_{FCL} is presented in Figure 2-47e and Figure 2-47f. The first peak is taken over by the varistor. The varistor resistance increases and its current drops to zero after the first voltage surge. Thus, the follow fault current is conducted only by the resistor R_{FCL}.

The energy dissipation due to the first fault current peak is, therefore, taken over by the varistor. Figure 2-48a shows that the varistor dissipates heat only at the moment of fault inception. The energy dissipation in the resistor R_{FCL} is shown in Figure 2-48b. The same type of analysis may be used validly for the hybrid FCL.

A varistor can be used as the only fault-limiting impedance of the FCL. Such an FCL topology would, actually, operate as a fault current interrupter. The fault current would be interrupted after its first peak, see in Figure 2-49. Premature interruption of the fault current can affect the coordination of protective schemes as they might not be able to detect the fault.

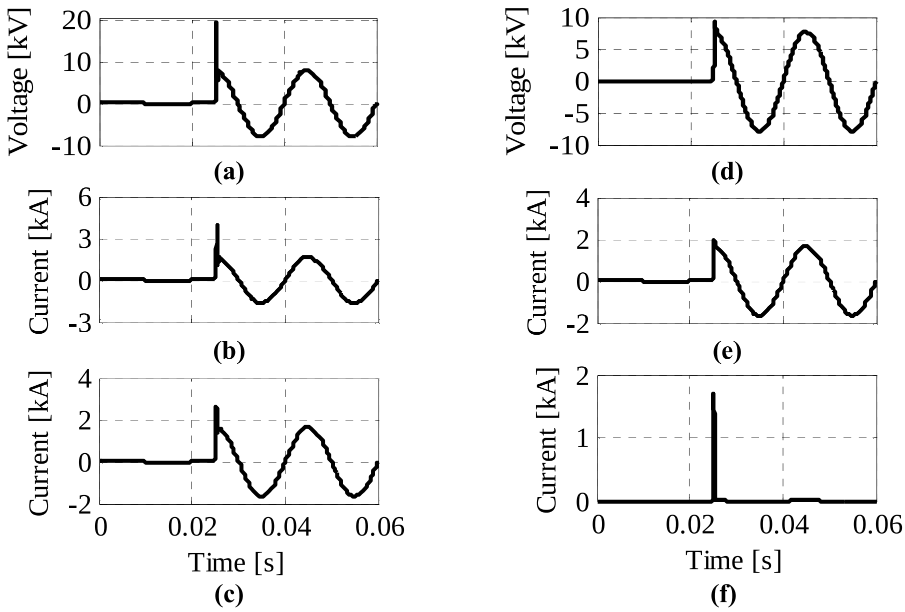

Figure 2-47: Simulation results for the FCL without the varistor: (a) FCL voltage; (b) Line current; (c) Resistor current, and for the FCL with the varistor: (d) FCL voltage; (e) Resistor current; (f) Varistor current.

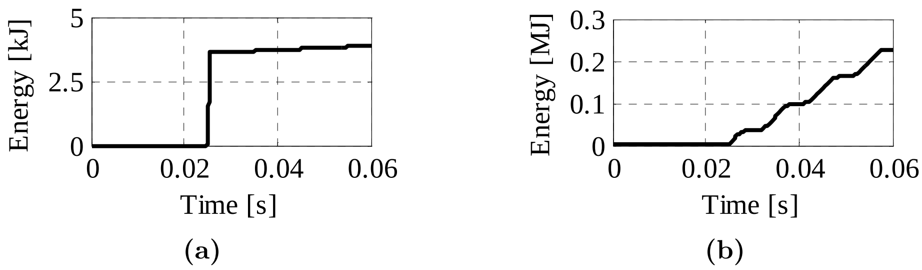

Figure 2-48: Energy dissipation in the FCL: (a) In the varistor; (b) In the resistor.

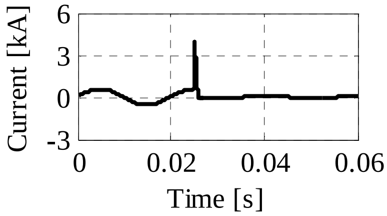

Figure 2-49: The line current with the FCL using only a varistor as a limiting impedance.

The flow of the follow current could be maintained by special switching control of semiconductors: by turning them off and on every time the fault current reaches an upper or lower threshold value, respectively [Ahme 06]. The obtained current waveform is presented in Figure 2-50a, where upper and lower threshold values are I_{upper}=1600 A and I_{lower}=500 A. Each time one of the semiconductors is turned off, the over-voltage peak activates the varistor which takes over the current. The FCL voltage and varistor current are presented in Figure 2-50b and Figure 2-50c, respectively. The limited fault current comprises higher harmonics, which could cause protective schemes to malfunction and lose coordination. Due to the applied control, the heat dissipation in the varistor does not remain at zero after the first fault current peak, see Figure 2-50d.

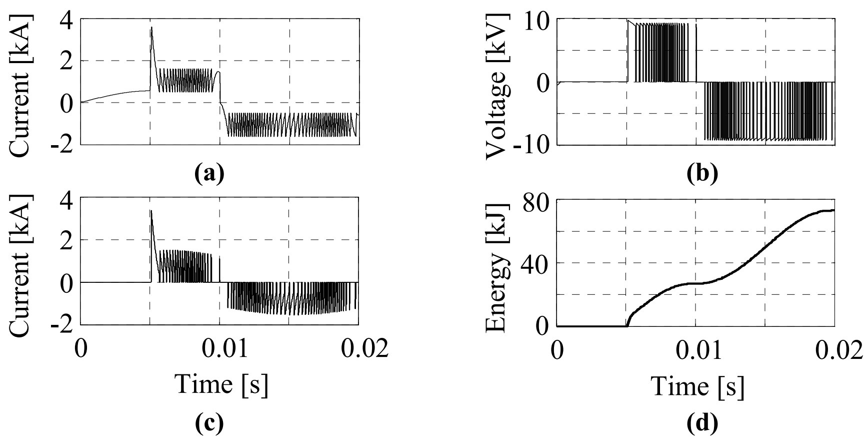

Figure 2-50: The results for the FCL with applied control to the semiconductors during a fault period: (a) Line current; (b) FCL voltage; (c) Varistor current; (d) Energy dissipation in varistor.

2.6.4 Energy dissipation in a CB

It will be shown that inserting an FCL impedance into the line reduces the amount of energy that has to be dissipated by a CB during an opening action. Since the CB is normally opened during the flow of the follow current, the first fault current peak and the fault-reaction delay of the FCL are of no relevance for its operation. However, the amount of energy dissipated by a CB varies depending on the type of impedance of an FCL: reactive or resistive.

The energy dissipated by a CB (see Figure 2-42) when an FCL is not placed in the line is approximately equal to the energy E_L stored in the stray inductance of the system

L_L during a fault:

$$E_L = \frac{1}{2} L_L I_{L,f}^2 = \frac{1}{2} L_L \left(\frac{U_{L,CB}}{\sqrt{R_L^2 + X_L^2}} \right)^2, \tag{2.19}$$

where $U_{L,CB}$ is the system voltage in the moment when the CB opening action is triggered.

Equation 2.19 is an approximation which is more accurate when the duration of the opening action is relatively short, e.g. one cycle.

The system parameters are changed when a resistive FCL is placed in a line. The follow current and the energy stored in the line inductance L_L are mainly determined based on the FCL resistance R_{FCL}. The energy dissipation $E_{CB,RFCL}$ imposed on the CB is:

$$E_{CB,RFCL} = \frac{1}{2} L_L I_{L,\lim}^2 = \frac{1}{2} L_L \left(\frac{U_{L,CB}}{\sqrt{(R_{FCL} + R_L)^2 + X_L^2}} \right)^2. \tag{2.20}$$

The same type of consideration is valid when an inductive FCL is placed in the line. The difference is that in this case, the CB dissipates both the energy stored in the system inductance L_L and in the FCL inductance L_{FCL}:

$$E_{CB,XFCL} = \frac{1}{2} \left(L_L + L_{FCL} \right) I_{L,\lim}^2 = \frac{1}{2} \left(L_L + L_{FCL} \right) \left(\frac{U_{L,CB}}{\sqrt{R_L^2 + (X_{FCL} + X_L)^2}} \right)^2. \tag{2.21}$$

The reduction of the heat dissipated in the CB can be defined as the ratio between the energy without an FCL and that with an FCL in the line (2.22). It is given by (2.23) and (2.24) when the inductive or the resistive FCL is used:

$$k_E = \frac{E_{withoutFCL}}{E_{withFCL}}, \tag{2.22}$$

$$k_{E,XFCL} = \frac{X_L}{X_L + X_{FCL}} \frac{R_L^2 + (X_L + X_{FCL})^2}{R_L^2 + X_L^2}, \tag{2.23}$$

$$k_{E,RFCL} = \frac{(R_L + R_{FCL})^2 + X_L^2}{R_L^2 + X_L^2}, \tag{2.24}$$

where $k_{E,XFCL}$ and $k_{E_R FCL}$ are the energy reduction factors when a reactive or resistive FCL are installed in the line, respectively.

Figure 2-51 graphically illustrates the reduction ratio k_E for both cases. It can be seen that the amount of energy imposed on the CB is significantly reduced in both situations.

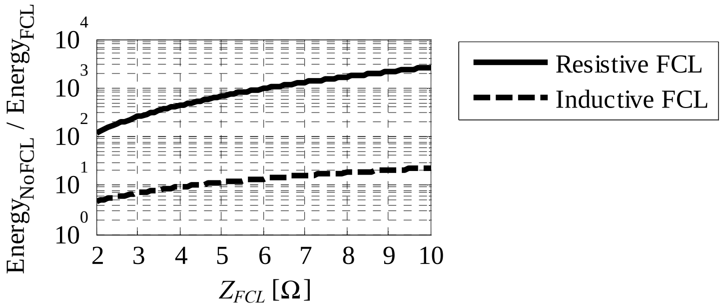

Figure 2-51: Ratio of energy dissipation in a CB with and without an FCL.

2.7 Conclusions

The analysis of the three main types of FCLs is presented: superconductive, semiconductor-based and saturated-core FCLs. It shows their operational advantages and drawbacks and the challenges that are to be solved before FCLs can be integrated in power systems.

Superconductivity is a promising technology for fault current limiting applications. Superconductive FCLs do not introduce a voltage drop in the line during normal regime and have a very fast inherent reaction to a fault. However, drawbacks such as slow post-fault recovery time, scalability and high cost have to be solved before SFCLs are applied to power systems. New superconductive materials, such as MgB_2, are being investigated.

Developments in semiconductor technology have allowed the use of power switches for power applications in the range of several hundred MW. FCLs based on power semiconductors have been investigated extensively. The following issues are of principal concern:

i. The fault-reaction delay of FCLs is of principal concern. For the typical parameters of an MV grid, it is shown that this delay has to be shorter than 1 ms.

ii. To limit the fault current, the FCL must dissipate a considerable amount of energy, which is proportional to the length of the limiting period. The analysis shows that this amount is in the range of hundreds kJs for a typical MV system. The thermal energy storage capacity (size) of the limiting impedance has to be sufficient to store this heat without being damaged.

iii. The thermal capacity of the cooling system has to be sufficient to remove the dissipated heat from the limiting impedance fast enough to enable FCL reaction to consecutive faults.

iv. Employment of surge protection devices (varistors) is necessary. They have to be inspected and possibly replaced after each operation of the FCL, which increases both maintenance and investment costs.

v. Reliability of power switches is an issue that has to be taken into account. Introduction of redundant modules would affect the size and cost of the FCL.

Hybrid FCLs do not suffer power loss during the normal regime. However, the short fault-reaction delay requirement imposes a challenge on the design of a mechanical switch, especially when an FCL is scaled-up to higher voltages. A longer fault-reaction delay leads to a higher first peak of the fault current and a larger amount of dissipated heat in the limiting impedance. The design challenges of solid-state FCLs also apply.

Saturated-core FCLs are the most attractive type of FCLs because of their operational advantages:

i. There is no fault-reaction delay,
ii. There is no post-fault recovery delay,
iii. The duration of the fault-limiting period is unrestricted,
iv. There is no operational deterioration when limiting consecutive faults,
v. Power dissipation during the normal regime is negligible.

These characteristics satisfy all the functional requirements from the point of view of grid integration. The remaining design challenges are: the amount of required material and the induced over-voltage should be reduced. Although a number of different topologies were proposed in literature, saturated-core FCLs are still not commercialized. They have to be further improved before they can be integrated in the power grid.

The following chapter introduces a new topology of saturate-core FCLs. The amount of required material is significantly reduced.

Chapter 3

NOVEL DESIGN OF AN FCL WITH PARTIAL MAGNETIC DECOUPLING

3.1 Introduction

THE previous chapter introduced the benefits and drawbacks of inductive saturated-core FCLs. The inherent reaction to a fault, no post-fault recovery delay and the unlimited duration of the limiting period are significant advantages of this FCL type over other types of FCLs. However, inductive FCLs have not been commercialized due to their large weight and the associated cost of material as well as the over-voltage induced in the dc windings during fault operation.

This chapter introduces a new design of an FCL which enables a significant reduction of weight and cost. Before the new topology is introduced, section 3.2 presents the design principle used to reduce the core size and clarifies why this principle is not applicable to the already-existing FCL topologies. Namely, the insertion of a gap in the core of the state-of-the-art FCL configurations would enable employment of the smaller cores for the same voltage level. However, this would also result in a significant increase in the reluctance of the dc magnetic path. As a consequence, a considerably increased number of dc turns would be required to drive the core to saturation.

Section 3.3 introduces two FCL topologies which represent the design steps leading from the existing, gapped FCL topology to the new FCL design. Analysis of these intermediate FCL configurations helps in understanding the operation of the final design. A double-core per-phase FCL topology is presented first. It represents the improvement of the FCL with the total magnetic decoupling, analyzed in the previous chapter. The operation of the subsequent single-core per phase FCL topology with partial magnetic decoupling is depicted at the end of this section. Single-core topology brings an advantage of the reduced amount of magnetic material in comparison to the typical FCL configuration.

In section 3.4, the final design of the single-core single-phase FCL configuration with partial magnetic decoupling is introduced. In comparison to the previous inter-step FCL structure, it uses considerably less magnetic material. Its operation is confirmed through simulations and lab-scale experiments.

To further reduce the amount of FCL material needed, a new single-core three-phase FCL with a trifilar arrangement of the phase windings is proposed. It is presented in section 3.5. The new trifilar arrangement of the phase windings reduces considerably the impedance of the FCL during normal operation.

The operation of the three-phase single-core FCL topology is validated by means of Finite Element models developed in Ansys Classic and by lab-scale experiments. Chapter 5 of this thesis presents the details and guidelines for development of an FE FCL model. The current chapter contains only FE simulation results.

3.2 Inductive saturated-core FCL with a gapped magnetic core

The dependency of core size on gap insertion in a core will be investigated in this section. The principle of gap insertion is well known in the field of inductor design. It is used to reduce the size of the core for the given application. It is important to determine whether this principle can be applied to the design of inductive FCLs and what advantages and drawbacks it brings.

When designing an inductive FCL, its inductance value has to meet the following criteria: during a fault, the inductance of an FCL must be large enough to limit the fault current below a specified value and small enough so that the peak of the fault current is still detectable by present protective schemes of the system.

$$L_{FCL,min} \leq L_{FCL} \leq L_{FCL,max}, \tag{3.1}$$

where $L_{FCL,min}$ and $L_{FCL,max}$ are the minimal and the maximal acceptable FCL inductances, respectively.

The inductance value of an FCL with a closed core, during a fault regime, can be calculated to a fair approximation from:

$$L_{FCL} = \mu_0 \mu_r \frac{N_{ac}^2 A_{core}}{l_{mean}}, \tag{3.2}$$

where μ_0 and μ_r are the permeability of air and the relative permeability of the magnetic material, N_{ac} the number of winding turns, A_{core} the cross-section of the magnetic material and l_{mean} the mean length of the flux path.

The number of turns of the ac winding and the cross-section of the core are related to each other through Faraday's law:

$$\int_{\frac{T_{per}}{4}} u_{FCL}\left(t\right) dt = N_{ac} A_{core} k_{sat} B_{sat}, \tag{3.3}$$

where $u_{FCL}(t)$ is the applied voltage across the inductor, T_{per} the voltage period, k_{sat} the saturation factor ($0 \leq k_{sat} \leq 2$), which defines the maximal acceptable variation of the B field after the core is desaturated, and B_{sat} the saturation flux density of the magnetic material.

For an FCL design, (3.3) can be interpreted in the following way: for a given number of ac turns N_{ac} and voltage across an ac winding $u_{FCL}(t)$, the minimal cross-section of a core that has to be used to avoid resaturation of the core during a fault regime is A_{core}.

For better understanding, equations (3.1), (3.2) and (3.3) are graphically presented in Figure 3-1. Each curve in the figure is obtained for a different constant value of the core's cross-section A_{core} and the saturation factor k_{sat}=1. The curves illustrate the dependency between the FCL inductance L_{FCL} and the number of ac turns N_{ac} [Cvor 09]. It can be seen from the figure that the minimal acceptable cross-section of the core, for which both conditions (3.1) and (3.3) are satisfied, is A_{core3}. The corresponding number of ac turns is N_{ac3}. If a smaller core's cross-section is used, e.g. A_{core4}, the inductance of the ac winding would be too large at the moment when condition B=B_{sat} is satisfied. In other words, conditions (3.1) and (3.3) cannot be satisfied at the same time for any number of the ac turns. Curve 3 in Figure 3-1 shows that for a core without an air gap the minimal size of the core is, therefore, determined by the maximal acceptable value of the ac winding inductance $L_{FCL,max}$ and the value of B_{sat}.

Generally, an air gap is used in inductor design (see Figure 3-2) in order to reduce the cross-section of the core for the given value of inductance.

For a gapped FCL (see Figure 3-2), the inductance of the ac winding, during a fault period, can be approximated as follows:

$$L_{FCL} = \mu_0 \frac{N_{ac}^2 A_{core}}{l_{gap}}, \tag{3.4}$$

where l_{gap} is the gap length.

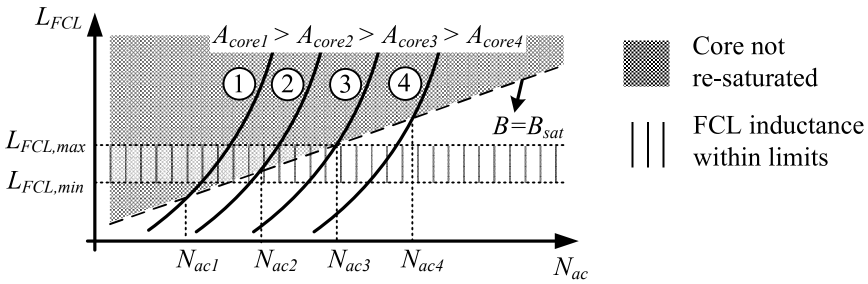

Figure 3-1: The inductance of the FCL versus the number of ac turns N_{ac} for different constant values of the cross-section A_{core}.

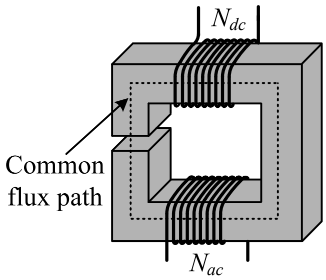

Figure 3-2: Saturable inductor with an air gap.

Figure 3-3 graphically represents the new system of equations (3.1), (3.3) and (3.4) [Cvor 09]. Each curve in the figure is obtained for a different gap length and satisfies the condition $N_{ac}A_{core}$ = const. This condition derives from equation (3.3) for the given voltage $u_{FCL}(t)$, the saturation factor k_{sat} and the saturation flux density B_{sat}. Curves 1 and 2 in Figure 3-3 are obtained for the gap lengths 0 and l_{gap2}, respectively. Both curves satisfy the condition $L_{FCL} = L_{FCL,max}$ when the number of ac turns is equal to N_{ac1} and N_{ac2} respectively, where $N_{ac2} > N_{ac1}$. From the condition $N_{ac}A_{core}$ = const, which applies to both curves, it can be concluded that $A_{core2} < A_{core1}$. Therefore, gap insertion in the core enables the reduction of the required cross-section of the core for the given voltage $u_{FCL}(t)$. The same analysis can be applied to the 2 and 3 curves. Thus, the larger the gap is, the smaller the cross-section of the core can be used.

As already stated, when the cross-section of the core is reduced, the number of ac turns has to be increased to avoid resaturation of the core. In doing so, the normal FCL impedance becomes larger. Thus, a compromise has to be made between the size of the core and the FCL impedance during normal operation.

Although it brings the benefit of smaller core size, an air gap has been mostly avoided in the FCL design since it increases the reluctance of the common ac-dc magnetic path $\Re_{ac-dc}$ (see Figure 3-2) and therefore requires more dc turns N_{dc} to saturate the core. Figure 3-4 shows the increase of number of dc turns N_{dc}, relative to its value in the design without a gap, versus the length of the gap l_{gap}. The increase in the number of dc turns

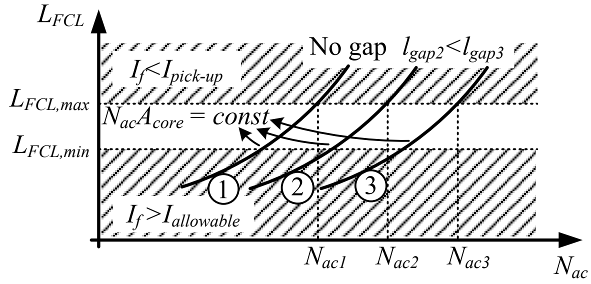

Figure 3-3: The inductance of FCL L_{FCL} versus the number of ac turns N_{ac} for the different gap lengths l_{gap}.

is significant even for relatively small gap lengths. The presented results are obtained for a specific FCL design, but it is general enough to demonstrate the explained dependency of N_{dc} and l_{gap}.

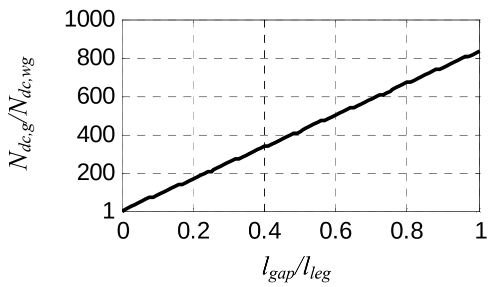

Figure 3-4: The number of dc turns N_{dc}, required to drive a core to a specific saturation point B_{dc}, versus length l_{gap} of the gap.

An air gap, nevertheless, could be used in the design of inductive FCLs if it would be part of the ac magnetic circuit, but not part of the dc magnetic circuit. The configuration of a core and the arrangement of the ac and dc windings should be such that the ac and dc fluxes are partially decoupled. Namely, provided that there is a part of the magnetic path through which only the ac flux flows, the gap could be inserted into the core without increasing the reluctance of the dc magnetic circuit. In this way, the number of dc turns required to drive the core to saturation would not be affected while at the same time, smaller cores could be used.

The previous chapter presented an analysis of the known FCL topology that uses a gapped core: an FCL with total magnetic decoupling of the ac and dc magnetic circuits. This topology is used as a basis for the development of a new FCL configuration which will eliminate the existing disadvantages. The following section gives the steps through which the design is changed before reaching the final FCL structure. These intermediate steps help in understanding the final FCL design.

3.3 Saturated-core FCL with partial magnetic decoupling

As shown in section 2.4.3, the drawback of an FCL with total magnetic decoupling is that an ac leg of the core cannot be deeply saturated by a dc winding placed in another leg of the core. The ac leg would be desaturated even by a normal current, resulting in increased FCL impedance during normal operation. It was concluded that the size of the core must be significantly enlarged to achieve an acceptably low value of the normal FCL impedance.

An improved FCL design, an FCL with partial magnetic decoupling, is presented in Figure 3-5 [Cvor 08b]. An auxiliary dc winding is added to the ac leg of the core to drive it deeper into saturation. The influence of the auxiliary dc winding on the level of core saturation is shown in Figure 3-6. The auxiliary dc winding moves the dc operation point away from the knee of the BH curve.

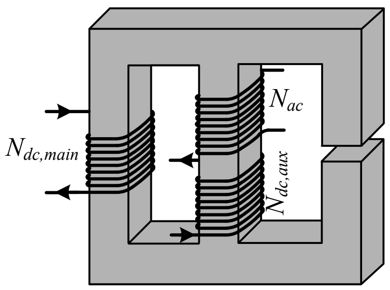

Figure 3-5: FCL with partial magnetic decoupling.

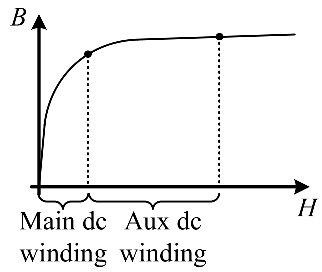

Figure 3-6: Auxiliary dc winding provides deep saturation of the ac leg.

The number of turns of the auxiliary dc winding $N_{dc,aux}$ is determined from:

$$N_{dc,aux} I_{dc} = N_{ac} I_L, \tag{3.5}$$

where $N_{dc,aux}$ is the number of turns of the auxiliary dc winding, I_{dc} the value of dc current and I_L the line current.

The results obtained from the Saber model of the presented FCL configuration confirm its principle of operation. To enable a design comparison with the previously discussed FCL topology with total magnetic decoupling, the data presented in Table 2-2 in the previous chapter are used as a starting point of design. Table 3-1 gives both the parameters from Table 2-2 and the design parameters of the FCL with partial magnetic decoupling. The parameters of the electrical circuit are the same as those given in Table 2-2.

Table 3-1: Parameters of the FCL models with total and partial magnetic decoupling in Saber.

Parameter	FCL with total magnetic decoupling	FCL with partial magnetic decoupling
Number of ac turns	30 turns	60 turns
Number of dc turns	500 turns	500 turns
Number of aux. dc turns	–	80 turns
DC current	450 A	450 A
Cross-section of ac leg	0.2 m^2	0.2 m^2
Cross-section of middle leg	0.4 m^2	0.4 m^2
Cross-section of dc leg	0.2 m^2	0.2 m^2
Gap length	0.5 m	0.5 m

The variation of magnetic flux density B in the ac leg, during both normal and fault operations of the system, is presented in Figure 3-7a. During normal operation, the core is not driven out of saturation, resulting in a continuously low impedance of the ac winding. The peak of the normal current, presented in Figure 3-7b, is 0.996 p.u..

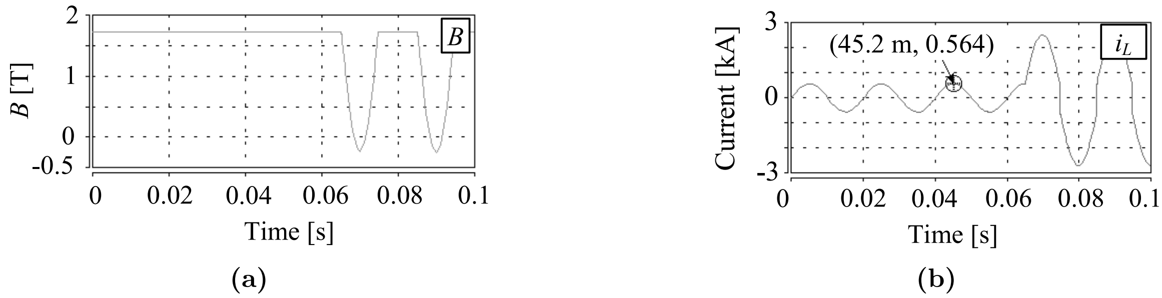

Figure 3-7: The results from Saber simlations: (a) Variation of B field in the ac leg - it is not desaturated during normal operation; (b) The waveform of the line current.

Since both the ac and auxiliary dc windings are placed on the same leg, they are magnetically coupled, resulting in an induced over-voltage across the dc current source during a fault. However, the main dc winding is still decoupled from the ac flux so that the total induced voltage is reduced. The waveform of the voltage induced in the auxiliary dc winding is presented in Figure 3-8.

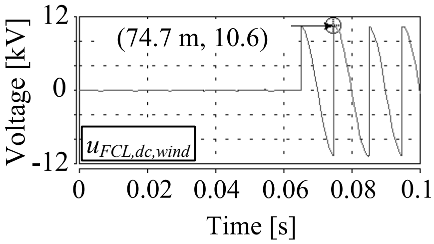

Figure 3-8: Induced voltage in auxiliary dc winding.

Since the dc winding has to be placed in the same leg as ac winding, the induced over-voltage in the dc current source cannot be avoided.

Table 3-2 presents an overall comparison of FCL topologies with total and partial magnetic decoupling. The amount of required material is significantly reduced if an FCL with partial magnetic decoupling is used.

Table 3-2: Comparison of FCL topologies with total and partial magnetic decoupling.

Parameter	**FCL with total magnetic decoupling**	**FCL with partial magnetic decoupling**
Mangetic material	100%	39%
Winding material	100%	85%
AC resistance	100%	81%
DC resistance	100%	140%

FCL topology with a short-circuited dc winding

Although the main dc winding has a much larger number of turns than the auxiliary dc winding, its contribution to the saturation of the ac leg is much smaller, see Figure 3-6. The large number of turns of the main dc winding is required in order to increase the reluctance of the dc leg and to divert the ac flux through the gapped leg. Otherwise, the distribution of the ac flux through the dc leg would further increase the induced voltage in a dc current source.

If the main dc winding is replaced with a short-circuited winding, the operation of an FCL would not be altered, see Figure 3-9. The flow of the ac flux through the dc leg induces a current in the short-circuited winding which, in turn, diverts the ac flux from that leg. In that case, the dc leg would not be deeply saturated. It would be driven to the knee of the saturation curve by the auxiliary dc winding. However, this would not increase the impedance of the FCL during normal operation since the ac flux does not flow through this leg.

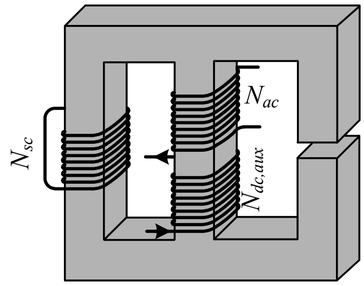

Figure 3-9: The FCL with a short-circuited winding.

The induced current in the short-circuited winding is proportional to the rate of change of the flux in the dc leg and inversely proportional to the number of turns of the winding. If the number of turns of this winding is decreased, the value of the induced current will increase. In this way, the total amount of dc winding material can be considerably decreased:

$$N_{sc} << N_{dc,main}, \tag{3.6}$$

where N_{sc} is the number of turns of the short-circuited winding and $N_{dc,main}$ the number of turns of the main dc winding.

Since the induced current flows only during a fault-limiting period, the dissipated heat can be absorbed by the heat capacity of the winding itself.

The simulation results obtained from the Saber model of the FCL presented in Figure 3-9 prove that it operates in the same way as the topology shown in Figure 3-5. The main dc winding of 500 turns (see Table 3-1) is replaced by the short-circuited winding with N_{sc}=30 turns. Figure 3-10a shows the B field in the dc leg and the gapped leg for both FCL configurations. As can be seen, in both cases there is no flux variation in the dc leg and the flux variation in the gapped leg is the same. The comparison of the current waveforms of both FCLs is presented in Figure 3-10b. They match very well. Thus, the normal impedance of the FCL with the short-circuited winding is not increased because of the non-deep saturation of the dc leg.

By replacing the main dc winding with a short-circuited winding, the total amount of winding material of the FCL with partial magnetic decoupling is reduced by 80%.

The FCL topology shown in Figure 3-9 uses two cores per phase. To further reduce the amount of magnetic material, it is possible the combine these two cores into one. The single-phase topology is presented in Figure 3-11. As can be seen from the structure of the core, the dc leg is removed, since its only function is to provide a low reluctance path for the dc flux. In the new design, an additional ac leg replaces this function of the dc leg. The dc flux, produced by two dc windings, flows as indicated in Figure 3-11. The

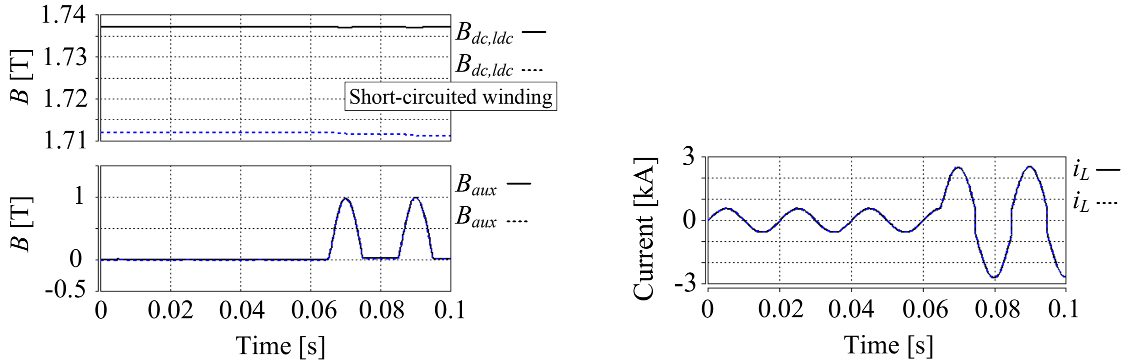

(a) **(b)**

Figure 3-10: The results from Saber simlations: (a) The magnetic flux density B in the dc leg and the gapped leg; (b) The waveforms of the line current of both FCL topologies with the main and short-circuited dc windings.

short-circuited windings are still employed and their function is to divert the ac flux of each ac winding to the neighboring gapped leg. For example, the ac flux, which is a result of the ac winding on the left side of the core closes its path through the left gapped leg, see Figure 3-11.

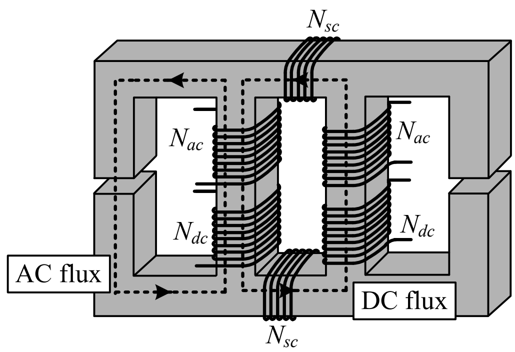

Figure 3-11: A single-core FCL topology with the short-circuited windings.

The design of the FCL topology shown in Figure 3-11 can further be improved, so that the size of the core and consequently the amount of magnetic material is further decreased. This final design of an FCL with partial magnetic decoupling is presented in the following section.

3.4 Novel single-core FCL with reduced core size

3.4.1 Topology and principle of operation

A new topology of an inductive saturated-core FCL is presented in Figure 3-12 [Cvor 09]. It is obtained from the FCL configuration shown in Figure 3-11 by removing one of the gapped legs and both short-circuited windings. Since two legs of the core, each having one ac winding, are desaturated alternately from one half-cycle to another, one gapped leg is sufficient to conduct the ac flux generated in these two legs. Thus, the new topology has three magnetic legs, where each outer leg has one ac and one dc winding. The ac windings are connected in series to a line, whereas the dc windings are connected in series to a dc current source. A gap is placed in the middle leg.

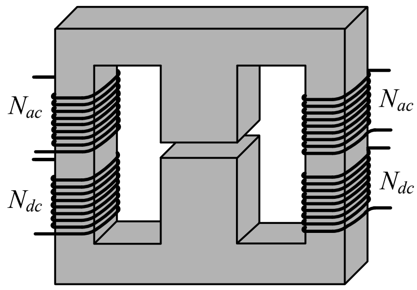

Figure 3-12: A single-phase topology of an inductive FCL.

The new topology enables the inserted gap to be part of the ac magnetic circuit, but not part of the ac magnetic circuit. The principle of operation is depicted in Figure 3-13. The dc windings are connected in such a way that they provide circular flow of the dc flux, see Figure 3-13a. Thus, the outer legs are saturated, but the dc flux does not flow through the middle leg of the core (3.7). As a result, the level of dc saturation is not dependant on the gap length l_{gap} (3.8).

$$B_{dc,mid} = 0, \tag{3.7}$$

$$B_{dc,outer} = \mu_{r,sat}\frac{N_{dc}I_{dc}}{l_{mean,outer}} + \left(B_{sat} - \mu_{sat}H_{sat}\right), \tag{3.8}$$

where $B_{dc,mid}$ and $B_{dc,outer}$ are the dc flux density in the middle leg and the outer leg of the core, respectively, $\mu_{r,sat}$ the relative permeability of the saturated core, N_{dc} the number of dc turns, $l_{mean,outer}$ the mean-length of the outer leg and H_{sat} the saturation value of the magnetic field.

The middle leg provides a shunt path for the ac flux and therefore enables the air gap to be inserted only in the ac magnetic circuit. The distribution of the ac flux in one half-cycle is presented in Figure 3-13b. After a fault is initiated, the left and right legs of

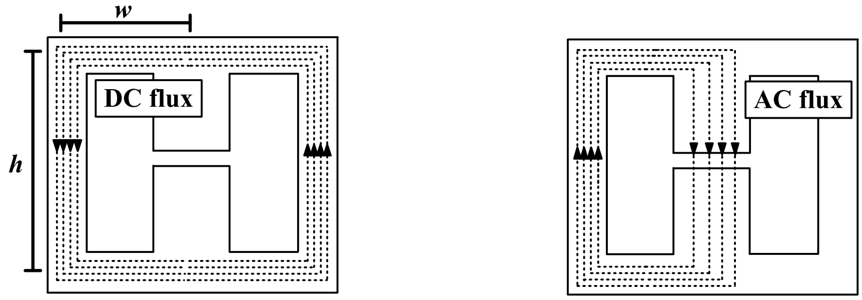

(a) (b)

Figure 3-13: The flux distribution in the core: (a) The dc flux; (b) The ac flux in one half-cycle.

the core are alternately driven out of saturation; the connection of the ac windings is such that during one half-cycle the dc and the ac fluxes align in one outer leg and counteract each other in the other outer leg. As shown in Figure 3-13b, the ac flux of the left leg closes its path through the middle leg because the reluctance of the core's right leg (or conversely during the other half-cycle) is very large due to saturation.

In each half-cycle during the fault period, one of the outer legs is driven out of saturation, resulting in an increased impedance of the associated ac winding. The FCL's inductance during the normal and fault regimes can be approximated as follows, respectively:

$$L_{FCL,sat} = \mu_0 \frac{N_{ac}^2 A_{core,outer}}{l_{mean,outer} + l_{gap}} = \mu_0 \frac{N_{ac}^2 A_{core,outer}}{\left(\frac{l_{mean,outer}}{l_{gap}} + 1\right) l_{gap}}, \tag{3.9}$$

$$L_{FCL,lin} = \mu_0 \frac{N_{ac}^2\, 2A_{core,outer}}{l_{gap}} = f\left(2A_{core,outer}\right), \tag{3.10}$$

where $L_{FCL,sat}$ is the inductance of the FCL in saturation, $A_{core,outer}$ the cross-section of the outer leg of the core and $L_{FCL,lin}$ the FCL's inductance out of saturation (in fault regime). The relative permeability of a core in saturation $\mu_{r,sat}$ is equal to 1.

The difference between the FCL inductances in the normal and fault regimes is a function of the ratio of the length of the outer leg and the gap length $l_{mean,outer}/l_{gap}$.

For a proper design, the variation of flux density in the outer leg during a fault is nearly $2B_{sat}$. This leg is driven by the fault current from one saturation region of the BH curve to the other. The middle leg is not saturated during normal operation and, in order to achieve large FCL impedance, it has to remain in the linear regime during the fault. This means that the maximum allowable flux variation in the middle leg is B_{sat}. To avoid the resaturation of the outer legs, the equation (3.11), based on Gauss's law, has to be satisfied. The cross-section of the middle leg, thus, has to be two times larger than that of the outer leg:

$$B_{sat}A_{core,mid} = 2B_{sat}A_{core,outer} \quad => \quad A_{core,mid} = 2A_{core,outer}, \tag{3.11}$$

where $A_{core,mid}$ is the cross-section of the middle leg of the core.

The number of required dc turns N_{dc} can be calculated as:

$$N_{dc} = \frac{H_{dc}}{I_{dc}} l_{mean,ldc}, \tag{3.12}$$

where $l_{mean,ldc}$ is the mean-length of the dc flux path.

In comparison to that of a typical FCL configuration, or an FCL with total magnetic decoupling, the number of dc turns can be reduced, due to the short length of the dc-magnetic path. Namely, the length $l_{mean,ldc}$ is reduced from value $2(w+h)$ to $2w+h$, see Figure 3-13a. The reduction is a function of the ratio w/h.

As a result, the value of the voltage induced across the dc current source during the fault period, which is proportional to the ratio of dc and ac number of turns, is reduced:

$$u_{FCL,dc,wind} = u_L \frac{N_{dc}}{N_{ac}}, \tag{3.13}$$

where $u_{FCL,dc,wind}$ is the voltage induced across the dc current source and u_L is the line voltage.

The operation of the single-phase FCL topology is confirmed in the following section through both modeling and experimental testing. The design procedure includes three modeling steps, see Figure 3-14.

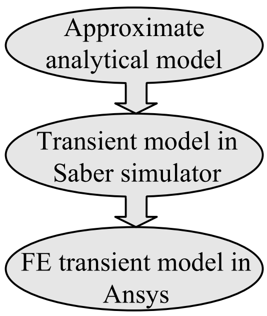

Figure 3-14: FCL modeling procedure.

The initial estimate of the FCL design parameters is obtained using a developed analytical model which is presented in Appendix C. Such a model does not take into account leakage fluxes, i.e. it assumes an ideal magnetic coupling between the windings. Also, it does not accurately account for fringing flux in the gap.

The first FCL design is obtained using a transient FCL model in the Saber simulator. The model gives the waveforms of the signals and makes it easier to assess the operation of the FCL during both normal and fault regimes. The parameters of the FCL, obtained from the analytical model, can be further tuned in this modeling stage. The advantage of the FCL model in Saber is that it is relatively simple to build, in comparison to an FE model for example, and it consumes little computational time (usually less than a minute for the models used here). The accuracy of the Saber results is, however, dependent on gap length. Namely, this model does not fully account for leakage and fringing fluxes, which can have a considerable influence on the results. The fringing effect must be taken into account for the lengths of the gap which are large relative to the width and depth of the core's leg.

As the last modeling stage, a transient 3D FE FCL model is developed in Ansys. This model takes into account both leakage and fringing flux effects and gives very accurate results. It requires considerably more computational time. It is, therefore, recommended to use the FE model as the final design step.

A lab-scale FCL demonstrator is built and tested. The experimental results are presented at the end of the following section. They validate the principle of operation of the proposed single-phase FCL topology.

3.4.2 Validation of FCL principle of operation

Analytical estimate of FCL design parameters

The relation between the FCL parameters, in the case with no gap, is described with equations (3.2) and (3.3). Equation (3.2) is an approximate expression, which assumes an ideal coupling between the windings. To design the FCL, three unknown parameters have to be calculated: the cross-section of the core A_{core}, the mean-length of the flux path l_{mean} and the number of ac turns N_{ac}. The number of dc turns N_{dc} is another unknown parameter, but it is proportional to the number of ac turns and can be determined in the later modeling stage.

For the design of the lab prototype, an available silicon-steel magnetic core is used. The saturation flux density is B_{sat}=1.8 T. Figure 3-15 and Table 3-3 give the dimensions of the core. Thus, two of three unknown variables, the cross-section of the core and the mean-length of the flux path, are predetermined. The number of ac and dc turns remains to be calculated.

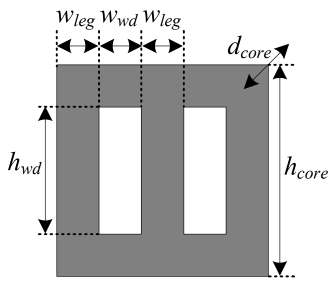

Figure 3-15: The parameters of the experimental core.

Table 3-3: The dimensions of the core.

Parameter	Value
Core height, h_{core}	13 cm
Window height, h_{wd}	7.8 cm
Window width, w_{wd}	2.5 cm
Leg width, w_{leg}	2.6 cm
Core depth, d_{core}	2.5 cm

The numbers of ac and dc turns are calculated using the given equations. The nominal voltage and current values of the setup are U_L=20 V$_{rms}$ and I_L=3.5 A$_{rms}$, respectively. It is assumed that the maximal variation of the B field during the fault period is B_{var}=0.6 T. Figure 3-16a shows the obtained relationship between the cross-section of the core A_{core} and the number of ac turns N_{ac}. The cross-section of the core is already known (A_{core}=6.5 cm^2) and the corresponding number of ac turns is N_{ac}=170. The inductance value of the FCL as a function of the number of ac turns is given in Figure 3-16b. Its value is close to 0.2 H for N_{ac}=170.

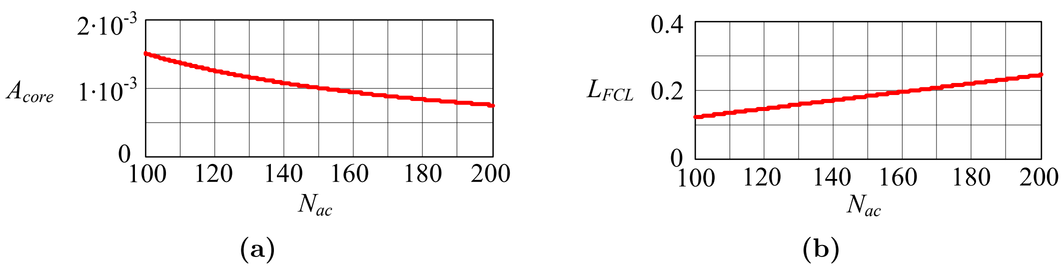

Figure 3-16: Design results obtained from analytical model: (a) The cross-section of the core; (b) The FCL inductance.

The available dc current source provides a current of I_{dc}=10 A. The approximated number of dc turns is a function of the ac mmf $N_{ac}I_L$, the value of dc current I_{dc} and the width of the safety zone I_{saf}, shown in Figure 2-19:

$$
\begin{aligned}
N_{dc}I_{dc} &= N_{ac}I_L + N_{dc}I_{saf} \\
N_{dc} &= \frac{N_{ac}I_L}{I_{dc} - I_{saf}},
\end{aligned}
\tag{3.14}
$$

where the safety zone I_{saf} is the maximum increase of the peak normal current I_L for which the core will still remain in saturation.

For the chosen width of the safety zone I_{saf} =5 A_{peak} and the determined ac mmf of 850 A-turns, the number of dc turns is calculated N_{dc}=170. The expected peak of the limited fault current is $I_{L,lim}$=8.44 A_{peak}.

The above-calculated FCL parameters are obtained for the case l_{gap}=0 mm. Experiments are conducted for the gap lengths 0 mm and 3.5 mm to verify that:

i. Gap insertion changes the value of FCL fault impedance,
ii. Gap insertion does not alter the level of core saturation, i.e. it does not change FCL normal impedance.

The experimental results will be presented later in this section.

The effect of a gap on impedance can be calculated from the equation (3.4). This approximation is improved by adding the part which represents the flux fringing effect in the gap (3.15) [Boss 02]. The detailed equations are presented in Appendix C.

$$L_{FCL} = N_{ac}^2 \left(\mathrm{P}_{gap} + \mathrm{P}_{fring}\right), \tag{3.15}$$

where P_{gap} is the permeance of the gapped core and P_{fring} the permeance due to the fringing effect of the flux.

The variation of FCL inductance versus gap length is presented in Figure 3-17a. For the gap length l_{gap}=3.5 mm the FCL inductance is equal to $L_{FCL,gap}$=8.6 mH. The expected peak of the limited fault current is $I_{L,lim}$=18.554 A_{peak}.

In the case that a gap is inserted in the dc magnetic circuit, the number of dc turns N_{dc} would have to be increased in order to preserve the level of core saturation (3.16). Figure 3-17b shows the factor by which the number of dc turns would have to be increased as a function of gap length. For l_{gap}=3.5 mm the number of dc turns would be larger by a factor of 23.

$$N_{dc} = \frac{B\left(\frac{l_{mean}}{\mu_0\mu_{r,sat}} + \frac{l_{gap}}{\mu_0}\right) - l_{mean}\left(\frac{B_{sat}}{\mu_0\mu_{r,sat}} - H_{sat}\right)}{I_{dc}} \tag{3.16}$$

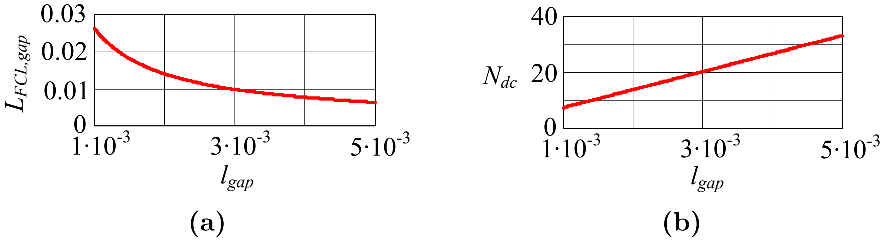

Figure 3-17: Design results for the gapped FCL: (a) The FCL inductance; (b) Influence of the gap on the number of required dc turns.

Table 3-4: The parameters of the designed single-phase FCL.

FCL parameter	Value
Cross-section of the leg	6.5 cm^2
Number of ac turns	170 turns
Number of dc turns	170 turns
DC current	10 A
Gap length	3.5 mm
Inductance of the non-gapped FCL	0.2 H
Inductance of the gapped FCL	8.6 mH

The parameters of the designed FCL model are summarized in Table 3-4.

The FCL model in Saber is built using these calculated parameters. The model is presented below.

FCL design in Saber

The Saber simulator enables the modeling of combined magnetic and electrical circuits. The magnetic calculations are based on network modeling with reluctances and flux sources as main elements. The reluctances are calculated by Saber. A transient model of an FCL is presented in Figure 3-18. Both the ac and dc electrical circuits are created by using electrical elements, such as a voltage source, a resistor etc. The windings present the link between the electrical and magnetic domains. They conduct both an electrical current and a magnetic flux. The magnetic circuit is built using magnetic elements. Each element represents a part of the magnetic circuit, such as one leg of the core or an air gap. Each element requires that the BH curve, mean-flux path length and gap length are defined.

Saber assumes that the total flux is uniformly distributed over the cross-section of the element. This means, among other thing, that leakage fluxes and fringing are not accounted for.

The parameters of the built FCL model have the values equal to those given in Table 3-4. The resistance of the ac windings was not taken into account in the analytical model. Since its value is not negligible (equal to R_{wind}=0.6 Ω) it has to be accounted for and is added to the Saber model.

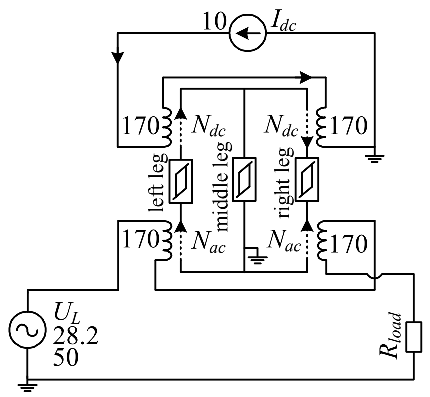

Figure 3-18: Saber model of the FCL lab setup.

The waveforms of the line current are presented in Figure 3-19a, for both cases l_{gap}=0 mm and l_{gap}=3.5 mm. A fault is incepted at moment t_f =35 ms. Due to the added resistance of the ac windings, the actual peak values of the fault currents are lower than was calculated. Still, it can be concluded that the analytical and Saber models give comparable results. The inductance waveform of one ac winding, when l_{gap}=3.5 mm, is shown in Figure 3-19b. The peak value during the fault period is approximately equal to the calculated value of 8.6 mH.

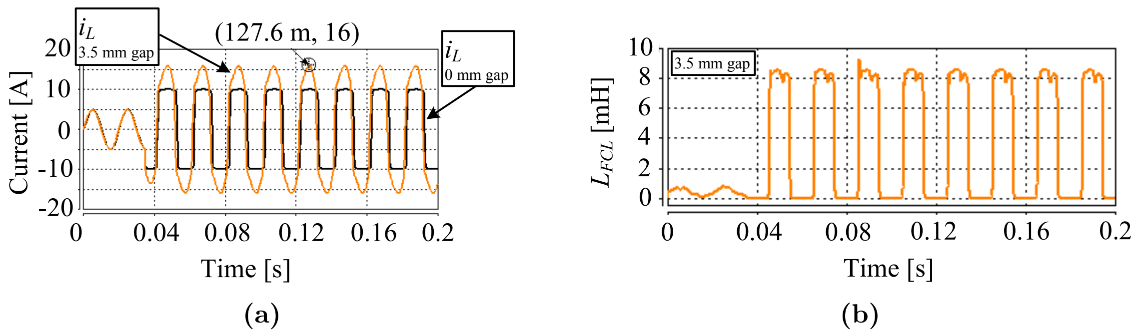

Figure 3-19: FCL simulation results in Saber: (a) Current for two lengths of the gap; (b) The inductance.

Flux distribution in the single-phase FCL topology can be understood from Figure 3-20a. During the normal regime, the core's outer legs are saturated and the flux level in the middle leg is nearly equal to zero; the dc flux flows only through the outer legs.

The left and right legs are alternately driven out of saturation, from one half-cycle to another, after fault inception. In each half-cycle, the ac flux from the desaturated outer leg is transferred through the middle leg of the core.

Figure 3-20b shows the variation of the B field in the left leg of the core for both lengths of the gap. The insertion of the gap does not change the level of the saturation of the outer leg, i.e. the gap is not in the dc magnetic path.

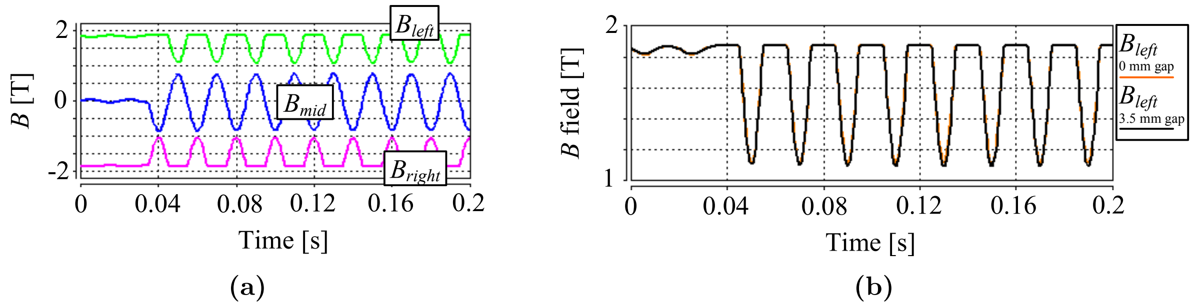

Figure 3-20: The flux variation during fault regime: (a) In the three core's legs; (b) In the left leg for two gap lengths.

The model in Saber gives the first approximate design of the FCL. This model does not account for the fringing and leakage fluxes, since it cannot model 'air' around the FCL. Such an idealized representation can introduce considerable error into the results, especially for the larger gap lengths. It is therefore required to use an FE FCL model as the last design step.

The transient FE FCL model takes into account all the flux effects as well as the geometrical structure of the core and windings. The model is built in Ansys Classic. As will be seen later, the FE and experimental results match very well. Since FE simulations require a considerable amount of modeling and computation time, it is recommended to use them as the last verification stage. The following subsection presents the results obtained from the transient FE FCL model.

The final FCL design in Ansys

Both the 2D and 3D transient FE FCL models are built in Ansys Classic. They are shown in Figure 3-21a and Figure 3-21b, respectively. The 2D model of an FCL is a plane structure, with a defined z-dimension. Each winding is represented by two planes. The 3D FE FCL model represents the complete device; Figure 3-21b shows one half of an FCL due to the applied plane symmetry, which makes the simulations faster. The parameters of the FCL model are equal to those in Table 3-3 and Table 3-4. The number of the modeled ac and dc number turns is equal to 3; thus, the factors n_{ac} and n_{dc}, representing the ratio between the real and modeled numbers of turns of the 3D FE FCL model, are equal to 170/3=56.67. For an explanation regarding the factors n_{ac} and n_{dc}, as well as additional details about the modeling of an FCL in Ansys, refer to Chapter 5.

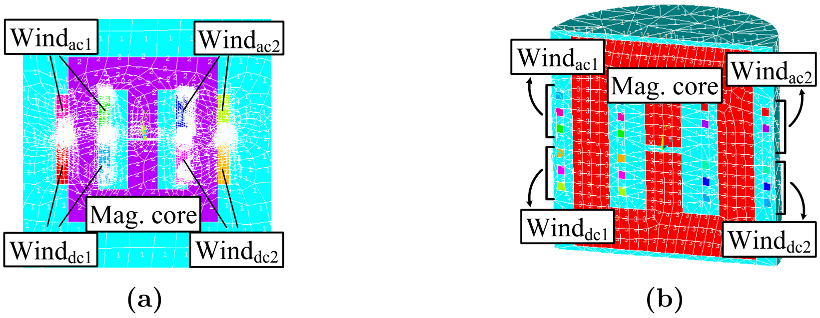

Figure 3-21: FE FCL models in Ansys: (a) 2D model; (b) 3D model.

The obtained results for the current waveforms are presented in Figure 3-22. The peak of the current, in the case that a gap is inserted in the core, is smaller than the one obtained from the Saber model. The reason for this is that the FE model takes into account effects such as fringing and leakage fluxes, leading to a different FCL inductance result.

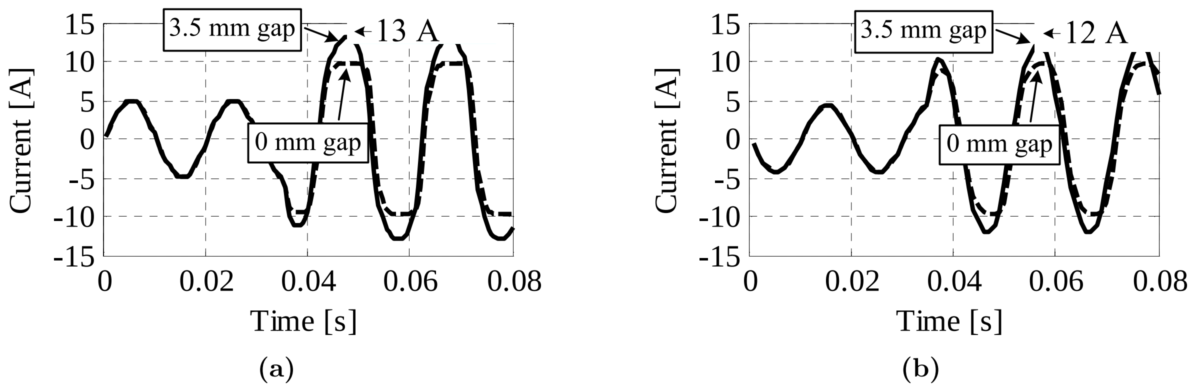

Figure 3-22: Currents with and without a gap: (a) 2D FE simulations; (b) 3D FE simulations.

The plots of the B field in the core, during normal and fault regimes, are presented in Figure 3-23a and Figure 3-23b, respectively. They explain and confirm the principle of operation of the proposed FCL topology. Namely, the plot of B during the normal regime shows that the dc flux does not flow through the middle leg and its value is, therefore, not dependent on the gap length. During the fault period, the ac flux in one half-cycle deeply saturates one of the outer legs and drives the other outer leg out of saturation. The ac flux from the desaturated outer leg closes its path through the middle leg and the gap, as shown in Figure 3-23b. Thus, the gap is a part of the ac magnetic circuit.

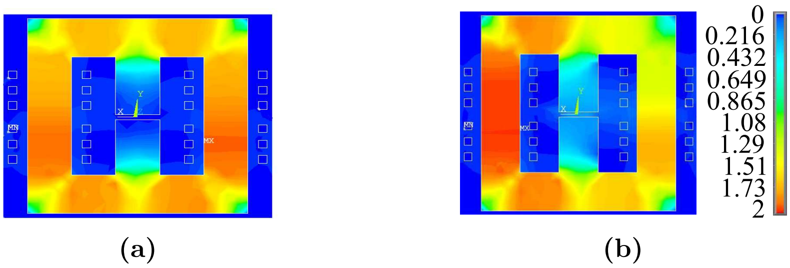

Figure 3-23: A snap-shot of the B field in the FCL: (a) During normal operation; (b) In one half-cycle during fault operation.

It is shown that there is a difference between the results from Saber and those from Ansys. This difference will increase for larger gap lengths. An FE model should be used as the last design step, before the experimental testing is done. There is a difference between 2D and 3D FE results. Again, a larger mismatch is expected for larger gap lengths. A comparison with the experimental measurements will determine the accuracy of the models presented above. The experimental setup and results are presented in the following subsection.

Experimental testing of the single-phase FCL

The operation of the designed lab-scale FCL prototype is validated experimentally. The electrical experimental circuit is shown in Figure 3-24. Its parameters are given in Table 3-5.

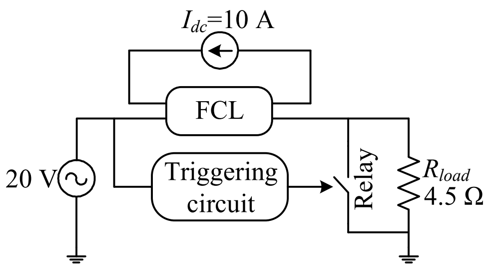

Figure 3-24: The experimental electrical circuit for testing of single-phase FCL.

The fault-inception (triggering) circuit, whose block diagram is shown in Figure 3-25, is used to trigger a fault at the desired moment relative to the zero-crossing of the source voltage. The moment of fault inception and the duration of the fault are set by adjusting the 'Moment of fault inception timer' and 'Fault duration timer', respectively, see

Table 3-5: The parameters of the electrical circuit.

Parameter	Value
Supply voltage,[V_{peak}]	28.2
DC current, [A]	10
Pre-fault resistance, [Ω]	5.7
Post-fault resistance, [Ω]	1.2

Figure 3-25. The first peak of the fault current is a function of the moment of fault inception; thus, to fully test the operation of the FCL, it must be possible to trigger a fault at different moments. A 'Manual double-fault set' circuit is used to enable the inception of two consecutive faults, where 'Double-fault timer' defines the time interval between these two faults. The switch S_{EN} enables a fault triggering operation. The fault is manually incepted using the switch S_F, located in the 'Manual fault inception' circuit. The detailed schematic of the fault inception circuit is presented in Appendix D.

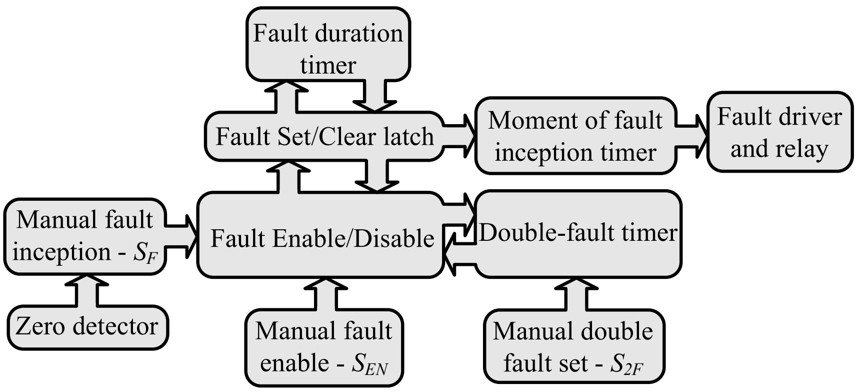

Figure 3-25: The block diagram of the fault-inception (triggering) circuit.

A laminated silicon-steel magnetic core, with wound ac and dc windings, is shown in Figure 3-26a; both the number of dc turns N_{dc} and ac turns N_{ac} are equal to 170. The saturation value of the B field is 1.8 T.

Figure 3-26b shows the waveforms of the measured currents for the cases when the gap length is equal to 0 mm and 3.5 mm. The results match those obtained from the 3D FCL model in Ansys very well, see Figure 3-22b. The peak of the experimental fault current with a gap in the core is equal to 11.5 A_{peak}, whereas the one obtained from the 3D FE FCL model has a value of 11.99 A_{peak}. The difference is negligible and can be caused by an inaccurate measurement of the windings' resistance or by the slight difference between the real BH curve and the one used in the simulations.

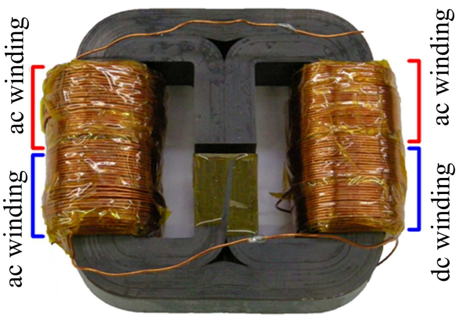

(a)

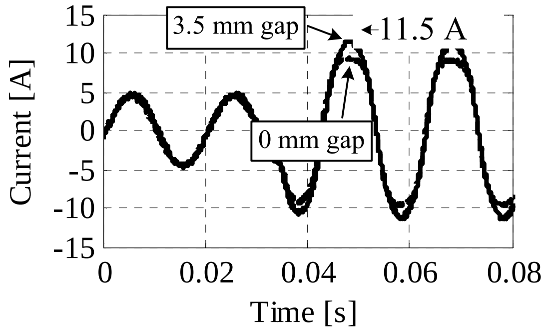

(b)

Figure 3-26: Lab-scale experiment: (a) The experimental core with the ac and dc windings; (b) The measured current waveforms for two gap lengths.

Figure 3-22 shows that the 2D FE model of the FCL gives less accurate results than the 3D model. Although the error might appear acceptably small in this case, it is expected to increase for larger gap lengths. Namely, the fringing effect has a larger influence on the FCL impedance for the larger gap lengths. This means that the calculation error of the fringing effect will also become more dominant with the gap length and will cause a larger discrepancy in the final results.

The 2D FE results (see Figure 3-22a) are more accurate than those obtained from Saber (see Figure 3-19a) because the 2D FE model partially calculates the fringing and leakage fluxes.

The obtained results confirm the principle of operation of the proposed single-phase FCL configuration: the gap is part of the ac, but not of the dc magnetic circuit. As can be seen from Figure 3-26b, gap insertion does not influence the peak of the normal current. This means that the gap is not part of the dc magnetic circuit and that the level of dc saturation is not lowered by the gap insertion. On the other hand, the fact that the peak of fault current is increased with the gap insertion indicates that the gap is part of the ac magnetic circuit and that it has direct influence on the FCL fault impedance.
Thus, the benefits of the proposed single-phase FCL topology can be summarized as:

i. The FCL core size (amount of magnetic material) can be decreased in comparison to other FCL topologies, due to the gap insertion. The proposed configuration provides the possibility of the employment of smaller cores for the same power rating in comparison to a typical FCL, an FCL with a common dc winding and an open-core FCL. At the same time, the amount of dc winding material is not increased by the gap insertion and is, therefore, not a function of the gap length.

ii. The induced voltage across the dc current source is lower than with the typical FCL topology due to the shorter mean-length of the dc magnetic path.

3.4.3 Inductive FCL configurations for a three-phase system

Since an FCL is a device intended for application in three-phase power systems, a three-phase topology has to be considered. A three-phase FCL consists of three single-phase units, see Figure 3-27. The windings of each phase are, thus, placed on separate cores and do not interact with each other. Therefore, the operation of the three-phase FCL can be analyzed by considering the single-phase device.

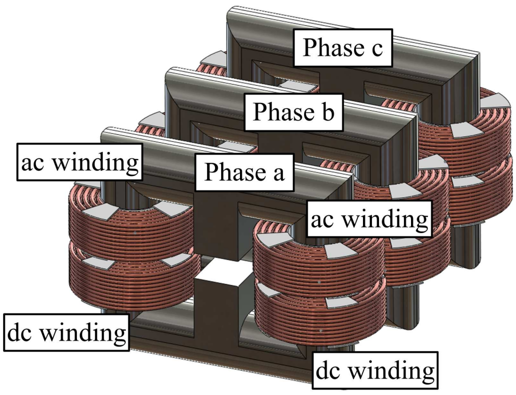

Figure 3-27: Three-phase FCL comprising three single-phase FCL units.

To have a more compact structure of the three-phase FCL, three single-phase FCL units can be arranged as shown in Figure 3-28 and Figure 3-29. With this arrangement, the three single-phase FCLs have common dc windings. The latter FCL topologies make the structure of three-phase FCL more compact, but do not bring the advantage of further material reduction. Three magnetic cores are still used, each having two ac windings. The cores are still magnetically insulated from each other. The total number of dc windings is reduced from 6 in Figure 3-27 to 2 in Figure 3-28 and to 3 in Figure 3-29. However, the length of a single turn of the new dc windings is larger so the total amount of dc winding material remains nearly the same for all three topologies.

The question is, however, whether the three-phase FCL topology can be further integrated in order to reduce the amount of required material. Such a design would additionally improve the applicability of the proposed FCL topology to the power systems. The following section presents the integrated three-phase FCL with the considerably reduced amount of magnetic material.

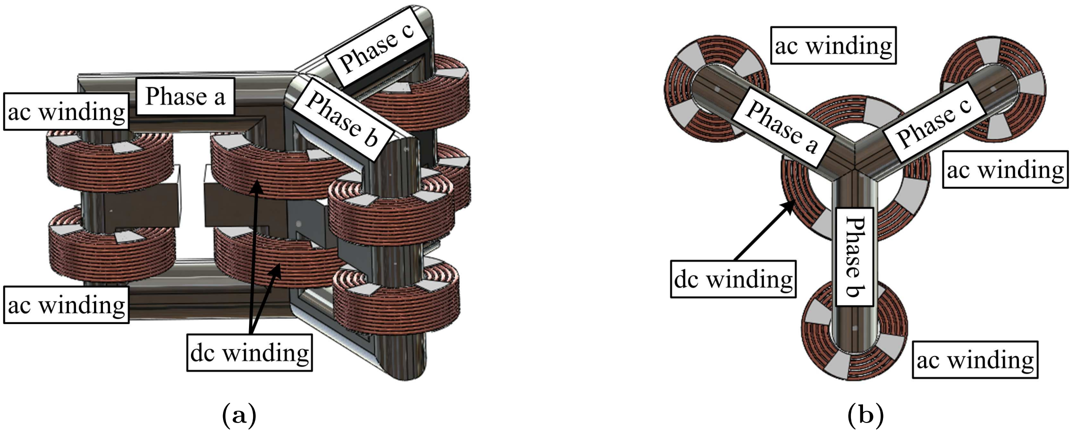

Figure 3-28: Three-phase FCL topology with two dc windings : (a) Side view; (b) Top view.

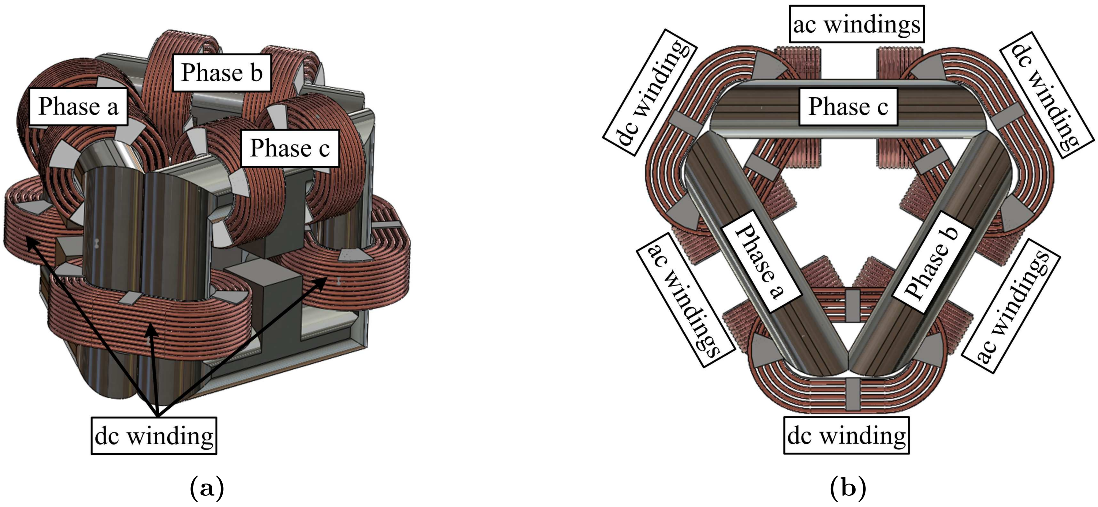

Figure 3-29: Three-phase FCL topology with three dc windings : (a) Side view; (b) Top view.

3.5 A three-phase inductive FCL with a common core and trifilar windings

3.5.1 Conceptual considerations

For the protection of a three-phase system three individual single-phase, gapped FCLs can be used, one for each phase. The total amount of magnetic material can be further reduced by applying one gapped core where the ac windings of all three phases are placed on the outer legs. Such a three-phase FCL structure, with the designated ac and dc windings, is presented in Figure 3-30. The amount of the total FCL material is thus reduced by nearly a factor of 3.

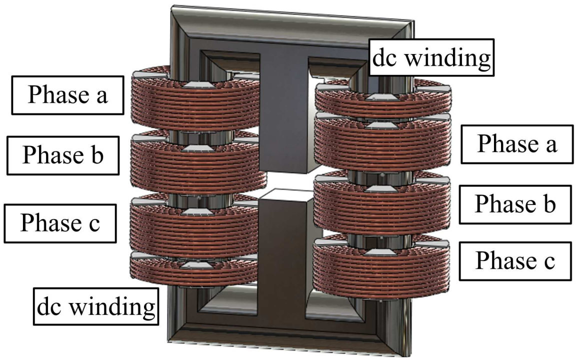

Figure 3-30: The three-phase FCL topology.

A similar topology can be found in literature [Shim 92]. This configuration uses one magnetic core for all three phases. The dc windings are not employed since, during the normal regime, the ac fluxes produced by the phase currents cancel each other out. The resulting FCL normal impedance is very low.

The new three-phase topology employs the new single-core 3-leg FCL design. It also uses dc windings which produce a circular flux flow so that the outer legs are driven to saturation during normal operation, see Figure 3-13. The phase fluxes are displaced from each other by 120°, which results in zero ac flux in the outer legs, during normal, balanced operation of the system. Since the ac fluxes cancel each other out, the normal phase impedance of the FCL is very low. The dc windings saturate the core deep enough so that an imbalance of the phase currents does not desaturate the core.

After fault inception, the flux, which is caused by the fault current, closes its path as shown in Figure 3-13b and desaturates the corresponding core's outer leg. The outer legs are desaturated alternately from one half-cycle to another. The resulting increased impedance of the FCL limits the fault current.

A three-phase FCL topology cannot limit faults which involve more than one phase. Since all three phase windings are placed on the same leg of the core, the ac fluxes caused by the fault current cancel each other out and keep the core in saturation. A single-phase fault occurs in 95% of fault cases. This topology presents a compromise between the cost of an FCL and its functionality.

The following subsection offers a more detailed analysis of the operation of the FCL during faults involving one and two phases. In the case of a three-phase (symmetrical) fault, the system behavior can be analyzed without taking FCL presence into account, as will be explained later.

3.5.2 System operation during different fault scenarios

When considering the fault operation of a three-phase FCL topology, coupling between the phase windings has to be considered. Keeping this in mind, the following fault scenarios will be analyzed: single-phase, two-phase to ground, phase to phase, three-phase and three-phase to ground fault.

Single-phase to ground fault

Figure 3-31 presents a three-phase circuit with an FCL and single-phase to ground fault in phase a. The load resistor in phase a is removed to present a short-circuit.

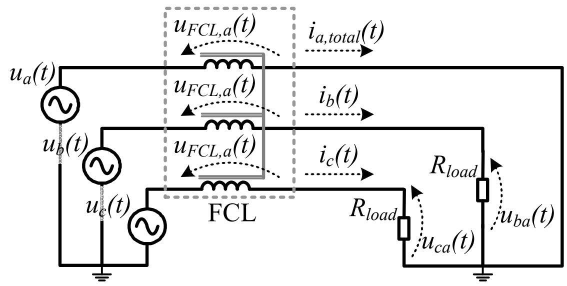

Figure 3-31: Three-phase circuit with a single-phase to ground fault.

Under the assumption that the fault impedance of the FCL is Z_{FCL}=$\omega \cdot L_{FCL}$, the short-circuit current in the faulted phase-a is:

$$\hat{I}_{a,f} = \frac{U_a \angle \theta_a}{Z_{FCL} \angle -90^\circ} = I_{a,f} \angle 90^\circ, \tag{3.17}$$

where it is assumed that θ_a=0°.

However, the total current in phase a $i_{a,total}(t)$ is influenced by the currents in phases b and c because of the magnetic coupling of the phase windings. Namely, during a fault the phase a winding is short-circuited. A current, proportional to the currents in the other two phases, is induced in this winding. The induced current, on the basis of Lenz's law, is equal to the negative sum of the currents in the other phases. Thus, the total current in phase a is:

$$\hat{I}_{a,total} = \hat{I}_{a,f} - \left(\hat{I}_b + \hat{I}_c\right). \tag{3.18}$$

The currents in b and c phases can be determined by taking magnetic coupling into account. The phase a voltage is imposed across the phase a winding, due to the short-circuiting of the corresponding load. This voltage is induced in each of the other two windings. Consequently, the currents in phases b and c are:

$$\hat{I}_b = \frac{\hat{U}_b - \hat{U}_a}{R_{load}} = \frac{\hat{U}_{ba}}{R_{load}}$$
$$\hat{I}_c = \frac{\hat{U}_c - \hat{U}_a}{R_{load}} = \frac{\hat{U}_{ca}}{R_{load}}. \tag{3.19}$$

From equation 3.19, the line-to-line voltage appears across the load in the unfaulted phases. Therefore, the corresponding currents are enlarged by a factor of 1.73. The described behavior of the three-phase circuit is presented by a phasor diagram in Figure 3-32.

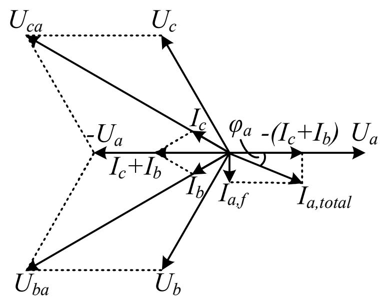

Figure 3-32: Phasor diagram of a three-phase circuit with a single-phase to ground fault.

Two points in the presented analysis should be emphasized:

i. The total fault current $i_{a,total}(t)$ is lagging the phase voltage $u_a(t)$ by an angle of $\varphi_a < 90°$. This might not be expected since phase a comprises only FCL inductance. The phase difference φ_a can be as low as 20°, and it is a function of the FCL fault impedance and power factors of the unfaulted phases.

ii. The minimal peak of the total fault current $\left|\hat{I}_{a,total}\right|$ in phase a is determined by the currents in b and c phases and is equal to $\left|\hat{I}_b + \hat{I}_c\right|$. The increase of the FCL fault impedance reduces only the magnitude of the fault current $i_{a,f}(t)$ (3.17) and not the magnitudes of the currents in the unfaulted phases (3.19).

It can be concluded from (3.18) that, due to coupling between the phases, the FCL impedance in the faulted phase appears to be lower than the designed value Z_{FCL}. The term 'effective' fault impedance of the FCL $Z_{FCL,eff}$ can be defined. It is equal to the ratio between the phase voltage and total fault current (3.20). The angle of the FCL effective impedance is equal to φ_a, see Figure 3-32.

$$|Z_{FCL,eff}| = \frac{\left|\hat{U}_a\right|}{\left|\hat{I}_{a,total}\right|}. \tag{3.20}$$

Two-phase to ground fault

As has already been stated, the three-phase FCL topology cannot limit a two-phase to ground fault. The behavior of the system with the installed FCL can be more thoroughly understood based on the three-phase circuit given in Figure 3-33.

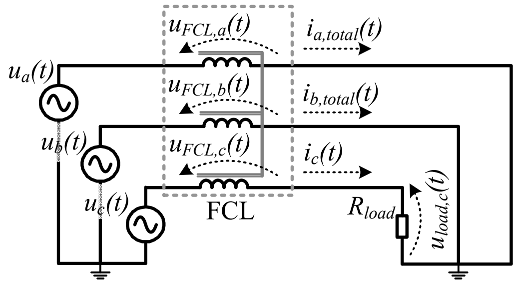

Figure 3-33: Three-phase circuit with a two-phase to ground fault.

The loads in phases a and b are removed to present the fault. In this case, the voltages of phases a and b are imposed across the corresponding FCL windings. The induced voltage across the third FCL winding $u_{FCL,c}(t)$ and the current in that phase $i_c(t)$ are equal to:

$$\hat{U}_{FCL,c} = \frac{\hat{U}_{FCL,a} + \hat{U}_{FCL,b}}{2} = \frac{\hat{U}_a + \hat{U}_b}{2}$$
$$\hat{I}_c = \frac{\hat{U}_c - \hat{U}_{FCL,c}}{R_{load}} = \frac{\hat{U}_{load,c}}{R_{load}}. \tag{3.21}$$

The currents in the faulted phases are equal in magnitude, but shifted by 180° from each other, i.e. $i_{a,f}(t)$=$-i_{b,f}(t)$. Their peak value is limited by the system's stray impedance, which is not presented in Figure 3-33. The current from phase c is induced in the faulted phases. The total fault currents in these phases have the following values:

$$\hat{I}_{a,total} = \hat{I}_{a,f} - \frac{\hat{I}_c}{2}$$
$$\hat{I}_{b,total} = \hat{I}_{b,f} - \frac{\hat{I}_c}{2}. \tag{3.22}$$

Phase to phase fault

The equivalent three-phase circuit for a phase to phase fault scenario is shown in Figure 3-34. Phases a and b are short-connected at the points before the corresponding loads.

The voltages across a and b FCL phase windings have the following values:

$$\hat{U}_{FCL,a} = -\hat{U}_{FCL,b} = \frac{\hat{U}_a - \hat{U}_b}{2}. \tag{3.23}$$

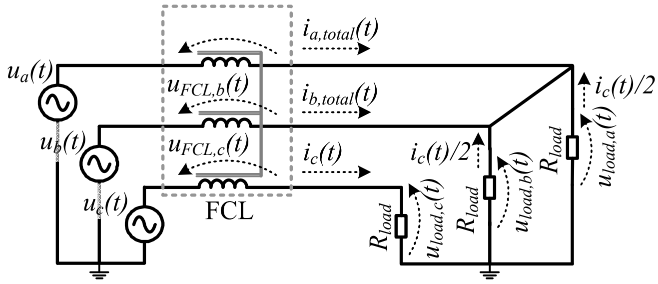

Figure 3-34: Three phase circuit with phase to phase fault.

The fault currents in phases a and b are equal to each other in magnitude and opposite in sign, $i_{a,f}(t) = -i_{b,f}(t)$. The fault current is limited only by the stray line impedance (not shown in Figure 3-34) and the resistance of the FCL windings. According to Lenz's law, the total currents in the faulted phases are influenced by the current from the third phase:

$$\hat{I}_{a,total} = \hat{I}_{a,f} - \frac{\hat{I}_c}{2}$$
$$\hat{I}_{b,total} = \hat{I}_{b,f} - \frac{\hat{I}_c}{2}. \tag{3.24}$$

It can be seen from Figure 3-34 that the load voltages, as well as the load currents, in the faulted phases are equal to each other. The load currents in both phases are equal to $-i_c(t)/2$, which means that the load voltage in these two phases is:

$$\hat{U}_{load,a} = \hat{U}_{load,b} = R_{load} \cdot \left(-\frac{\hat{I}_c}{2}\right) = -\left|\frac{\hat{U}_{load,c}}{2}\right| = -\left|\frac{\hat{U}_c}{2}\right|. \tag{3.25}$$

The current and load voltage, in the unfaulted phase c, have the same values as before fault inception:

$$\hat{I}_c = \frac{\hat{U}_{load,c}}{R_{load}} = \frac{\hat{U}_c}{R_{load}}. \tag{3.26}$$

Symmetrical fault

The equivalent three-phase circuits for a three-phase fault and a three-phase to ground fault are given in Figure 3-35a and Figure 3-35b, respectively.

In both scenarios, the fault currents are not limited and their sum is equal to zero. In the case of a three-phase fault, see Figure 3-35b, the load currents are equal to zero and the point of short-connection between the phases is at zero potential. This means that these fault scenarios are equivalent to each other.

Chapter 4 presents the design and testing results of a full-scale MV FCL prototype. To validate the developed FE FCL model, used for the design of the full-scale prototype, the design and testing of a three-phase lab-scale demonstrator is done. The following section gives the details of this prototype and presents the comparison between the FE and experimental results.

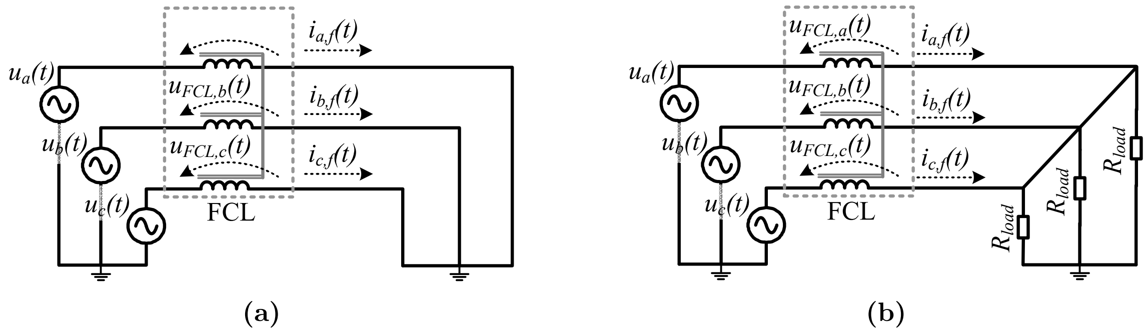

Figure 3-35: Equivalent three-phase circuit: (a) Three-phase to ground fault; (b) Three-phase fault.

3.5.3 Three-phase lab-scale FCL demonstrator

This section presents the modeling and testing of a three-phase lab-scale FCL demonstrator. Similar to section 3.4.2, it includes the following subsections:

i. The first estimate of the FCL parameters using an analytical model,
ii. The first FCL design in Saber,
iii. A 3D FE design in Ansys,
iv. Experimental testing,
v. The comparison of the FE and experimental results.

Analytical estimate of FCL design parameters and Saber simulations

A lab-scale demonstrator of the presented three-phase FCL topology is designed and tested in the lab. Having the input parameters given in Table 3-6, the dimensions of the magnetic core and the number of ac and dc windings' turns are obtained using the first order analytical model presented in Appendix C, see Table 3-6.

Thus, the steady-state peak of the fault current is equal to $I_{L,f}$=63 A_{peak} and the variation of the magnetic induction in the core during the fault is $k_{sat}B_{sat}$=0.9 T.

The Saber FCL model is built using the calculated parameters. The current waveform obtained during the pre-fault and fault operation is presented in Figure 3-36a. The steady-state peak of the fault current is $I_{L,f}$=57 A_{peak}. It is comparable to the one from the analytical design. The simulated fault-inductance of the FCL is equal to 3 mH, whereas its value obtained from the analytical model is 2.9 mH.

Variations in the B field in the core is presented in Figure 3-36b. During the normal regime, the value of the B field is constant since the fluxes from three phase windings cancel each other out. As expected based on the analytical design, the core is desaturated to B=1 T during the fault period.

Table 3-6: The parameters of the electrical circuit and the FCL.

Input parameters		Output parameters	
Circuit parameter	**Value**	**FCL parameter**	**Value**
Supply voltage U_L, $[V_{rms}]$	65	Cross-section of outer leg $A_{core,outer}$, $[m^2]$	$15 \cdot 10^{-4}$
Nominal current I_L, $[A_{rms}]$	3.5	Core width w_{core}, $[m]$	0.2
Load resistance R_{load}, $[\Omega]$	10	Core height h_{core}, $[m]$	0.4
Prospective $I_{L,pros}$, $[A_{rms}]$	400	Core depth d_{core}, $[m]$	0.04
Unbalanced current, $[A_{rms}]$	$0.25I_L$	Window width w_{wd}, $[m]$	0.04
Specifications for FCL	**Value**	Window height h_{wd}, $[m]$	0.32
DC current I_{dc}, $[A]$	10	Gap length l_{gap}, $[m]$	0.025
B variation $k_{sat}B_{sat}$, $[T]$	0.9	Number of ac turns N_{ac}, $[turns]$	125
Limited current $I_{L,lim}$, $[A_{rms}]$	45	Number of dc turns N_{dc}, $[turns]$	40
		FCL fault inductance $L_{FCL,lin}$, $[mH]$	2.9

Thus, the model of the FCL in Saber confirms the FCL parameters obtained from the first order analytical model. As already explained in section 3.4.1, the FE FCL model is used as the last design step.

3D FE model of a three-phase FCL

The created geometry of a 3D FCL model in Ansys is presented in Figure 3-37. The number of modeled ac turns per winding is equal to 9 and the number of modeled dc turns per winding is also 9. Thus, the factors n_{ac} and n_{dc} for this model are 13.89 and 4.44, respectively. The explanation of function of these factors in FE FCL modeling is given in Chapter 5. The parameters of the FE FCL model are given in Table 3-6.

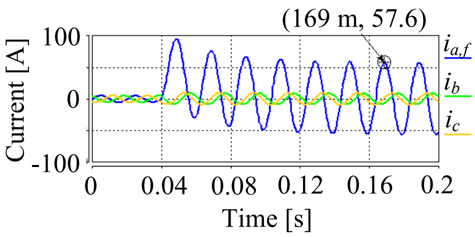

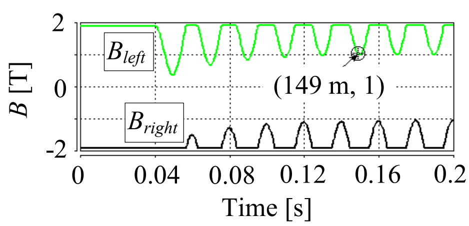

Figure 3-36: Saber simulation results for three-phase FCL: (a) Phase currents; (b) Variation of the B field in the core's left and right legs.

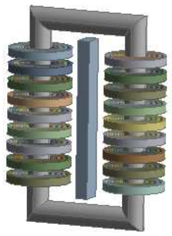

Figure 3-37: The geometry of the 3D FE FCL model in Ansys.

The used dc windings do not provide deep saturation of the core. Their function is only to prevent the core's desaturation because of a possible imbalance of the phase currents. Even though the saturation is not deep, the normal impedance of the FCL is very low due to the mutual cancelation of the phase fluxes. It was shown in the previous subsection that, in the ideal case, the placement of the phase windings on the common leg results in a complete cancelation of phase fluxes, see Figure 3-36b. The Saber FCL model represents the ideal case because no surrounding air can be added to the model. Since the leakage flux is forced to be zero, i.e. all the flux must flow through the predefined magnetic paths, the phase fluxes completely cancel each other out.

When running the 3D FE FCL model, it has been noticed, however, that magnetic coupling between the phase windings is not ideal. As a consequence, the normal impedance of the FCL was increased. This issue is addressed in the following subsection.

Problem of a non-ideal magnetic coupling of the phase windings

The self and mutual inductances of a winding, $L_{self,i}$ and $L_{mutual,ij}$ respectively, are a function of the total co-energy E_{mag} of the magnetic field that is stored in the system and the currents that are flowing through the windings:

$$L_{self,i} = \frac{d^2 E_{mag}}{dI_i^2}\,;\;\; L_{mutual,ij} = \frac{d^2 E_{mag}}{dI_i dI_j}\,;\;\; L_{total,i} = L_{self,i} + \sum_{j=1;\,j\neq i}^{n} L_{mutual,ij}. \tag{3.27}$$

The magnetic co-energy is calculated as shown in:

$$E_{mag} = \int_{\Omega}\int_{H} BdH\, d\Omega, \tag{3.28}$$

where I_i and I_j the currents of the windings i and j, respectively, $L_{total,i}$ the total inductance of the winding i, n the number of windings of the system and Ω is the volume enclosing the core and the windings.

When the phase fluxes $\phi_{a,b,c}$ cancel each other out they reduce the amount of stored magnetic co-energy E_{mag} in the system. Thus, the self-inductance L_{self} and the mutual inductance L_{mutual} of the windings are also reduced.

The arrangement of the phase windings in the simulated 3D FE FCL model can be seen in Figure 3-38a. Each of two outer legs contains one winding from each phase. Blue, red and green colors denote the windings of phases a, b and c, respectively. Each phase winding has nine turns and the ac windings from the same phase are connected in series. One dc winding with nine turns, marked with black color in Figure 3-38a, is placed on each outer leg. Figure 3-38b shows that the resulting total ac flux density in the core is different from zero. Consequently, the inductance of the FCL windings is enlarged in comparison to that in the case of ideal cancellation of the phase fluxes.

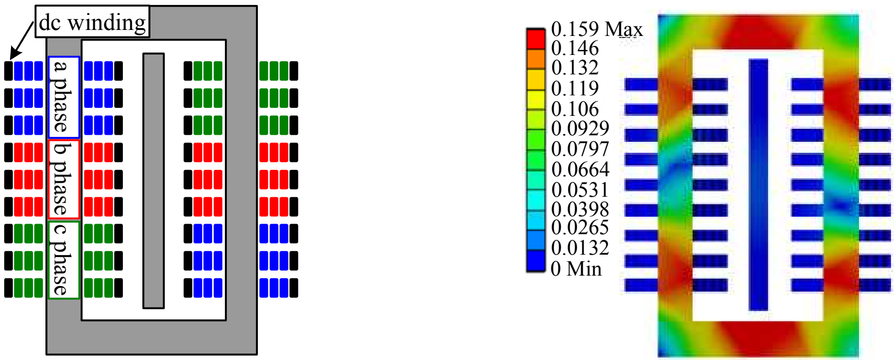

(a) **(b)**

Figure 3-38: Three-phase FCL with separately placed phase windings: (a) Cross-section of the core, phase windings and dc windings; (b) The B field in the FCL as a result of non-ideal magnetic coupling of the phase windings.

The asymmetric spatial position of the phase windings results in differences in their stray fields. The normal impedance of the designed FCL is therefore different for the different phases. This can be seen by checking the peaks of the phase currents. In a circuit with only the resistance of the load R_{load} (see Figure 3-24), the peak of the current during normal operation is $I_L = 5.08\ A_{peak} = 1$ p.u.. The peaks of a, b and c phase currents are 0.895 p.u., 0.97 p.u. and 1.04 p.u., respectively, see in Figure 3-39. Thus, the impedance of the FCL during normal operation has a large influence on the phase currents. Such an operation of the FCL is not acceptable.

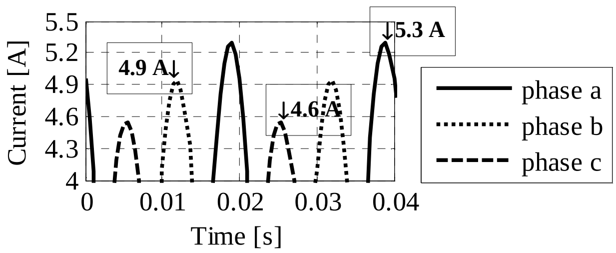

Figure 3-39: Peaks of normal phase currents influenced by different phase-impedances of the FCL.

To improve the flux coupling between the phase windings and, thereby, to reduce the impedance of the FCL during normal operation, a trifilar arrangement of the phase windings is proposed. The following subsection introduces the new concept.

Trifilar arrangement of the phase windings

This subsection introduces a trifilar arrangement of the phase windings and the benefit that it brings. An FE model of the designed lab-scale FCL prototype with trifilar windings is shown in Figure 3-40a. The phase windings are wound simultaneously (see Figure 3-40b) so that the three-turn layer of one winding is placed between layers of the other two windings. Each phase winding has nine turns and the windings from the same phase (one on each outer leg) are connected in series. The arrangement of the dc windings is not changed in comparison to that shown in Figure 3-38a.

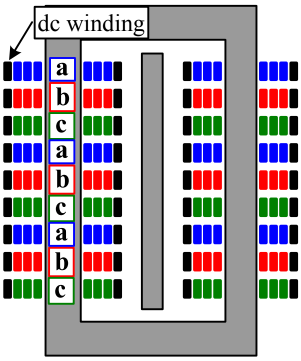

(a)

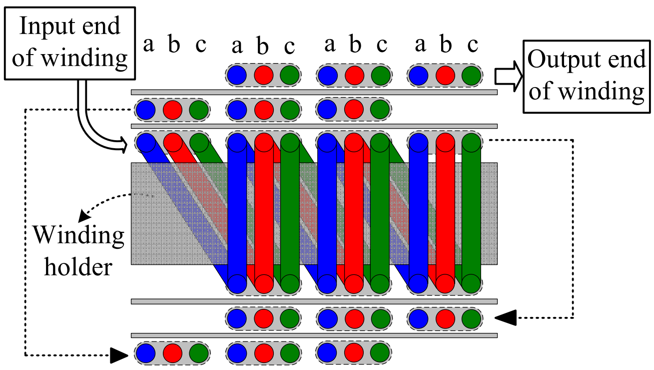

(b)

Figure 3-40: Three-phase FCL with trifilar phase windings: (a) Cross-section of the core, phase windings and dc windings; (b) Three-phase trifilar winding.

Figure 3-41a shows the resulting B field in the core with the trifilar windings. If compared to the results from Figure 3-38b, it can be seen that the value of the ac flux is considerably reduced. As a result, the amount of stored magnetic co-energy in the whole system and the impedance of the FCL during normal operation are also considerably lower.

The reduction of the FCL impedance can be seen by checking the peaks of the phase currents in the normal regime, see Figure 3-41b. When compared to Figure 3-39, it is clear that the FCL impedance in all phases is almost equal. The impedance is significantly reduced in comparison to that of the FCL with concentrated windings. The peaks of the phase a, b and c currents are equal to 0.98 p.u., 0.98 p.u. and 0.99 p.u., respectively. The impedance of phase a winding is reduced by a factor of 8.5, see Table 3-7.

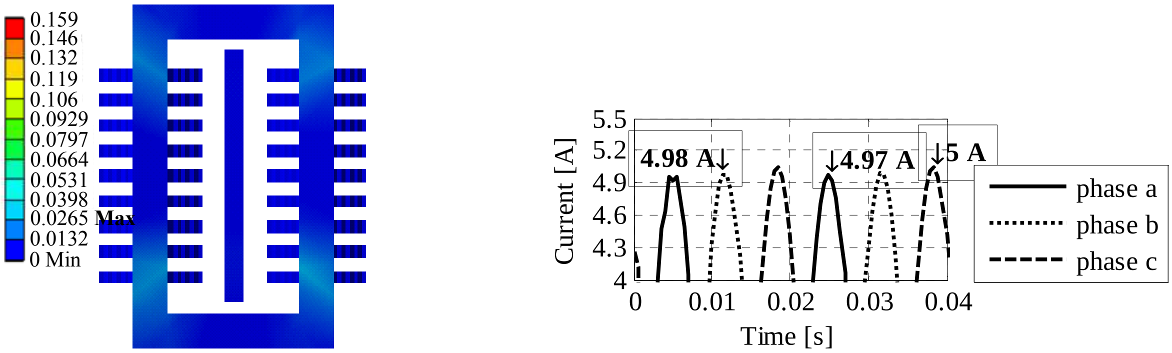

(a) (b)

Figure 3-41: Three-phase FCL with trifilar phase windings: (a) The B field in FCL; (b) The peaks of the normal phase currents - the FCL normal impedance is decreased considerably.

Table 3-7: Simulated reactance value of phase a winding for both arrangements of the phase windings.

Windings' arrangement	**Phase a current**	**Phase a FCL reactance**
Separate	$4.55\angle -7.2°$	1.47 Ω
Trifilar	$4.97\angle -0.9°$	0.17 Ω

To confirm that the trifilar placement of the windings can indeed reduce their inductance values, an experiment with the air-core inductors is carried out. The air-core inductor is used since its permeability is close to the permeability of the FCL during normal operation - the permeability of the saturated-core. Three windings are wound in a trifilar manner, see Figure 3-42. The number of turns and the physical spacing between the turns is nearly equal to those from the simulations.

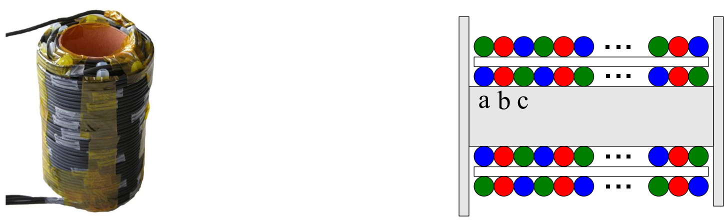

(a) (b)

Figure 3-42: Experimental trifilar winding: (a) Built demonstrator; (b) Arrangement of the windings.

In the first measurement, only one winding is conducting the current, so that the other two windings do not have an influence on its inductance. In the second measurement, all three windings are star-connected to a three-phase voltage source. The measured inductance values in both cases are given in Table 3-8. The obtained ratio between phase a inductance is 7.1, which is very close to the ratio obtained in simulations. The inductance of the winding is calculated as follows:

$$\frac{U_a}{I_a}\angle\varphi_a = R_{FCL,a} + jX_{FCL,a}, \tag{3.29}$$

where U_a is the voltage of phase a, I_a the phase a current, φ_a the phase a angle, $R_{FCL,a}$ resistance of phase a FCL winding and $X_{FCL,a}$ the reactance of phase a FCL winding.

Table 3-8: Measured reactance values of phase a winding.

	Phase a winding			
Windings' arrangement	**Voltage**	**Current**	**Resistance**	**Inductance**
Separate	2.58 V	$19.09\angle-7.2°$	0.127 Ω	0.05 mH
Trifilar	2.61 V	$20.31\angle-1°$	0.127 Ω	0.007 mH

Having obtained satisfactory results from the simulations regarding the value of the FCL normal impedance, the lab-scale FCL is built and tested. The following section presents the experimental setup of the designed three-phase FCL prototype.

The testing of the three-phase FCL

A lab-scale demonstrator of the three-phase FCL is built. The design parameters are presented in Table 3-6, with the difference that the cross-sections of the outer leg and the middle leg are equal to $A_{core,outer}$=$13.5 \cdot 10^{-4}$ m^2 and $A_{core,mid}$=$9 \cdot 10^{-4}$ m^2, respectively. The magnetic core is made from grain-oriented silicon-steel sheets (0.35 mm thickness); the commercial material grade is ET 150-35 and the grade according to EN 10107 : 2005 standard is M 150 − 355. The typical magnetic-flux saturation level is B_{sat}=1.84 T at H_{sat} = 800 A/m. The windings are made of low-voltage installation copper-wire, with a cross-section of A_{cu}=4 mm^2. The diameter of the wire, including the insulation layer is D_{wire}=3.3 mm. The dc windings are wound as a single layer over the ac windings. The experimental core is presented in Figure 3-43a. For better placement of the phase windings, the cross-section of the core's outer legs is made more or less circular, see Figure 3-43b. The resistance of the ac windings, per phase, is R_{wind}=0.29 Ω.

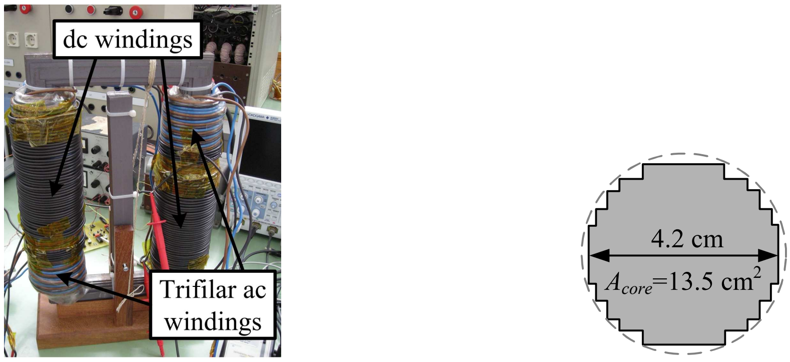

(a) (b)

Figure 3-43: Lab-scale experiment: (a) Built three-phase FCL demonstrator; (b) The cross-section of the core's outer leg.

The three-phase experimental circuit is shown in Figure 3-44. A three-phase transformer is connected to a three-phase resistive load via the FCL. Although the power factor of the real grid load is different from 1, the resistive load used in the lab is sufficient to prove the FCL operating principle. The line impedance is omitted for the same reason.

The three-phase transformer supplies line-to-line voltage of $U_{L,L} = 65\ V_{rms}$. The short-circuit current of the transformer is equal to $I_{L,f}$=400 A_{rms}. However, the rating of the built-in fuse is I_{fuse}=80 A_{rms}, so the maximum fault current was not measured. The resistor bank $R_{load,bank} = 3 \times 11\ \Omega$ is used as a three-phase load. The FCL is driven to saturation by the current source of I_{dc}=10 A.

A fault is initiated by short-circuiting one of the phase resistors using an electromechanical relay. The relay is operated by the fault-inception (triggering) circuit, presented in Figure 3-25. A triggering circuit can perform the following functions:

i. A fault inception at any moment during a cycle,

ii. An adjustable fault duration time,

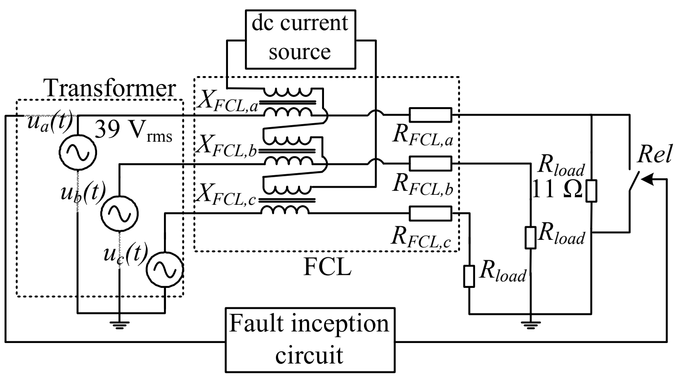

Figure 3-44: Three-phase experimental circuit.

iii. A triggering of two consecutive faults,

iv. An adjustable duration of a time interval between two consecutive faults.

Due to the synchronization of the control signal with the zero-crossing of the source voltage, the fault can be incepted at any desired moment. Since the first peak of the fault current is a function of the moment of fault inception, it is necessary to be able to trigger the fault at different moments, relative to the zero-crossing of the voltage, to fully test the operation of the FCL. The fault is incepted manually. The duration of the fault and the time interval between two faults can be adjusted to any desired number of cycles. The double-fault function is provided to confirm that the FCL is capable of restraining the intermittent faults without functional degradation.
The full experimental setup is presented in Figure 3-45.

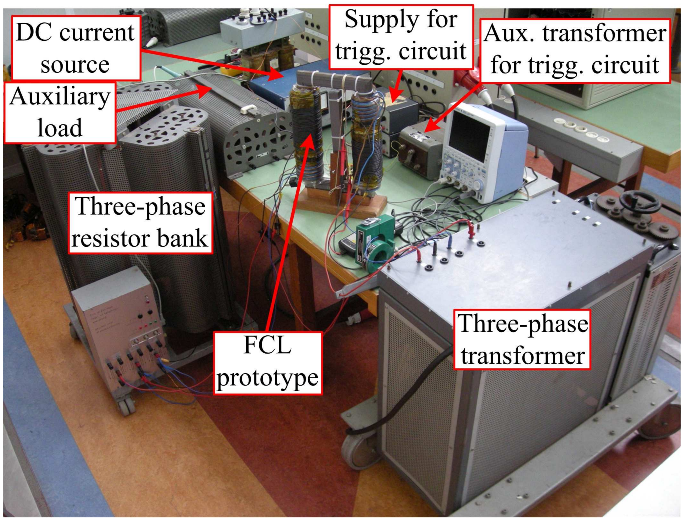

Figure 3-45: The full experimental setup with the designated components.

The following subsection gives a comparison between the FE simulation and the experimental results.

Comparison of the simulation and the experimental results

Figure 3-46 shows the measured phase-current waveforms for the fault incepted at 5 ms relatively to voltage zero-crossing of the faulted phase. The fault is cleared after six cycles by opening the relay. The current amplitude during normal operation is 5 A_{peak}. Due to the moment of the fault inception, the first fault peak is lower than the steady-state fault peak, being equal to 17.7 A and 22.2 A (see Figure 3-46), respectively. The maximum absolute peak of the fault current is equal to 25.2 A. As stated previously, the prospective fault current peak, due to the transformer stray impedance, is $I_{L,f}$=400 A_{rms}.

Thus, the FCL introduces a limiting factor of 23. After the fault is cleared, the system enters steady-state operation without a recovery delay, i.e. the FCL impedance drops to its normal value immediately.

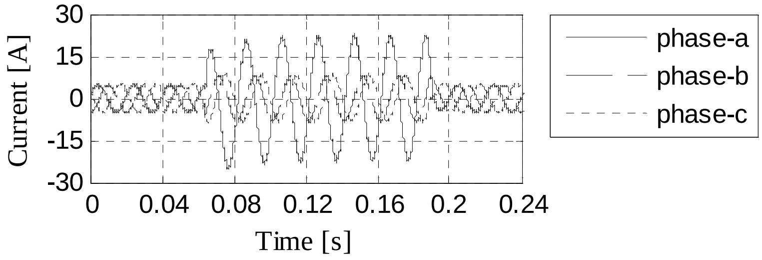

Figure 3-46: The measured current waveforms for a fault incepted in phase a at t_f =5 ms.

Figure 3-47a shows the line current waveforms for two different moments of fault inception. The first fault peak reaches $I_{L,lim}$=33 A_{peak} when the fault is started at t_f=0 ms relative to the voltage zero-crossing. In both cases, the FCL operates successfully and restrains the fault. After one or two cycles the fault current reaches steady-state behavior.

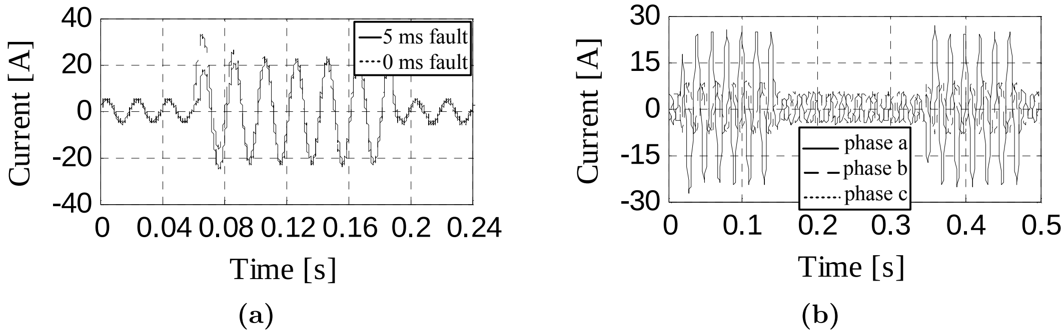

Figure 3-47: Measured currents: (a) The fault current for the two moments of fault inception: 5 ms and 0 ms; (b) Two consecutive faults, each incepted at t_f=5 ms.

The FCL can successfully restrain consecutive faults. In Figure 3-47b, the experimental current waveforms are presented for the case when two faults are initiated with a time interval of $T_{f,f}$=0.2 s. The duration of both faults is the same and equals to six cycles. There is no FCL functional deterioration; the fault currents are limited to $I_{L,lim}$=22.2 A.

The voltage drop across the FCL during normal and fault operation is presented in Figure 3-48. During normal operation, it is equal to 2.4% of the source voltage. The voltage drop is mainly due to the resistance of the windings of the lab FCL, which can be seen from its phase angle which is very close to zero degrees (see the left graph in Figure 3-48). In the case of the full-scale FCL design, the winding resistance is much lower, resulting in the significantly lower voltage drop.

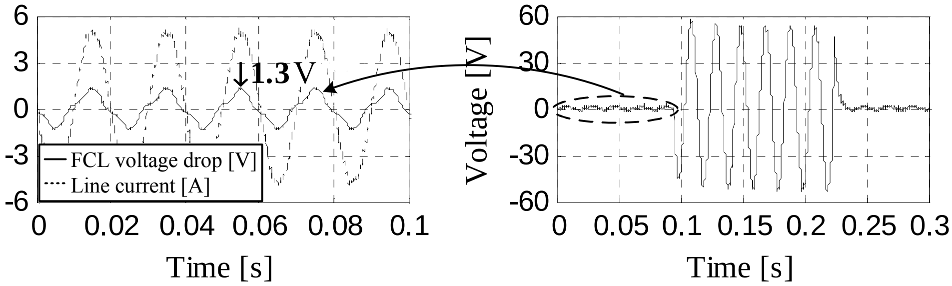

Figure 3-48: The voltage drop across FCL during normal and fault regimes.

The 3D FE model of the FCL gives very accurate results. The waveform of the line current matches the experimental waveform very well, see in Figure 3-49a.

The variation of the B field in the core's left and right outer legs through time is presented in Figure 3-49b. During normal operation the core is in saturation, whereas after fault inception the outer legs are alternately driven out of saturation. The 3D FE and experimental results match very well. If compared to the analytical results and those achieved in Saber (see Figure 3-36b), it can be seen that certain differences exist. Because of its high accuracy, the 3D FE model should be used to accurately predict the operation of the FCL.

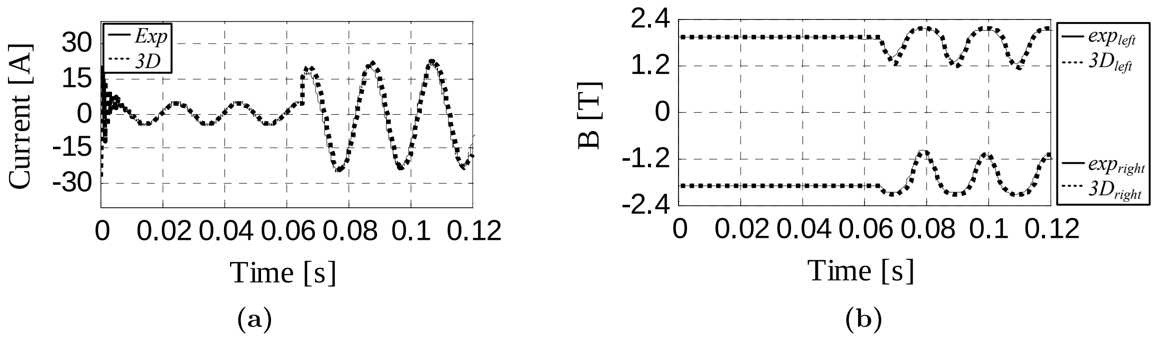

Figure 3-49: Comparison of experimental and 3D FE results: (a) Current waveforms for t_f=5 ms; (b) Variation of magnetic flux density B in the outer legs of the core.

The performed lab experiment confirmed the principle of operation of the proposed three-phase FCL topology with the trifilar arrangement of the phase windings. In addition, the developed 3D FE model of the FCL in Ansys is validated. The simulation results and the experimental results match very closely. It is shown that using FEM tools is necessary to get an accurate prediction of FCL operation during a fault.

3.6 Conclusions

The size of FCL magnetic cores for a given power level could be decreased with the insertion of a gap in the core. The reason why a gap is not utilized in the state-of-the-art FCL topologies is that it would considerably increase the number of required dc turns. The inserted gap would be part of the dc magnetic circuit and would increase its reluctance. To drive the core to saturation the number of dc turns would have to be, therefore, increased.

The existing saturated-core FCL topologies do not appropriately decouple dc and ac magnetic paths. The new proposed FCL topology decouples the dc and ac magnetic paths. This topology uses one magnetic core per phase with three legs. The middle leg of the core is used as a shunt path for the ac flux, i.e. it provides a magnetic path where only ac flux flows. Gap insertion into the middle leg, therefore, has no influence on the reluctance of the dc magnetic circuit. The benefits that the single-phase FCL topology brings can be summarized as follows:

i. The FCL core size (amount of magnetic material) can be decreased, in comparison to other FCL topologies, due to the gap insertion. The presented configuration provides the possibility of employing smaller cores for the same power rating in comparison to a typical FCL, an FCL with common dc winding and an open-core FCL. At the same time, the amount of dc winding material is not affected by the gap insertion and is, therefore, not a function of gap length.

ii. The induced voltage across the dc current source is lower than in a typical FCL topology due to the shorter mean-length of the dc magnetic path.

A new three-phase FCL topology with a common core and trifilar windings is proposed. A single magnetic core is used for all three phases. The amount of magnetic material is reduced nearly by a factor of 3. The impedance of the FCL during normal operation is considerably reduced by placing the phase windings in the trifilar arrangement. In this way, the phase fluxes cancel each other out and reduce the amount of stored magnetic co-energy in the system, which directly decreases the inductance of the phase windings. It is shown that the FCL phase impedance during normal operation is decreased by a factor of 8. The dc windings are used, but only to prevent core desaturation because of an asymmetrical current in the system. The number of dc turns and the associated induced over-voltage are considerably decreased in comparison to a single-phase FCL.

The latter FCL topology can limit only single-phase to ground faults. In the case of multi-phase faults, the fault current would flow through more than one phase winding making the fault 'invisible' to the FCL. A single-phase fault occurs in 95% of cases. This topology presents a compromise between the cost of the FCL and its functionality.

Table 3-9 summarizes the presented and analyzed FCL topologies. A figure of each topology, the main design features and the properties in comparison to the previous topology in the table are given.

Table 3-9: Summary of the analyzed FCL topologies.

FCL topology	**Design features**	**Properties**
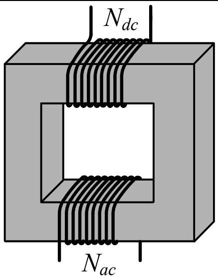 Typical topology without gap	◇ No air gap ◇ Two cores per phase	
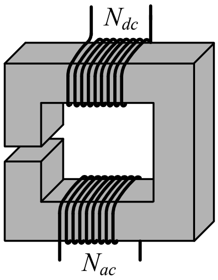 Typical topology with gap	◇ Air gap ◇ Two cores per phase	◇ Smaller core's cross-section ◇ Increased volume of winding material ◇ Increased induced voltage in dc windings
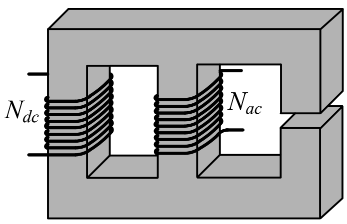 FCL with total magnetic decoupling	◇ Air gap ◇ Two cores per phase ◇ Total magnetic decoupling of ac and dc fluxes ◇ Non-deep saturation of core's ac leg	◇ Larger core's cross-section ◇ No induced voltage in dc windings ◇ Increased FCL normal impedance

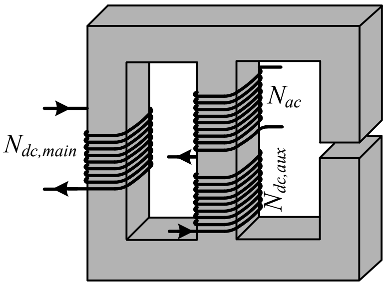 FCL with partial magnetic decoupling	◇ Air gap ◇ Two cores per phase ◇ Partial magnetic decoupling of ac and dc fluxes	◇ Smaller core's cross-section ◇ Induced voltage in dc windings ◇ Reduced FCL normal impedance
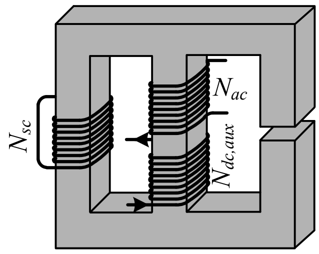 FCL with partial magnetic decoupling	◇ Air gap ◇ Two cores per phase ◇ Short-circuited main dc winding ◇ Partial magnetic decoupling of ac and dc fluxes	◇ Reduced volume of winding material
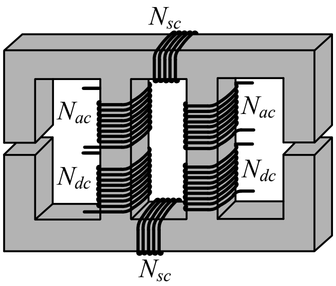 FCL with partial magnetic decoupling	◇ Air gap ◇ One core per phase ◇ Partial magnetic decoupling of ac and dc fluxes	◇ Reduced volume of magnetic material
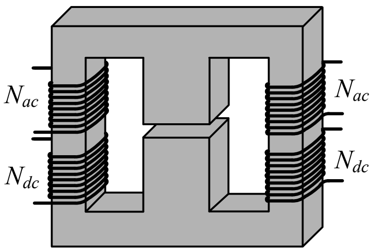 FCL with partial magnetic decoupling	◇ Air gap ◇ One core per phase ◇ Partial magnetic decoupling of ac and dc fluxes	◇ Reduced volume of magnetic material ◇ Reduced volume of winding material

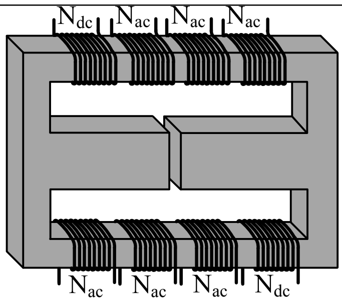 FCL with partial magnetic decoupling	◇ Air gap ◇ One core for three phases ◇ Partial magnetic decoupling of ac and dc fluxes	◇ Reduced volume of magnetic material ◇ Reduced volume of winding material ◇ Reduced induced voltage in dc windings ◇ Only faults involving one phase limited

Chapter 4

DESIGN AND TESTING OF A FULL-SCALE 10 KV FCL PROTOTYPE

4.1 Introduction

THE previous chapter introduced the new topology of inductive FCLs. It uses one magnetic core for all three phases with the phase windings placed in trifilar arrangement on the outer legs. The principle of operation is proved by means of simulations and lab-scale testing.

A full-scale prototype has been built to prove that the proposed FCL topology can protect a live grid from over-currents. This chapter presents the design and testing results of the full-scale 10 kV FCL prototype.

As the first step, the 10 kV FCL is designed using a three-step modeling method. This is presented in section 4.2. This section also presents the optimization of the core design with respect to the cross-section of the middle leg. Such optimization led to a reduction in the weight of an FCL.

Section 4.3 gives the final parameters of the FCL prototype. These final FCL design parameters are different from those presented in section 4.2. Namely, the core's dimensions are readjusted to make them equal to the one available in the manufacturer's catalogue. The changed FCL design is verified through FE simulations.

Section 4.4 shows the test results. The testing was done in two stages. In the first stage, all fault scenarios were tested at the low voltage of 400 V. The goal was to show that the FCL reacts to each of the fault types in the expected way. In addition, it was necessary to verify that the electrical connections in the FCL itself are properly assembled. The second testing phase is done at the full voltage of 10 kV, where the all fault scenarios are repeated.

4.2 Design of a 10 kV FCL prototype

4.2.1 Analytical design and simulations in Saber

An analytical model is used to obtain the first estimate of design parameters for the full-scale FCL prototype. A mathematical model is presented in Appendix C. The input and output parameters of the model are given in Table 4-1.

Table 4-1: The parameters of the power system and the FCL.

Input parameters		**Output parameters**	
Grid parameter	**Value**	**FCL parameter**	**Value**
Power voltage U_L, $[kV_{rms}]$	10	Core's cross-section $A_{core,outer}$, $[m^2]$	0.2
Normal current I_L, $[A_{rms}]$	200(400)	Core width w_{core}, $[m]$	2.3
System stray resistance R_L, $[\Omega]$	0.255	Core height h_{core}, $[m]$	2.38
System stray reactance X_L, $[\Omega]$	0.128	Core depth d_{core}, $[m]$	0.44
Load resistance R_{load}, $[\Omega]$	22.72(11.36)	Window width w_{wd}, $[m]$	0.26
Load reactance X_{load}, $[\Omega]$	17.04(8.52)	Window height h_{wd}, $[m]$	1.5
Power factor $\cos\varphi$	0.8	Gap length l_{gap}, $[m]$	0.2
FCL parameter	**Value**	Number of ac turns N_{ac}, $[turns]$	70
DC current I_{dc}, $[A]$	450	Number of dc turns N_{dc}, $[turns]$	20
B variation $k_{sat}B_{sat}$, $[T]$	1.8	FCL fault inductance $L_{FCL,lin}$, $[mH]$	11
Asymmetric current $I_{asymmetric}$, $[A_{rms}]$	$0.25I_L$		
Limited fault current $I_{L,lim}$, $[A_{rms}]$	$3-7I_L$		

The transient FCL model in Saber is used as the first verification step of the analytical design. The obtained phase currents are presented in Figure 4-1a. As can be seen, the peak of the steady-state fault current in phase a is equal to 2553.1 A_{peak}. The corresponding FCL fault inductance is equal to 10 mH. This result is very close to the analytically calculated value, see Table 4-1.

The variation of the magnetic flux density in the core is given in Figure 4-1b. During the fault period, the absolute maximal variation of the flux density, in the core's left and right legs, is equal to 1.73 T. It is close to the value of 1.8 T, used in the analytical calculations.

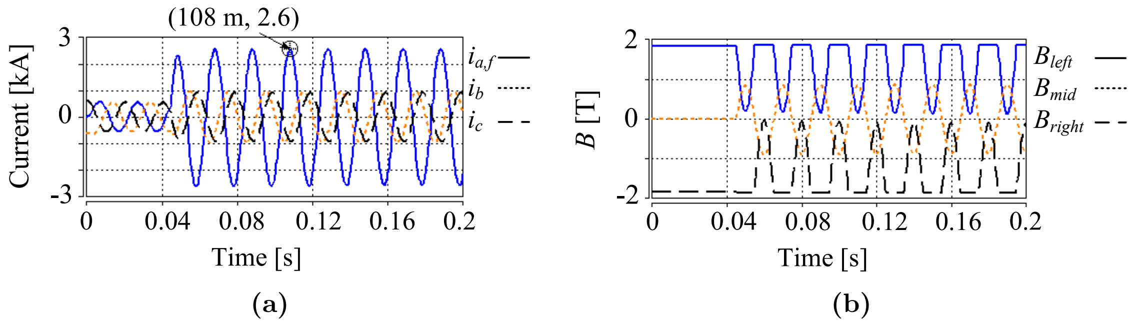

Figure 4-1: The results from the Saber FCL model: (a) The phase currents; (b) The variation of the magnetic flux density in the three legs.

The following subsection presents the finite element (FE) modeling results. As explained in Chapter 3, the FE FCL model is used as the last design verification step.

4.2.2 2D FE modeling results

The first part of this section presents the FE simulation results which validate the FCL modeled in Saber. The second part of the section concerns the further improvement of the FCL design with respect to the FCL's weight. It was not possible to perform this analysis in Saber due to the idealized characteristics of the FCL model, i.e. there is no option of modeling stray magnetic fields. In the last part, the final FE simulation results of the optimized FCL structure are presented. The dimensions of the final magnetic core are changed in comparison to those from Table 4-1 in order to meet the manufacturer requirements.

FE validation of the Saber FCL design

To validate the FCL simulation results from Saber, a 2D FE FCL model is built in Ansys. The design parameters are given in Table 4-1. An FCL structure with overlapped windings is used to improve the magnetic coupling between the phases. The waveform of the phase currents and variation of the magnetic flux density in the outer legs are given in Figure 4-2a and Figure 4-2b, respectively. The achieved results match those from the Saber model very closely.

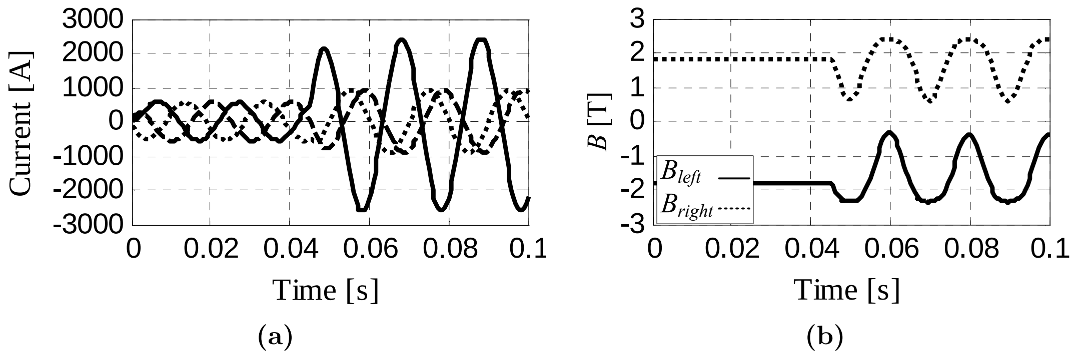

Figure 4-2: The 2D FE results: (a) Phase currents; (b) Magnetic flux density in the outer legs.

Reduction of the size of the middle leg - FCL design improvement

According to the results from the Saber model, the cross-section of the middle leg $A_{core,mid}$ must be two times larger than that of the outer leg. If the cross-section $A_{core,mid}$ would be decreased, the weight of the FCL would be diminished considerably. It is expected however that the FCL fault impedance would be decreased as well.

The possibility to further reduce the FCL weight is investigated in the following analysis where FE FCL model is used.

The FCL model in Ansys is created using the parameters from Table 4-1. The operation of the FCL during a fault period is simulated for several values of the cross-section $A_{core,mid}$, whose value is decreased incrementally from $2A_{core,outer}$ to $0.4A_{core,outer}$. Figure 4-3 shows the created 2D FE FCL geometry for the maximum and minimum values of the cross-section of the middle leg.

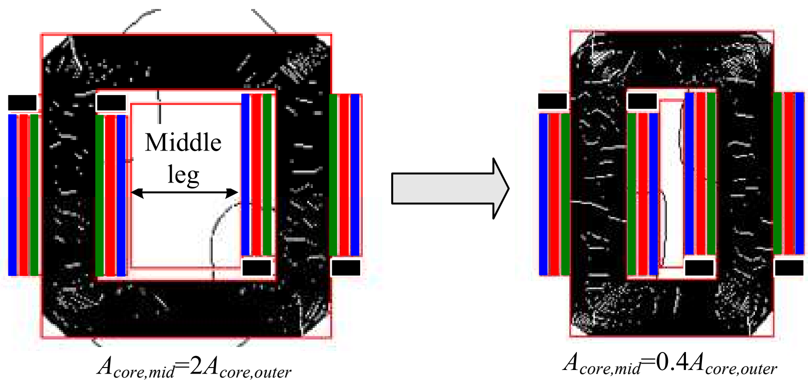

Figure 4-3: 2D FE FCL model with different values of the cross-section of the middle leg.

Figure 4-4a presents the variation of the steady-state peak of the fault current as a function of ratio of cross-sections of core's middle and outer legs. It can be seen that the fault current peak increases if the cross-section of middle leg is reduced. However, the limiting ability of the FCL is not significantly decreased. It limits the fault current to a large extent even when the cross-section of the middle leg is reduced to $0.4A_{core,outer}$.

Figure 4-4b shows the variation of the amount of magnetic material relative to the amount used when the cross-section of the middle leg is equal to $2A_{core,outer}$. As can be seen, the amount of core material is reduced by 30% of the total when the cross-section of the middle leg is decreased to $0.4A_{core,outer}$.

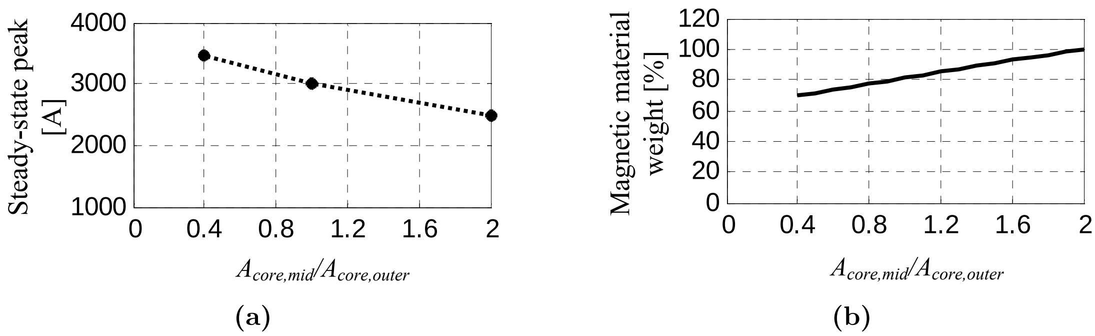

Figure 4-4: The design improvement results expressed as a function of the ratio between cross-sections of middle and cross-section of outer core leg: (a) Variation of the fault current peak; (b) Weight of magnetic material relative to that when $A_{core,mid}$=$2A_{core,outer}$. The results are obtained for the FCL design parameters given in Table 4-1.

It can be concluded that the FCL can limit the fault current successfully even when the cross-section of the middle leg is decreased. Which cross-section value is most efficient for the specific design of FCL remains to be decided during the design process.

The following section presents the final design of a full-scale FCL prototype. The cross-section of the middle leg is significantly reduced in this design.

4.3 The final FCL design

4.3.1 Core dimensions and windings arrangement

The magnetic core used in this FCL is manufactured by the Smith Transformatoren company in Germany. At the manufacturer's request, the dimensions of the FCL core are adapted to match one of the cores available in their catalogue. Figure 4-5a shows the final FCL design with the designated dimensions of the chosen magnetic core. The cross-section of the core's outer leg is equal to 0.149 m^2, i.e. 25.6% smaller than initially designed. It is made more or less circular (see Figure 4-5b) so that windings are more easily mounted. The cross-section of the middle leg is equal to 0.12 m^2, which is 82% of the cross-section of the outer leg. The size of the middle leg is, in this case, decided by the dimensions of the chosen core. The core is made of silicon-steel sheets (0.27 mm thick, grade M4) with a saturation flux density of 1.8 T. The dc magnetization curve of the core is presented in Figure 4-6.

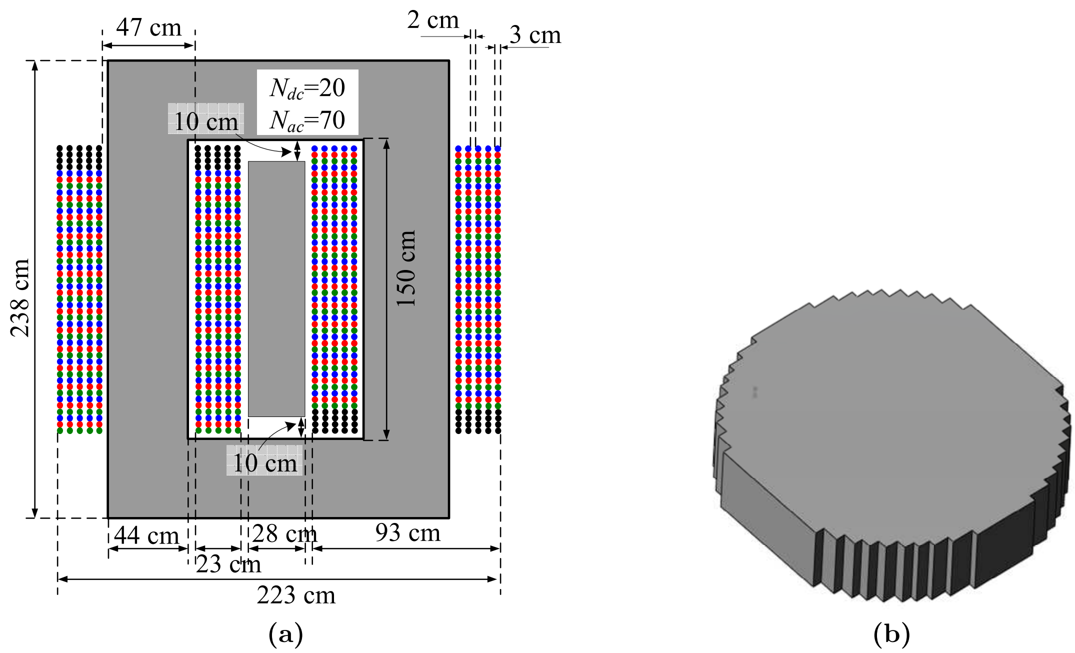

Figure 4-5: The final FCL design: (a) The dimensions; (b) The circular cross-section of the outer legs.

As already shown in Figure 4-5a, the ac windings are wound in trifilar manner. This winding technique is introduced in Chapter 3. The ac windings are placed in five vertical layers, each with 42 turns. A space of 2 cm is left between layers to enable adequate heat removal. The dc windings are arranged in five four-turn layers, with the same spacing of 2 cm between them.

To provide proper dielectric inter-turn insulation, the windings are made of MV cables, see Figure 4-7a. Without such insulation, the required inter-turn spacing would be much larger. The windings are made of aluminum of 400 mm^2 cross-section.

The middle leg is made wide enough to fill the space between the windings. Its width is 28 cm and its cross-section is rectangular. The gap is divided in two parts in order to reduce the fringing effect of the flux. The total gap length is 0.2 m. The 3D drawing of the final core geometry is presented in Figure 4-7b.

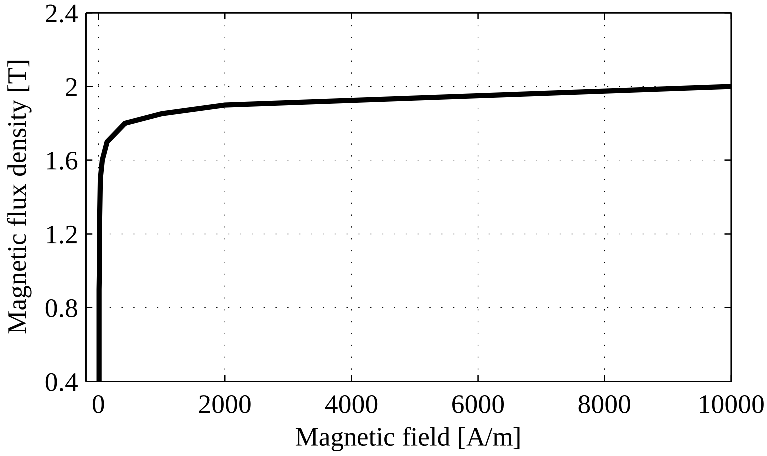

Figure 4-6: The dc magnetization curve of the silicon-steel core (grade M4) used for the full-scale FCL prototype.

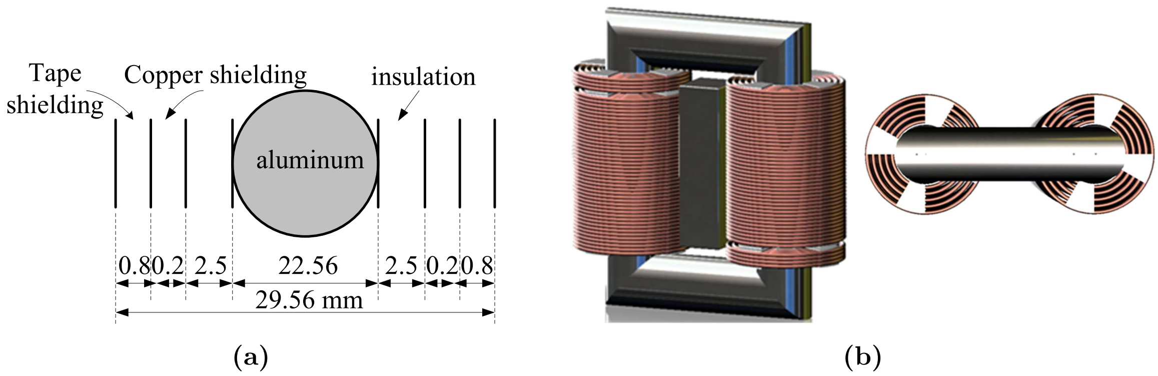

Figure 4-7: The FCL design: (a) the MV cable structure; (b) the final geometry.

4.3.2 2D FE modeling results

The 2D FE FCL model with the new dimensions of the core is simulated in Ansys. To evaluate the FCL's performance, the following simulations are done: single-phase to ground fault, two-phase to ground fault and FCL normal operation with Δ-connection of the load. The parameters of the electrical circuit are given in Table 4-1.

For the single-phase fault at t_f=45 ms, Figure 4-8a and Figure 4-8b show the current waveforms and flux density in a core during normal and fault regimes, respectively. The fault current is limited to an approximately 3.5 kA steady-state peak, whereas the prospective fault peak is 28.6 kA. The variation of the flux density in the core during the fault is nearly equal to 1.8 T.

The normal and fault inductances of the FCL are calculated using equation (4.1). The

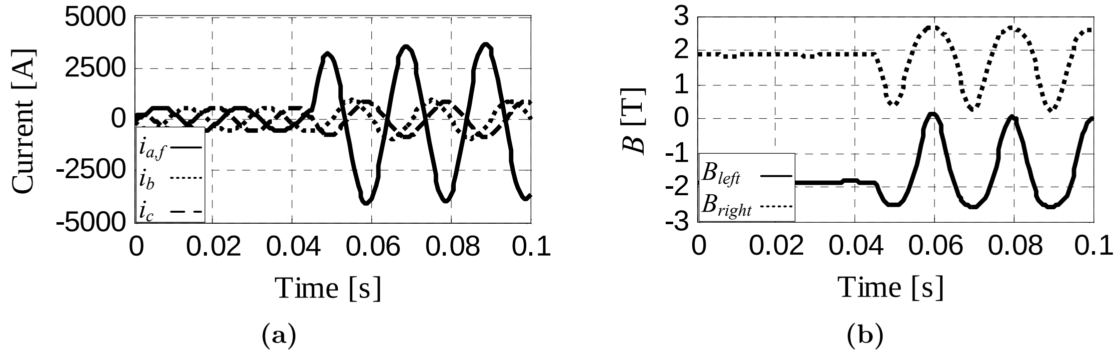

Figure 4-8: The 2D FE results for a single-phase to ground fault: (a) The phase currents; (b) The variation of magnetic flux density in the outer legs.

results are presented in Table 4-2.

$$(R_{load} + R_L) + j\,(X_L + X_{load} + X_{FCL\_i}) = \frac{U_i\angle\theta}{I_i\angle\psi_i} = Z_i\angle\varphi_i, \quad i = a, b, c \tag{4.1}$$

Table 4-2: The calculated normal and fault FCL impedances.

	Phase a	**Phase b**	**Phase c**
I_L	$393.94\angle-36.9°$	$398.53\angle-156.9°$	$398.63\angle-277.02°$
X_{FCL} normal	0.15 Ω	0.05 Ω	0.07 Ω
X_{FCL} fault	0.15 Ω		

The flux distribution in the core at moment t=58 ms is presented in Figure 4-9a. It demonstrates the principle of operation. As can be seen, the ac flux generated in the left outer leg is transferred through the middle leg and the gap. The right outer leg remains in saturation in the corresponding half-cycle. The plot of the B field, at the same moment, is given in Figure 4-9b.

As explained in Chapter 3, the FCL topology cannot limit two-phase to ground fault, see Figure 4-10. For the fault in phases a and b, the fault current reaches a peak of 23 kA$_{peak}$. It is nearly equal to the prospective fault current peak.

The results presented above are obtained for a star connection of the load. Figure 4-11a shows a three-phase electrical circuit with the FCL, where the load is connected in Δ-arrangement. The simulation shows that the FCL still operates successfully during a fault, see Figure 4-11b. The fault current is limited to 3 kA$_{peak}$.

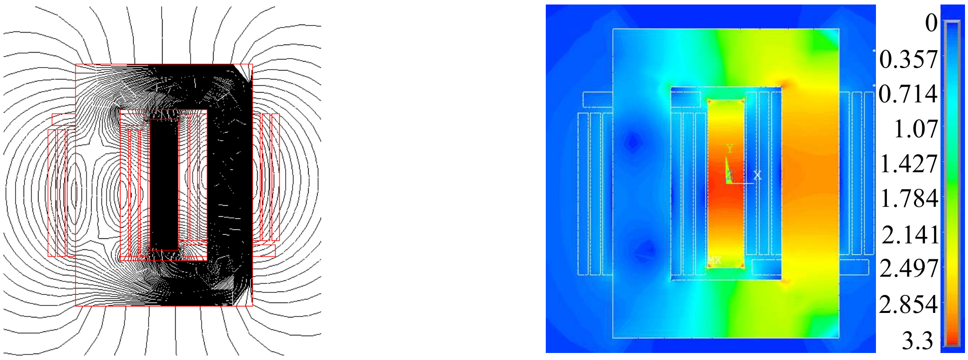

(a) (b)

Figure 4-9: The snapshot at t=58 ms of the 2D FE results presented in Figure 4-8: (a) The ac flux distribution; (b) The plot of magnetic flux density B .

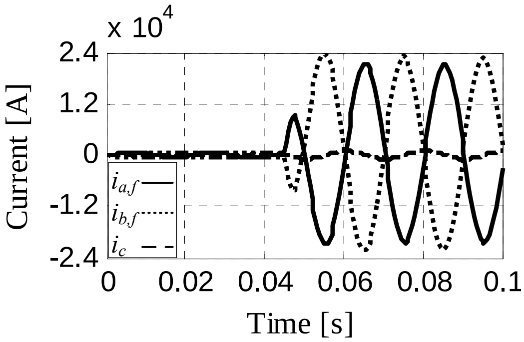

Figure 4-10: The 2D FE results for a two-phase to ground fault.

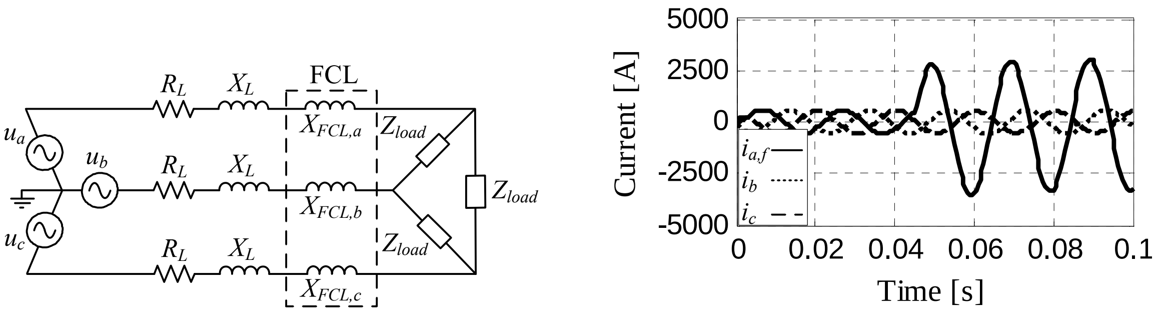

(a) (b)

Figure 4-11: The 2D FE FCL simulation with Δ-connected load: (a) The electrical circuit; (b) The current waveforms for a single-phase fault at 45 ms.

4.3.3 3D FE modeling results

As the final modeling step, the 3D FE model is simulated in Ansys. The geometry of the FCL model is presented in Figure 4-12a. As can be seen, the number of modeled ac turns per phase is equal to 6. The number of dc turns per winding is 3. Thus, the factors representing the ratio between real and modeled number of turns are n_{ac}=11.667 and n_{dc}=6.667. These factors have to be taken into account when modeling an electrical circuit. Further details and explanations can be found in Chapter 5. The meshed geometry is shown in Figure 4-12b.

The dimensions of the air, surrounding the FCL, are sufficiently large to account for the stray flux. The simulation is done for single-phase to ground fault in phase a, incepted at 65 ms. A star connection of the load is used. Figure 4-13a and Figure 4-13b show the simulated phase currents and flux variation in the outer legs of the core, respectively. The peak of the fault current is considerably lower than in the 2D simulation, suggesting that the 2D FE FCL model should not be used for the final design verification. The variation of flux density in the core is very close to 1.8 T, which validates the results from the previous modeling steps.

To check the influence of the FCL on the normal operation of the system, the zoomed peaks of the normal currents are presented in Figure 4-14. It can be seen that the peaks in different phases are unequal. However, the difference is in a range of 1%. Such operation of the FCL is considered satisfactory. The final FCL design parameters are summarized in Table 4-3.

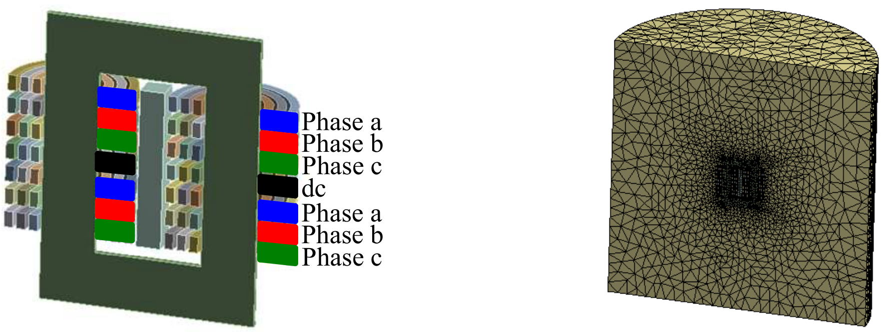

(a) (b)

Figure 4-12: The 3D FCL model: (a) A half of the geometry with the designated phase and dc windings; (b) The meshed geometry.

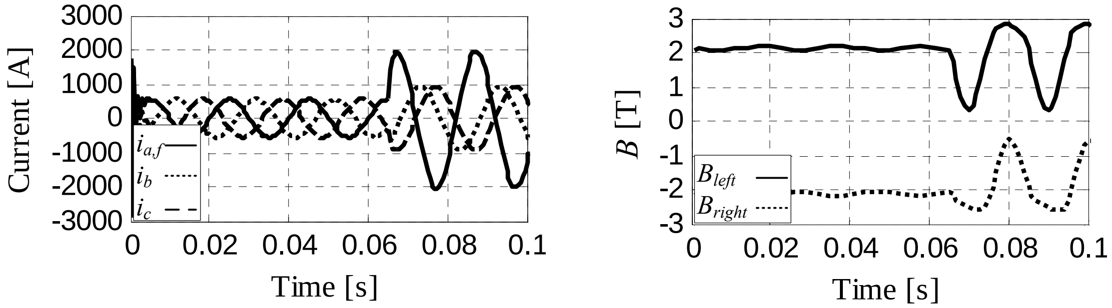

(a) **(b)**

Figure 4-13: The 3D FE results for a single-phase to ground fault: (a) The phase currents; (b) The variation of magnetic flux density in the core.

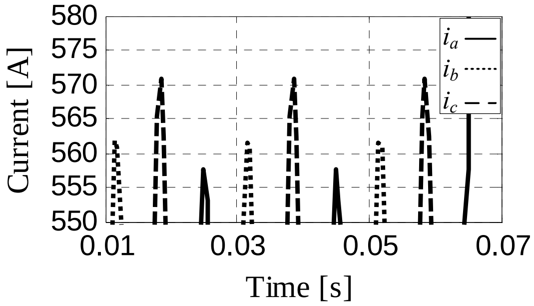

Figure 4-14: Zoomed peaks of the phase currents during normal operation of the system.

Table 4-3: The final FCL design parameters.

<table>
<tr><th>Parameter</th><th>Value</th><th colspan="2">Parameter</th><th>Value</th></tr>
<tr><td>Core's cross-section $A_{core,outer}$, $[m^2]$</td><td>0.15</td><td colspan="2">Gap length l_{gap}, $[m]$</td><td>0.2</td></tr>
<tr><td>Core's cross-section $A_{core,mid}$, $[m^2]$</td><td>0.11</td><td colspan="2">Number of ac turns N_{ac}, $[turns]$</td><td>70</td></tr>
<tr><td>Core width w_{core}, $[m]$</td><td>1.74</td><td colspan="2">Number of dc turns N_{dc}, $[turns]$</td><td>20</td></tr>
<tr><td>Core height h_{core}, $[m]$</td><td>2.38</td><td rowspan="3">FCL normal impedance, $[\Omega]$</td><td>Phase a</td><td>0.15</td></tr>
<tr><td>Core depth d_{core}, $[m]$</td><td>0.41</td><td>Phase b</td><td>0.05</td></tr>
<tr><td>Window width w_{wd}, $[m]$</td><td>0.29</td><td>Phase c</td><td>0.07</td></tr>
<tr><td>Window height h_{wd}, $[m]$</td><td>1.5</td><td colspan="2">FCL fault impedance $Z_{FCL,f}$, $[\Omega]$</td><td>4</td></tr>
</table>

4.4 Testing results of a 10 kV FCL prototype

4.4.1 The assembling of the FCL

Figure 4-15 shows the FCL being manufactured and assembled. In Figure 4-15a the trifilar phase windings are manufactured by winding three cables simultaneously. The prepared windings are placed on the core's outer legs, see Figure 4-15b. The dc windings are placed on the top of trifilar windings on both legs. They are made of black colored cables. As the last step, the core is closed and the middle leg is inserted between the windings.

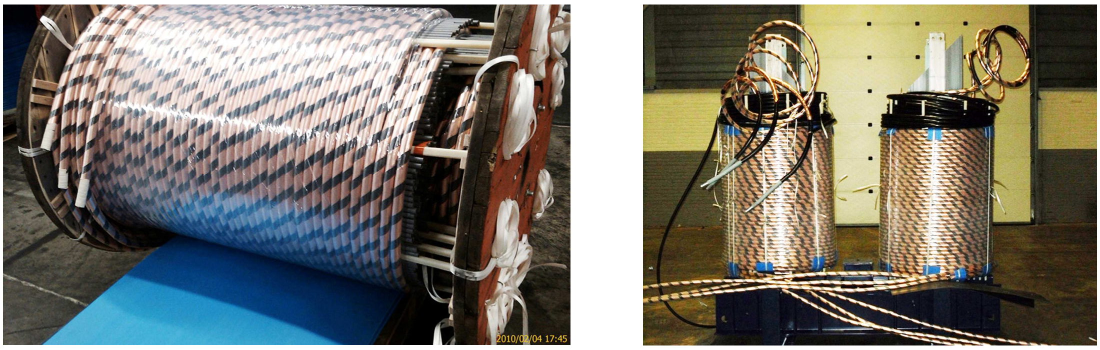

(a) **(b)**

Figure 4-15: Manufacturing the FCL prototype: (a) A trifilar winding; (b) The windings placed on the outer legs of the core.

The front and back view of the completed FCL are presented in Figure 4-16.

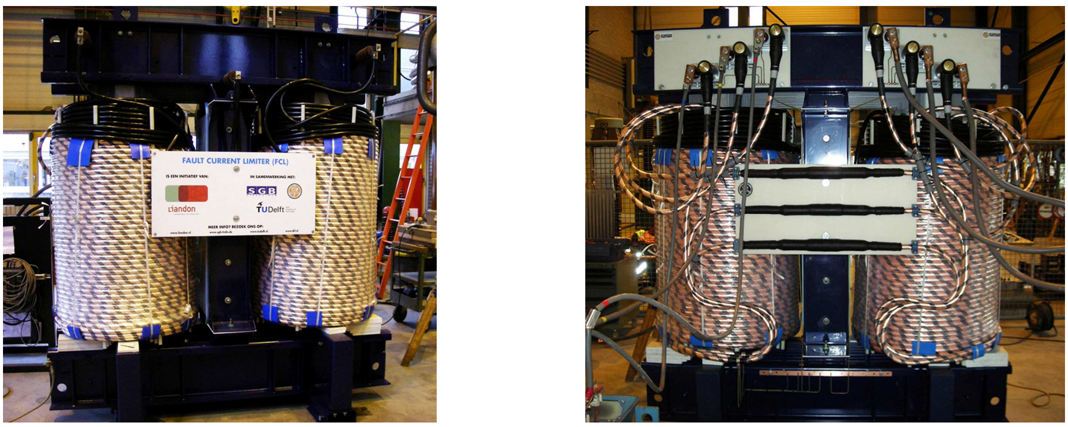

(a) **(b)**

Figure 4-16: The assembled FCL prototype: (a) Front view; (b) Back view.

4.4.2 FCL testing at voltage of 400 V

The FCL testing is divided into two stages. In the first stage, low voltage 400 V testing is performed. It is intended to verify that the FCL operates according to the design expectations, i.e. that it limits the fault current in both half-cycles. In addition, it was important to confirm that all the electrical connections of the windings are properly attached. Since the voltage was quite low, the problems such as dielectric insulation failure were not expected.

The electrical schematic of the test setup is presented in Figure 4-17a. The first transformer steps a given voltage down to 400 V, while the second transformer provides a desired voltage level in the range of 0 to 400 V. A motor is connected to provide additional short-circuit power during a fault. The FCL is tested for fault scenarios involving one, two and three phases. It was important not only to show that the FCL limits the single-phase to ground fault, but also that it does not operate for faults involving more than one phase. A fault is manually incepted by operating an electromechanical relay. Input and output voltages and currents from all three phases are measured. Figure 4-17b shows the dc electrical circuit. The dc voltage source is connected to an electrolytic capacitor which is protected from an inverse voltage by a parallel-connected diode. The other diode ensures that the current does not flow in the opposite direction. The dc voltage and dc current are measured. The setup is shown in Figure 4-17c.
The impedances of the first and second transformer are calculated respectively:

$$\begin{aligned} Z_{base} &= \frac{U_L^2}{S_L} = \frac{(0.23k)^2}{133.33k} = 0.396\,\Omega \\ Z_t &= 0.04 \cdot Z_{base} = 0.016\,\Omega, \end{aligned} \tag{4.2}$$

$$\begin{aligned} Z_{base} &= \frac{U_L^2}{S_L} = \frac{(0.23k)^2}{33.33k} = 1.587\,\Omega \\ Z_t &= 0.04 \cdot Z_{base} = 0.063\,\Omega. \end{aligned} \tag{4.3}$$

Therefore, the total impedance of the experimental circuit is 0.079 Ω. The maximum unlimited fault current is obtained for U_L=400 V and is equal to $I_{L,f}$=2.9 kA. This is the value of the fault current without a contribution from the motor. The motor can supply an additional 3 kA.

In the first testing a single-phase to ground fault is initiated. As shown in Figure 4-18a, the fault current in phase a is limited to 113.6 A_{peak}. Figure 4-18b shows that the limited fault current does not contain higher harmonics.

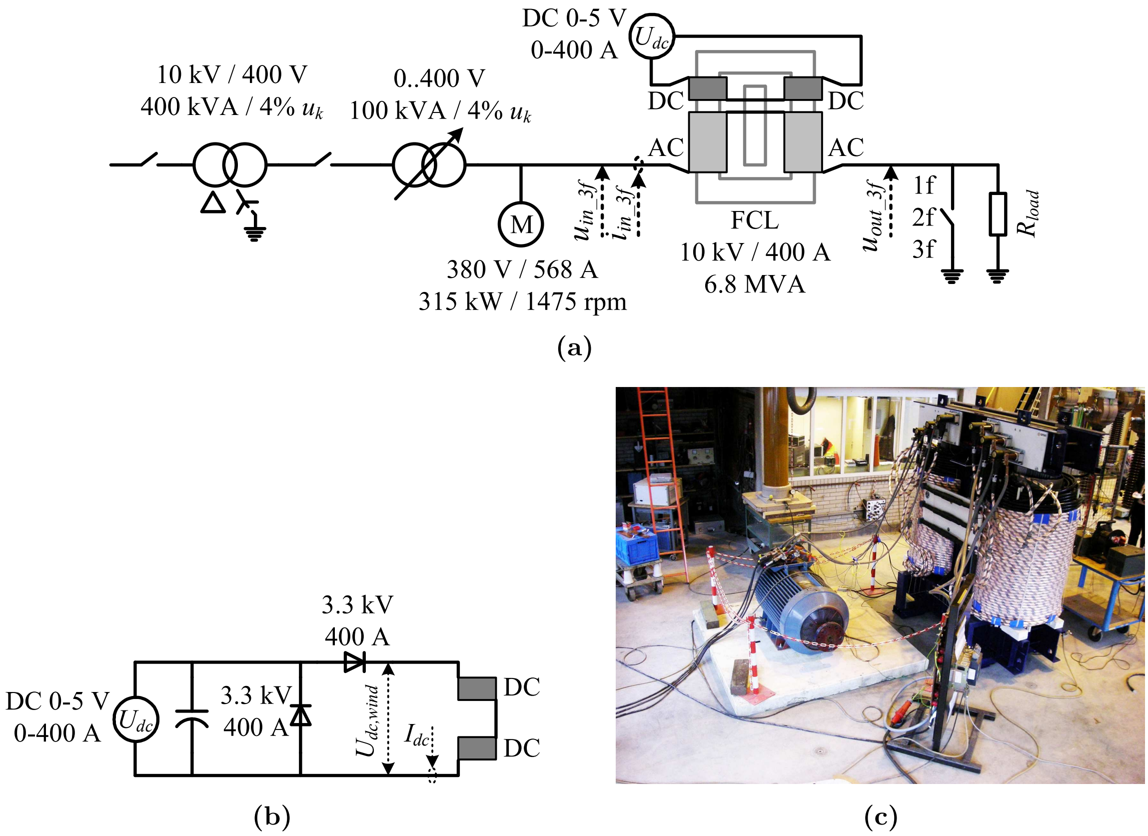

Figure 4-17: The 400 V setup: (a) The full electrical circuit; (b) The dc circuit; (c) The built setup.

It is explained in Chapter 3 that the total fault current in phase a is equal to the sum of the limited fault current of phase a and the currents in phase b and c with negative signs (3.18). This can be shown by analyzing the measured data. Namely, the measured total fault current in phase a is equal to $\hat{I}_{a,total} = 113.6\angle 15.85°$ and the negative sum of the currents in the other two phases $-\left(\hat{I}_b + \hat{I}_c\right) = 109\angle 0°$. As can be seen, the relationship between these currents is in agreement with the phasor diagram shown in Figure 3-32, i.e. $113.6 \cos(15.85°) = 106$ A. The value of the short-circuit current in phase a is $113.6 \cdot \sin(15.85°) = 31$ A. This current would be obtained in phase a if the other two phases would not be conducting during the fault period. To prove this, a fault test without a connected load is performed. Thus, the unfaulted phases b and c are not conducting at any moment. Figure 4-19 shows the measured fault current. It is equal to $\hat{I}_{a,f} = 39\angle 90°$, i.e. comparable to the previously calculated 31 A.

The voltage drop across the FCL is shown in Figure 4-20. During normal operation it is equal to approximately 23 V_{peak}, which amounts to 7% of the line voltage. It cannot be

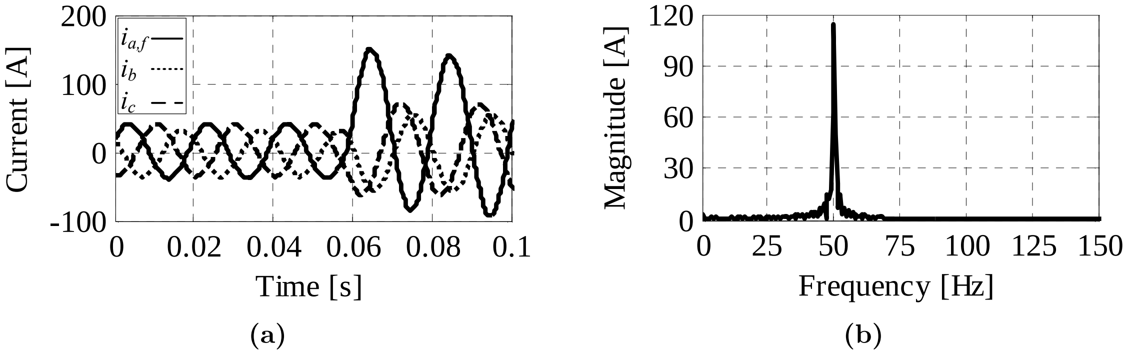

Figure 4-18: Single-phase fault measurements: (a) Phase currents; (b) The harmonic analysis of the limited fault current - there is no harmonic distortion.

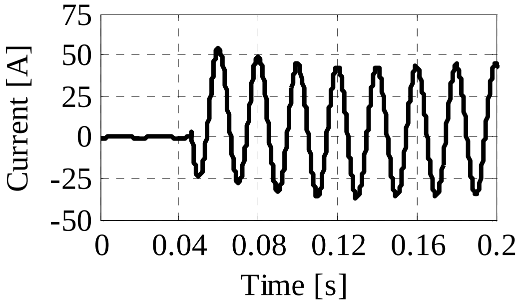

Figure 4-19: The measured fault current in phase a for the case that the other two phases are disconnected.

considered negligible. The voltage drop would be much smaller if the FCL was designed for a 400 V level; the stray impedance would be reduced due to the smaller cross-section of the core and smaller number of ac turns. The relative voltage drop is expected to be much lower than 7% during the full voltage test.

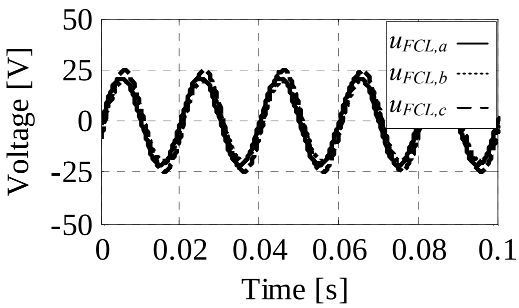

Figure 4-20: The voltage drop across the FCL during normal operation.

It is also important to notice that the voltage drop is approximately equal for all three phases. In other words, the FCL impedance during nominal regime is nearly equal for all three phases. This is one of the advantages of using a trifilar arrangement of phase windings.

The measured phase currents for two- and three-phase faults are given in Figure 4-21. As expected, the FCL does not limit a fault involving more than one phase.

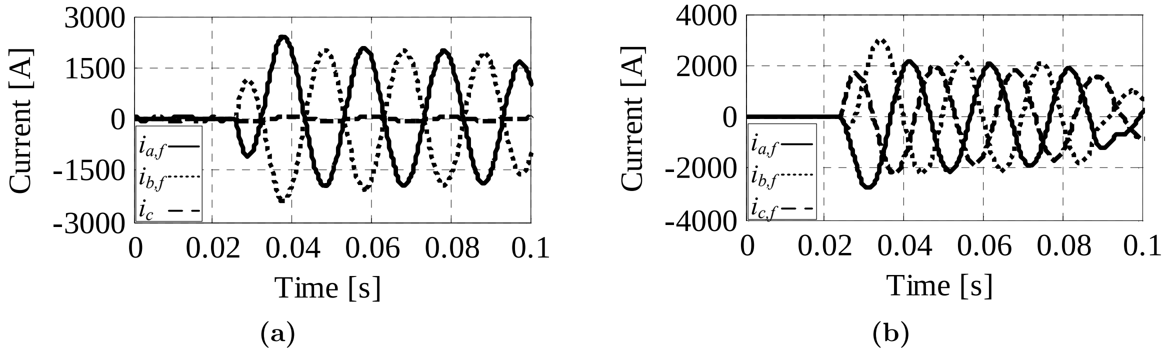

Figure 4-21: The phase current measurements for multi-phase to ground faults: (a) Two-phase to ground fault; (b) Three-phase to ground fault.

During a fault, the voltage that is induced across the dc windings influences the value of the current in the dc circuit. The variation of the dc current is shown in Figure 4-22.

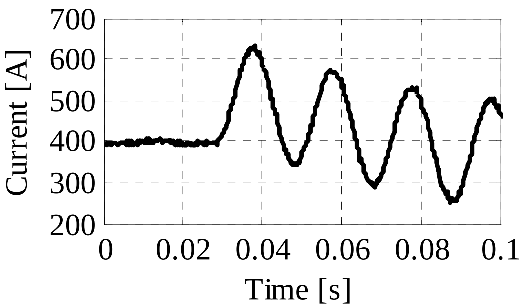

Figure 4-22: The measured current in the dc circuit.

The simulation results showed that the value of the induced current can be very high, in the range of 10 kA, for testing at the full voltage of 10 kV. It can influence the peak of the limited fault current, increasing it to a much higher level. To preserve the value of the limited fault current it is necessary to interrupt the induced current in the dc circuit. This can be done by employing an active semiconductor instead of a series diode. After fault inception, the semiconductor could be turned off, which would break the dc circuit. Furthermore, it would be necessary to turn off the dc current source, since it would be left in the open circuit. The mentioned design changes are made before full voltage testing is done.

4.4.3 FCL testing at the full voltage of 10 kV

The full-scale testing is performed at laboratory of KEMA. It was divided in four stages. Starting from the value of 10 kA, the prospective fault current was increased in each consecutive stage by 10 kA. The experimental setup is presented in Figure 4-23. Power is supplied from generator G via transformer to the FCL and load. A fault is initiated by closing relays.

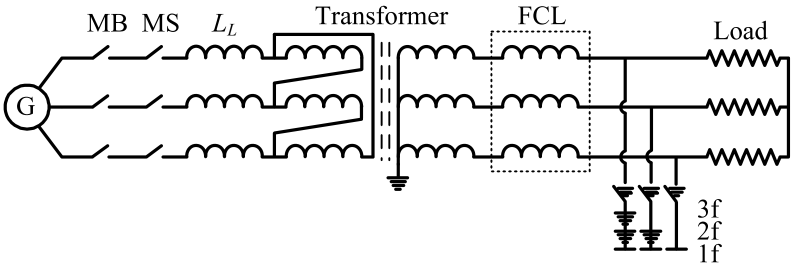

Figure 4-23: The experimental setup for full-scale testing of the FCL.

Before each testing stage, the value of an inductor L_L was adjusted to get the desired prospective fault current. Then the FCL is switched in the circuit and measurements are done. Figure 4-24a and Figure 4-24b show the experimental setup and the FCL at the testing site at KEMA laboratory, respectively.

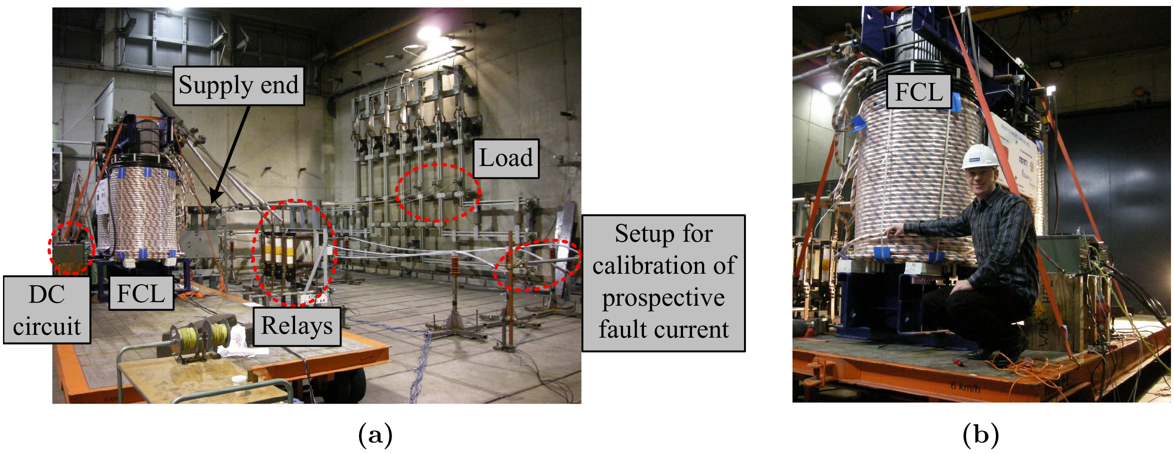

Figure 4-24: KEMA laboratory: (a) The FCL testing setup for 10 kV measurements; (b) The FCL prototype.

During each testing, the load current was set to be 50 A instead of 400 A. Accordingly, the dc current was reduced to 50 A. These differences in comparison to simulations and low-voltage testing do not influence the FCL operation on fault and the final results. The dc circuit was modified in the way it was explained in the previous section. Therefore, the dc current source was not exposed to an over-voltage and it was prevented that a large induced current appear in the dc circuit during a fault.

Testing results for 10 kA prospective fault current

In the first testing stage, the prospective fault current was set to be 10 kA. For a single-phase fault, the waveform of the measured fault current is presented in Figure 4-25(a). The normal currents in all three phases are presented in Figure 4-25(b).

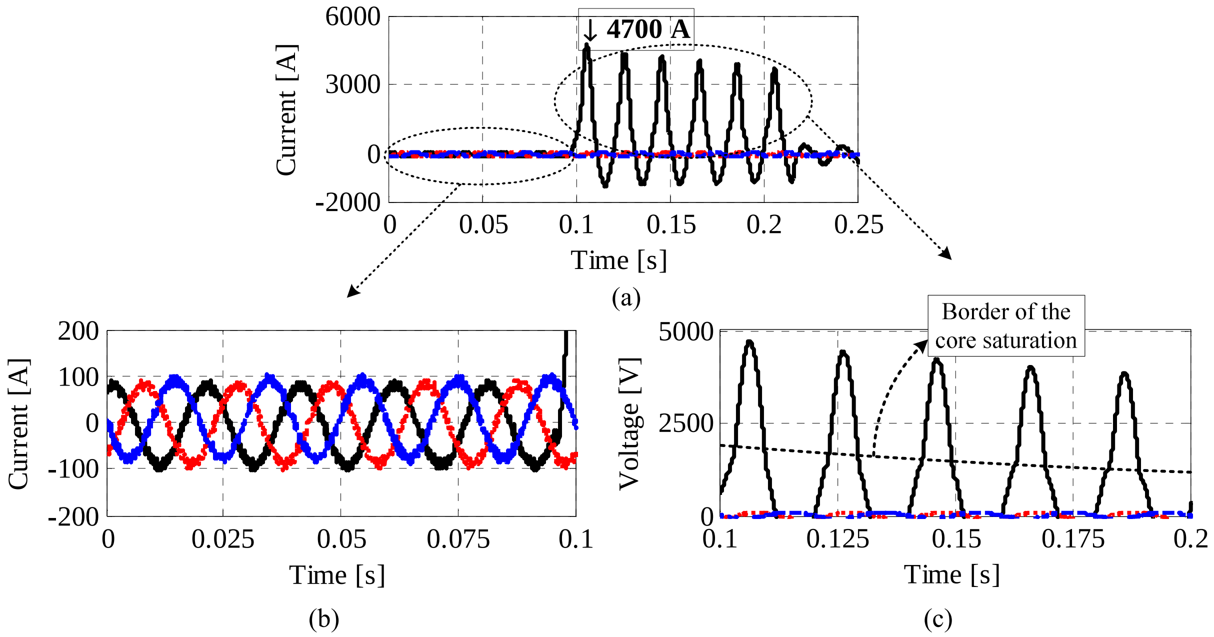

Figure 4-25: The measured current at 10 kV, 10 kA testing: (a) The phase currents; (b) The phase current during the normal operation; (c) The limited fault current.

The difference between their peak values is around $2-3\%$. It is larger than the difference obtained in FE simulations, where it was in the range of 1%. It can be seen that the first peak of the fault current is limited to 4.7 A, whereas the peak of the steady-state fault current is equal to 2.8 kA. In comparison to the results from 3D FE simulations (see section 4.3.3) the dc offset of the fault current has larger value. However, it is not clear here whether the offset indeed appears because of the inductive nature of the system impedance. It can be seen that both negative and positive current peaks decrease with time, which should not be the case. Normally, when closing the circuit with inductive impedance, peaks with one sign decrease while peaks with the opposite sign increase. Thus, it is likely that the existence of the dc component in the measured current is not caused by the inductive nature of the circuit impedance. On the other hand, it can be noticed that the current waveform is not completely sinusoidal. It seems as the core is driven to saturation at the certain moment and the current from that moment rises much faster. This behavior might be caused by the saturation of the gapped leg or some other

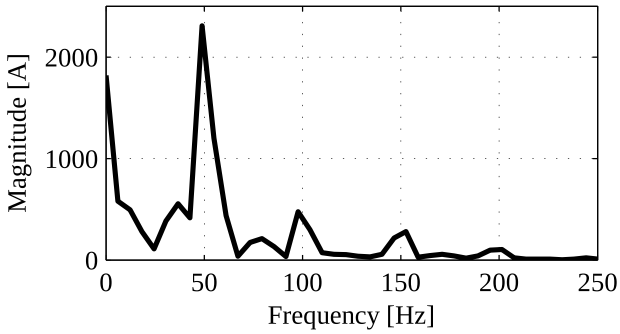

Figure 4-26: Spectrum of the limited fault current: the current contains higher harmonics which can be caused by partial saturation of the core.

part of the core. Unfortunately, this cannot be directly confirmed since the change of the flux density in the core was not measured. When the peaks of the fault current are more closely inspected (see Figure 4-25(c)), it can be stated that there is a level of the fault current after which the current increases much faster. Such behavior is normally caused by saturation of a core. The spectral analysis of the limited fault current (see Figure 4-26) shows that the current contains harmonics, which also can be caused by saturation of a core. The 3D FE results indeed showed that the middle leg of the core would be driven to saturation during a fault, but the influence of this effect on the peak of the limited fault current was not as large. It can be concluded that the core was driven partially to saturation which resulted in the increased peaks and larger dc component of the current. The final conclusion is that the FCL successfully limited single-phase fault.

The voltage drop across the FCL is shown in Figure 4-27. After the fault inception, it increases which results in limitation of the fault current. The voltage drop in the normal regime is around 1% of the full voltage, which is acceptably small.

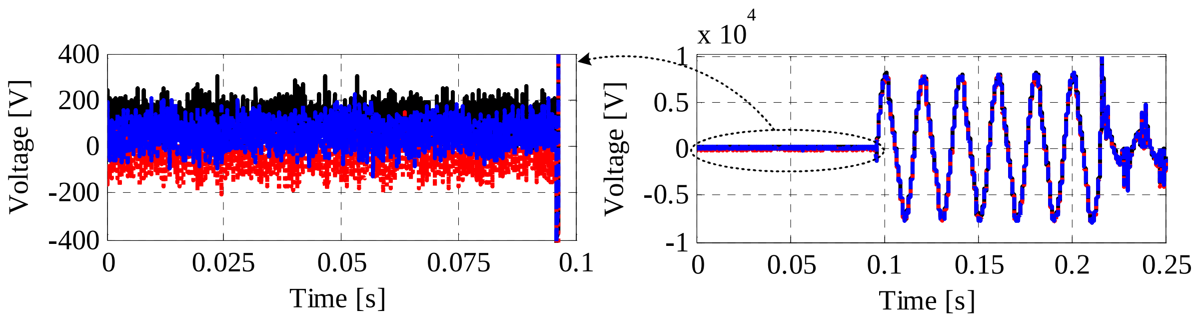

Figure 4-27: The voltage drop across the FCL during both the normal and fault regimes.

Figure 4-28 show the measured current for two- and three-phase fault scenarios, respectively. As was expected, the FCL did not react on these faults.

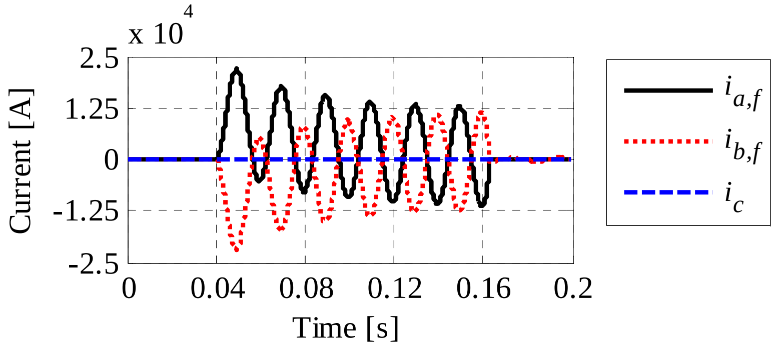

(a)

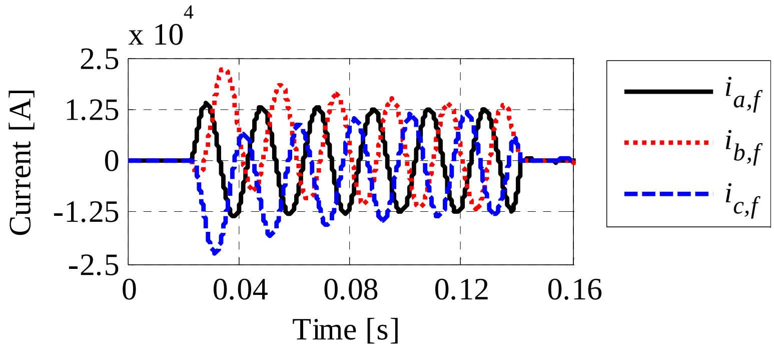

(b)

Figure 4-28: Measured phase currents for the case of: (a) A two-phase to ground fault; (b) A three-phase to ground fault.

Testing results for 20, 30 and 40 kA prospective fault current

In the first testing it was determined that the FCL will not limit faults involving multiple phases. Therefore, in the measurements with higher prospective fault currents, only single-phase faults were considered. Figure 4-29 presents the measured results for single-phase to ground fault for different prospective fault current levels. In each case the fault current is limited to approximately the same level. It was concluded that the FCL limited successfully single-phase to ground faults, as it was expected from the modeling results.

4.5 Conclusions

This chapter introduces the design and testing results of a full-scale 10 kV FCL prototype. It is proved that the FCL can be used for the protection of the live grid from the over-currents. The FCL can successfully limit a single-phase to ground fault. It does not react

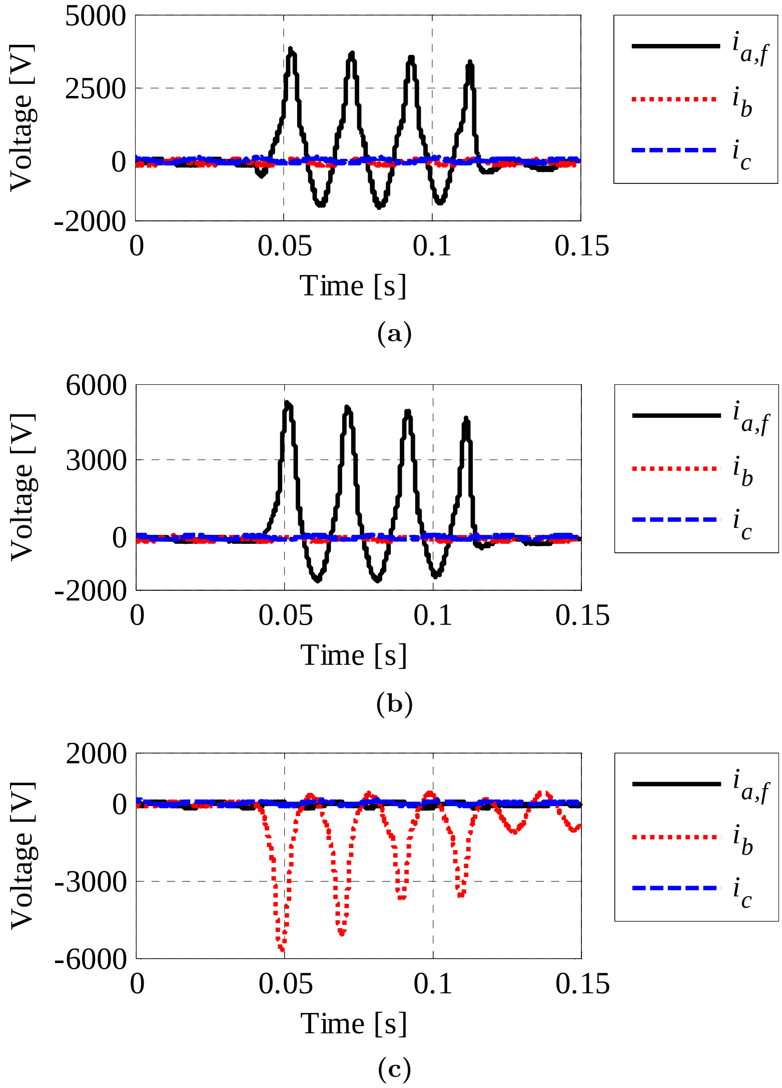

Figure 4-29: Measured phase currents for the case of a single-phase fault with the prospective fault current equal to: (a) 20 kA; (b) 30 kA; (c) 40 kA

to the faults involving more than one phase.

The analysis with the goal to decrease the required amount of magnetic material is performed using an FE FCL model. It is shown that the FCL can limit a fault current even when the cross-section of the middle leg is considerably decreased. In the presented design, the cross-section is reduced from $2A_{core,outer}$ to $0.4A_{core,outer}$, where $A_{core,outer}$ is the cross-section of the core's outer leg.

The testing is done in two stages, namely, a low voltage 400 V stage and a full voltage stage at 10 kV. The initial low voltage testing was performed in order to verify that all the electrical connections in the FCL are properly assembled. In addition, it is used to confirm that the FCL reacts to all fault scenarios as expected. The correspondence between the simulation and experimental results is very good. The performed full-voltage testing confirmed the 3D FE simulation results. The single-phase faults were successfully limited to the steady-state level of 2 kA, and the faults involving multiple faults were not restrained by the FCL. It was observed that the partial saturation of the core during a fault has larger influence on the fault current than it was obtained in simulations. The peak of the fault current was increased from 2.8 kA to 4.7 kA.

Chapter 5

FCL MODELING USING FEM TOOLS

5.1 Introduction

THE previous chapter introduced the design of the full-scale prototype of the three-phase three-leg 10 kV FCL. Finite Element simulation results, obtained from an FE FCL model built in Ansys, are used to validate the design of the FCL prototype. It was shown that these models should be used as the last modeling stage as they deliver very accurate results. FE FCL models account for all flux effects, such as leakage and fringing effects and allows the non-linear characteristics of ferromagnetic materials to be fully defined. A compromise between accuracy and required computational time can be made by changing the mesh size in an FE model.

Building a transient FE FCL model in Ansys is time consuming and difficult. The main difficulty are the many necessary steps involved, many of which are not included in available program tutorials. The limited applicability of certain elements in Ansys requires a number of additional 'tricky' steps if the model is to be developed. It would be very useful if appropriate guidelines, explaining all modeling difficulties and additional steps, would be available. FE modeling would become considerably easier and more time-effective. The objective of this chapter is to introduce developed guidelines for creating a transient FE model of saturated-core FCLs. The guideline outlines each required modeling step in detail. In addition, the modeling procedure is illustrated through the modeling of a small-scale FCL demonstrator.

Section 5.2 introduces guideline for building a transient FE model of a saturated-core FCL in Ansys. The guideline clarifies the main design steps and challenges for both 2D and 3D modeling.

Section 5.3 introduces guideline for the development of an FE FCL model in Comsol

Multiphysics. This software is not used in the previous chapters for the validation of the operation of the FCL prototype. The development of an FCL model in Comsol provides insight into the mathematical background of FE modeling and helps to deeper understand the way these models work. Having the FE models in both Ansys and Comsol, which are conceptually very different, enables a comparison of the modeling results and, therefore, the validation of the models.

5.2 FE transient nonlinear model of saturated-core FCL in Ansys

The development of a transient non-linear model of an inductive FCL in Ansys consists of the three main steps:

i. The structure of an inductive FCL is created, comprising magnetic cores and windings,
ii. Electrical circuits are created within the same design project. They comprise a single- or three-phase voltage source, load impedances and stray impedance of line and a dc current source. Many other electrical components (elements) are also available,
iii. The electrical circuits and the FE FCL model are coupled by means of common nodes. The coupling defines the common parameters of these two parts of the model, whose values are exchanged in each time step of a simulation.

The following two subsections introduce details of the modeling procedures for both 2D and 3D FE FCL models in Ansys.

5.2.1 2D FE transient non-linear model of saturated-core FCL

This section presents a method for the 2D FE modeling of an inductive FCL and points out the main modeling challenges:

i. The appropriate element types for all parts of the model have to be chosen,
ii. Coupling between the electrical circuit and the FE FCL model has to be done.

The FCL geometry is presented as planar geometry in $x-y$ plane and the depth of the model is set to its real value since the default assumption that it is infinitely long is not valid. Figure 5-1 shows a 2D model of the single-core FCL comprising an electrical circuit and a 2D FE model of the FCL. Such a model is, obviously, missing the FCL's front and back sides, which affects the accuracy of the results. Each winding is represented by two planes.

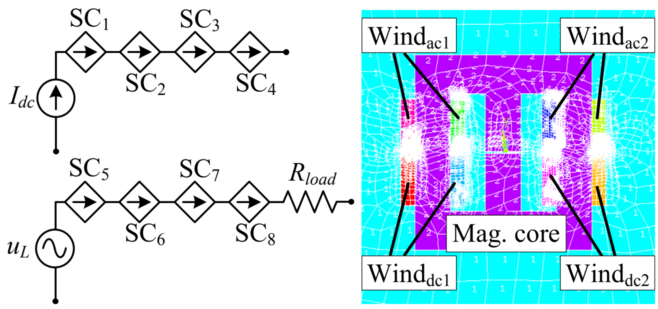

Figure 5-1: 2D model of an inductive FCL: the electrical circuits to the left and the FE FCL model to the right.

The electrical circuit is built using the element type CIRCU124. Option-set Keyopt(1) of element CIRCU124 can have a value from 0 to 12, defining which component is being modeled, e.g. a resistor, a current source, a stranded conductor (SC) etc. The element PLANE53 is applied to the areas of the windings, the magnetic core and air. Permeability and conductivity options of the element PLANE53 can be set for each of these materials, differentiating them. A non-linear BH curve of the core can be defined, for example, using a point-by-point method, i.e. by defining a certain number of (B,H) pairs.

The coupling between the electrical circuits and the FE FCL model is done by defining common nodes, belonging to both the electrical circuit and the FE model. Stranded conductor elements (SCi in Figure 5-1) of the electrical circuit are used to define the coupling. For each winding plane in the FE model, one SC component has to be used, and the K node of the SC has to have the same node number as one of the nodes from the winding plane. The SC component is obtained by setting the value of Keyopt(1) of the element PLANE53 to 5. In the given example, two ac windings are defined by using four planes in the FE model. For each of these planes, one SC element is used in the ac electrical circuit. The same applies to the two dc windings and the dc electrical circuit. The current density vector in the windings has only one component, in z-direction, which makes it simple to apply.

During a simulation, the following computations are done automatically at each time step: the electrical current flowing through the electrical circuit is transferred to the windings in the FE model and an induced voltage across the winding (i.e. the winding inductance) is transferred back to the electrical circuit. The value of the current in the next time-step is determined by the calculated induced voltage, and its value is applied back to the windings. Thus, the electrical current flowing through the windings is a function of the FCL impedance:

$$u_L(t) - i_L(t)\, Z_{load} = u_{FCL}(t) = i_L(t)\, Z_{FCL}(t)\,, \tag{5.1}$$

where $u_L(t)$ is the line voltage, $i_L(t)$ the line current, Z_{load} the load impedance, $u_{FCL}(t)$ the total induced voltage across the FCL ac windings and $Z_{FCL}(t)$ the FCL impedance.

Ansys calculates the FCL inductance L_{FCL} using the magnetic co-energy-based method; energy is one of the most accurately calculated quantities of FE analysis [Ansy]. Magnetic co-energy E_{mag} (see Figure 5-2) is obtained from (3.28).

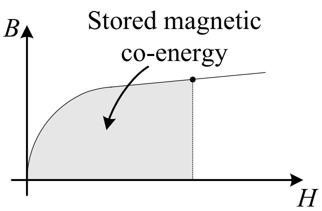

Figure 5-2: The stored magnetic co-energy within the volume of the FE model.

For 2D problems, the magnetic co-energy is integrated over the 2D model plane and multiplied by the predefined z-dimension of the model. The self and mutual inductances of a winding, $L_{self,i}$ and $L_{mutual,ij}$ respectively, are calculated from (3.27).

The fact that the computation of the FCL inductance L_{FCL} and its influence on the line current is a built-in function of Ansys simplifies the modeling considerably.

The accuracy of the results obtained from the 2D model is decreased due to the fact that the front and back sides of the model are missing. Such an incomplete model makes it impossible to completely account for the fringing flux effect. In a design without a gap, the accuracy of the results is very good and a 2D model can be used as the final modeling step. However, the error of the results is not negligible when the gap is used and increases with gap length. For the FE modeling of the proposed single- and three-phase topologies, which contain a gap, the use of the 3D model is recommended.

5.2.2 3D FE transient non-linear model of saturated-core FCL

In comparison to the 2D FE FCL modeling in Ansys, the following differences in development of a 3D FE model can be pointed out:

i. The 3D current density vector has to be defined separately for each element of the 3D windings. The vector is a function of the (x,y) coordinates of the elements.

ii. It is more difficult to create 3D than 2D geometry. Ansys Workbench should be used for this purpose as it has an improved graphical user-interface. Afterwards, the created geometry can be imported into Ansys Classic where a simulation is performed.

iii. An element type SOLID117 is available for the 3D modeling of structures that comprise magnetic materials, e.g. an iron core. This element requires that time-integrated voltage is applied to its nodes instead of the voltage itself. This fact requires changes be made to the model of the electrical circuit.

iv. A real constant set of the element SOLID117 does not offer the possibility of representing the complete winding with a single 3D body, i.e. each turn of the winding has to be modeled (drawn) separately. Having large number of turns makes it impossible to draw them all. Instead, a smaller number of turns is calculated and modeled and the electrical circuit is changed in a way to compensate for these differences.

The mentioned modeling challenges are clarified in the rest of the section.

i. When the windings are modeled in 2D, the current vector $\overrightarrow{J}$, applied to the windings, has a component only in z-direction:

$$\overrightarrow{J} = \overrightarrow{J}_z = |J|\,\overrightarrow{k}, \tag{5.2}$$

for the case that the winding is in the $x-y$ plane.

When the winding is modeled as a 3D object, the current density vector has two components. Under the assumption that the winding is drawn in $x-y$ plane and extruded in z-direction (see Figure 5-3), the current density vector comprises x and y components. In Figure 5-3 the n^{th} element of the winding, with the coordinates (x_n,y_n), is highlighted.

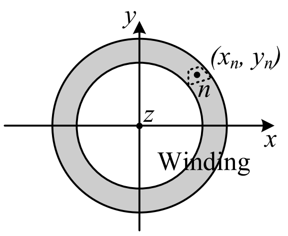

Figure 5-3: The 3D winding with the designated n^{th} element.

The vector $\overrightarrow{J}$ has to be defined for each element of the winding. For the circular geometry of the winding in $x-y$ plane, the current density vector can be written as:

$$\overrightarrow{J}_{3D_n}(x_n, y_n) = \frac{-y_n}{\sqrt{x_n^2+y_n^2}}\,|J_{3D}|\,\overrightarrow{i} + \frac{x_n}{\sqrt{x_n^2+y_n^2}}\,|J_{3D}|\,\overrightarrow{j}\,. \tag{5.3}$$

ii. As stated earlier, Ansys Workbench (WB) should be used to create a 3D geometry, which can then be imported into Ansys Classic. The other advantage of using Ansys WB is that the current density vector is automatically applied to all the elements of the meshed winding body. This is also valid for non-circular shaped windings. Therefore, using Ansys WB solves the first two issues listed regarding 3D modeling. The meshed 3D geometry of a single-core FCL topology is presented in Figure 5-4.

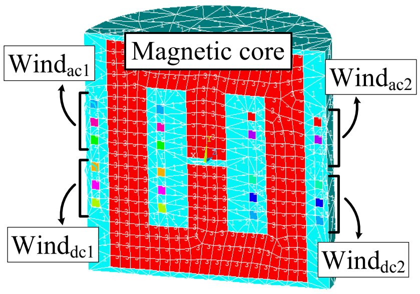

Figure 5-4: 3D geometry of an FCL, created in Ansys WB. One half of the model is visible due to the applied symmetry.

iii. As in 2D modeling, the appropriate element types have to be chosen. For 3D FE modeling of electromagnetic field problems, two elements are available: the nodal-based SOLID97 and the edge-based SOLID117. The nodal-based element SOLID97 has the advantage that its real-constant set allows the number of winding turns to be defined for the single 3D object representing the winding. However, this element cannot be used for models comprising materials with different relative permeability μ_r. The nodal-based solution means that a magnetic vector potential A is calculated for each node placed in the corners of the meshed elements. In the case that two neighboring elements have different permeability, the obtained solution for the normal component of the vector A is not continuous [Ansy]. Thus, the element SOLID97 cannot be used for FCL modeling as the permeability of air is not equal to that of a magnetic core. The problem of discontinuity of the normal component of the vector A does not appear if the edge-based element SOLID117 is used. In this case the magnetic vector is calculated in the nodes placed in the centers of the mesh elements edges.

When the element SOLID117 is applied, however, it must be taken into consideration that it requires the time-integrated voltage as an input variable. If such a voltage is set as a source in the electrical circuit, additional changes have to be applied to the circuit to maintain an unchanged waveform of the current. The resistive load has to be presented as a capacitor (5.4). Namely, if the voltage is applied across a resistor R_{load}, the resulting current is the same as when the integrated voltage is applied across a capacitor $1/R_{load}$.

$$u_L = R_{load} i_L \qquad \int u_L dt = \frac{1}{C_{load}} i_L,$$
$$C_{load} = \frac{1}{R_{load}}, \tag{5.4}$$

where R_{load} and C_{load} are the load resistance and the equivalent capacitance, respectively.

iv. Other important characteristic of the element SOLID117 is that it requires each turn of the windings to be drawn separately. In the case the winding has many turns, it becomes nearly impossible to draw them all. To make the modeling of windings with multiple turns feasible, the following method is proposed: if the real number of ac turns is N_{ac1}, only N_{ac2} number of turns is created and the electrical circuit is changed to take the factor n_{ac}=N_{ac1}/N_{ac2} into account, see Figure 5-5. The number of modeled dc turns is also decreased by a factor of n_{dc}. The required changes of the electrical circuit are:

a. The supply voltage is decreased $2 \cdot n_{ac}$ times,
b. The load is diminished $2 \cdot n_{ac}^2$ times,
c. The line current is increased n_{ac} times,
d. The dc current is enlarged n_{dc} times.

Although the numbers of turns are changed, it is important to keep the dimensions of the core unaltered. Figure 5-5 shows the 3D model of the FCL with the applied changes.

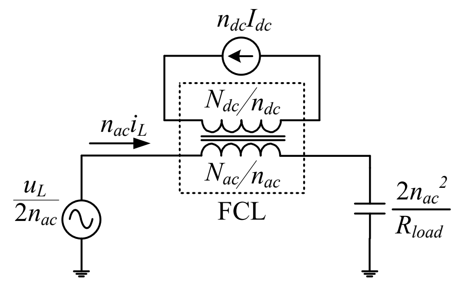

Figure 5-5: The 3D model of the FCL in Ansys, with the applied modifications of the electrical circuit.

Because the number of ac turns is reduced by a factor of n_{ac}, the inductance of the FCL is decreased n_{ac}^2 times (valid if the magnetic co-energy of the system remains the same (3.27)). In addition, the inductance is reduced by a factor of 2 as only one half of the geometry is modeled (FCL geometry is reflective-symmetrical). To preserve the amount of magnetic co-energy stored in the system, leaving the dimensions of the core unchanged, the magnetomotive force (mmf) $N_{ac}i_L$ must remain unchanged:

$$\begin{aligned} N_{ac1}i_{L1} &= N_{ac2}i_{L2} \\ i_{L2} &= n_{ac}i_{L1}, \end{aligned} \tag{5.5}$$

where i_{L1} and i_{L2} are the values of the line current before and after the required changes have been applied to the electrical circuit.

Thus, the line current i_{L1} must be increased by a factor of n_{ac}. This is done by altering both the load impedance and the supply voltage: to have all the impedances in the model scaled evenly, the load is reduced $2 \cdot n_{ac}^2$ times and the voltage is diminished by a factor of $2 \cdot n_{ac}$. As the last step, the mmf of the dc winding has to remain unchanged, which implies that the dc current must be increased by a factor of n_{dc}. All the changes are applied to the model shown in Figure 5-5. Because the resulting current i_{L2} is increased n_{ac} times, it must be divided by this factor to obtain the final result.

The developed FE FCL models in Ansys are validated by comparing the simulation results to the experimental measurements. Figure 5-6a and Figure 5-6b show the comparison between the 2D FE and the 3D FE simulation results and the experimental measurements from the lab-scale single-core FCL demonstrator. The details of the model and the experimental setup can be found in Chapter 3. Each simulation is run from t_{st}=0 s to t_{end}=0.08 s and a fault is incepted at t_f=0.035 s. The comparison is shown for two gap lengths 3.5 mm and 0 mm. The matching between the simulation and the experimental results is very good, which validates the proposed FE FCL models. The results of the 2D simulations show larger discrepancy in case that the gap has non-zero length. Since the 2D model is missing the front and the back sides, the effect of the flux fringing cannot be taken into account properly. As a result, the impedance of the FCL is lower, i.e. the fault current has higher peak, see Figure 5-6a. The fringing effect is much better computed in the 3D model.
The following section introduces the FE FCL models built in Comsol Multiphysics.

5.3 FE transient non-linear model of saturated-core FCL in Comsol

The modeling procedure of the inductive FCL in Comsol is very different from that in Ansys. Ansys has built-in mechanisms, i.e. equations, for calculation of an induced voltage across the winding when current is flowing through it. In other words, the inductance

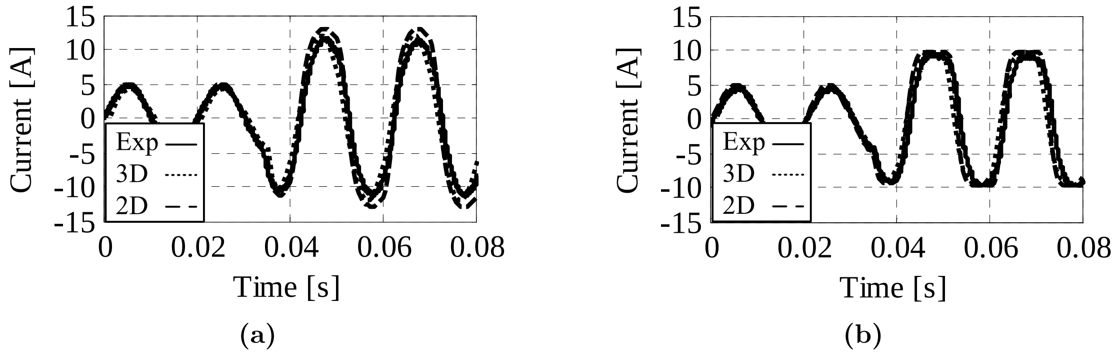

Figure 5-6: The experimental, 3D and 2D FE current waveforms: (a) l_{gap}=3.5 mm; (b) l_{gap}=0 mm.

of the winding is automatically computed and its influence on that current is taken into account.

Comsol is more 'mathematically' oriented software, as explained below. When performing electromagnetic simulations, the fundamental magnetic quantities, such as a magnetic vector potential A, are automatically computed for each node of the model. For example, if the electrical current is flowing through the given winding, the resulting magnetic field in the surrounding space will be calculated by default. However, the relationship between the inductance of the winding and the stored magnetic co-energy is not a built-in function. By default, the winding will not 'posses' any impedance and it will not, therefore, impose any limiting effect on the current flowing through it. Thus, when building the model of an inductive FCL, which comprises the windings, the appropriate conversion from the magnetic to the electrical domain must be added to the model. A mathematical model which will perform this conversion has to be developed and embedded in the FE model.

The following two subsections present the designed 2D and 3D FE FCL models in Comsol. Each is introduced through the developed field-circuit coupled mathematical models. To validate the models, a comparison of the FE results in Comsol and the experimental measurements is presented.

5.3.1 2D FE transient non-linear model of saturated-core FCL

A model of an inductive FCL in Comsol contains only the FE model of the FCL. There is no possibility of creating an electrical circuit, as it is in Ansys. The FE geometry of the FCL, including the core and windings, is equivalent to the one in Ansys, see Figure 5-1.

In Ansys, it is required to choose an appropriate element type for each created object, i.e. each plane in 2D modeling, and to define its characteristics through the available set of options. In Comsol there are no element types. Each object is created in the following way: the geometry is defined and the material is then determined by choosing the desired properties from a predefined set of options. For example, a magnetic core is defined by setting a magnetization curve. The complete mathematical model of the 2D FE model is explained below.

The current density vector $j_{wind}(t)$ is an input variable and is applied to the surfaces that represent the winding:

$$j_{wind}(t) = \pm N_{ac} \frac{i_{wind}(t)}{A_{wind}}, \tag{5.6}$$

where N_{ac} is the number of ac winding turns, $i_{wind}(t)$ the current flowing through the winding and A_{wind} the surface area representing the winding.

As in the Ansys model, each winding is represented by two planes. A positive sign is applied to one and a negative sign to the other plane to define a 'closed' current path.

The equation for the current $i_{wind}(t)$ in the ac coil(s) is an algebraic correlation that ensures that the sum of a resistive and an induced voltage $u_{FCL}(t)$ is equal to an externally applied voltage at all times:

$$(R_{wind} + R_{load})\, i_{wind}(t) + u_{FCL}(t) = u_{applied}(t), \tag{5.7}$$

where R_{wind} and R_{load} are the resistances of the ac windings and the load respectively and $u_{applied}(t)$ the external source voltage.

The relation between the applied current density and the generated magnetic field is given by a partial differential equation (5.8). This equation is already embedded in Comsol and the magnetic field is, therefore, computed automatically.

$$-\frac{\partial}{\partial x}\left(\nu \frac{\partial A_z}{\partial x}\right) - \frac{\partial}{\partial y}\left(\nu \frac{\partial A_z}{\partial y}\right) = J_z, \tag{5.8}$$

where A_z is the z-component of the magnetic vector potential and J_z the z-component of the current density.

The electrical conductivity of the core is set to zero in order to incorporate the lamination of the core. In reality, induced currents exist in the core. However, this effect is negligible for the overall performance of the FCL.

During the simulations, it is noticed that each of the winding planes causes an induced current in the other plane. In practical terms, this would mean that the winding was causing the induced effects in itself, which is not realistic. Because the conductivity of the winding is set to zero, to combat this effect, the equation (5.8) does not include a component representing the induced effects (a time-dependent component). The applied current density does not depend on the electrical conductivity of the windings. The resistance of the windings and the voltage drop, which is a result of the applied current, are, however, still taken into account in equation (5.7).

The missing link between the magnetic and electrical domains is the computation of the induced voltage across the ac windings $u_{FCL}(t)$, i.e. the winding's inductance. This is the only unknown variable in the equation (5.7). There are two ways to compute the induced voltage. First, it can be calculated as a product of the number of ac turns N_{ac} and the time variation of the magnetic flux through the cross-section of the core A_{core} in the $x - z$ plane:

$$u_{FCL}\left(t\right) = N_{ac}\frac{d}{dt}\int_{A_{core}} B_y\left(t\right)\, dA_{wind}, \tag{5.9}$$

where $B_y(t)$ is the magnetic flux density in y-direction.

The other way to obtain the value of the induced voltage is to calculate it separately for each of the two planes representing the single winding. The total induced voltage is found as the difference between these two values (5.10). The induced voltage in one of the planes is given with the expression (5.11).

$$u_{FCL}\left(t\right) = u_{FCL,1}\left(t\right) - u_{FCL,2}\left(t\right) \tag{5.10}$$

$$u_{FCL,i}\left(t\right) = \frac{N_{ac}l_z}{A_{wind,i}}\int_{A_{wind,i}} E_z\left(t\right)\, dA_{wind}, \tag{5.11}$$

where $u_{FCL,i}(t)$ is the induced voltage in the plane i of the given winding, l_z is the z-dimension of the winding and $E_z(t)$ the z-component of the electrical field.

The equations (5.7), (5.8) and (5.9) or the equations (5.7), (5.8) and (5.11) fully describe the magnetic part and the electrical part of the model. They are sufficient to model an inductive FCL in Comsol.

As can be seen, the developed FE model does not calculate the inductance of the windings but rather the voltage induced across them. The calculation of the inductance would either reduce the model's accuracy or cause convergence problems. One way to compute the inductance is to use approximate expressions, such as equation (3.4), which would introduce nearly the same error in the results as if the analytical model were used.

The other way to find the inductance is to apply the energy-based method:

$$L_{FCL} = \frac{2\, dE_{mag}}{dI_{wind}^2}, \tag{5.12}$$

where E_{mag} is the magnetic co-energy of the model and I_{wind} the current in the winding.

This equation is valid for a single-winding system. For a multi-winding system the mutual inductance would have to be accounted for.

Although this method is very accurate, a drawback is that the calculation of the inductance is not possible in the case that the current derivative dI_{wind} equals to zero.

The nonlinear BH curve of the magnetic core is defined using the analytical function:

$$\mu_r = \frac{1}{bha + \dfrac{(1-bha)\cdot B^{bhb}}{B^{bhb}+bhc}}, \tag{5.13}$$

where $bha = 2.12 \cdot 10^{-4}$,$bhb = 7.358$ and $bhc = 1.18 \cdot 10^6$.

The function defines actually the relation between the core's relative permeability μ_r and magnetic flux density B. The shape of the curve can be adjusted by changing the given constants. If desired, it is possible to insert the BH curve using point-by-point method.

The dc current source is modeled by setting the conductivity of the dc winding to zero. In this way, the induced current is contained at zero and the total current through the dc winding is constant and equal to the externally applied one.

A fault is modeled by allowing the value of the load resistance R_{load} to drop to a very low value at a particular time instance. To ensure the convergence of the solution, the change of the resistance is smoothed using Heaviside function:

$$R_{load} = R_{load}\left(1 - flc2hs\left(t - t_f, T_{smooth}\right)\right), \tag{5.14}$$

where $flc2hs$ is a smoothed Heaviside function with a continuous second derivative without overshoot [Mult 08], t_f the moment of fault inception and T_{smooth} the time-interval after which the load resistance reaches the final value. The change of the load is presented in Figure 5-7.

The FE FCL model is realized by using the perpendicular current quasi-static application mode of Comsol. The circuit relation (5.7) is implemented using the ordinary differential equation setting.

A 3D FE model of inductive FCLs in Comsol is presented in the following subsection.

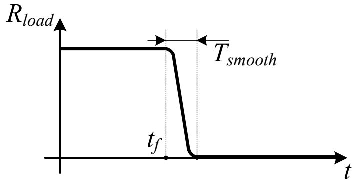

Figure 5-7: Change of the load resistance - represented by a smoothed Heaviside function.

5.3.2 3D FE transient non-linear model of a saturated-core FCL

This section presents a 3D FE model of saturated-core FCLs in Comsol Multiphysics. The field-circuit coupled model consists of a partial differential equation for the magnetic field in the FCL, coupled with an ordinary differential equation for the current in the ac coil. Both are coupled by the magnetically induced voltage in the ac coil.

The ordinary differential equation for the current in the ac coil is given in (5.7). The current density in the ac and the dc windings is an input variable for the model. The difference in comparison to the 2D model is that the current vector has two components, one in the x- and one in the y-direction. The so-called coil winding function $f_{wind}(x, y)$ is introduced [De G 04]-[Dula 04] in such a way that the applied current density in the windings can be written as:

$$j_{wind}\left(t, x, y\right) = \frac{N_{wind} i_{wind}\left(t\right)}{A_{wind}} f_{wind}\left(x, y\right), \tag{5.15}$$

where $j_{wind}(t, x, y)$ is the current density in the winding and N_{wind} the number of winding turns.

For the circular geometry of the winding in the $x - y$ plane and extruded in the z-direction, the current density vector is defined by (5.3). When the winding geometry is rectangular (see Figure 5-8), the current density can be defined by (5.16). The equation (5.16) defines the current density vector in a counterclockwise direction. To set the current flow in a clockwise direction the sign of both x and y vector components in the equation (5.16) have to be changed.

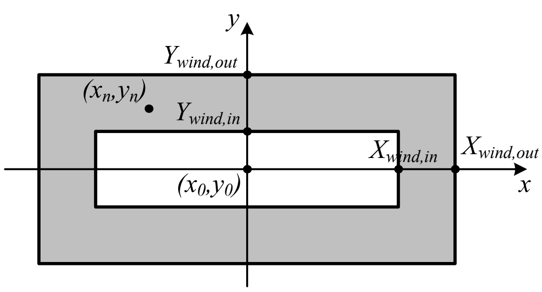

Figure 5-8: Rectangular winding geometry.

$$f_{wind,x}\left(x_n, y_n\right) = \begin{cases} -\mathrm{sgn}(y)\ if\ \left|y_n - y_0\right| > \frac{Y_{wind,in}}{X_{wind,in}}\left|x_n - x_0\right| \\ 0\ \ Otherwise \end{cases}$$
$$f_{wind,y}\left(x_n, y_n\right) = \begin{cases} \mathrm{sgn}(x)\ if\ \left|y_n - y_0\right| \le \frac{Y_{wind,in}}{X_{wind,in}}\left|x_n - x_0\right| \\ 0\ \ Otherwise \end{cases} \tag{5.16}$$

Contrary to Ansys Classic, Comsol can represent a whole winding with a single 3D body. It is not necessary to draw each turn separately, which simplifies the modeling considerably.

The electrical conductivity of the complete geometry is set to zero, in this way negating all induced effects. Accounting for this, the partial differential magnetic field equation can be written as:

$$\nabla \times \mu_0^{-1}\mu_r^{-1}\left(\nabla \times A\right) = J_{wind}, \tag{5.17}$$

where A is the magnetic vector potential.

To close the system of equations representing the model, the induced voltage U_{FCL} in the ac winding has to be calculated in one of the ways described before and inserted in the equation (5.7). The induced voltage presents the missing link between the magnetic and electrical domains. It is calculated by a homogenization procedure over the turns in the winding, i.e. by integrating the electrical field E in the direction of the winding over the volume of the winding Ω_{ac}:

$$u_{FCL}\left(t\right) = \frac{N_{ac}}{A_{wind}} \int_{\Omega_{ac}} E\left(t\right) \cdot w\ d\Omega. \tag{5.18}$$

In the case of a single-core FCL configuration, the induced voltage consists of two contributions corresponding to the separate ac coils. They have to be summed before being inserted into (5.7).

A fault inception is simulated by allowing the load resistance R_{load} to drop to a low value at a particular time instance, as described by equation (5.14).

A non-linear BH curve can be specified using a point-by-point method or using expression 5.13. As in the 2D model, the electrical conductivity σ is set to zero in both the coils and the core to negate the induced currents.

Convergence of the simulation process at the initial time step is obtained by providing a good initial estimate. Such an estimate is obtained by solving a separate application model in which only the dc windings are excited.

As the first verification step, the simple FE model comprising a single winding is created. The equivalent experimental winding is built. The dimensions of the winding are: $X_{wind,in}$=3.75 cm, $Y_{wind,in}$=2.5 cm, $X_{wind,out}$=4.75 cm, $Y_{wind,out}$=3.5 cm (see Figure 5-8) and the z-dimension is 3 cm. The number of turns is 200. The measured inductance is equal to 3.43 mH, whereas the computed inductance is 3.6 mH. A computational error of 5% is considered sufficiently low. The proposed method for the inductance computation is validated.

As the next step, a full FE model of the single-core FCL topology is built, based on the presented field-circuit coupled mathematical model. The meshed geometry of the model is presented in Figure 5-9. The input parameters to the model are given in Table 3-3 and Table 3-4.

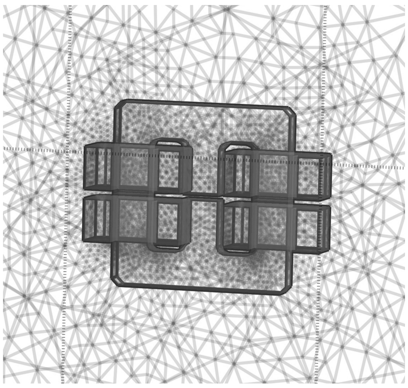

Figure 5-9: Meshed 3D geometry of single-core FCL in Comsol.

The obtained results are compared to the experimental measurements. Figure 5-10a and Figure 5-10b show the simulation results of the current for the gap lengths l_{gap} equal to 0 mm and 3.5 mm, respectively. The agreement with the experimental measurements is very good. The presented results validate the developed 3D FCL model in Comsol.

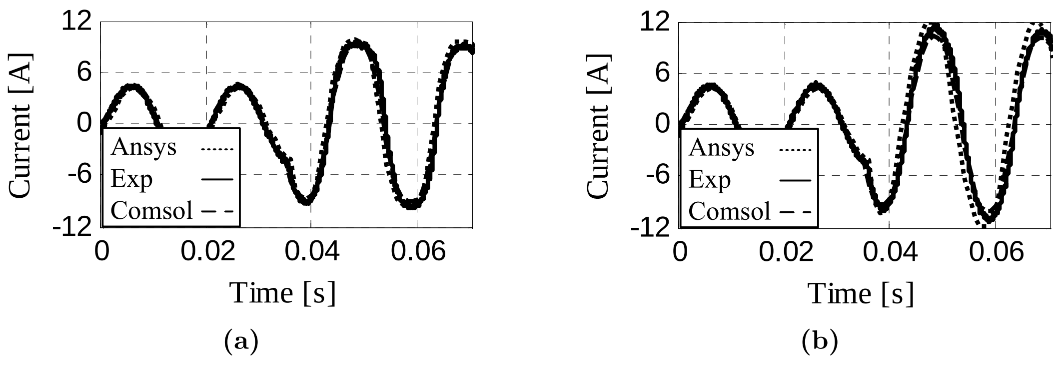

Figure 5-10: The comparison of the simulation and the experimental results: (a) l_{gap}=0 mm; (b) l_{gap}=3.5 mm.

5.4 Conclusions

This chapter introduced guidelines for the FE modeling of saturated-core FCLs in Ansys and Comsol Multiphysics. Both 2D and 3D models are developed and validated. The given guidelines explain the main modeling steps and challenges.

The advantages of creating the FE FCL model in Ansys Classic are the built-in computation of winding inductance and the possibility of modeling an electrical circuit. When electrical current flows through the winding, the inductance of the winding is automatically calculated and its influence on the current is taken into account.

The disadvantage of the 3D modeling in Ansys is that the element SOLID117, which is used for the modeling of the windings, does not allow one solid body to represent multiple turns. Each turn must be drawn separately. In the case of the winding having many turns, it is nearly impossible to draw them all. The given guideline introduces a modeling procedure which solves this problem. Namely, the number of the modeled winding turns can be lower than the real one and the electrical circuit can be modified to take this difference into account and give correct final results. Additionally, attention must be paid to the element SOLID117 requiring the integrated value of input voltage to be applied to its nodes. To have a properly working model, the electrical circuit must be modified. As explained in the introduced guidelines, the resistive load has to be replaced by the capacitive one. The developed FCL model is verified through the comparison of the obtained results with the experimental measurements.

Comsol Multiphysics is more 'mathematically oriented' software. Namely, to create the FCL model, it requires both the equation for the calculation of the FCL impedance and the equation for the electrical circuit be defined separately. In Ansys, these equations are a part of built-in electromagnetic computation.

The field-circuit coupled model of inductive FCLs is presented for both 2D and 3D domains. The core of the model consists of a circuit relation for the electrical current and a partial differential equation which gives the relation between the applied current density and the generated magnetic field. The remaining, third equation gives the missing link between the magnetic and the electrical domains, i.e. it calculates the FCL reactive impedance. The calculation of the FCL impedance is done indirectly through the calculation of the induced voltage in the windings. The FCL model in Comsol provides more insight into the mathematical background of FE modeling and helps to better understand the way FE models work.

In general, the 2D FE model requires less computational time, but introduces larger error in the results than the 3D model. Therefore, as the last modeling step, it is recommended to use the 3D FE model.

FE models represent a valuable tool for the design of saturated-core FCLs. As shown through comparison with the experimental measurements, the error of the 3D FE results is around 5%, which is acceptably small.

Chapter 6

FCL IN THE GRID

6.1 Introduction

THE previous chapters of the thesis consider the design and operation of different types of FCLs. The FCLs are, however, intended to become a part of power systems. Before the FCLs are installed, it is essential that the interaction between the FCLs and the power system is analyzed.

The functionality of the power system protection, power quality and power system stability must be preserved at all times. It is of the utmost importance to determine whether an FCL's installation in the system would have a detrimental effect on some of these operational aspects of the system and in which way the arising problems could be solved. This chapter aims at analyzing the given issues. The analysis includes the following principal points:

i. The positioning of the FCLs in the power system,
ii. The interaction between the FCLs and the existing protective schemes,
iii. The interaction between the FCLs and the circuit breakers (CBs),
iv. The influence of the FCLs on power quality,
v. The influence of the FCLs on system stability.

Before the interaction between the FCLs and the power system can be analyzed, it is necessary to determine at which locations in the power system the FCLs can be installed. The functional requirements imposed on an FCL can vary for the different FCL positions. This is presented in section 6.2.

A number of relay protective schemes are used in power systems. Section 6.3 analyzes whether the installation of FCLs could affect their operation. In such cases the schemes must be adapted to the new operating conditions. The proper protection of the power systems must be preserved at all times.

Installation of FCLs is expected to ease the burden imposed on CBs during an opening action. Since the CBs are the only protective units which can interrupt the fault current, it must be ensured that their operation during a fault is accurately determined. Section 6.4 analyzes the interaction between the FCLs and the CBs.

Power quality and system stability issues are addressed in sections 6.5 and 6.6, respectively.

Some of these topics have been investigated extensively in last decade and a corresponding section gives an overview of the published results.

6.2 FCL positioning in a power system

A very important issue to be addressed is the positioning of FCLs in the power grid. FCLs can be placed at different locations and, thus, can have different effects on a faulted system. The different locations impose different functional requirements on the FCLs. For example, an FCL placed in the bus-tie position is required to actually interrupt the fault current as fast as possible, rather than only limiting it, thus, operating more like a CB. On the other hand, an FCL placed in a feeder where DGs are installed has to ensure that the DGs are not disconnected from the network in case of a fault in neighboring feeders.

As there has already been much research into the various possible locations of FCL placement in a power system, no new research of this topic has been done and the conclusions of this thesis are based on available findings. Figure 6-1 shows all proposed locations where an FCL could be installed [Schm 06].
The FCL's function in each of these positions is described below [Koza]:

1) The FCL limits the contribution to the fault coming from the generator unit, i.e. it reduces the short-circuit power capacity of the network.
2) The FCL restrains the short-circuit contribution of the substation auxiliary components.
3) Coupling of the networks is usually advantageous. The FCL restrains the contribution from one sub-network to the fault in the other.
4) Busbar coupling increases the reliability of the energy supply (similar function as in 3)).
5) The same as in 4).

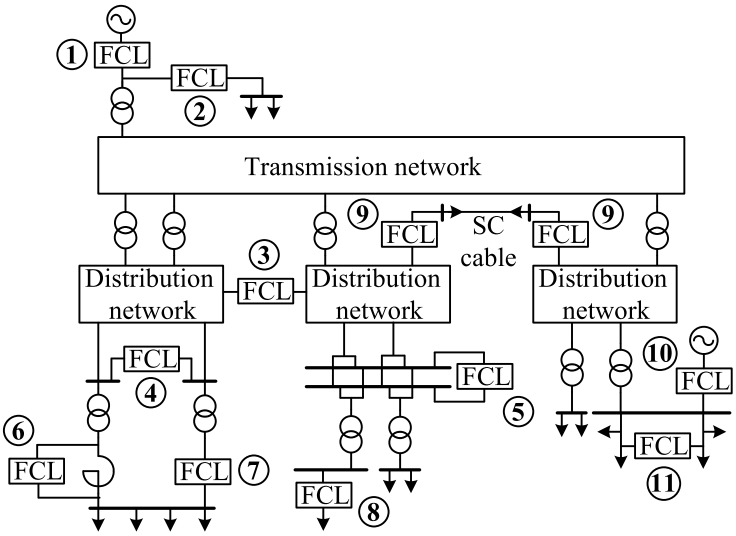

Figure 6-1: FCL positioning in a power system.

6) The FCL serves as the shunt path for the current limiting reactor, so as to avoid increased losses and voltage drop during nominal regime.
7) The FCL can be installed in the transformer (incoming) feeder. It restrains the contribution to the fault incepted in the subsequent (lower-ranked) feeders.
8) The installation in the outgoing feeders requires more FCLs, but the strain imposed on each during a fault is lowered as they have to deal only with the part of the fault current passing through that feeder.
9) The FCLs can be combined with other superconductive devices to protect them from quenching in the case of excessive currents.
10) Locally installed generating units can be coupled to the network through an FCL. The FCL protects only the generator in whose feeder it is installed and restrains only that part of the fault current. More FCLs are required if more DGs are to be connected.
11) FCLs can close ring circuits to provide a safer supply of the electrical energy. In case of a fault, the FCL would separate the linked feeders.

For locations 2, 3, 4, 5, 6 and 11, it is desirable that the FCL not only limits the fault current, but also interrupts it as fast as possible. The introduction of very high impedance has the same effect as the disconnection of the sub-grids. In this way, a contribution to the fault from the neighboring sub-grids and feeders is avoided. Thus, such installation of an FCL does not limit the fault current in the corresponding grid, but prevents possible contributions to the fault from other parts of the system. If the fault current is to be fully restrained (as is the final aim), additional FCL units are required, such as the ones in locations 6, 7, 8 and 10. Such common use of multiple FCLs in different location is shown in Figure 6-2 [Eckr 05]. In the case of a fault, the busbar coupling FCL disconnects the busbars, while the FCLs installed in the transformer's outgoing feeders limit the fault current.

Figure 6-3 shows the possible benefit of installing an FCL for the coupling of DGs to the grid. Instead of coupling a DG to a high voltage network, where the cost of high-voltage transformers and switchgear for connection is inevitable, it can be connected directly to a medium voltage grid via the FCL.

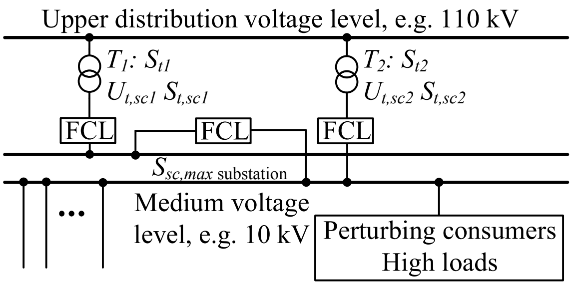

Figure 6-2: The installation of FCLs in different locations.

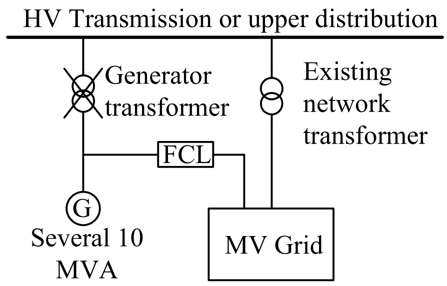

Figure 6-3: The connection of a DG by employing an FCL.

The number of required FCLs and their appropriate locations in the system must be determined for each individual system. In principle, it is important to have an FCL in each incoming feeder. The number of in-feed lines and loads and the number of interconnections are the system parameters that have to be considered. After each of the FCLs is installed in the system, it has to be checked that the coordination and discrimination between the protection relays is maintained [Kuma 06].

The following subsection addresses the issue regarding the interaction between FCLs and existing protective schemes of power systems. It must be determined whether the FCLs could cause malfunctioning of the relays and, if so, what measures can be taken to restore their proper operation.

6.3 FCLs and power system protection

Fault current limiters can be installed in existing power systems as well as in new systems whose initial design accounts for the presence of FCLs [CIGR 07]. In either case, it must be determined whether the operation of FCLs will affect relay protection schemes; in that case the protection would have to be adjusted to the new parameters of the system.

The requirements that the relay protection schemes have to fulfill at any moment are: sensitivity, selectivity, rapidity and reliability. The objective of this section is to examine the interaction between the system protection and FCLs.

The following items should be considered when investigating the mentioned interaction [CIGR 07]:

i. The existing protection principle,
ii. The FCL location,
iii. The type of FCL,
iv. The fault location.

Whether the employed protection relays will fail to operate is determined by both the type of protective scheme and the type of installed FCL. The analysis takes into account two types of FCLs: a resistive and an inductive FCL and the following protective schemes [Wrig 93]:

i. Over-current protection,
ii. Differential protection,
iii. Distance (impedance) protection,
iv. Directional protection.

The principle of operation of each of these protective schemes will be explained before its interaction with FCLs is analyzed. Each protection type will be considered in a separate subsection.

One of the main parts of the given protective schemes are current transformers (CTs). Before the schemes are investigated, the possible changes in the design of CTs due to the FCL installation will be assessed. The following subsection presents this analysis.

6.3.1 Influence of FCL installation on design of current transformers

When designing a CT, it is important to ensure that it will not get saturated during large asymmetrical faults. Otherwise, some protective schemes, such as low-impedance differential protection, would maloperate. After the first fault operation, the value of the flux density B in the core of the current transformer is equal to the remanent flux level B_r, see Figure 6-4. A minor flux loop, due to the normal current of the system, will be positioned in the vicinity of this new working point (loop PO) instead of around the origin.

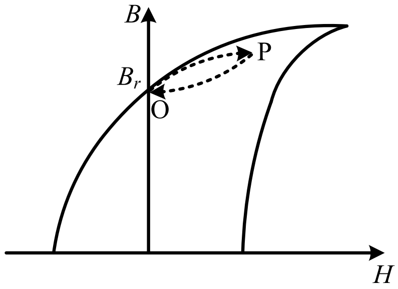

Figure 6-4: The flux loop, due to the normal current, is displaced from the origin.

To avoid saturation of the core, the flux range between the remanent point and saturation must be large enough to accommodate for the change in flux, which is a result of the asymmetrical fault current [Wrig 93]. This condition covers the worst fault scenario case when two consecutive asymmetrical fault currents flow in the same direction.

The size of the core is directly proportional to the maximum expected peak of the fault current. The installation of FCLs would lower the fault peak and reduce the associated range of the flux change. As a result, smaller cores could be used for the design of CTs.

If the FCL is installed before the first fault operation of the relay, the change of the fault flux in the core would not follow the maximal BH curve (curve 1 in Figure 6-5). Due to the reduced peak of the fault current the smaller curve, e.g. curve 2, will be followed. Consequently, after the fault is cleared, the remanent B field in the core will have a lower value than in the case of an unlimited fault. The flux difference between the remanent point and the saturation region would therefore be larger, which implies that the core size of the CTs can be further reduced.

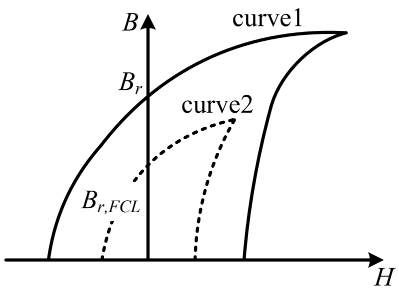

Figure 6-5: A reduced fault current peak causes a smaller flux change in the core.

In essence, the core size reduction is beneficial only in case of newly installed relays. The replacement of existing protection schemes would not be economically justified since they would continue to operate properly with the FCL installed in a line.

If the CTs are going to be designed for a grid protected by FCLs, the operation of the FCLs has to be reliable and fail-safe. Any failure to restrain the fault current to the preset value would result in the malfunctioning of the protective scheme due to the saturation of the CTs.

The following subsections analyze the interaction of the mentioned four protective schemes and the FCLs. Each protective scheme is addressed in a separate subsection.

6.3.2 Over-current protection

To distinguish between a normal and fault condition, the measured current value (e.g. magnitude or *rms* value) of a line current is compared to the preset threshold level. If that threshold is exceeded the relay will trip. Over-current relays protect a given part of the system, defined as the protection zone or reach of the relay. To react to a fault, two basic requirements have to be fulfilled [Kund 03]:

i. The short-circuit current should be higher than the maximum over-load current,
ii. The duration of the short-circuit current must be longer than the delay time of the last upstream relay.

The drawback of over-current protection is its sensitivity to the type of incepted fault and the impedance value of the source. Namely, the reach of the relay (operation zone) depends on whether a line-to-ground, line-to-line of three-phase fault is incepted (see Figure 6-6a). Also, the reach of the relay is affected by the change in source impedance (see Figure 6-6b).

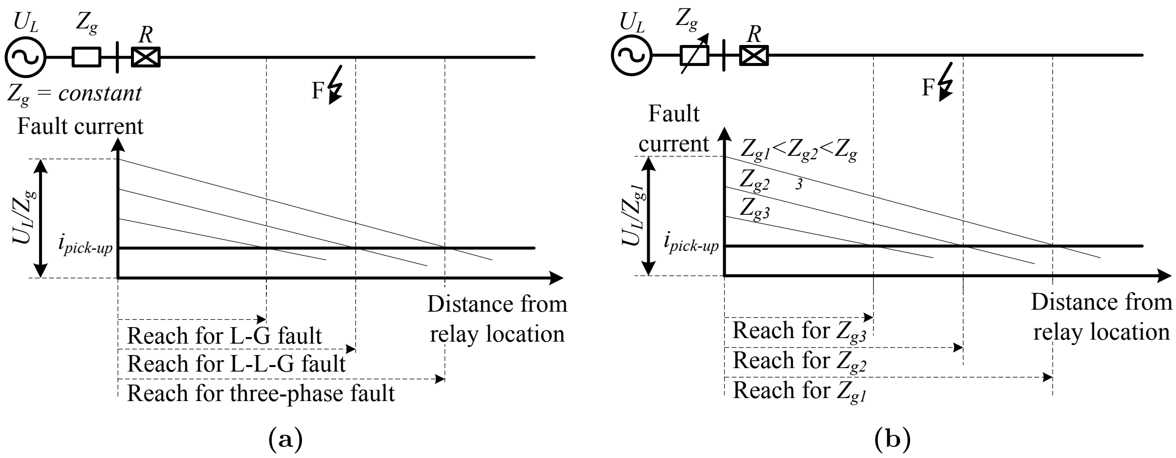

Figure 6-6: Relay's reach zone as a function of: (a) Type of a fault [Pait]; (b) Source impedance [Pait].

Three types of the over-current (magnitude) relays are in use today [Pait]:

i. Definite-current relays (current grading, instantaneous relays) - identification 50,

ii. Definite-time relays (time grading) - identification 51,
iii. Inverse-time relays - identification 51.

Definite-current relays are instantaneous relays, triggered by a certain value of the line current. They are installed in the part of the network whose impedance is larger than the impedance of the source, i.e. where the levels of the fault current are dependent on the fault position and they increase as the fault location moves toward the source.

The installation of an FCL in the part of a network protected by over-current relays would influence the operation of all the downstream relays, relative to the position of the FCL, see Figure 6-7. Since the relays are triggered by the predetermined current level, they would not detect the fault if the level of the fault current would be too far reduced. Either the FCL limiting factor has to be adjusted (to be low enough) or the pick-up settings of the protection relays have to be changed.

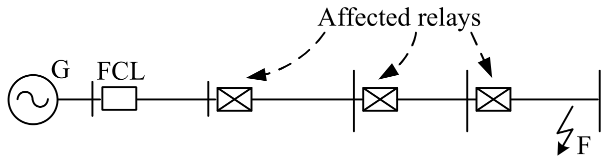

Figure 6-7: Over-current relays affected by an FCL placed upstream.

Because of the presence of FCL impedance, variations in the fault current level, due to different fault positions, will be much smaller. The current grading between the neighboring relays must therefore be readjusted. However, this protection technique might be inapplicable because of the small differences between the fault current levels.

Definite-time relays allow adjustment of different reaction time delays for different current levels. They employ time-based discrimination, where the relay closest to the end of the line has the fastest reaction. If the limited fault current is lower than the lowest pick-up value of the relay, the settings of the relays must be adjusted. The reaction times of all of the fault current levels can be shortened, i.e. scaled-down, since the maximum expected peak of the fault current is reduced.

Inverse-time relays operate with a different time delay for different fault levels. The higher the fault current, the faster the reaction is. The relays furthest from the source have the shortest reaction time for the given current level, thereby providing time-based discrimination. The FCL can cause maloperation if the limited fault current is lower than the relay's lowest pick-up value. As explained for the definite-time relays, relay's operating characteristics can be adapted to the new fault operation of the system.

The over-current relays are usually set so they do not react to inrush currents, as caused by motors or magnetizing currents of transformers. The minimal limited fault current should be higher than these values if the fault is to be detected by the relays. Some relays employ special techniques for the detection of magnetizing currents, e.g. the detection of the level of the second harmonic, and can clearly distinguish between these phenomena and the fault condition. The operation of these relays can be affected if the FCL introduces harmonic distortion to the fault current. More specifically, in the case that the installed FCL introduces the second harmonic, the relays might see this fault as the magnetizing current and maloperate. Given that no harmonics are generated by the FCL, the fault is detectable by the relays even if its magnitude is lower than that of the magnetizing current.

In the case of inter-feed connections, as shown in Figure 6-8a, attention must be paid to the fact that the current passing through the FCL is not equal to the current sensed by the relay [CIGR 07]. The current i_{FCL} is equal to the sum of the currents i_R and i_1. The pick-up setting of the relay has to be set to detect current i_R and not i_{FCL}. Figure 6-8b shows another situation where the current of the relay is equal to the FCL current.

Figure 6-8: Influence of in-feed current contribution on a relay pick-up setting: (a) In-feed is between the relay and the FCL; (b) In-feed is downstream from both the relay and the FCL [CIGR 07].

The coordination between over-current relays can also be affected by the presence of FCLs, such as solid-state FCLs (SSFCL), which introduce significant harmonic distortion in the line current [Pan 08], see Figure 6-9. An SSFCL is installed in a system with two downstream distance relays R_1 and R_2, where relay R_1 measures the peak and relay R_2 the fundamental component of the fault current. Assuming that the SSFCL is set to trip for the fault F incepted on the feeder BC, it is shown that the harmonic distortion of the fault current can cause the tripping time of relay R_1 to be shorter than that of relay R_2. Since the feeder BC is the primary protection zone for relay R_2, this relay should react to the fault first. Thus, the coordination between these two relays, employing different measurement techniques, is affected by the operation of the SSFCL. An example of a distorted waveform of the limited fault current is given in Figure 6-10 [Ahme 04].

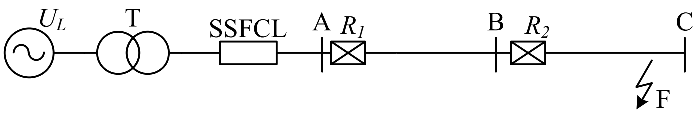

Figure 6-9: Network example for the study of SSFCL influence on the coordination of distance protection.

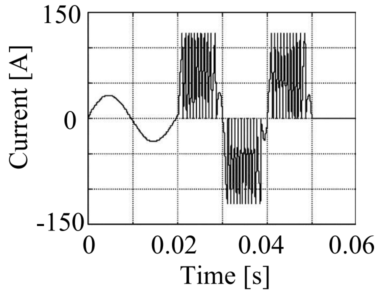

Figure 6-10: The waveform of the limited fault current.

6.3.3 Differential protection

Differential schemes are used for the protection of a specific unit, e.g. transformer, motor, generator, within the system [Wrig 93]. They measure the currents at the end of the protected zone and use their vector and/or scalar sums to distinguish between the normal and fault conditions. Two differential means of protection are used: low impedance (code number 87-Low) and high impedance (code 87-High). High impedance protection is not sensitive to the saturation of current transformers.

FCL influence on the operation of low-impedance differential protection

A single-line scheme of low-impedance differential protection is presented in Figure 6-11. The current through the relay i_R is equal to the vector sum of the secondary currents $i_{ct,sA}$ and $i_{ct,sB}$ of the CTs. If the fault current is limited by the FCL, the relay current i_R will also be decreased. It must be ensured that the relay current is large enough to trip the relay. Otherwise, the FCL would cause blinding of the relay.

FCLs can prevent the false tripping of a relay due to the characteristics mismatch of two CTs. The principal cause of the measurement error when the CTs are used is presence of transformer exciting current i_e, see Figure 6-12.

Since the excitation characteristics of two cores are highly nonlinear, excitation currents of two CTs can be unequal, resulting in unequal secondary currents $i_{ct,sA}$ and $i_{ct,sB}$ for the same primary current. In the case of large external fault currents, the difference in secondary currents $i_{ct,sA}$ and $i_{ct,sB}$ (see Figure 6-11) would flow through the relay and possibly cause false tripping. Since even a very small mismatch of the excitation curves of CTs can be significant when large fault currents, e.g 20 p.u., are flowing, a biasing

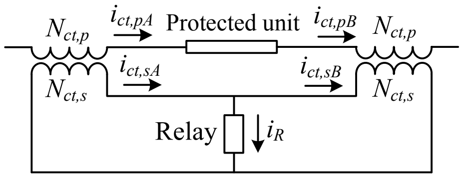

Figure 6-11: Single-phase scheme of differential protection [Wrig 93].

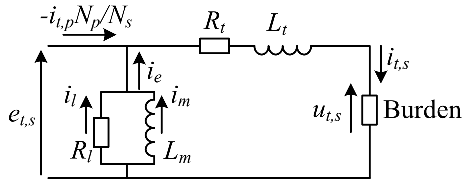

Figure 6-12: Equivalent circuit of a current transformer referred to the secondary [Wrig 93].

technique is used to ensure the proper functioning of the differential protection [Wrig 93]. However, this technique reduces the sensitivity of the protection to internal faults.

When the fault current is limited to a much smaller value, e.g. 2 p.u., the error, resulting from the mismatch of CT excitation characteristics, would likely be too small to cause a relay malfunction. The biasing windings would not be required which would simplify the design of the differential protection. The sensitivity of the differential protection on the internal faults would be increased.

Even when the excitation characteristics are well-matched, the saturation of one of the CTs would result in relay tripping. False tripping can be avoided by installing FCLs and thereby controlling the maximum fault peak. The reliability of the low-impedance differential schemes would be improved. It must, however, be ensured that all of the in-feed ends are protected by the FCLs. As shown in Figure 6-13a, the installed FCL provides saturation-protection for the CTs in case a fault is incepted on the right side relative to the position of the CTs. However, if a fault is commenced between the FCL and the CTs (see Figure 6-13b), the fault-current contribution $i_{L,f2}$ would not be restrained and it would possibly saturate the CTs. To prevent this, an additional FCL should be used to limit the current $i_{L,f2}$.

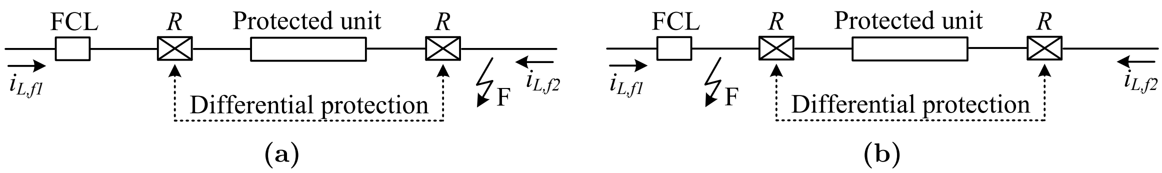

Figure 6-13: The FCL installation on one side of the protection zone is not sufficient for saturation-protection of the CTs: (a) CTs are protected from saturation, (b) CTs are exposed to unlimited current $i_{L,f2}$ and might be saturated.

Installation of the FCLs within the protection zone would not provide saturation-protection for the CT if a fault was incepted between the FCL and CT. It is not recommended to install the FCL in such a way.

In the case that an FCL limits only one of the fault currents, $i_{L,f1}$ or $i_{L,f2}$, for a fault incepted inside the protection zone, it could produce a significant phase shift of the limited fault current depending on the X_{FCL}/R_{FCL} FCL factor. This could reduce the vector sum of the secondary currents in the relay and cause its maloperation [CIGR 07]. The scalar sum of the secondary currents would remain unchanged, reducing the sensitivity of the relay.

FCL influence on the operation of high-impedance differential protection

If one of the CTs used in the low-impedance differential protection becomes saturated during an external fault, a relay would maloperate due to an artificial imbalance of the secondary currents. High-impedance differential protective schemes are used to avoid such saturation problems. Figure 6-14 presents a scheme of this type of protection, a restricted earth-fault protection. It detects faults which involve a small number of transformer turns. The relay has very high impedance and it is voltage-operated. The imbalance of the secondary currents of the CTs is transferred through the saturated CT by this high impedance, preventing maloperation of the relay.

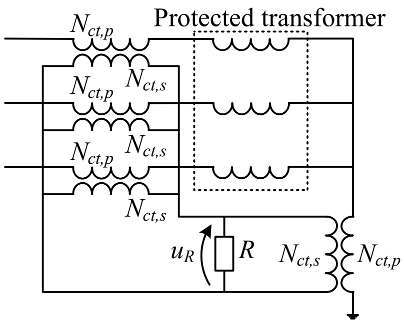

Figure 6-14: Restricted earth-fault differential protection.

To avoid the maloperation of the relay during large external faults, the minimal setting of the voltage u_R (see Figure 6-14) has to be determined for the worst possible fault scenario: all three phases conducting zero sequence currents, which sum up in the neutral connection of the transformer and cause the saturation of the star-point CT [Wrig 93]. However, the higher the value of the voltage u_R the lower the sensitivity of the protection to internal faults.

If the maximum through-fault (external) current is limited by the FCL, the minimum setting of the voltage u_R, which ensures that the relay will not maloperate for the external faults, would be reduced, thus increasing the sensitivity of the protection.

The level of internal faults, to which this protection reacts, is too low to trip the FCL. Thus, the FCL cannot cause blinding of the relay.

6.3.4 Distance (impedance) protection

Distance protection schemes are used for the protection of lines in both transmission and distribution networks [Wrig 93]. One end of the protection zone is defined by the position of CTs and voltage transformers (VTs) and the other end by the impedance setting of the relay. By measuring the line current and voltage and comparing their ratio to the relay impedance setting, the normal and fault operation of the system can be clearly distinguished. Several types of distance relays exist:

i. Simple impedance relay,
ii. Reactance relay,
iii. Mho relay.

The following subsections investigate the interaction between an FCL and the distance protection schemes.

Simple impedance relay

The operating characteristic of an impedance relay is a circle in the complex $R-X$ plane with its center in the coordinate zero, as shown in Figure 6-15a. The circle corresponds to the threshold value of the measured impedance. The relay will trip in the case that the measured impedance is lower than the threshold setting. The relay will react to a fault in both forward and backwards directions, relative to its position in the system.

Since an FCL changes the fault impedance of a line, it can affect the operation of the relay, see Figure 6-15b. Both inductive X_{FCL} and resistive R_{FCL} impedances can change the value of the impedance seen by the relay so that the fault appears to be outside of the protection zone Z_R. The relay would experience an under-reach. The impedance setting of the relay has to be changed to the new value $Z_{R,new}$ to account for the presence of the FCL impedance.

Figure 6-16 shows an example where the impedance relay R_1 would trip with a delay even though a fault is in its primary zone AB. Because of the insertion of the FCL impedance, the relay measurement would indicate that the fault is in secondary zone BC.

In case the impedance of the faulted line is measured on the basis of the voltage and current values from that line, the positioning of the FCL up-stream or down-stream

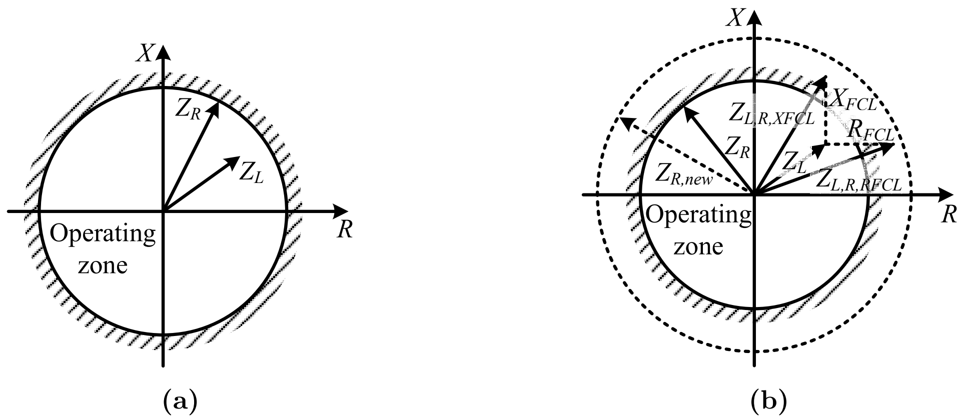

Figure 6-15: Simple impedance (distance) relay: (a) Operating characteristic; (b) Under-reach due to the installation of an FCL.

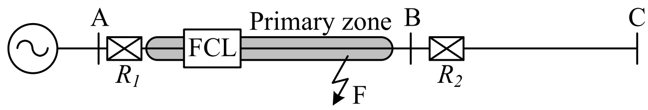

Figure 6-16: An example of under-reach of the distance relay due to the presence of FCL impedance.

the impedance relay might have a different impact on the operation of the relay, see Figure 6-17 [Henr 03]. Namely, the current measured by the relay Rel_1 in both cases would be the same, but the voltage of bus A would have different values $|U_{A,FCL,out}| < |U_{A,FCL,in}|$, see Figure 6-18. So, if the FCL is installed downstream relative to relay Rel_1, the measured impedance would have a larger value than when the FCL is positioned upstream of the relay. The fault could appear to be in section BC and the relay would, therefore, maloperate.

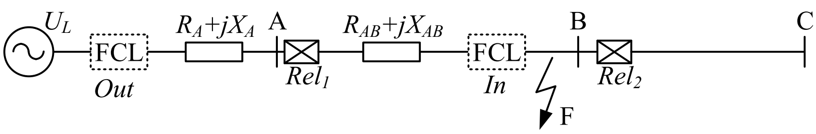

Figure 6-17: FCL installation inside or outside the protection zone of the distance relay.

Reactance relay

By measuring only the reactance of a line, the sensitivity of the distance protection to the resistance of the fault-arc is prevented [Wrig 93]. This means, at the same time, that the reactance relay will not be affected if a resistive FCL is installed inside its protection

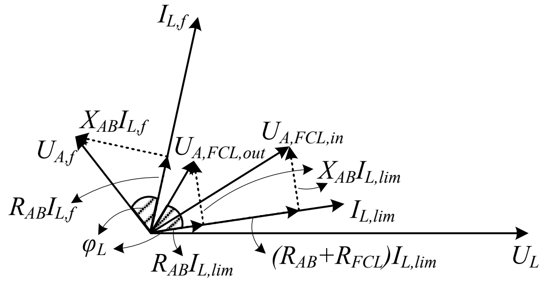

Figure 6-18: The voltage measured by the relay in three cases: no FCL (U_A), FCL outside ($U_{A,FCL,out}$) and FCL inside the protection zone ($U_{A,FCL,in}$).

zone. However, an inductive FCL could cause the relay under-reach, see Figure 6-19. The fault located at distance Z_L from the relay, could appear to be at distance $Z_{L,R,XFCL}$ and fall outside of the zone.

In the case that the FCL has capacitive impedance, it can introduce a compensating effect to the line reactance. The effect of FCL installation on the reactance relay would be an extension of the relay operating zone, see Figure 6-20.

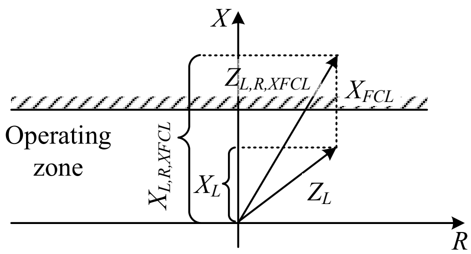

Figure 6-19: Under-reach of the reactance relay caused by installation of the inductive FCL.

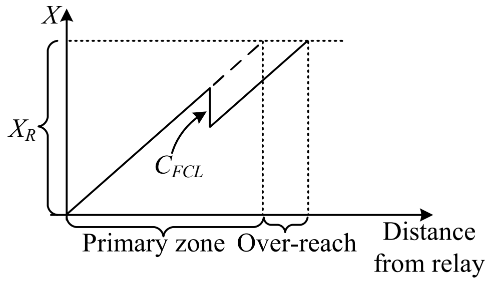

Figure 6-20: The extension of the relay's reach zone caused by the FCL capacitance.

If an FCL has an inductive impedance, the stray capacitance would not change the effect already illustrated in Figure 6-19. Namely, since the FCL reactance X_{FCL} has a significantly larger value than the stray capacitance $C_{FCL,stray}$ (in range of nF), it is likely that the relay would still experience the under-reach.

A resistive FCL could alter the measured value of line reactance if an additional in-feed line was connected between the relay and the FCL, see in Figure 6-21. The voltage drop across the FCL resistance $i_{L,f}R_{FCL}$ is not in phase with the relay current i_R and the associated voltage drop across the resistance R_1. The measured reactance is lower by $X_{R,error}$.

Mho relay

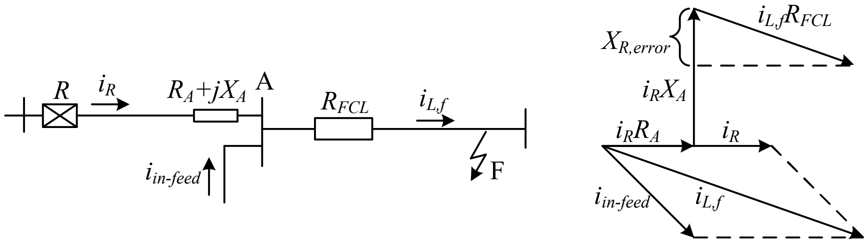

Figure 6-21: The error in the relay measurement due to the presence of an in-feed current and the installation of a resistive FCL [Gers 98].

Mho relay is an impedance relay with inherent directional fault sensing. Its operating characteristic is a circle whose circumference passes through the coordinate origin, see Figure 6-22. As is the case with simple impedance relay, the operation of Mho relay can be affected by the FCL fault impedance, both inductive and resistive.

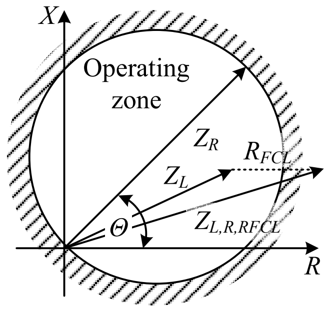

Figure 6-22: Mho relay operation affected by the installation of a resistive FCL.

Figure 6-22 shows that the installation of a resistive FCL within the protection zone of the relay can cause under-reach of the Mho relay. The impedance seen by the relay $Z_{L,R,RFCL}$, equal to the sum of the system impedance without the FCL Z_L and the FCL resistance R_{FCL}, falls outside of the relay operating zone. The relay will not trip to a fault within its protection zone. The operating characteristic of the relay should be adjusted to take the FCL impedance into account:

$$Z_R = 0.8\left(\sqrt{(R_L + R_{FCL})^2 + (X_L + X_{FCL})^2}\right)$$

$$\Theta = \arctan\left(\frac{X_L + X_{FCL}}{R_L + R_{FCL}}\right), \tag{6.1}$$

where the factor 0.8 means that 80% of the line is covered by the first protection zone of the relay.

The completely polarized Mho relay will not operate properly when the resistance of the FCL is larger than the assumed fault-resistance of the arc. Its characteristic must therefore be adjusted to the presence of the FCL impedance.

6.3.5 Directional relays

To achieve proper discrimination in the interconnected networks, the employment of directional relays, in addition to the use of over-current schemes, is required. The directional relays trip only on faults where the power flow is in one of two directions [Wrig 93]. The direction of the power flow can be determined by phase comparison of the current and voltage signals. It is common not to use both signals from the faulted line, since the relay reaction can be distorted by the collapsed voltage in the faulted line.

Usually fault currents lag their phase voltages by a very large degree due to the predominantly inductive fault impedance of the system. The angle of the maximum torque (AMT) of the relay is adjusted accordingly. An example is given in Figure 6-23. The relay is polarized by the voltage $\hat{U}_{bc}$ and the phase current $\hat{I}_a$, for the detection of a fault in phase a. However, its AMT is set to $-\pi/6$, which means that the maximum torque will be obtained when the current $\hat{I}_a$ lags its phase voltage $\hat{U}_a$ by $\pi/3$.

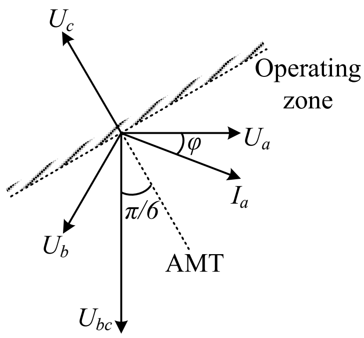

Figure 6-23: The polarization signals and the operating zone of the directional relay [Wrig 93].

Whether the fault impedance of an FCL can affect the operation of a directional relay depends on the type of FCL limiting impedance and the nature of the short-circuit impedance of the system. In the previous example, it was assumed that the fault phase current lags the phase voltage by $\pi/3$, i.e. the short-circuit impedance of the system is mainly inductive. Having an FCL with purely resistive impedance in the line, this angle would be decreased. The current $\hat{I}_a$ and the voltage $\hat{U}_a$ would nearly be in phase. The resulting torque of the relay would be reduced, but the relay would operate adequately, since the current vector would still fall in the forward operating zone. In the worst case of mismatch of the FCL impedance and the system impedance the relay would still operate properly. The installation of an FCL is therefore not expected to cause directional relays to malfunction. However, the adjustment of the relay's AMT is necessary in order to increase torque and obtain a faster reaction to a fault.

The following subsection analyzes the interaction between FCLs and CBs. Since CBs are the only protective units used for a line interruption, it is important to determine what influence an FCL has on a CB's breaking duty.

6.4 FCLs and the breaking duty of Circuit Breakers

The interrupting stress imposed on CBs during an opening action is a function of both the current flowing through the CBs (usually, a fault current) and a transient recovery voltage (i.e. rate of rise of recovery voltage - RRRV) that appears across the CBs [Cali 04]. An increase of any of these two parameters could result in a failure of CBs to clear the fault.

The installation of FCLs in series in a line limits the value of a fault current. From this point of view, the breaking burden imposed on CBs is decreased. However, to fully asses the interaction between FCLs and CBs, how the installation of FCLs influences RRRV across CBs terminals must also be examined. In the analysis, two main types of FCLs are considered, namely, resistive and inductive FCLs. The position of the FCL relative to the CB is found to have no influence on the interrupting duty of the CB [Alci 06].

In the case that a resistive FCL is installed, the RRRV would be reduced for all fault positions relative to the CB, see Figure 6-24 [Cali 04]. The CBs' breaking duty decreases with increase of the FCL resistance.

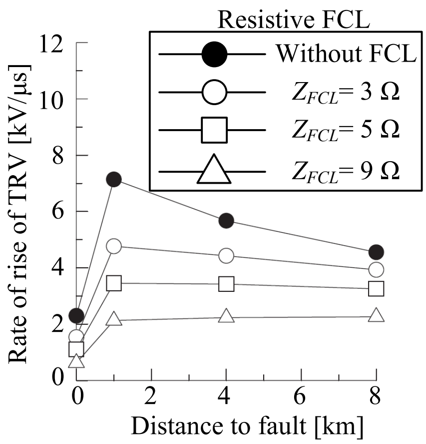

Figure 6-24: Variation of RRRV with distance to fault for the resistive FCL [Cali 02; Cali 04].

The analysis of CB operation during a fault becomes more complex when inductive FCLs are used. Namely, it has already been shown that the insertion of inductance (e.g. current limiting reactor) in series with a line increases the RRRV imposed on CBs during the opening action [Peel 96]. The reason is that the stored magnetic energy in the inductor produces electromagnetic voltage waves, which propagate through the system even after the interruption of the current. These voltage waves reflect against transformers, increase in amplitude, and travel back to the terminals of the CBs [Slui 01]. As a result of this transient phenomenon, the transient voltage across the terminals of the interrupting device has a higher value. Since an inductive FCL is practically an inductor, its installation in the system can increase, thus, the stress imposed on CBs by the transient recovery (TRV) voltage and possibly cause their failure [Cali 04].

The negative effect of installation of inductive FCLs on the RRRV can be mitigated if a capacitor is installed in parallel to the FCL inductor [Peel 96]. The capacitor ensures that the magnetic energy stored in the inductance oscillates locally, being exchanged between these two elements. The possible stray capacitance of the installed FCL has to be taken into account in the calculations since it has the same effect on the RRRV as an externally applied capacitor.

To reduce the RRRV across CBs terminals, the value of the parallel capacitances has to be sufficiently large. For the analyzed network, it is shown that the TRV is increased for any distance between the fault and the CB, when the FCL stray capacitance has a value of 10 nF [Cali 04], see Figure 6-25a. A similar analysis is presented in [Qing 08]. As a result, although an inductive FCL is installed, the CB may experience failure due to an increased RRRV. If the FCL stray capacitance value was 100 nF, the TRV would be lower for most fault locations, see Figure 6-25b.

For the given value of the FCL stray capacitance, the increase in FCL impedance (inductance) lowers the TRV across the CB terminals.

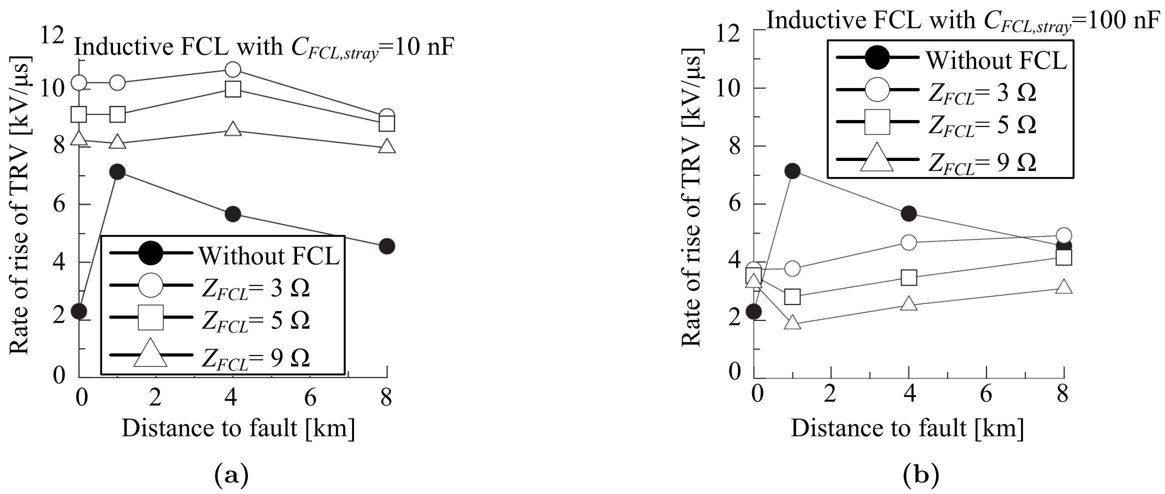

Figure 6-25: Variation of the RRRV with distance to the fault for an inductive FCL with the stray capacitance of: (a) 10 nF; (b) 100 nF [Cali 04].

These analyses suggest that, from the RRRV severity point of view, it is better to have a larger FCL stray capacitance or to install a capacitor in parallel to the inductive

FCL.

Equation 6.2 calculates an expected RRRV across CBs terminals for the given FCL limiting factor α_{FCL} (ratio between the limited and unlimited fault current) and the given values of the stray capacitances [Qing 08]:

$$RRRV = 2U_L\alpha_{FCL} + U_L\left(1-\alpha_{FCL}\right)\cdot \cdot \frac{1-\cos\sqrt{\dfrac{\alpha_{FCL}C_{L,sg,CB-G}\pi^2}{\left(1-\alpha_{FCL}\right)\left(C_{FCL,stray}+C_{L,sg,CB-FCL}\right)}}}{\pi\sqrt{L_L C_{L,sg,CB-G}}}, \quad (6.2)$$

where U_L is the maximum line voltage, $C_{L,sg,CB-G}$ and $C_{L,sg,CB-FCL}$ the system stray capacitances to ground, on the source- and FCL- sides of the CB, respectively, $C_{FCL,stray}$ the FCL stray capacitance and L_L the system stray inductance.

6.5 FCLs and power quality

The number of 'sensitive' loads, whose operation can be affected by disturbances in power supply, is increasing worldwide. Voltage dips are a major problem concerning the power quality [Boll 03]. Voltage sag is a reduction in *rms* voltage (0.1 p.u. - 0.9 p.u.), with a duration between half a cycle and several seconds [Ahme 02]. Around 80% - 90% of customer complaints regarding power quality concern voltage dips. They can be caused by motor starts, transformer energizing and short-circuit faults.

The most severe voltage sags are caused by fault currents. The voltage drop across the system impedance R_L and L_L (see Figure 6-26) increases considerably when large fault currents flow. The installation of FCLs in the system can help improve power quality [Ahme 02; Chan 01; Tosa 01]. By limiting the fault current to a value comparable to the normal current, the voltage sags are significantly reduced. The principal lay-out of the simulated circuit is given in Figure 6-26 [Tosa 01]. The resonant FCL is installed between the faulted load and source.

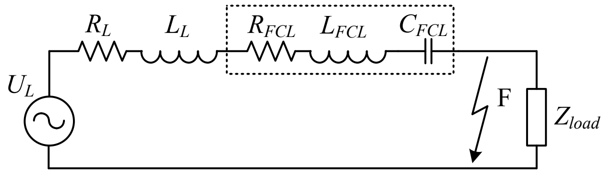

Figure 6-26: A schematic of the simulated circuit [Tosa 01].

Figure 6-27a shows the dip in the power voltage due to the fault current. The sag is severe. After the installation of an FCL, the level of the fault current is limited significantly, see Figure 6-27b. The dip of the line voltage is negligible.

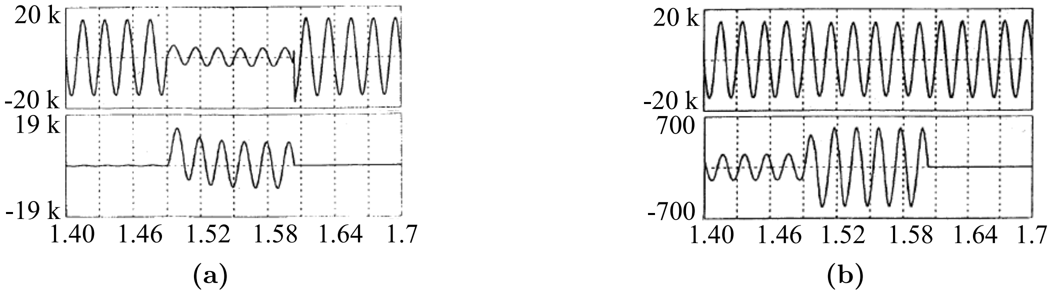

Figure 6-27: The simulation results: (a) The voltage dip (upper graph) and the unlimited fault current (lower graph); (b) The line voltage (upper graph) and the limited fault current (lower graph) [Tosa 01].

The presented results are obtained for the case that a solid-state FCL is installed in a grid. It can be shown that the integration of an inductive saturated-core FCL in the grid would bring the same improvement in power quality.

6.6 FCLs and system stability

The stability of a power system can be divided into steady-state stability and transient stability. The system is steady-state stable if, after experiencing a small disturbance, it returns to essentially the same steady-state condition of operation. The system is transiently stable if, after experiencing a large disturbance, it attains significantly different yet steady-state operation [Grai 94].

Short-circuit faults belong to large disturbances of the power system. They can severely affect its stability and, possibly, cause the system to become unstable. Considering the operation of a synchronous generator, during steady-state operation the balance between a mechanical P_{mech} and electrical power P_{el} is maintained and expressed by swing equation:

$$\frac{2H}{\omega_s}\frac{d^2\delta_{mech}}{dt^2} = P_{mech} - P_{el}, \tag{6.3}$$

where H is a constant proportional to the inertia constant M of a machine, ω_s the synchronous angular velocity and δ_{mech} the angular displacement of the rotor in mechanical radians.

A fault inception results in a significant reduction of consumed electrical power. Usually, the studied time is one second after fault (large disturbance) inception. The scale of such a transient phenomenon is less than one second. The mechanical power of the machine is considered constant during this period which results in the increased speed of the rotor. If the system is to remain stable, the fault has to be cleared before the rotor displacement angle exceeds the critical angle δ_{cr} [Grai 94]. The stable operation of the induction machines is affected by the fault currents in the same way. The fault has to be cleared before the speed of the machine exceeds its critical value. Otherwise, the generator will not be able to regain the stable operation.

Since FCLs are expected to provide protection for future power systems, it is essential to investigate their influence on system stability. This issue has been extensively addressed in literature. The rest of this section will provide a summary of the presented results.

In general, the installation of FCLs improves the rotor angle of generators by increasing the consumption of electrical power during a fault and thereby reducing rotor acceleration. This can be simply demonstrated by using the equal area criterion for a single-machine infinite-bus system. Figure 6-28a shows the change in rotor speed connected to the faulted feeder when no FCL is used, whereas Figure 6-28b shows the same situation with an installed FCL. The inserted FCL fault impedance reduces the difference between the mechanical and electrical power, resulting in the smaller increase of the rotor speed $\delta_1' < \delta_1$ [Soko]. The critical clearing time t_{cr} of the fault is increased [Shir 08].

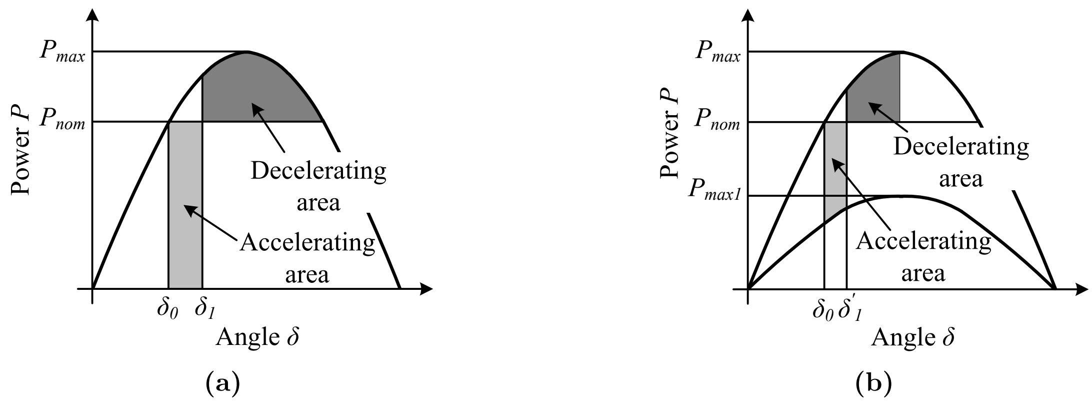

Figure 6-28: Acceleration and deceleration areas: (a) Without FCL; (b) With FCL.

The analysis presented in [Alme 09] shows that resistive and inductive FCLs have different influences on system stability. A system topology comprising one generator, two feeders and one infinite bus is examined. The FCL can be installed in the main feeder, see Figure 6-29a, or in the one of two parallel lines, see Figure 6-29b. In both cases the fault is incepted in the parallel feeder l_2 between the FCL and infinite bus.

When the resistive FCL is used, the stability of the generator can be improved or can be worsen, depending on the resistance value. For certain values of the resistance,

Figure 6-29: Analyzed power system with an FCL: (a) In the main feeder; (b) In the parallel feeder [Alme 09].

the consumption of electrical power can be increased above the maximum generator output during a fault. As a result, the generator will slow down instead of speeding up. The resulting oscillation of the rotor speed could be larger than without an FCL, see Figure 6-30.

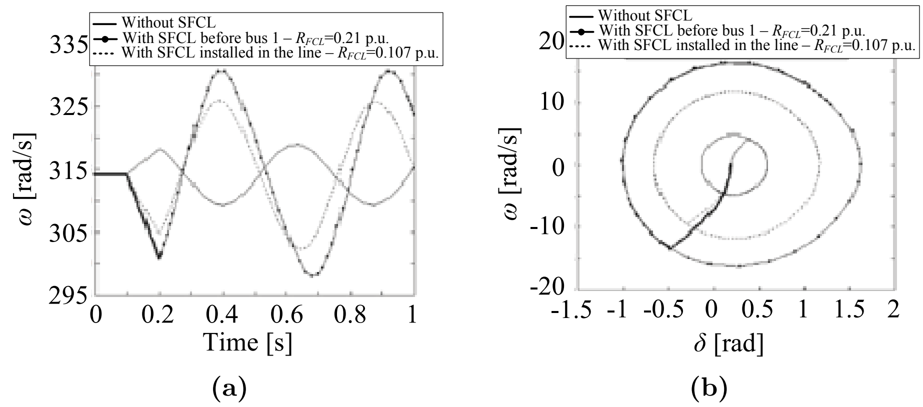

Figure 6-30: Generator behavior with and without FCL: (a) Rotor angular velocity; (b) Phase space representation [Alme 09].

Thus, a resistive FCL should be designed not only to limit the fault current but also to preserve or improve system stability. The change of power consumption with the resistance value is given in Figure 6-31 [Tsud 01]. To reduce the amount of consumed power, the resistance has to either be reduced below or increased above a certain value. The method is proposed in [Tsud 01]. Similar analyses are presented in [Seun 01; Shir 08; Soko 04]. An appropriately designed resistive FCL can improve the transient stability of synchronous generators.

The results from [Alme 09] show that the installation of an inductive FCL improves system stability when the FCL is installed in the parallel feeder, see Figure 6-32. The FCL has no influence on stability when placed in the main feeder. The real power consumption is still zero due to the zero voltage at the infinite bus.

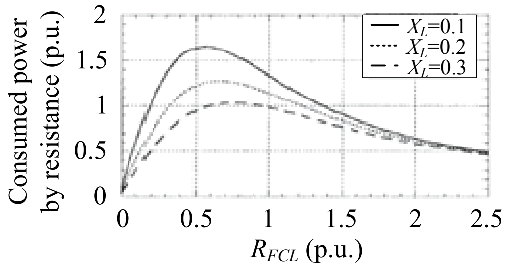

Figure 6-31: Consumed electrical power as a function of the FCL resistance [Tsud 01].

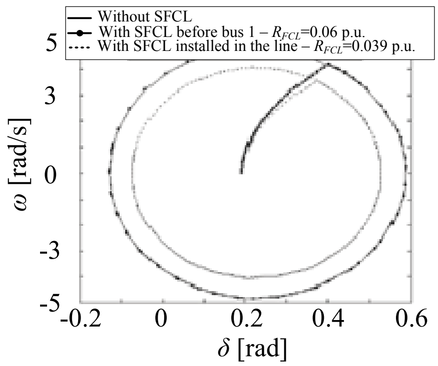

Figure 6-32: Phase space representation: without an FCL, with an FCL in the main feeder and with an FCL in the parallel feeder [Alme 09].

Employment of FCLs can improve the transient stability of dispersed induction generators [Emhe 09]. By inserting fault resistance, the consumption of electrical power is increased, which reduces the acceleration of the rotor. The FCL resistance has to be large enough to ensure that the electrical power exceeds the mechanical power of the generator, i.e. establish the damping torque. The minimal FCL resistance $R_{FCL,min}$ is then defined as equality of electrical torque T_{el} and mechanical torque T_{mech}, i.e. $T_{el} = T_{mech}$, and can be calculated as proposed in [Emhe 09].

In Figure 6-33, curves B and C depict the change in the electrical torque during a fault for the cases without and with an FCL, respectively. Curve C shows that the transient stability of the generator can be ensured if the FCL resistance is large enough to provide $T_{el} = T_{mech}$. A further increase of the FCL resistance imposes the damping torque resulting in the speed reduction of the generator. The stability of the generator is ensured regardless of the fault clearing time [Emhe 09].

Installation of FCLs can prevent undesired disconnections of dispersed micro-generation, which would increase power reliability and availability. Induction generators can be directly connected to a grid without loss of stability in the case of remote faults [Emhe 09].

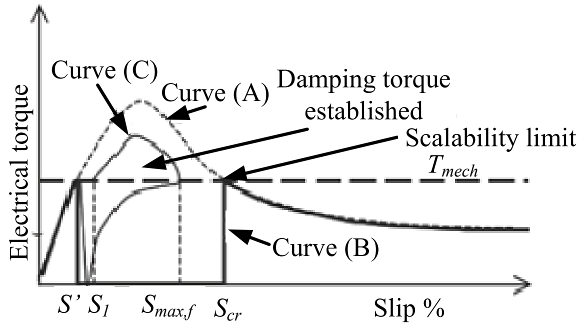

Figure 6-33: Impact of a resistive FCL on the stability margin of induction generators [Emhe 09].

6.7 Conclusions

When analyzing the integration of FCLs in power systems, it is important to investigate their possible influence on system protection units, power quality and system stability.

This chapter presents an analysis of the interaction between two types of FCLs, resistive and inductive, and four types of protective schemes: over-current, differential, distance (impedance) and directional protection. The results show that FCL installation could lead to blinding and maloperation of protective relays. If the fault current is limited too much, the over-current protection will not detect a fault. Installing an FCL in the reach zone of the impedance relay increases the sensed value of the line fault impedance. If the measured impedance is too large, the relay will not detect a fault; it will appear to be outside the protection zone of the relay. The FCL fault impedance becomes the dominant impedance of the faulted line and the magnitude of the current is not a function of the fault distance from the source. Current- and time-grading protective schemes become ineffective in this situation. The differential protection low could fail to detect the fault if the fault current is limited too much. Therefore, readjustments of the relay settings and schemes might be required. Before the FCLs are introduced into the system, it is of the utmost importance to analyze and ensure that the existing protective schemes will operate properly.

Severity of breaking duty of CBs depends on both the magnitude of the fault current and rate of rise of recovery voltage (RRRV) across CBs terminals. By limiting the fault current, FCLs are expected to reduce the severity of CBs' breaking duty. However, the installation of inductive FCLs could increase the RRRV and cause a failure of the CBs. The possible increase of the RRRV has to be determined for each given system. Attention has to be paid to the value of the stray capacitance of the inductive FCLs. The analysis shows that for the analyzed system, by increasing the stray capacitance to 100 nF, the RRRV can be reduced to an acceptable level regardless of the fault distance to the CB. Installation of an additional capacitor in parallel to the inductive FCL is a way to increase the FCL stray capacitance.

It is shown that both power quality and system stability can be improved by installing the FCLs. The voltage sags are considerably reduced by limiting the fault currents. The transient stability of synchronous and induction generators is improved. The FCLs increase the electrical torque during a fault and therefore reduce the acceleration of the generators. As a result, the critical clearing time, by when the fault has to be removed, is increased. Excessive power consumption of the resistive FCL could result in undesired fast braking of the rotor. The oscillation of the rotor angular velocity, after the fault is cleared, could be even larger when an FCL is used. Therefore, the FCL resistance has to be within a specific range, which will ensure improved transient performance of the system. Inductive FCLs would either improve the transient stability of the system or they would have no influence on it. It depends on the configuration of the system and locations of the fault and the FCL.

When determining the FCLs' cost-effectiveness as a power system protection solution, apart from comparing their cost and the cost of CBs, the potentially positive effects that the FCLs have on power quality and system stability should be taken into account.

Chapter 7

CONCLUSIONS AND RECOMMENDATIONS

7.1 Conclusions

IT is determined that, based on the applied technology, the numerous types of Fault Current Limiters (FCLs) can be divided into three main groups: non-semiconductor-based, solid-state and hybrid FCLs. On the other hand, based on one of the most important FCL operating characteristics, namely fault-reaction delay, FCLs can be classified into two groups: FCLs with inherent reaction to a fault and FCLs with a fault-reaction delay. The performed analyses have shown that saturated-core FCLs, belonging to non-semiconductor-based FCLs, have significant operational advantages over other FCL types:

i. They do not have fault reaction or post-fault recovery delays,
ii. The duration of the fault-limiting period is unlimited,
iii. They do not experience operational deterioration when limiting consecutive faults,
iv. The power dissipation during the normal regime is negligible,
v. The reliability is high as there are no active components in the current-conducting path.

The goal of this thesis is to develop a saturated-core FCL with better characteristics than currently available. Namely, the remaining design problem of state-of-the-art saturated-core FCL topologies is the large mass of magnetic material, which results in high initial cost and large size of the device.

To solve the problem of large mass and associated high cost, a novel three-leg configuration of an FCL magnetic core is proposed. The volume of magnetic material required by this core topology is reduced by applying the principle of a gap insertion in a core. This principle is typically used for non-linear inductors. It is not possible to use a gap with state-of-the-art FCL core configurations because the gap contributes not only to the ac but also to the operation of dc magnetic circuit. In such a case, it is very difficult to saturate the core and reduce the FCL's normal impedance. In our novel design, the FCL core has three legs and the arrangement of ac and dc windings in such a way that the dc flux does not flow through the middle leg of the core. The dc flux circulates only through the two outer legs. Therefore, a gap can be inserted in the middle leg without having to increase the dc mmf to saturate the core. This gap ensures smaller core size for the same voltage level.

Based on the new core design, two new FCL topologies are proposed: a single-phase single-core and a three-phase single-core FCL.

Novel single-phase topology of saturated-core FCL

The proposed single-phase FCL topology uses only one three-leg magnetic core per phase. The arrangement of the ac and dc windings provides that in each half cycle during a fault one of the two outer legs is driven out of saturation and limits the fault current. Due to the partial decoupling of the ac and dc magnetic circuits, the middle leg of the core is a part of only the ac magnetic circuit and it can, therefore, contain a gap. By employing the new FCL structure, the total weight of the FCL is reduced by approximately 70% compared to the conventional inductive FCL design. Since the gap is not in the dc magnetic circuit, the core can be saturated without increasing the number of dc turns. Three single-phase units are needed for the protection of a three phase system. The principle of operation of the novel FCL topology is proved by means of simulations and lab-scale experiments. The results agree very well.

Novel three-phase topology of saturated-core FCL

The amount of required material is further decreased by using novel three-phase single-core FCL topology. The windings from all three phases are wound on a common three-leg core, which reduces the amount of magnetic material to nearly one third of a single-phase FCL topology. Since the fluxes from three-phase windings cancel each other under normal operation, the number of dc turns which is needed to drive the core into saturation is considerably decreased. The dc windings are used only to compensate for a possible asymmetric current of the system. If this current is assumed to be one quarter of the nominal line current, the number of dc turns can be reduced by nearly a factor of four in comparison to the single-phase FCL topology. The amplitude of the induced voltage across the dc windings is proportionally diminished. To reduce the impedance during normal operation, a trifilar arrangement of the phase windings is proposed. The simulations and experimental testing showed that trifilar arrangement improves magnetic coupling between the phases and reduces the normal FCL impedance by a factor of approximately 8. To improve the inter-turn insulation, the windings are made of MV cables. The drawback of the three-phase FCL topology is that it is only capable of limiting single-phase to ground faults. Due to magnetic coupling between phase windings, the current in the faulted phase is affected by the currents from the two healthy phases increasing it to a larger value. Thus, due to the coupling between phases, the FCL limiting impedance appears to be lower than the designed value. The 'effective' fault impedance is equal to the ratio between the phase voltage of the faulted phase and the total fault current. Faults involving more than one phase are invisible to the FCL due to the cancellation of fluxes produced by the different phase windings and the core remains in saturation even during a fault. For example, in the case of a two-phase fault, the fault current flows through the both phase windings but in opposite directions which results in flux cancellation in the core. Since the core is not driven out of saturation, the FCL impedance remains low during the fault. The operation of the proposed topology is validated by simulations and testing of lab-scale demonstrators, where the results match very well.

FCL design procedure

A novel three-step modeling procedure for the design of saturated-core FCLs is introduced. The following three FCL models are developed and used in the corresponding modeling steps:

i. An analytical first-order FCL model,
ii. An FCL transient model in Saber simulator,
iii. A 3D Finite Element (FE) transient FCL model.

The initial estimate of the FCL design parameters is obtained using an analytical model in Mathcad. The model does not take into account leakage fluxes, i.e. it assumes an ideal magnetic coupling between the windings. Also, it does not accurately account for the fringing flux in a gap.

The first FCL design is obtained using a transient FCL model in Saber simulator. The model gives the waveforms of the signals and makes it easier to assess the operation of an FCL during both normal and fault regimes. The parameters of the FCL, obtained from the analytical model, can be further tuned in this modeling stage. The advantage of the FCL model in Saber is that it is relatively simple to build, in comparison to an FE model, for example, and it requires little computational time (usually less than a minute for the used models). The accuracy of the results of the Saber model is however dependent on the gap length. More specifically, this model does not fully account for leakage and fringing fluxes which can have considerable influence on the results. The fringing effect must be taken into account when the length of the gap is large relative to the width and depth of the core's leg.

In the final modeling stage, a transient 3D FE FCL model is developed in Ansys. This model takes into account both leakage and fringing flux effects and gives very accurate results. However, it requires considerably more modeling effort and computational time than the previous two models. It is therefore recommended to use the FE model as the final design step. The proposed three-step design procedure for saturated-core FCLs is very effective and accurate.

In addition to the FE model in Ansys, a model of saturated-core FCLs is built in Comsol Multiphysics as well. The development of the FE FCL model in Comsol provides insight into the mathematical background of FE modeling and allows a better understanding of how these models work. Having two FE models, in Ansys and Comsol, which are conceptually different, enables the comparison of modeling results and, therefore, the validation of the models. For these reasons the FE FCL model in Comsol Multiphysics is regarded as a valuable tool for the design of saturated-core FCLs. The results obtained from Ansys and Comsol FE FCL models match very closely, showing that both models are very accurate.

FCL modeling on two software platforms has advantages and disadvantages. It is more difficult to create 3D geometry of windings with multiple turns in Ansys than in Comsol. In Ansys, each turn has to be drawn separately, and in the case that the windings have many turns it is nearly impossible to draw them all. A modeling procedure where the number of modeled turns is lower than in reality is proposed; the electrical circuit is modified to account for this difference. Also, Ansys requires the integrated value of voltage to be applied to an FCL model as an input variable instead of its real value. The modeling of the electrical circuit in this case requires the resistive load to be replaced by a capacitive load. On the other hand, the advantage of Ansys is that it has a built-in mechanism for winding inductance computation and the possibility of modeling a full electrical circuit. Comsol is more 'mathematically oriented' software and requires equations to be inserted for calculation of both winding inductance and electrical circuit parameters. All modeling issues are solved in both 2D and 3D domains and guidelines for the development of both

FE models are presented.

Furhter improvement of an FCL design

Using an FE FCL model in Ansys, the design of the proposed FCL topologies is further improved from the point of view of the required volume of magnetic material. Based on results from the analytical and Saber FCL models, the cross-section of the core's middle leg has to be two times larger than that of the outer leg. However, FE simulations showed that the cross-section of the middle leg can be reduced by a factor of five without significantly impairing the FCL's fault limiting ability. In the analysis performed on three-phase single-core FCL design, the volume of magnetic material was reduced by 30.4% while the fault current was increased by 40% (from 4.4 p.u. to 6.1 p.u.). Such an increase of the fault current value is insignificant while the FCL weight is considerably reduced.

Full-scale FCL prototype

On the initiative of industry partners, a full-scale 10 kV prototype of a three-phase single-core FCL has been designed and tested to prove that the FCL is able to protect real power grids. Testing of the FCL prototype was done in two steps. In the first, low-voltage stage, the FCL was tested for all fault scenarios at 400 V. The obtained results showed that the FCL limits single-phase to ground faults and that it does not react to faults involving more than one phase. The agreement with 3D FE simulation results was very good. During a fault period, induced voltage in the dc windings resulted in the large value of the induced current in the dc circuit. The dc electrical circuit was modified to interrupt the induced current, which would otherwise reduce the FCL limiting factor at 10 kV operation.

As the next step, a full-voltage testing is performed at laboratory of KEMA. In four testing stages, the prospective fault current was increased in steps from 10 kA to 40 kA. In each stage, the FCL successfully limited the fault current to an expected steady-state value of approximately 2 kA. The faults involving multiple phases were not limited. The experimental measurements confirmed, therefore, the simulation results and proved that the proposed FCL topology can protect the real power grids from single-phase fault currents. It can also be concluded that the developed 3D FE FCL model in Ansys can be used for design of saturated-core FCLs.

Interaction between FCLs and power grid

The issues regarding the installation of the FCL in power systems are addressed in the end of this thesis, where the following topics are considered: the positioning of FCLs in power systems, the interaction between FCLs and existing protective schemes, the interaction between FCLs and circuit breakers (CBs) and the influence of FCLs on power quality and system stability.

Some of these aspects have been extensively investigated in literature in the last decade and an overview of the available results and conclusions is provided. In the analyses, two principal types of FCLs are considered, reactive and resistive.

Regarding the positioning, it is important to install FCLs in the incoming feeders so that the contribution of each to a fault is limited. Based on this principle, the number of FCLs that are needed can be determined for each network case.

The influence of FCL installation on four protection schemes (over-current, differential, distance and directional protection) is also analyzed in this thesis. Since the FCLs change the system short-circuit impedance and, therefore, the fault current, the operation of over-current, distance and differential protection low can be affected. In this case, the relay's pick-up setting must be readjusted. The FCL fault impedance becomes the dominant impedance of the faulted line and the magnitude of the current is not a function of the fault distance from the source. Current- and time-grading protective schemes become ineffective in this situation. The operation of directional protection should not be affected, but readjustment of the pick-up settings might be required to provide maximal relay torque during a fault.

By limiting the fault current, FCLs are expected to reduce the stress imposed on CBs during opening action. However, the installation of inductive FCLs could increase the rate of rise of recovery voltage across CBs and cause their failure. RRRV depends on the value of the stray capacitance of inductive FCLs. Installation of an additional capacitor in parallel to the inductive FCL is a way to reduce RRRV.

Both power quality and system stability can be improved by installing FCLs. Voltage sags are considerably reduced by limiting fault currents. The transient stability of synchronous and induction generators is improved. The FCLs increase the electrical torque during a fault and therefore reduce the acceleration of generators. Excessive power consumption of resistive FCLs could result in the undesired fast braking of the generator's rotor. In such a case, the oscillation of the rotor angular velocity, after the fault is cleared, could be even larger when an FCL is used. Therefore, the FCL resistance has to be within a specific range which will ensure improved transient performance of the system. The inductive FCLs either improve the transient stability of the system or have no influence on it, depending on the configuration of the system and locations of the fault and the FCL.

While determining the cost-effectiveness as a power system protection solution, the positive effects that the FCLs have on power quality and system stability should be included.

7.2 Recommendations for future work

The following issues could be addressed in the future research:

i. The proposed three-phase single-core FCL topology limits only single-phase to ground faults. A design improvement that enables limitation of all types of faults would be valuable. This could be achieved by using a different number of turns on individual phase windings. As a result, during double-phase faults, for example, the phase windings on one core's leg would have a different mmf and the total flux change in that leg would be different from zero. Thus, the core could be driven out of saturation which would result in the limitation of fault current. The possible resulting operational setbacks, such as increased FCL normal impedance due to weakened magnetic coupling between the phases, have to be considered. In this situation, the cores will have to be driven deeper into saturation in the normal regime, which requires an increased number of dc turns. The value of the induced voltage in the dc winding will increase accordingly.

ii. The proposed analytical FCL model can be improved. A better analytical calculation of the fringing effect for larger gap lengths would be valuable. Expressions for the calculation of the fringing effect may be obtained by fitting the results from FE simulations. This implies that the FCL design procedure needs only two steps, and the analytical design parameters can be directly used in an FE FCL model. The modeling would be faster and easier.

iii. The FE FCL models give as output the most important variables which characterize FCL operation during both the normal and fault regimes: variation of the FCL impedance and, therefore, a waveform of the line current. FE FCL models can be further improved to simulate other important aspects of FCL operation:

a. To calculate power dissipation in a magnetic core and windings,

b. To simulate the required capacity of a cooling system which would prevent overheating of the windings; the model could determine whether the windings should be cooled by a passive or active cooling systems and how large the spacing between the layers of windings' turns should be.

c. To calculate the electromagnetic forces on the windings during a fault period. In this way it could be determined whether the windings could be damaged during a fault in the case that the fault current is not limited. This model could be used for the design of the proposed three-phase FCL topology, which does not limit multiple-phase faults and is, therefore, exposed to large electromagnetic forces during these faults,

d. To calculate the induced currents and voltages in a dc circuit during a fault, to give better insight in the overall operation of the designed FCL.

iv. To increase the effective length of a gap, the gap could be divided into several smaller gaps and distributed along the length of the middle leg. Such a distributed gap could enable further reduction of the core size. This concept can be investigated through FE simulations.

v. The optimization of an FCL design can be performed. The optimization criterion could be the minimization of both the required volume of FCL material and losses in windings with the constraint that an FCL inductance remains unchanged. The optimization could be done using 3D FE model in Comsol and appropriate optimization algorithm realized in Matlab. In the analysis, the following FCL parameters can be varied: the number of ac turns, a gap length and the cross-sections of the core's middle and outer legs.

Appendix A

OVERVIEW OF SOLID-STATE AND HYBRID FCL TOPOLOGIES

Chapter 2 introduces the main configuration for each type of solid-state FCLs. A number of additional topologies with certain design differences are proposed in literature. These additional FCL topologies are described below.

A.1 Solid-state FCL topologies

Bridge-type FCL topologies

The typical FCL bridge topology (see Figure 2-13) can be designed without a dc biasing source, as shown in Figure A-1a [Hosh 01]. When a load is connected, a line current will flow through an inductor for couple of cycles before the level of a dc current is established. The dc current flows through the inductor and semiconductors. The duration of the transient period is a function of the FCL time constant L_{FCL}/R_{FCL}, where R_{FCL} is the resistance of the diodes and inductor. In the steady-state operation the ac current flows through the semiconductors, see Figure A-1a.

If a load is increased, an undesired drop of the load voltage occurs, see Figure A-1b. Namely, during each half-cycle, the inductor is inserted in the line when the load current exceeds the value of the FCL dc current. This transition period ends once the new sufficiently-high level of the dc current is established.

Thyristors Th_1 and Th_2 are fired every half-cycle during both normal and fault regimes. The line current can be interrupted by leaving the thyristors in off-state. Failure of the control circuit would result in the interruption of the load current.

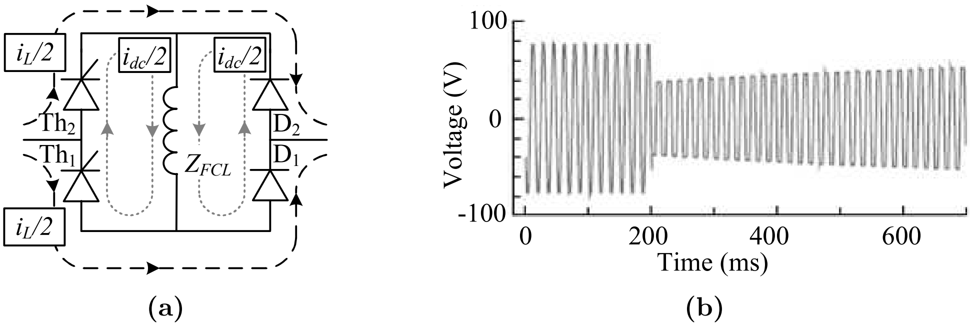

Figure A-1: Active bridge FCL without a dc bias current source: (a) Topology; (b) Drop of a load voltage when a load is increased.

Design of a fully-controllable bridge without a dc bias source is presented in [Boen 02]. A bias dc current in the bridge can be established by applying a proper thyristor control. This FCL topology is known as a fault current controller (FCC), since the desired value of limited fault current can be adjusted by changing the firing angle of the thyristors.

Bridge-type FCL with non-inductive reactor The FCL employs two coils, triggering and main, with the same number of turns. The coils are magnetically coupled in a way that their fluxes counteract each other during normal operation, see Figure A-2 [Sali 04]. The resulting reactance of the FCL is very low. The load current is evenly shared between the two coils, resulting in equal associated fluxes. The fundamental difference from the FCL with inductive reactor is that a load current flows through the bridge coils, i.e. at any time only two semiconductors are conducting.

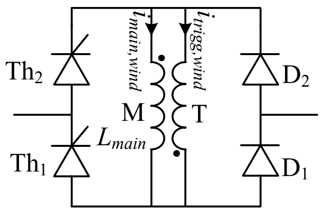

Figure A-2: Bridge-type FCL with a non-inductive reactor [Sali 04].

The triggering coil is made of superconducting (SC) material. When a load current increases above the given threshold, this coil quenches and forces most of the load current through the main coil. The reactance of the main coil increases, due to unequal fluxes and limits the fault current.

To reduce the recovery time of the SC triggering coil, the FCL configuration in Figure A-3 is proposed [Sali 04]. Both coils are installed in the separate bridge rectifiers. This enables the triggering coil to be isolated, i.e. cut off from the system, as soon as the S/N transition takes place. In this way, the amount of dissipated energy in the superconductor is reduced and its recovery from normal to superconducting state requires less time.

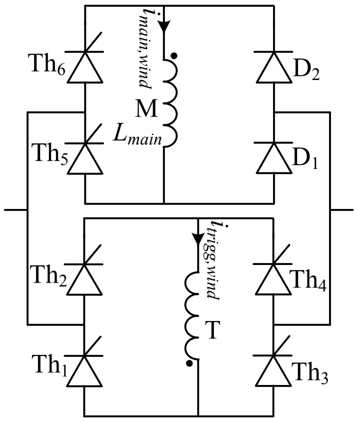

Figure A-3: FCL with separated triggering and main coils [Sali 04].

Magnetic coupling between two coils imposes the constraint that all four switches in the auxiliary bridge have to be controllable in order to interrupt the current flow through the triggering coil. The obvious drawback of this topology is that an increased number of semiconductors is used, which increases the price of the FCL and reduces its reliability.

An FCL with a bypass inductor The triggering coil T is placed in the bridge and conducts a half of the line current during normal operation. The main coil is placed as a bypass inductor and conducts the other half of the line current [Gang 04; Zhen 03]. Due to magnetic coupling between the coils (see Figure A-4a), the total reactance introduced in the line is very low. The voltage drop is equal to two times the voltage drop across the thyristor. After a fault is incepted, the triggering coil quenches and the FCL impedance increases. By turning off the semiconductors, the current through the SC coil is interrupted, which enables the faster cooling and recovery of the SC material.

A voltage-surge arrester (varistor) is usually placed in parallel to the inductor M to protect the bridge from over-voltages. An FCL topology with only two active switches and two diodes can be used. However, due to magnetic coupling between the coils, the current through the triggering coil cannot be interrupted with such an arrangement.

The topology presented in Figure A-4bis designed for higher voltage applications [Gang 04]. The transformer lowers the voltage imposed on the bridge rectifier and enables usage of only four switches.

Bridge-type FCL using one active switch To minimize the number of active switches and simplify the control algorithm, the topology presented in Figure A-5 is proposed [Noe 07b]. During normal regime the IGCT (Integrated Gate Commutated Thyristor) is continuously gated and conducts the normal line current. Three active switches are always connected in series, which produces a larger voltage drop than with

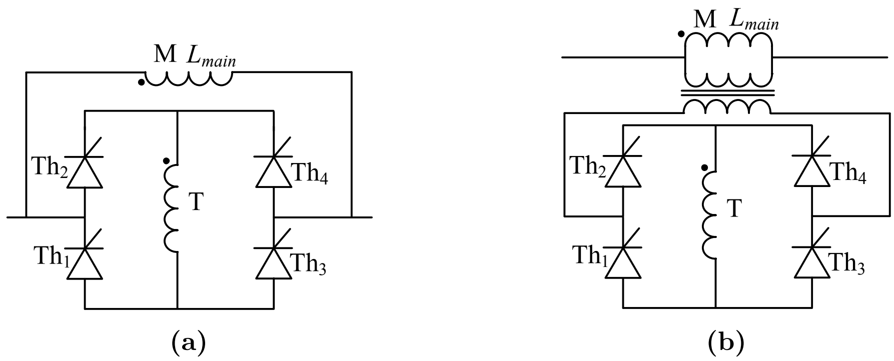

Figure A-4: A bridge-type FCL with a bypass inductor [Gang 04]: (a) For low-voltage application; (b) For high-voltage application.

the previous topologies. Upon fault inception, the IGCT is turned off and thyristor Th is activated, diverting the fault current onto the limiting impedance R_{FCL}. After the first zero-crossing of the fault current, thyristor Th will be turned off and the fault current will be interrupted.

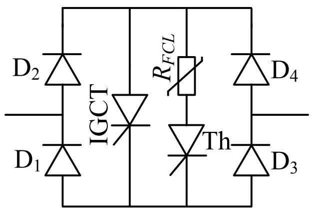

Figure A-5: The FCL bridge topology with one active switch [Noe 07b].

However, the flow of the limited fault-current can be maintained, allowing it to flow through the limiting impedance R_{FCL}. This can be achieved by either activating thyristor Th after each zero-crossing of the current or by phase angle control of the IGCT. In the latter case, the resulting waveform of the limited fault-current can be highly distorted.

Similar FCL topologies can be designed using other semiconductor switches, such as SPETO (self-powered emitter turn-off thyristor) [Zhan 04]. The SPETO comprises a self-power generation unit and does not require external power supply; it has built-in current, voltage and temperature sensors [Bin 03b]. The operation and control of the FCL comprising SPETO is simplified in comparison to that with the IGCT [Bin 06]. The FCL topology is presented in Figure A-6. More switches can be connected in series for higher-voltage applications.

Gate-commutated thyristor (GCT) semiconductors can be turned off without a snubber circuit, which simplifies the design of the FCL. Employment of a varistor in parallel to the switch would be sufficient to reduce voltage peaks during the fault transients. Several topologies, with a different number of active and passive switches, can be found in

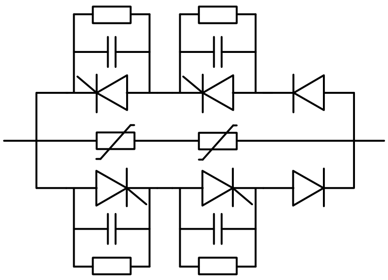

Figure A-6: SPETO-based fault current limiter.

[Meye 04b].

By combining different types of power semiconductors, their benefits can be combined for better performance of the FCL [Hann 03]. By placing fully-controllable GTO (Gate Turn Off) switches in the main conducting path, instead of thyristors, the fault current can be interrupted at any moment. After fault inception the GTOs are turned off and the fault current is transferred to the auxiliary branch with thyristors. Thyristors are capable of conducting larger fault currents than GTOs (see Figure A-7).

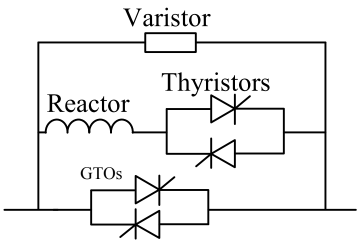

Figure A-7: FCL topology using both GTOs and thyristors [Hann 03].

Fault current controller with two thyristors The FCL topology is presented in Figure A-8 [Otet 04]. It has two thyristors and two inductors. During normal operation, both thyristor Th_1 and Th_2 are conducting currents I_{Th1} and I_{Th2}, respectively. These currents are equal to the vector sum of the line current and currents I_{wind1} and I_{wind2}, respectively. The inductors' currents are constant (the time constant is large) and equal to each other:

$$I_{wind1} = I_{wind2} = const > |i_L| \,. \tag{A.1}$$

Since the line current is lower than currents of the inductors L_1 and L_2, both thyristors are always forwardly biased and the total voltage drop (losses) across the FCL is equal to the sum of voltage drops across thyristors Th_1 and Th_2.

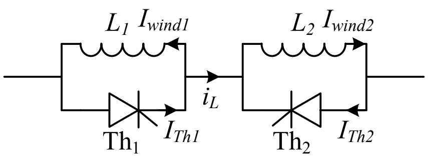

Figure A-8: Fault current controller (FCC) with two thyristors [Otet 04].

In the case of a fault, the fault current exceeds the value of the dc current of the inductor and turns off the corresponding thyristor. In this way, the limiting impedance is inserted in the line and limits the fault current. The magnitude of the fault current can be controlled by changing the phase angle of the thyristors.

An FCL with a discharging capacitor

An FCL with one discharging capacitor To simplify the design of an FCL with a discharging capacitor, one precharged capacitor can be used instead of two. The capacitor is placed in the bridge rectifier [Meye 04a], as shown in Figure A-9. By activating two of four active semiconductors in the bridge, the capacitor C can be discharged in the desired direction (opposite to the fault current).

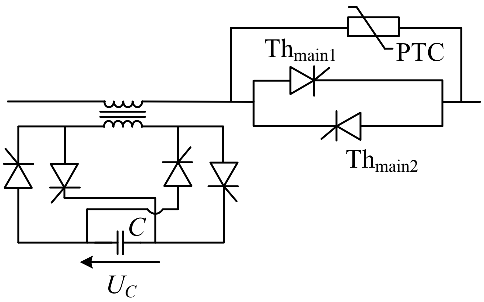

Figure A-9: FCL with one discharging capacitor [Meye 04a].

The fault current is transferred onto a PTC (Positive Temperature Coefficient) resistor and limited. The disadvantage of this topology is that it contains a transformer and more active switches, which decrease its reliability.

A.2 Hybrid FCL

The FCL design presented in Figure A-10 employs a mechanical switch in each of the three branches. Its design is similar to the one presented in Figure 2-17.

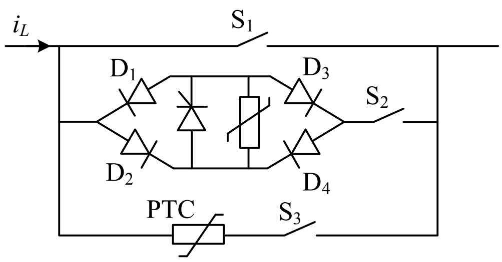

Figure A-10: Hybrid FCL with three mechanical switches [Noe 07b].

The operating principle is the same. A difference is that the middle branch contains only one active switch, which simplifies the control circuit. By opening the mechanical switch in the third branch S_3, the limited fault current can be interrupted [Noe 07b].

Appendix B

PROJECTS AND PLANS FOR FCL DEVELOPMENT AND TESTING

This appendix gives an overview of the worldwide experiences, on-going projects and future plans regarding the development and testing of the different FCL technologies.

The first part of the appendix is a tabular presentation of major achievements and results. The overview is based on the activities of separate companies or institutions and data are sorted in alphabetical order based on the company name, grouping all the material regarding different FCL types from the same company.

The second part is a textual overview of the data presented in the table, but with additional pieces of information and broader explanations. The data are arranged in alphabetical order, but on the basis of the FCL type. In this way, the activities and achievements of different companies regarding the same type of the FCL are placed together.

B.1 Tabular overview - sorted based on a company name

Table B-1: FCL projects and future plans.

FCL type	**Ref**	**Country /Year**	**Rating** V_{rms}	**Rating** A_{rms}	**Ph.**	**Material**	**Plans/Comments**	**Field Test**
				ABB				
Liquid metal	[Noe 08]	'06	1k	2k	1		Technology in early development.	No
	[Niay 04; Niay 06; Scho; Schm 06]	CH/'04		1k	1		Investigation of arcless current commutation.	No
Resistive SC	[Paul 01]	CH/'01	8k	0.2k	1	Bi-2212		No
	[Chen 02; Xin 07]	CH/'02	8k	0.8k	1	Bi-2212		No
	[Decr 03]	CH/'03	0.3k	0.001k	1	YBCO/Au	Uniformed overheating of SC.	No
	[Chen 04]	'04	Patent: Superconducting fault current limiter, US $6,819,536B2$					
Shielded iron core	[Leun 00]	CH/'93	0.84k	0.13k		Bi-2212		
	[Chen 97; Hass 04; Noe 07a; Paul 98]	CH/'96	10.5k	0.07k	3	Bi-2212	Abandoned.	Yes
	[Wtec]	CH	0.48k	$8k_{fault}$		Bi-2212	100 kW design.	Yes
		CH			3	Bi-2212	1.2 MW.	In op.
				Areva				
	[Noe 08]	fr/'05	3.8k	0.5k			No publications found.	

Saturated-core	[Chon; Raso 06]	fr/'06	0.4k	0.25k	1		A new principle: use of a demagnetized magnet in an air gap. Demonstrator under construction.	No
China								
Bridge SC	[Hui 06; Wang 06]	'06	10.5k	1.5k	3	Bi-2223	Presents design and testing of coils. Testing was successful.	Yes
Saturated-core		'07	0.22k	0.03k	3	Bi-2223	Plan: 35 kV/1.5 kA.	Plan
	[Hong 09; Xin 09]	'09	35k	1.5k	3	Bi-2223	Installed at Puji substation. Operation in normal regime satisfactory. Fault operation not yet verified.	Yes
	[Noe 09]		220k		3	Bi-2223	Plan for 2010, 300 MVA.	Plan
CRIEPI, TEPCO, Toshiba								
Bridge SC	[Koya 04; Ohta 04; Saka 06; Ueda 03; Yasu 05; Yaza 03; Yaza 04a; Yaza 05]	jp/'00-'05	66k	0.75k		Bi-2223		No
	[Yaza 01]	jp/'01	6.6k	0.36k	1	Bi-2223	Investigate feasibility for HV.	No

	[Yaza 04b]	jp/'04				Bi-2223	Mechanical performance of HTS coil tested: no deterioration after extensive loading with 70% of the critical hoop stress.	
	[Hass 04]	jp/'09	67k	3k	3	Bi-2223		
	[Tayl 05]		Test of 500 kV planned for 2010.					
Flat-type shielded iron core	[Maru 07; Mats 05]	jp/'05				YBCO Bi-2223	YBCO has higher impedance than Bi-2223. It can be scaled up.	
Resistive SC	[Hass 04; Taka 01]	jp/'01	0.2k	0.07k	3	YBCO	Super-ACE project.	No
			0.4k	0.07k	1	YBCO	Super-ACE project.	No
	[Shim 02]	jp/'02	0.2k	1k		YBCO	Super-ACE project.	No
	[Noe 07a]	jp/'04	1k	0.04k	1	YBCO	Super-ACE project.	No
	[Ueda 03; Yasu 05]	jp/'05	6.6k	0.1k	3	YBCO	Super-ACE project.	No
	[Noe 09]	jp/'08	6.6k	0.08k	3	YBCO	Super-ACE project.	
	[Koya 08]	jp/'08	6.6k	0.6k	1	YBCO	Super-ACE project.	No
	[Hass 04]	jp/'09	6.6k	2k		YBCO	Super-ACE project. Test planned for 2009.	
Shielded iron core	[Ichi 95; Kado 97]	jp/'97	6.6k	0.4k		Bi-2212		No
	[Ichi 03a; Ichi 03b]	jp/'03				Bi-2223	J_C increased to 5800 and 6000 A/cm^2 at 77 K.	
DOE, Powell, EPRI, SuperPower, American SuperConductor								

Matrix SC		US/'04	8.66k	25.6k	1	Bi-2212	Abandoned, initial plan 138 kV. SPI program.	No
Resistive SC	[Noe 08]	US/'06	1.2k		1			
	[Webe 08; Xie 07]	US/'07	Development of 2^{nd} generation HTS: the results are promising for practical use of SFCLs. Target is 138 kV. Alpha prototype will be built in 2009.					
	[Juan 08]	US/'08	Improvements of recovery under load (RUL) performance reported.					
Semiconductor based	[Noe 07a]	US/'02	15k	1.2k	3		Advancements in SiC technology expected to improve FCL performance.	Yes
	[Noe 08; Noe 07a]	US/'04 ('06)	8k	1.2k	3		Target 138 kV.	No
ERSE								
Resistive SC	[Gril 05]	it/'05				Bi-2223	Analysis of windings geometrical configuration for losses minimization. Limsat project.	
	[Mart 05]	it/'05	0.5k	0.08k	1	Bi-2223	I_{pros}=4.5 kA, I_{lim}=794 A, planned 120 kVA, 3-phase.	No
	[Mart 06]	it/'06	2k	0.15k	1	Bi-2223	I_{pros}=15 kA, I_{lim}=800 – 2200 A, planned 3ph demonstrator.	No
	[Mart 07]	it/'07	3.2k	0.2k	3	Bi-2223	I_{pros}=10.9 kA$_{rms}$, I_{lim}=2.1 kA$_{rms}$	No
		it/'07	0.5k	0.3k	3	Bi-2223	I_{pros}=10.4 kA$_{rms}$, I_{lim}=2.3 kA$_{rms}$	Yes
	[Dale 07]	it/'07	0.3k		3	MgB_2	I_{pros}=3.5 kA, I_{lim}=1.14 kA@4.2 K and @27 K	No
	[Nard 07]	it/'07	MgB_2 exhibits significant critical currents, up to 715 A @4.2 K. Applicable for both AC and DC applications.					

	[Gril 09]	it/'09	New method for computation of losses in YBCO CC based on FE model: 1D model much faster than 2D.					
	[Noe 09]	it/'09	9k	0.25k	3	Bi-2223	Installation and testing in 2010.	Plan
	[Mart 09]	it/'09	9k	1k	3	YBCO CC	FCL in incoming feeder, installation and testing in 2010.	Plan
Europian Superpoli project								
Resistive SC	[Leht 04; Usos 03; Verh 99]	'99/'03	20k	2k	1	Bi-2212, YBCO CC	1 GVA range power link, 200 m with 20 kV/28 kA nominal rating.	No
	[Tixa 07]	'07	Homogeneous quench of YBCO CC (2 m) when operated closer to critical temperature.					
	[Usos 07]	'07	Developed CC up to 100 m long, with good mechanical stability and improved critical current homogeneity.					
	[Rost 07]	'07	Presents losses computational method for CC, verified on 0.5 m sample. Goal 30 m, 10 V/1 A cable.					
KEPRI								
Reactive SC	[Min 05; Min 04; Seun 04]	kr/'04-'05	6.6k	0.2k	3	Bi-2223	Fabrication and testing of DC reactor for 6.6 kV/0.2 kA. 1^{st} ph DAPAS.	
	[Youn 06]	kr/'06	6.6k	0.2k	3	Bi-2223	1^{st} ph DAPAS.	No
	[Hyou 08]	kr/'08	22.9k	0.63k	1	YBCO CC	2^{nd} ph DAPAS, plan 154kV.	No
	[Noe 07a]	kr/'04	3.8k	0.2k	3	YBCO film	1^{st} ph DAPAS.	
	[Ok B 05]	kr/'05	6.6k	0.2k	3	YBCO film	1^{st} ph DAPAS.	No

Resistive SC	[Sim 07]	kr/’07	22.9k	0.6k	1	YBCO film	2^{nd} ph DAPAS, plan 154 kV.	No
	[Noe 09]	kr/’10	22.9k	3k	3	YBCO tape	2^{nd} ph DAPAS, testing planned for 2010.	Plan
	[Phas 04; Mati 06]	kr	DAPAS: Both resistive and inductive 22.9 kV/0.63 kA for 2007 (2^{nd} phase). By 2010, 154 kV/2 kA for inductive FCL.					
	[Hyo 01]	kr/’01	S/N transition of YBCO thin film superconductors: multiple operations without degradation.					
	[Hye 02]	kr/’02	The time dependency of the YBCO thin film resistance is investigated.					
	[Ok B 03]	kr/’03	Shunt-assisted quench method for simultaneous quench of YBCO thin film.					
	[Min 06]	kr/’06	Proved feasibility of YBCO CC application for current limitation.					
	[Kang 06]	kr/’06	Production process of 1 m long YBCO CC developed.					
	[Kim 07]	kr/’07	Theoretical prediction of quench for BSCCO-2212 bulk coil.					
	[Oh 09]	kr/’09	Improvements of fabrication of YBCO CC: reactive co-evaporation technique is used. Length of SC limited to 100 m.					
Nexans SC, ACCEL								
Fault current controller SC	[Juen 03]	DE/’02	Patent: Small model tested, small-scale demonstrator planned for 2007.					
	[Juen 08]	DE/’08	Patent: Modified fault current controller.					
Resistive SC	[Elsc 03]	DE/’03	Developed bifilar windings from Bi-2212 tubes, for 10 MVA SCFCL.					
	[Bock 05; Kreu 05; Neum 06]	DE/’04	10k		3	Bi-2212	First resistive SC test worldwide, 10 MVA, CURL10.	Yes
	[Noe 08]	DE/’05	6.9k	0.6k	3	Bi-2212	CURL10 project. Plan CURL100.	Yes
	[Elsc 06]	DE/’06	Resistive shunt concept not used for higher voltages. Instead, magnetic field assisted quench applied.					

	[Noe 08]	DE/’06	0.12k	1.8k	1	Bi-2212	Plan 110 kV FCL, CURL100.	No
	[Noe 07a]	DE/’07	Conceptual design of 110 kV SCFCL presented.					
	[Noe 08]	DE/’07	14.4k	0.8k	1	Bi-2212	CURL10	
	[Noe 08]	DE/’08	6.9k	0.8k	3	Bi-2212	CURL10	Yes
	[Domm 10; Noe 09]	DE/’09	12k	0.1k	3	Bi-2212	CURL10	Yes
		DE/’09	12k	0.8k	3	Bi-2212	CURL10	
Rolls Roys								
Resistive SC	[Tekl 99]	’99	19k	0.4k	1	Bi-2212	Concept uses magnetic field as a triggering mechanism.	No
	[Noe 09; Noe 07a]	’06	6.6k	0.4k		MgB_2	Private communication. 11.5 kV/0.4 kA FCL design planned.	
	[Lin 07; Majo 07]	’07	MgB_2 quenches when exposed to over-currents - it can be used for current limitation.					
Siemens, AMSC								
DC res. SC	[Krae 05]	DE/’05	0.86k	1k		YBCO		
Resistive SC	[Utz 97]	DE/’97	Developed technique for YBCO film deposition on very large areas					
	[Grom 99]	DE/’99	0.75k	0.13k		YBCO	Design of 1 MVA	No
	[Hass 04; Krae 03; Noe 07a]	DE/’00	4.2k (7.2k)	0.1k	3	YBCO		No
	[Noe 09]	DE/’07	7.5k	0.3k	1	YBCO		No
	[Libr; Noe 08; Noe 09]	DE/’07	13k	0.3k	1	YBCO	66 kV planned for ’11; 115 kV/1.2 kA 3φ FCL planned for ’12.	No

	[Neum 07; Schm 07]	DE/'07	Rapid cooling, fast and uniform switching shown for YBCO. Successful 120 kVA demonstrator built.					
Semiconductor based	[Noe 07a]	DE/'04	6.9k		3		Designed FCL for 25 MVA.	
Southern California Edison								
Bridge SC	[Leun 97]	US/'97	2.4k	0.15k	1	Bi-2223	Planned 15 kV/1.2 kA design.	No
	[Leun 00]	US/'99	12.5k	1.2k	1	Bi-2223	Flash to ground experienced in auxiliary equipment.	No
	[Wayn 03]	US/'03	13.7k	1.2k	1	Bi-2223		No
University Erlangen/Nuremberg								
Semiconductor based	[Rube 08; Rube 07a; Rube 07b]	DE/'07	0.25k	4.8k	3			No
Zenergy Power								
Saturated-core	[Mari 09]	US/'09	13.8k		3	Bi-2223	Fault current restrained by 20% at 20 kA. Fault operation up to 82-cycles and RUL recovery. Consecutive faults restrained.	
	[Ener; Mari 09; Noe 09]	US/'09	12k (15k)	1.1k	3	Bi-2223	Normal impedance less than 1%. 25 kA fault current restrained by 45%.	
	[Marc 09; Mari 09]	US/'09	Planned installation of 26 kV FCL in the grid by 2010. 138 kV/1.2 kA designed, testing planned for 2011. The grid test expected in 2012.					

B.2 Textual overview - sorted based on an FCL type

Bridge-type superconducting FCL (SCFCL)

Design and successful testing of superconducting coils for the FCL prototype 10.5 kV/1.5 kA 3φ, made of Bi-2223/Ag, is presented in 2006 [Wang 06]. The complete FCL is installed and tested in the real grid (substation Loudi) in August 2005. Three-phase-to-ground short-circuit testing in the grid is reported in [Hui 06], where the prospective fault current of 3.5 kA is restrained to 635 A. The FCL is installed in a 110 kV/10.5 kV substation with a 1 MVA load.

A reactive-type SFCL, based on Bi-2223 tape wiring reactor, is developed and tested. Three-phase 6.6 kV/200 A testing is successfully carried out in 2006 [Youn 06]. Design and testing of the DC reactor, used for the reactive FCL fabrication, is presented in [Noe 07a; Min 05; Min 04; Seun 04]. The first phase of the DAPAS program is completed. In 2008, a reactive YBCO CC SCFCL, rated at 22.9 kV/630 A, is designed and tested [Hyou 08]. The prospective fault current of 30 kA$_{rms}$ is successfully restrained to 3.6 kA$_{rms}$. It is reported as the first YBCO CC SFCL prototype in the world. The final goal is to achieve transmission level 154 kV FCL.

Successful tests on a 6.6 kV/36 A FCL are carried out in 2000 [Yaza 01]. The design will be scaled for higher voltages and currents, using parallel and series connection of the tested element. From 2000 to 2004 a 66 kV/750 A SC FCL magnet, comprising six Bi-2223 coils rated at 66 kV/125 A, is designed and tested [Ohta 04; Yaza 03; Yaza 04a; Yaza 05]. Current flowing tests of HTS coils were successfully carried out at the uniform temperatures of 71 K and 65 K sub-cooled nitrogen - normal current test. Fatigue tests of HTS coil were performed in 2004, where the coil did not deteriorate after 104 times loading of 70% of the critical hoop stress at 4.2 K [Yaza 05; Yaza 04b]. Successful short-circuit test of the completed FCL (magnet and bridge rectifier) are reported in 2006 [Yaza 06]. For 2009, test of a 66 kV/3 kA FCL is planned [Hass 04]. Plan of 500 kV FCL testing is reported in [Tayl 05]. No other reports found.

A test on a 2.4 kV/150 A FCL demonstrator, using Bi-2223 coil, is performed in 1997 [Leun 97]; testing of 15 kV/1.2 kA, with a prospective fault current of 20 kA, is announced for 1998. The FCL rated at 12.47 kV/1.2 kA is tested in 1999, where the flush to ground was experienced in an auxiliary piece of equipment [Leun 00]. Planned 3φ tests are not done. In 2003 the successful tests of 13.7 kV/1.2 kA single-phase FCL are reported [Wayn 03]. The prototype comprised thyristors. The device is called fault current controller (FCC) due to its ability to control the peak of the fault current. No further reports found.

Liquid-metal FCL

In 2006 a single-phase test is performed, with FCL ratings 1 kV/2 kA [Noe 08]. The technology is in the early stage of development.

A new technique of arcless current braking is introduced and investigated [Niay 04; Niay 06; Scho; Schm 06]. No further reports or plans found.

Resistive SFCL

In 2001, a test of 8 kV/0.2 kA is performed, where the prospective fault current of 13.2 kA is limited to 4.3 kA [Paul 01]. Due to over-heating the current was reduced to 1 kA. The following year, a successful test of 8 kV/0.8 kA FCL is reported (based on Bi-2212); the prospective fault current of 20 kA was reduced to 10.6 kA - the first peak and 3.2 kA - the follow current [Chen 02]. New testing of SC materials are reported in 2003 [Decr 03]. Uniform over-heating of YBCO/Au is achieved: initial dissipative length is split into many dissipative regions which avoids localization of the power. No further reports found. A patent is applied for in 2004 [Chen 04].

In 2001 a successful FCL test is conducted, rated at 400 V/70 A. YBCO film material is used. The test proved that the device reacts fast enough and can be applied to real power systems [Hass 04; Taka 01]. In 2004, YBCO-based FCL 1 kV/40 A is successfully tested [Noe 07a]. No other reports found. Mitsubishi Electric Corporation developed an FCL 200 V/1 kA 1φ based on YBCO films [Shim 02]. It is successfully tested in 2004 [Noe 07a].

In 2005, three-phase current limiting modules, made of YBCO thin films, are successfully tested at 6.6 kV/100 A, where the maximum fault current of 3.5 kA is reduced to 580 A [Ueda 03; Yasu 05]. Additional tests of the 3φ YBCO FCL, rated at 6.6 kV/75 A, are reported in 2008 [Noe 09]. For 2007, a test of 6.6 kV/600 A FCL demonstrator is planned, using YBCO CC [Noe 07a]. Successful testing is reported in 2008 [Koya 08]. The fault current is restrained from 10.4 kA to 2.1 kA. Further investigation has to be done regarding 'mechanisms of local voltage generation within the tape'. The test of 6.6 kV/2 kA YBCO-based FCL is planned for 2009 [Hass 04]. Successful testing of 6.6 kV FCL is reported in 2009 [Yaza 09]. The prospective fault current of 1.56 kA is restrained to 840 A. As the next step, on-site grid tests will be conducted.

A single-phase test is done on a 1.2 kV/NA device in 2006 [Noe 08]. No further publications found. A purely resistive FCL, with the goal 138 kV, is pursued [Xing 05]. For this purpose, 2G SC wire is tested and promising results are reported: superior electromechanical performance, large surface area available for cooling and availability in the long term [Xie 07]. The alpha prototype at 138 kV, planned for 2009 [Webe 08], can be designed using this SC. Achievements regarding recovery under load (RUL) are reported in 2008 [Juan 08]: connectors between copper and SC are improved and variables influencing RUL are studied.

FE analysis of the influence of magnetic field and geometrical configuration on loss behavior of a 200 kV FCL prototype composed of Bi-2223/Ag tapes is presented in [Gril 05]. The goal is to find the configuration with the lowest losses. It is found that the gap between the tapes has to be less than 0.2 mm in order to minimize the flux penetration. Bifilar windings reduce the losses in the central part of the device.

In 2005, a successful testing of 500 V/80 A 1φ FCL made of Bi-2223 is reported [Mart 05]. The prospective fault current of 4.5 kA is reduced to $300 - 800$ A, depending on the value of applied voltage. A single-phase $0.1 - 2$ kV/155 A FCL, made of Bi-2223, is tested in 2006 [Mart 06]. The prospective current of 15 kA is successfully restrained to $800 - 2200$ A. The FCL showed good limiting capability and no degradation of material.

A 1.2 MVA 3φ FCL demonstrator, made of Bi-2223, is designed and tested in 2007 [Mart 07]. A short-circuit test is done at voltage 3.2 kV and normal current 304 A_{peak}. The fault current is restrained from 15440 A_{peak} to 3045 A_{peak}. As the next step, a 400 V/200 kVA 3φ FCL demonstrator is built and tested at the voltage of 522 V. The fault current is restrained from 10.45 kA to 2.3 kA. A 3-phase SFCL prototype is ready to be field-tested at a test facility for DGs. It will be tested during a 3-month period [Mart 07]. FCLs rated at 9 kV/250 A 3φ and 9 kV/1 kA 3φ, made of Bi-2223 tape and YBCO tape respectively, are planned to be designed by 2010 and tested in the field [Noe 09].

A 500 kVA 3φ demonstrator is built using MgB_2 superconductor. Short-circuit tests show excellent current limitation capability of MgB_2, even after repeated faults. Normal voltage drop is negligible. In the case of two successive faults, the recovery time is prolonged. Tests are done for 300 V_{rms}, where the fault current is restrained from 5 kA_{peak} to 1620 A_{peak}. Tests are done at both 4.2 K (liquid helium) and 27 K (liquid neon), where the limitation capacity at 4.2 K was much better: 3.7 in comparison to 2.7 at 27 K. A 500 kVA single-phase MgB_2-based FCL passes all dc electrical testing at 4.2 K and will be exposed to short-circuit tests in liquid neon in 2007 [Dale 07]. The winding made of MgB_2 experience critical current up to 715 A at 4.2 K [Nard 07]. At 20 K, the critical current is up to 250 A. This research confirms that MgB_2 can be used for FCL applications; though some changes are necessary: ac loss-analysis showed that a majority of losses is generated in the nickel sheath (ferromagnetic hysteretic losses) which requires further investigation.

A 15 MVA/9 kV FCL prototype, made of 1G HTS, is planned for 2009. Other goals: optimize an FCL design for 2G HTS and continue research on MgB_2 [Supe 08; Mart 09].

A new method of computing current distribution and losses in YBCO CC using FE model is introduced [Gril 09]. Developed 1D model is much faster than standard 2D model when thin conductors are examined. Such a model can be used for the simulation of windings with multiple turns. Coupled integral equations are implemented in this model and given in [Bram 08].

Investigation of high current/MV superconducting power links, which will be utilized for fault current limitation, is performed. The final industrial objective is a 1GVA range power link with a length of 200 m, a three phase, nominal phase current of 28 kA_{rms} and line-to-line voltage 20 kV_{rms} [Leht 04].

The first goal, 2 m long cable rated at 20 kV, 2 kA normal and 5 kA prospective fault current, is presented in [Verh 99]. Two SC materials are under consideration: Bi-2212 bulk and YBCO. A demonstrator is built and successfully tested using YBCO-coated stainless steel tapes; the prospective fault current of 50 kA_{peak} is restrained to 4.13 kA_{peak} [Usos 03]. Observed quench time is from $0.1 - 0.5$ ms. Field implementation is considered a challenge. Homogeneous quench of the SC can be obtained if operated near critical temperature, higher than 77 K [Tixa 07]. Tests are done on a 2 m sample of YBCO material.

A loss-prediction model is built and verified through tests on a 0.5 m long sample of YBCO [Rost 07]. Current-sharing between the tapes is highly dependent on the contact resistance. The goal of this Super3C project is to build a 30 m cable, rated at 10 kV/1 kA.

Long lengths of YBCO, up to 100 m, are developed with good mechanical stability and improved critical current homogeneity [Usos 07]. A new method, ABAD (Alternating Beam Assisted Deposition) enabled the production of $0.2 - 6$ m long YBCO tapes with higher critical current 574 A per cm-width, where YBCO, made by the conventional technique, experiences 495 A. Similar improvement is expected for the lengths of $40 - 100$ m.

In 2007, the testing of a 13.2 kV/630 A FCL is performed, in cooperation with AMSC. The FCL is made of YBCO tapes and tested for single-phase operation [Noe 09].

The DAPAS program is started in 2001 with the goal of developing transmission-class FCL, rated at 154 kV/2 kA, by 2010 [Phas 04; Mati 06]. Successful tests of 3.8 kV/200 A and 6.6 kV/200 A 3φ YBCO-based resistive FCL are reported in 2004 [Noe 07a] and 2005 [Ok B 05]. The fault current was suppressed from 10 kA to 900 A. SFCL is very reliable for current limitation purposes, but the price of the SC material has to be reduced. YBCO thin film FCL is more expensive than the one made of BSCCO bulks. The time dependence of YBCO resistance and shunt-assisted simultaneous quench are investigated in [Hye 02; Ok B 03].

The second-stage goal is the development of a 22.9 kV/630 A FCL, based on YBCO thin film. Successful tests of a 22.9 kV/630 A 1φ resistive SFCL, using YBCO thin films are presented in 2007 [Sim 07]. All SC modules quenched simultaneously without any supplementary devices between the modules, which proves the feasibility of FCL development for higher voltages. Filed testing of 22.9 kV/3 kA 3φ FCL is planned for 2010 [Noe 09].

Testing of bifilar YBCO CC coils is reported in [Kang 06; Kim 07; Min 06]. Tests confirmed the feasibility of bifilar windings. A large-scale FCL using YBCO CC should be developed. A reactive co-evaporation technique is used for fabrication of the YBCO CC superconductor. After modification of the EDDC, part of RCE equipment, long lengths of YBCO, up to 100 m, are fabricated [Oh 09]. In the 3^{rd} phase of DAPAS, research will be focused on a reel-to-reel RCE process.

A new hybrid SFCL is introduced in 2008 [Lee 08]. It minimizes the use of SC to reduce the overall cost. A single-phase test of 22.9 kV/630 A was successful. The price is reduced to 10% of a typical SFCL. Three-phase FCL is developed and tested for 24 kV/630 A. Field test is planned for 2009 at KEPCO.

The third phase of the DAPAS program is on-going and includes development of a transmission voltage FCL, and the field testing and commercialization of FCL technology.

In 2003, bifilar Bi-2212 bulk windings are developed as a part of the CURL10 project, enabling achievement of longer lengths when connected in series [Elsc 03]. The first test of a resistive SFCL was reported in 2004 [Bock 05; Neum 06]. The 3-phase FCL is successfully tested for nominal voltage and power of 10 kV/10 MVA. From 2004, it has been installed at RWE at Netphen [Kreu 05]. For higher voltages, a magnetic field assisted quench will be used instead of the resistive shunt concept [Elsc 06]. The ac losses and required length of superconductor are significantly reduced in this way. Tests of 6.9 kV/600 A 3φ, 6.9 kV/800 A and 14.4 kV/800 A 1φ FCLs are reported in [Noe 08]. The design and testing of a 3φ 12 kV/600 A Bi-2212 bulk FCL is done in Germany in 2004 [Noe 09]. In 2009, a 12 kV/100 A 3φ Bi-2212 FCL is tested and installed in a grid. At the same time, a 12 kV/800 A FCL is designed [Domm 10; Noe 09].

A new FCL project, aiming for 110 kV/1.8 kA, is started in 2006, where the conceptual design is shown in [Noe 07a]. Test of 0.12 kV/1850 A 1φ is performed in 2006 [Noe 08].

In 1999, a Bi-2212 1φ FCL prototype, rated at 19 kV/0.4 kA, is successfully tested [Tekl 99]. A test of an FCL rated at 6.6 kV/400 A and based on MgB_2 is reported in [Noe 07a]. No other reports found. A three-phase FCL prototype rated at 11.5 kV/400 A is planned [Noe 09]. Testing of MgB_2 in 2007 showed its feasibility for use for current limitation purposes [Lin 07; Majo 07]. It quenches at 39 K and can be cooled using commercially available cryocoolers.

In 1997, advances in the production of YBCO are reported [Kind 97]. A new technique is introduced; it rotates an oxygen pocket instead of a substrate, which allows the simultaneous deposition of $20 \cdot 20$ cm^2. A 750 V/135 A FCL, made of YBCO films, is successfully tested in 1999. A shunt-layer made of Au is used to support homogeneous switching. Reported recovery time is about 2 s. The following step is design of 1 MVA device [Grom 99]. Test results of 1 MVA are reported in Fischer et al. 2000 [Noe 07a]. An investigation of the influence of the switching voltage, critical current and normal resistance on YBCO quenching effect showed that homogeneous quench can be achieved [Krae 03]. Kraemer et al. 2005 reports about the successful test of an 864 V/1 kA (0.9 MW) FCL [Krae 05]. The fast response of the FCL showed that it can be used for instantaneous decoupling of coupled grids. An FCL rated at 4.2 kV/100 A 3φ is tested in 2000 [Noe 07a]. No other reports found. In 2000, testing of an FCL rated at 7.2 kV/100 A 3φ reported in [Hass 04]. No other reports found.

In 2007, a FCL 13 kV/300 A (2 MVA) 1φ is tested successfully, as collaboration between Siemens and AMSC. It used 344S superconductor, produced by AMSC. The test showed that "FCLs are now able to achieve the commercial performance level needed for urban power grids" [Libr]. The same year, the testing of 7.5 kV/300 A 1φ YBCO FCL is performed successfully [Noe 09]. The test of an 66 kV FCL is planned for 2011 in cooperation with AMSC. The FCL is based on YBCO CC [Noe 08]. No other reports found.

Testing of a 115 kV/1.2 kA 3φ FCL, made of YBCO tape SC, is planned for 2012 [Noe 09].

YBCO wire is being produced in continuous lengths, based on RABITSTM/MOD. A major advantage of the new approach is that electrical, mechanical and thermal properties and dimensions can be tailored for specific applications [Li 09]. Further investigation of 344S SC (YBCO thin films) is reported. Bifilar coils are tested to demonstrate uniform tripping and recovery within several seconds. A single-phase 13.8 kV FCL demonstrator, using 50 m of tape, is under construction. The previous test of a 120 kVA prototype, with 20 m of tape, was successful [Neum 07; Schm 07].

Saturable-core inductive FCL

A new type of saturable FCL is proposed, using C-core and demagnetized magnet in the air gap. Simulations have been done to prove the principle of FCL operation. The plan is to build the prototype to verify the simulation results [Chon]. The reported characteristics of the FCL are [Raso 06]: heating of the magnet during normal and fault operation is critical, it has to be cooled; after the first fault operation the magnet remains magnetized - large impedance is introduced in the circuit. The influence on the normal current is not negligible, the third current harmonic is introduced.

The program is started in 2002. Successful testing of a 3φ lab-scale prototype for 380 V is reported in [Xin 07]. The design of a 35 kV/100 MVA Bi-2223-based grid prototype is initiated, rated at 1.5 kA nominal current, 41 kA maximum and 20 kA_{rms} limited fault current. The voltage drop in normal operation is reported to be 6%. A grid test is expected in 2007. The new design solves the problems of this FCL type: excess weight and high induced voltage.

A designed 35 kV/90 MVA FCL is installed at Puji substation, but only one minor fault has occurred since 2007, so the operation of the device was not fully evaluated [Hong 09; Xin 09]. The problem of excess weight is solved by placing six cores together so that only one dc coil and one cryostat are used. The problem of over-voltage is solved by switching off the dc current source in the moment when a fault occurs; this is done in less than 4 ms. The device introduces a limiting impedance of 0.5 Ω - 0.8 Ω. The maximum line voltage drop is less than 1%. Two more referenced papers about this prototype are listed as 'to be published'. It is planned to develop a 220 kV/300 MVA 3φ FCL by 2010, and to test it in the field [Noe 09].

A successful test of a 13.8 kV FCL, with fault levels up to 23 kA, is performed in 2009. The fault current is limited by 20% at 20 kA. The reduction of 30% is measured at 7 kV and 12 kA. The FCL successfully operated for faults with up to an 82-cycle duration and RUL conditions, as well as consecutive faults separated by 2 s of normal load current [Mari 09].

In 2009, 12 kV/1.2 kA and 15k V/1.2 kA FCLs are installed in Avanti Circuit of the Future. FCL impedance, inserted during normal operation of the system, is less than 1% and the fault current was restrained by 20%. The same year, testing of both 1φ and 3φ FCLs at the Powertech site demonstrated the FCL's ability to restrain the prospective fault current of 25 kA by 45% [Ener; Mari 09; Noe 09]. An FCL rated at 26 kV is being designed for installation in Seattle City Light's electrical grid by 2010. The prospective fault current would be restrained by 50% [Marc 09].

An FCL rated at 138 kV/1.2 kA is designed and its demonstration is planned for 2011. There are plans to install it in the utility grid of Southern California Edison in 2012 [Mari 09]. The prospective fault current of $60 - 80$ kA will be restrained by 20% to 40% [Marc 09]. The dc winding is built from 1G superconductor Bi-2223.

Semiconductor-based FCLs

In 2006, a 3φ FCL with a rating of 8 kV/1.2 kA is designed and successfully tested. The goal is 138 kV level [Noe 08; Noe 07a]. A full-scale three-phase 15 kV/1.2 kA FCL is tested in a laboratory in USA. The prospective current was 80 kA. The goal of this project is to build 115 kV device [Noe 07a].

In 2004 a test on a three-phase 6.9 kV/25 MVA FCL is done [Noe 07a]. No other reports found.

A three-phase thyristor bridge is located in a transformers neutral point with all possible methods of neutral point connections [Rube 07b]. Control and reactor size allow a direct influence on first peak and steady state current - faultless and faulty [Rube 07a]. In 2007, three-phase and two-phase tests were performed on a 0.25 kV demonstrator; the prospective three phase fault current of 4.8 kA was reduced to 2.9 kA - the first peak and 1 kA - the follow current [Rube 08]. In combination with a pyrotechnical FCL, a low-loss hybrid FCL is feasible.

Shielded iron core SFCL

An FCL device using SC rings made of Bi-2212 is designed [Chen 97]. The device is tested for 10.5 kV/70 A and installed in the field where it operated successfully for one year [Noe 07a; Paul 98]. A three-phase 1.2 MVA FCL prototype is installed at the station Lontsch in Switzerland [Wtec]. This concept was not followed further.

A 100 kVA prototype is constructed and tested using a stack of four Bi-2212 rings, in 1993. The FCL rating is 480 V/130 A and prospective fault current is 8 kA [Leun 00].

No further references found.

In 1997, the design of 6.6 kV/400 A FCL is reported, based on Bi-2223 bulk and Bi-2212 thick film. Better limiting performance is shown by Bi-2212. However, better SC materials are needed for a feasible SCFCL [Ichi 95]. Tests will be carried out to see whether practical performance confirms design expectations [Kado 97]. No other reports found. In 2003, the SC cylinder made of Bi-2223 thick film is developed with a current density J_c over 5800 A/cm^2 [Ichi 03a]. In the same year, the reported J_c was 6000 A/cm^2 [Ichi 03b], which is sufficient for practical use. The tests of Bi-2223 thick film on MgO cylinder (450 mm diameter) with Bi-2212 buffer layer are conducted [Kado 05]. The tests are conducted at 3.5 kV, where the prospective fault current of 11.3 kA was reduced to 7.97 kA. The goal is to improve evenness of the film and increase J_c; an FCL will be developed for practical use. No further reports found.

A flat-type shielded FCL is proposed in 2005 [Mats 05]. Two small-scale prototypes are designed using YBCO thin film and Bi-2223 bulk plate. The FCL is modular and can be scaled to higher voltages by increasing the number of modules. YBCO FCL showed larger limiting impedance. Further analyses regarding the fault operation of FCLs are presented in [Maru 07]. It can be scaled-up by connecting modules in series. A flat-type fault current limiter consisting of the pancake primary winding and a high-T_c superconducting (HTS) disk is proposed as a modified version of a conventional magnetic-shield-type FCL with the superconducting cylinder.

Appendix C

MATHEMATICAL MODEL OF SATURATED-CORE FCL

This appendix gives the details of the developed mathematical model of inductive saturated-core FCLs. The model is used throughout the thesis for the first estimate of design parameters of the lab-scale FCL demonstrators and the full-scale FCL prototype.

To better explain the analytical model, the modeling results are included where necessary. The following input parameters are used: $U_{L,L} = 10\,kV$, $I_L = 400\,A$, $I_{dc} = 450\,A$, $k_{fill-factor} = 0.23$, $A_{al} = 4 \cdot 10^{-4}\,m^2$, $B_{sat} = 1.8\,T$, $k_{sat} = 1$, where $U_{L,L}$ and I_L are the line-to-line voltage and line current, I_{dc} the dc current, $k_{fill-factor}$ the winding fill factor, A_{al} the cross-section of a wire and k_{sat} the saturation factor (explained later).

C.1 Saturated-core FCL without an air gap

The design procedure of an inductive FCL, shown in Figure C-1a, is practically equivalent to that of a typical inductor, shown in Figure C-1b. The FCL has an additional dc winding, used to saturate the core. This winding has, however, no influence on the design of the FCL fault inductance and it can be neglected from this point of view. The dc number of turns is calculated in a later design stage on the basis of the number of ac turns and the mean-length of the dc flux path.

When designing an inductor, two equations are used. The first equation represents Faraday's law (C.1) and gives the relationship between the number of inductor turns N_{ac}, the cross-section of a core A_{core}, the variation of the flux density in the core $k_{sat}B_{sat}$ and the applied voltage across the inductor $u_{FCL}(t)$. The factor k_{sat} defines the desired flux change relative to the flux saturation level B_{sat}. For a given voltage, the product of the

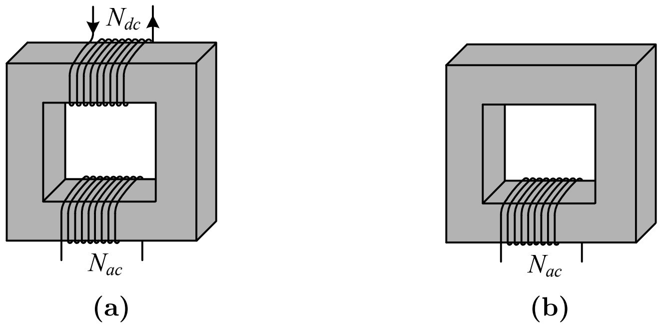

Figure C-1: Inductors' configurations: (a) Saturable inductor - an FCL; (b) The typical inductor design.

number of ac turns and the cross-section of the core can be calculated so that the change of the magnetic flux density B stays within the given range.

$$\int_0^{\frac{T_{per}}{4}} u_{FCL}\left(t\right) dt = N_{ac} A_{core} k_{sat} B_{sat} \tag{C.1}$$

To calculate the peak of flux change Φ_{max} in a core, it is necessary to integrate applied voltage over a quarter of the cycle, see Figure C-2.

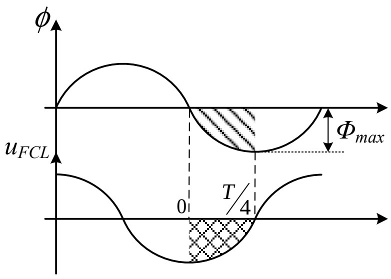

Figure C-2: The applied voltage across an inductor and the resulting flux in a core.

The second equation of the model is the approximate expression for the inductance value L_{FCL}, which assumes the zero leakage flux:

$$L_{FCL} = \mu_0 \mu_r \frac{N_{ac}^2 A_{core}}{l_{mean}}, \tag{C.2}$$

where μ_0 and μ_r are the permeability of air and the relative permeability of the core and l_{mean} is the flux mean-path length.

Using the given equations, a pair of variables (N_{ac},A_{core}) can be determined for the input parameters $u_{FCL}(t)$, k_{sat} and L_{FCL}. Figure C-3a and Figure C-3b show the cross-section of the core and the FCL inductance as a function of the number of ac turns.

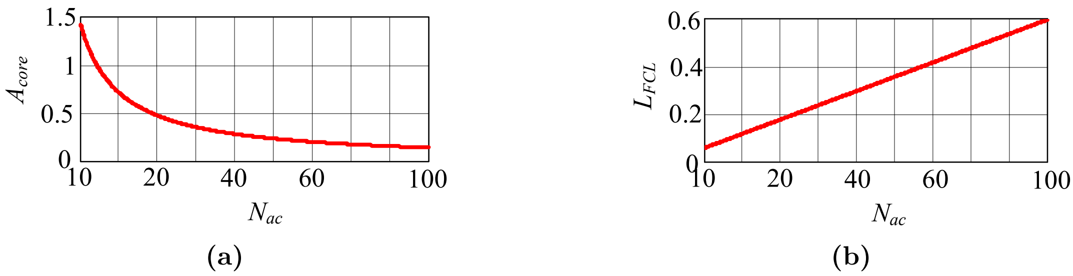

Figure C-3: The FCL modeling results: (a) The cross-section of a core; (b) The FCL inductance.

As can be seen, the cross-section of a core can be decreased if the number of ac turns is increased. Thus, smaller FCL cores can be employed. However, the resulting increase in FCL impedance leads to the decreased value of the limited fault current. The minimal size of the core is reached when the fault current peak reaches the pick-up level of protection relays.

C.2 Saturated-core FCL with an air gap

Improved calculation of an FCL inductance

The expression for inductance is changed when an air gap is inserted into an inductor's core. This expression assumes that there is no flux leakage and does not account for the fringing effect in the gap:

$$L_{FCL,typ} = \mu_0 \frac{N_{ac}^2 A_{core}}{l_{gap} + \frac{l_{mean}}{\mu_r}}, \tag{C.3}$$

where l_{gap} is the gap length.

This approximation can be improved by including a computation of the fringing effect [Boss 02]. The expression for the fringing effect is obtained by fitting the finite element simulation results. The permeance of the gap P_{gap} is increased by adding the fringing permeance P_{fring}:

$$L_{FCL,fring} = N_{ac}^2 \mu_0 \left(P_{gap} + P_{fring}\right). \tag{C.4}$$

The fringing permeance P_{fring} is a function of the geometry of the FCL. It can be explained by considering the structure of the single-core topology of inductive FCL. Figure C-4 shows the cross-sectional view of the FCL with designated dimensions.

Analyzing the FCL structure, it can be seen that the coefficients $F_{fring,coeff1}$ and $F_{fring,coeff3}$ can be applied for the fringing calculation [Boss 02], where P_{fring} is obtained

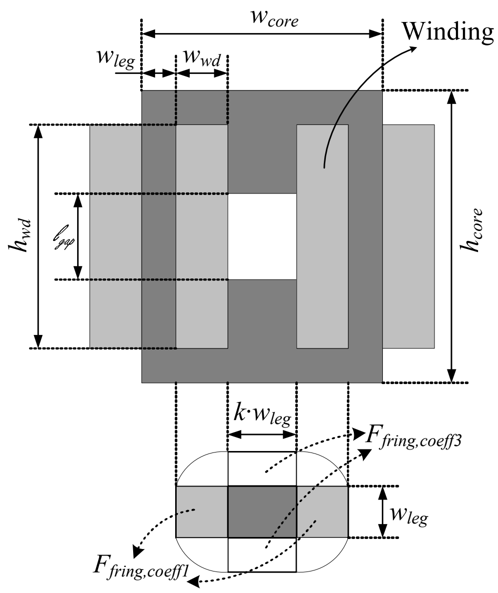

Figure C-4: A cross-sectional view of the FCL - fringing coefficients $F_{fring,coeff1}$ and $F_{fring,coeff3}$ can be applied.

from (C.5). Each coefficient is multiplied by the length of the corresponding leg to account for the third dimension [Boss 02].

$$P_{fring} = \frac{1}{2}\left(2 \cdot k \cdot w_{leg} \cdot F_{fring,coeff3} + 2 \cdot w_{leg} \cdot F_{fring,coeff1}\right) \tag{C.5}$$

The coefficients $F_{fring,coeff1}$ and $F_{fring,coeff3}$ are calculated from:

$$\begin{aligned} F_{fring,coeff1} = {} & \frac{2}{\pi} \ln \left(\frac{\frac{1}{w_{wd}} + \frac{1}{\frac{l_{gap}}{2}}}{\frac{1}{w_{wd}} + \frac{2}{h_{wd}}} \right) + \\ & + \frac{\left(\frac{h_{wd}}{2} - \frac{l_{gap}}{2}\right)^2 \left(\frac{h_{wd}}{2} - 0.26\frac{l_{gap}}{2} - 0.5 w_{wd}\right)}{3 w_{wd} \left(\frac{h_{wd}}{2}\right)^2} + \frac{w_{wd}}{3\left(\frac{h_{wd}}{2}\right)^2}, \end{aligned} \tag{C.6}$$

$$F_{fring,coeff3} = \frac{1}{\pi} k w_{leg} \cosh \left(3.395 \left(\frac{h_{core}}{l_{gap}}\right)^2 + 0.15 \left(\frac{h_{core}}{l_{gap}}\right) + 1.1155 \right). \tag{C.7}$$

Figure C-5a shows a comparison of the inductance values obtained from (C.3) and (C.4) and the ratio of the core height and gap length. The following FCL model parameters are used: w_{leg}=0.45 m, k=2, w_{wd}=0.35 m, h_{wd}=1.9 m, N_{ac}=50. Even if different values of the parameters are used, the final conclusions of this analysis would not be changed. The figure shows that the fringing inductance increases abruptly when the given ratio $r = h_{core}/l_{gap}$ exceeds a value of 5. The coefficient $F_{fring,coeff3}$ is calculated using $cosh(r)$ function, which is exponentially dependent on its argument r. Such an increase is certainly not representative of reality, implying that the fringing inductance can be calculated only for 'large' gap lengths, i.e. for $1 \leq r \leq 5$. To make equation (C.5) applicable for smaller gap lengths, the expression for the coefficient $F_{fring,coeff3}$ is altered. The exponent is changed from 2 to 1.5. As a result, the range of r is extended $1 \leq r \leq 10$, see Figure C-5b. By reducing the exponent further, this range could be further extended. For the built FCL model, an exponent of 1.5 is sufficiently small.

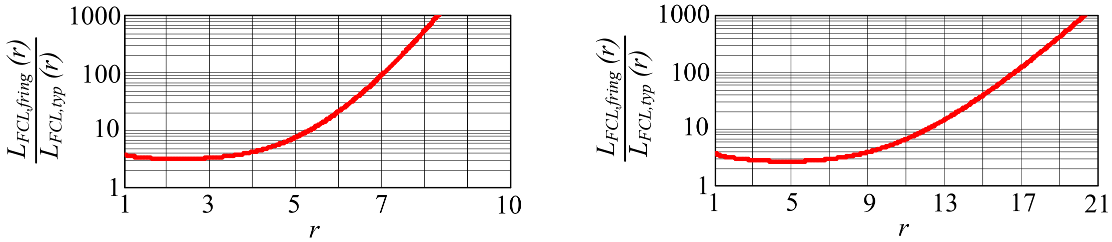

(a) (b)

Figure C-5: The ratio between the fringing and typical inductance compared to the relative gap length: (a) The exponent in $F_{fring,coeff3}$ coefficient is equal to 2; (b) The exponent in $F_{fring,coeff3}$ coefficient is equal to 1.5.

By taking the fringing effect into account, the calculated FCL inductance is increased by a factor of 3 to 5. However, as shown in Chapter 3, such an improved analytical model still delivers considerably different results than the 3D FE FCL model does. Thus, the analytical modeling should still be used only as a preliminary FCL design step.

The proposed analytical model comprises two equations, (C.1) and (C.4), and four unknown variables: the gap length l_{gap}, the number of ac turns N_{ac}, the cores's cross-section A_{core} and the FCL inductance L_{FCL}. To make the system of equations determined, the variables l_{gap} and N_{ac} are chosen to be input parameters.

According to (C.1), the cross-section of the core is determined by the chosen number of ac turns. Taking this into account, FCL impedance can be presented as a function of the number of ac turns and gap length (C.8). The calculated FCL inductance is shown in Figure C-6.

$$L_{FCL} = f\left(l_{gap}, N_{ac}\right) \tag{C.8}$$

As can be seen, the same FCL inductance $L_{FCL}(l_{gap}, N_{ac})$ can be obtained for a different number of ac turns by adjusting the gap length. For example: $L_{FCL}(0.2, 70) = L_{FCL}(0.55, 150) = 11$ mH. This is the crucial advantage of an inductive FCL with an air gap. The FCL fault impedance can remain unchanged with an increase in the number of ac turns. In other words, the cross-section of the core can be reduced without changing

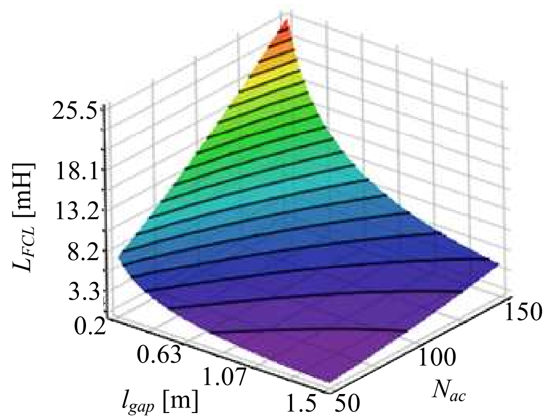

Figure C-6: The FCL impedance as a function of gap length and the number of ac turns.

(deteriorating) the FCL limit capability. For the example given above: $A_{core}(70) = 0.204$ m^2 and $A_{core}(150) = 0.095$ m^2, see Figure C-3a. Thus, the cross-section is reduced by a factor of 2.1.

Calculation of the number of dc turns

The required number of dc turns of a single dc winding can be found from:

$$N_{dc} = \frac{\frac{B_{sat}}{\mu_0 \mu_r} \overbrace{(h_{wd} + 2w_{leg} + 2w_{wd})}^{l_{mean}} + N_{ac} I_{asymmetric}}{I_{dc}}, \tag{C.9}$$

where $I_{asymmetric}$ is the maximal asymmetrical current of the system.

The calculated number of dc turns N_{dc} ensures that the core will remain in saturation during normal regime as long as the asymmetrical current of the system is below $I_{asymmetric}$.

FCL cost

The total cost of an FCL can be divided into two parts: the initial (material) cost and the operational (power losses) cost. The initial cost $FCL_{cost,inital}$ is proportional to the amount of FCL material:

$$\begin{aligned} FCL_{cost,initial} &= MM_{\cos t} \cdot MM_{wg} + WM_{\cos t} \cdot WM_{wg} \\ MM_{wg} &= \rho_{MM} \overbrace{(h_{core} \cdot w_{core} \cdot w_{leg} - 2w_{wd} \cdot h_{wd} \cdot w_{leg} - l_{gap} \cdot kw_{leg} \cdot w_{leg})}^{MM_{vol}}, \\ WM_{wg} &= \rho_{WM} \left(A_{al} \cdot 2 \overbrace{\left(\frac{w_{leg}}{\sqrt{\pi}} + \frac{w_{wd}}{2} \right)}^{l_{mean,wind,radius}} \pi \cdot (6N_{ac} + 2N_{dc}) \right. \end{aligned} \tag{C.10}$$

where MM_{cost} and WM_{cost} are the cost of magnetic and winding material per ton, respectively, MM_{wg} and WM_{wg} the weight of magnetic and winding material in tons, respectively, and ρ_{MM} and ρ_{WM} the specific density of magnetic and winding material respectively.

Figure C-7a and Figure C-7b show the weight of magnetic and winding material as a function of gap length and the number of ac turns, respectively. The core is made of steel with a specific weight of $\rho_{MM} = \rho_{steel} = 7.85$ tons/m^3 and the windings are made of aluminum with a specific weight of $\rho_{WM} = \rho_{al} = 2.65$ tons/m^3.

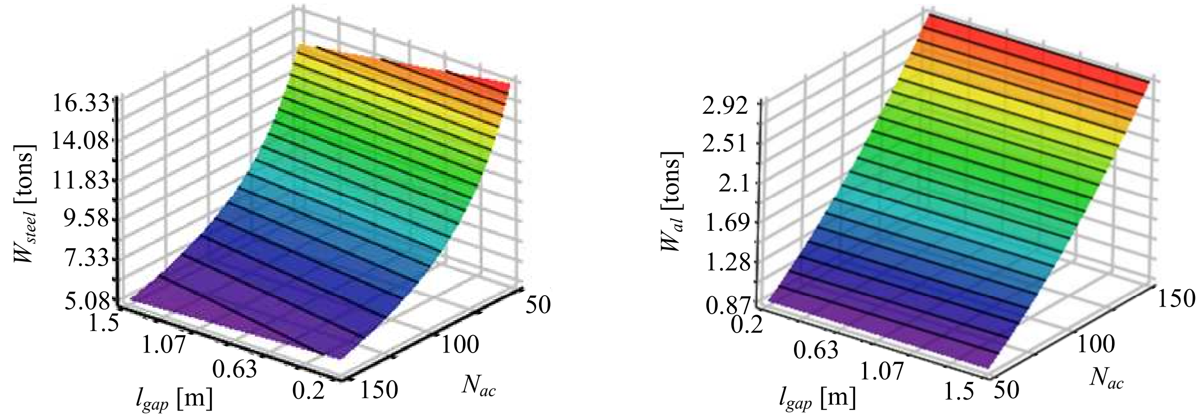

(a) **(b)**

Figure C-7: The FCL weight: (a) Magnetic material; (b) Winding material.

The amount of magnetic material decreases with the increase of the number of ac turns and gap length. For the example given above: $W_{steel}(0.2, 70) = 11.5$ tons and $W_{steel}(0.55, 150) = 5.5$ tons. On the other hand, the amount of winding material, as expected, increases with the increase of the number of ac turns: $W_{al}(0.2, 70) = 1.17$ tons and $W_{al}(0.55, 150) = 2.9$ tons. The overall weight and initial cost of the FCL are reduced for the larger number of ac turns, in this case, by 34%.

The operational cost is proportional to the power losses in the core and windings. The eddy current and hysteresis losses in the core are neglected because of lamination and operation of an FCL in the saturation region. The operational cost $FCL_{cost,op}$ is calculated from:

$$\begin{aligned} FCL_{cost,op} &= kWh_{\cos t} \cdot LifeTime_{hours} \cdot P_{FCL,total,diss}, \\ P_{FCL,total,diss} &= 6R_{FCL,ac,wind} I_{L,rms}^2 + 2R_{FCL,dc,wind} I_{dc}^2, \end{aligned} \tag{C.11}$$

where kWh_{cost} is the price of one kWh, $LifeTime_{hours}$ the device's expected life-time in hours, $P_{FCL,total,diss}$ the total losses in kW and $R_{FCL,ac,wind}$ and $R_{FCL,dc,wind}$ resistances of the ac and the dc windings, respectively.

The total power dissipation per phase in the windings is presented in Figure C-8. For the considered example the power losses per phase are equal to $P_{FCL,total,diss}(0.2, 70) =$ 4 kW and $P_{FCL,total,diss}(0.55, 150) = 10$ kW. As expected, they are proportional to the number of ac turns.

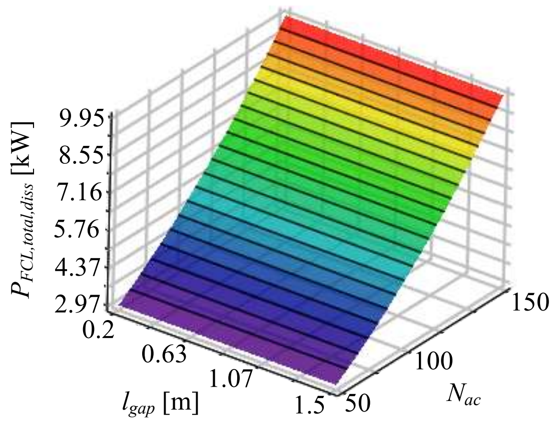

Figure C-8: Total power losses in FCL windings (specific resistance $\rho_{al} = 2.65 \cdot 10^{-8}$ Ω/m).

C.3 Block diagram of the model

The design steps of the analytical model are summarized in the block diagram in Figure C-9. As shown, the input parameters are the range of N_{ac} and l_{gap} of interest. The range of interest can be given by customer or assumed. In the following steps, the remaining FCL parameters are calculated as a function of N_{ac} and l_{gap}, based on the previously introduced equations.

The model produces two- and three-dimensional graphs which illustrate dependence between the parameters. The design requirements by customer are usually FCL impedance Z_{FCL} and either losses in windings (related to the number of ac turns) or core's cross-section (weight). Only one of the last two parameters can be specified because they are directly dependent through Faraday's law. Once the requirements are set, the remaining parameters N_{ac}, l_{gap} and either losses or core's cross-section can be easily determined from the obtained graphs.

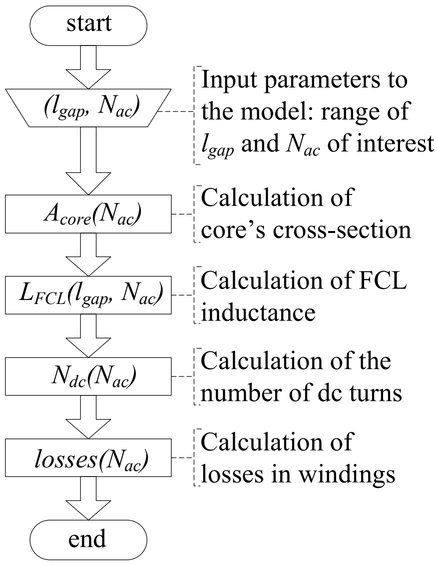

Figure C-9: The block diagram of the mathematical model used for FCL design.

C.4 Concluding remarks

The introduced mathematical model can be used for the first estimate of design parameters of a saturated-core FCL with an air gap. An FCL model should be developed in specialized software to validate and improve the analytical design. The FCL models in Saber and Ansys Classic are used for this purpose in this thesis.

The input parameters for the model are the length of gap l_{gap} and the number of ac turns N_{ac}. Three most important output parameters are the volume of FCL material (the initial cost), the power losses in the windings (the operational cost) and FCL impedance during nominal and fault periods. Figure C-10 shows a relationship between output parameters, i.e. the change of one of them is reflected in the others.

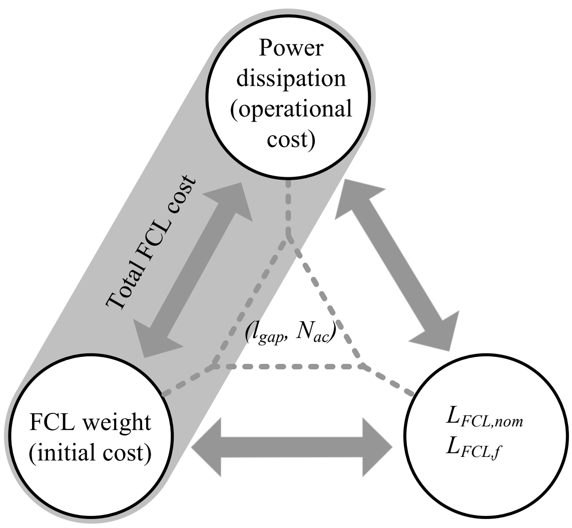

Figure C-10: The main input and output FCL design parameters.

Appendix D

A FAULT TRIGGERING CIRCUIT - DETAILED SCHEMATIC

A fault triggering circuit is designed and used for a controlled manual fault inception during testing of lab-scale FCL demonstrators. Its functional block diagram is already presented in Figure 3-25. This appendix gives detailed electrical schematic of the fault triggering circuit, see Figure D-1.

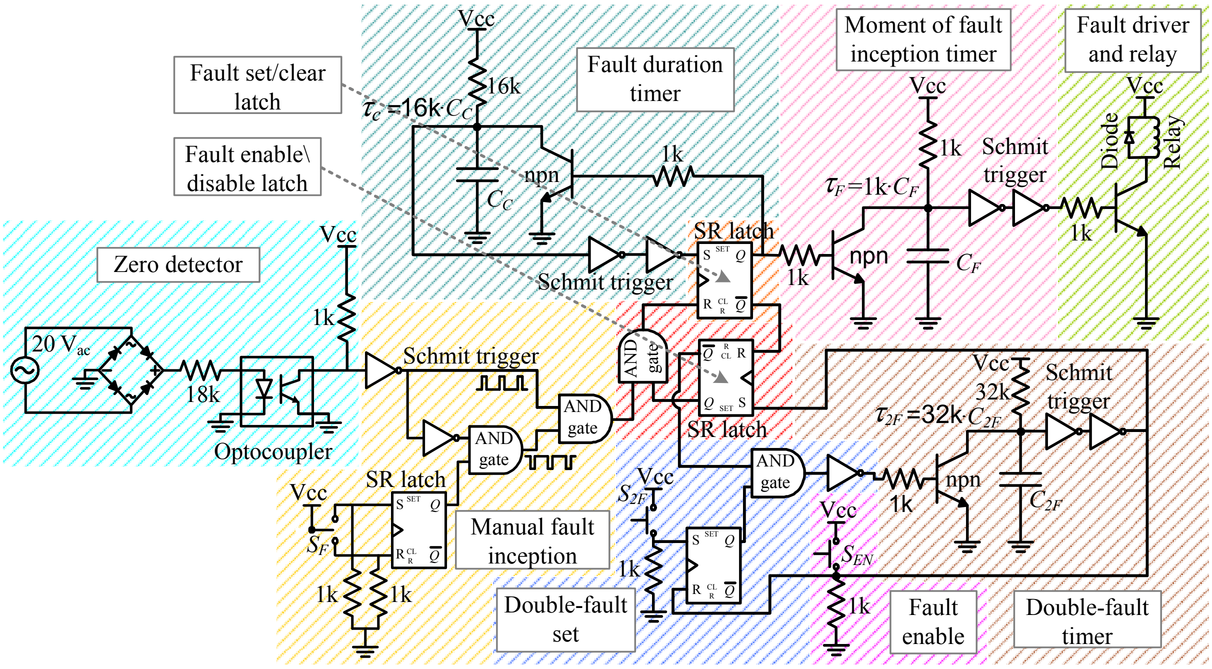

Figure D-1: Detailed electrical schematic of the fault triggering circuit.

The operation of the designed circuit is described below.

Supply voltage of the circuit is V_{cc}=10 V. The 'Zero detector' (ZD) gives zero impulse on each zero-crossing of power voltage. The maximum input voltage is equal to V_{max_ac}=20 V. The total width of the single impulse is 3.2 ms, and it is symmetrical relative to voltage zero-crossing (see in Figure D-2).

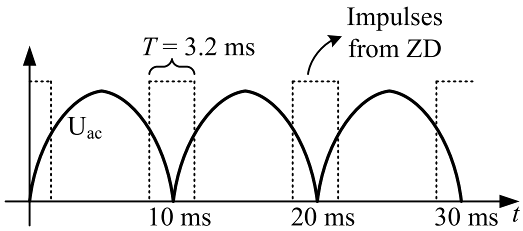

Figure D-2: Impulses generated by 'Zero detector' circuit.

The function of switch S_{EN}, located in 'Fault enable' part of circuit, is to enable operation of the whole fault triggering circuit.

When engaged, switch S_F sets corresponding SR latch and allows the first following zero-crossing impulse to resets 'Fault set/clear latch'. As a results, both timers 'Moment of fault inception timer' and 'Fault duration timer' are activated. Also, 'Fault enable/disable latch' is reset which through logical AND gate disables inception of the following fault.

Time constant of 'Moment of fault inception timer' τ_F=$1k \cdot C_F$ determines in which moment during voltage half-cycle a fault will be incepted. Taking into account that the schmitt trigger changes its output to logical 1 when its input voltage reaches value of 5.2 V, the moment of a fault triggering is found to be t_f=$0.74\tau_F$. After accounting for the delay of used electromechanical relay and the width of zero-crossing impulses, the final relation between τ_F and the moment of fault inception is given by:

$$t_f = 0.74 \cdot \tau_F - \overbrace{1.6\,ms}^{\substack{Half-width\,of\,a\,zero-\\crossing\,impulse}} + \overbrace{15\,ms}^{Delay\,of\,a\,relay} . \tag{D.1}$$

Since the value of the corresponding resistor is already defined R_F=1 kΩ, the value of the capacitor C_F can be simply determined. If the moment of fault inception is to be 5 ms (relative to voltage zero-crossing), the value of capacitor C_F has to be set to 11 μF. Similarly, the time constant of 'Fault duration timer' is determined from Equation D.2. As an example, to have a fault duration of five cycles, the capacitor of, more or less, C_c=10 μF should be used in combination with given resistor of 16 kΩ.

$$T_c = 0.74 \cdot \tau_c - \overbrace{0.74 \cdot \tau_F}^{Fault\,inception\,delay} - \overbrace{15\,ms}^{Delay\,of\,a\,relay} , \tag{D.2}$$

where T_c is desired duration of a fault.

After 'Fault inception timer' sets 'Fault set/clear latch', the fault is cleared. If 'Double-fault set' switch S_{2F} is engaged before the first fault is incepted, 'Double-fault timer' will be activated by 'Fault set/clear latch'. This timer measures the time interval after which the second fault will automatically be incepted. The interval between two fault T_{2F} is determined from the following equation:

$$T_{2F} = 0.74 \cdot \tau_{2F} + \overbrace{0.74 \cdot \tau_F}^{Fault\,inception\,delay} + \overbrace{15\,ms}^{Delay\,of\,a\,relay}, \tag{D.3}$$

where τ_{2F}=32 $k\Omega \cdot C_{2F}$.

For example, to have a time interval between two faults equal to 0.2 s, the capacitor of C_{2F}=7.5 μF has to be installed in series with 32 kΩ resistor.

Appendix E

LIST OF SYMBOLS AND ABBREVIATIONS

E.1 Latin letters

A	Cross-section of magnetic core	[m^2]
A	Magnetic vector potential	[$\mathrm{V{\cdot}s{\cdot}m^{-1}}$]
B	Magnetic flux density	[T]
C	Capacitor, Capacitance	[F]
D	Diameter	[m]
d	Depth	[m]
E	Energy	[J]
F	Fringing coefficient	
f	Function	
H	Magnetic field intensity	[$\mathrm{A{\cdot}m}$]
H	Constant proportional to inertia constant of machine	[$\mathrm{J{\cdot}(V{\cdot}A)^{-1}}$]
h	Height	[m]
I, i	Electrical current	[A]
J, j	Electrical current density	[$\mathrm{A{\cdot}m^{-2}}$]
k_E	Reduction factor of energy dissipation in a CB due to installation of a FCL	
$k_{fill-factor}$	Winding window fill-factor	

$k_{mid,outer}$	Ratio between cross-section of core's middle and outer legs	
k_{sat}	Variation of magnetic flux density in a core during a fault	
kWh_{cost}	Price of kWh	[euro]
L	Inductance	[H]
$LifeTime_{hours}$	Life time of a device expressed in hours	[hours]
l	Length	[m]
M	Inertia of a machine	[J·s·(mech rad)$^{-1}$]
MM	Magnetic material	
N	Number of winding turns	[turns]
n	Ratio between real and modeled number of turns	
P	Permeance of magnetic path	[H·turn^{-1}]
P	Real power	[W]
R	Resistance	[Ω]
R, Rel	Relay	
r	Ratio between core's height and gap length	
S	Complex power	[V·A]
S	Slip of a machine	
T	Time interval	[s]
T	Torque	[N·m]
T	Temperature	[°C, K]
t	Time moment	[s]
U, u	Voltage	[V]
W	Weight	[kg]
WM	Winding material	
w	Width	[m]
X	Reactance	[Ω]
x	x-coordinate	
y	y-coordinate	
Z	Complex impedance	[Ω]

E.2 Greek letters

α	FCL limiting factor	
δ	Angular displacement of rotor in mechanical radians	[mech rad]
δ	Critical rotor angle	[mech rad]
Θ	Impedance phase angle	[deg, °]
θ	Voltage phase angle	[deg, °]
μ	Magnetic permeability	[H$\cdot m^{-1}$]
$\Re$	Reluctance of a magnetic path	[turn$\cdot H^{-1}$]
ρ	Specific density	[kg$\cdot m^{-3}$]
σ	Electrical conductivity	[S$\cdot m^{-1}$]
τ	Time constant	[s]
Φ	Magnetic flux	[Wb]
φ	Impedance phase angle	[deg, °]
Ψ	Current phase angle	[deg, °]
Ω	Volume enclosing FCL model in FE simulations	[m^3]
ω	Angular velocity	[rad$\cdot$s^{-1}]

E.3 Subscripts

A, B	Feeder, bus or grid
a, b, c	Phase
ac	ac value
al	Aluminum
$allowable$	Allowable value of current
$applied$	Applied
$asymmetric$	Asymmetric
aux	Auxiliary leg of a magnetic core
$bank$	Resistor bank
$base$	Base
$bridge$	Bridge

$CB - FCL$	Between a CB and an FCL
$CB - G$	Between a CB and a generator
cl	Clear
$coeff1, coeff3$	Flux fringing coefficients
$core$	Magnetic core
$cost$	Cost
cr	Critical value
ct	Current transformer
cu	Copper
D	Diode
dc	dc
$diss$	Power dissipation
e	Excitation
eff	Effective value
el	Electrical
en	Enable
end	End
$error$	Calculation error
f	Fault
FCL	Fault current limiter
$fring$	Fringing effect
$fuse$	Fuse
g	Generator
gap	Gap
$heav$	Change of Heaviside function from original to asymptote value
i	Winding number
in	Inside of relay protection zone
in	Inner dimension of winding
ind	Inductor
$in - feed$	In-feed contribution
ini	Initial value
j	Winding number
$knee$	Knee of varistor characteristics
L	Power line
lac	ac leg of a magnetic core
ldc	dc leg of a magnetic core

$left$	Left leg of a magnetic core
leg	Leg of a magnetic core
$lgap$	Core's leg with a gap
lim	Limited or FCL limiting action
lin	Linear regime
$load$	Load
$lower$	Lower threshold value for a current control
m	Magnetizing
mag	Magnetic
$main$	Main
max	Maximal value
$mean$	Mean value of magnetic path of winding turn length
$mech$	Mechanical
mid	Middle leg of a magnetic core
min	Minimal value
MM	Magnetic material
$mutual$	Mutual inductance
new	New value of a variable
nom	Nominal value
op	Operational
out	Outside of relay protection zone
out	Outer dimension
$outer$	Outer leg of a magnetic core
p	Primary
per	Period of a power voltage
$pick-up$	Pick-up level of current of protective relays
$pros$	Prospective
R	Relay
r	Relative
r	Remanent
$radius$	Radius of a winding
res	Resonant
$RFCL$	Resistive fault current limiter
$right$	Right leg of a magnetic core
s	Secondary
s	Synchronous

saf	Safety zone
sat	Saturation regime
sc	Short-circuit
$self$	Self
sg	Stray line capacitance to ground
st	Start
$steel$	Steel
$stray$	Stray
t	Transformer
tf	Moment of a fault inception
th	Thyristor
$total$	Total value
$trigg$	Triggering
typ	Typical
$upper$	Upper threshold value for a current control
var	Variation of a variable value
vol	Volume
w	Width
wd	Window of a magnetic core
wg	Weight
$wind$	Winding
$wire$	Wire
WM	Winding material
$XFCL$	Reactive fault current limiter
x, y, z	Dimensions in Cartesian coordinate system
0	Air

E.4 Abbreviations

AMT	Angle of maximum torque
BSCCO	Bismuth strontium calcium copper oxide
CB	Circuit breaker
CC	Coated conductor
CHP	Combined heat and power

CT	Current transformer
D	Diode
DG	Distributed generator
E	Magnetic element, used in Saber modeling of an FCL
ETO	Emitter Turn-off Thyristor
Exp	Experimental
FCC	Fault current controller
FCL	Fault current limiter
FE	Finite element
flc2hs	Smoothed Heaviside function
G	Generator
GCT	Gate-Commutated Thyristor
GTO	Gate Turn-off Thyristor
HD-TGTO	Hard-Driven Transparent Gate Turn-off Thyristor
HTS	High temperature superconductor
HV	High voltage
HVDC	High voltage dc system
IB	Infinite bus
IGBT	Insulated-Gate Bipolar Transistors
IGCT	Integrated gate commutated thyristor
Lab	Laboratory
L-G	Line-to-ground
L-L-G	Line-to-line-to-ground
LN_2	Liquid nitrogen
LTS	Low temperature superconductor
LV	Low voltage
M	Main coil
MgB_2	Magnesium diboride
Mho	Impedance relay with inherent directional sensing
MV	Medium voltage
N/S	Normal/Superconducting transition
PFC	Power flow controller
PTC	Positive temperature coefficient
p.u.	Per unit
RMS	Root mean square
RRRV	Rate of rise of recovery voltage

RUL	Recovery under load
S	Mechanical switch
SC	Stranded conductor
SC	Superconductor
SCFM	Short-circuit failure mode
SFCL	Superconducting fault current limiter
Si	Silicon
SiC	Silicon carbide
S/N	Superconducting/Normal transition
SPETO	Self-Powered Emitter Turn-off Thyristor
SSFCL	Solid-state FCL
SW	Semiconductor switch
T	Transformer
T	Triggering coil
Th	Thyristor
TRV	Transient recovery voltage
Var	Varistor
VT	Voltage transformer
WB	Ansys WorkBench
(x_n, y_n)	Coordinates of the nth element in FE simulation
YBCO	Yttrium barium copper oxide
1G	The first generation
2D	Two dimensional
2G	The second generation
3D	Three dimensional

E.5 Vectors

$\hat{i}$, $\hat{j}$, $\hat{k}$	Unity vectors of x, y and z axes in Cartesian coordinate system

REFERENCES

[ABB 05] ABB. "4.5kV IGCT module Datasheet, 5SHY 35L4512". 2005.

[ABB 07] ABB. "5.5kV IGCT module Datasheet, 5SHX 19L6010". 2007.

[ABB 08] ABB. "6.5kV IGCT module Datasheet, 5SHY 42L6500". 2008.

[Ahme 02] M. M. R. Ahmed, G. A. Putrus, and L. Ran. "Power quality improvement using a solid-state fault current limiter". In: *Transmission and Distribution Conference and Exhibition 2002: Asia Pacific. IEEE/PES*, pp. 1059–1064, 2002.

[Ahme 04] M. M. R. Ahmed, G. A. Putrus, R. Li, and e. al. "Harmonic analysis and improvement of a new solid-state fault current limiter". *IEEE Transactions on Industry Applications*, Vol. 40, No. 4, pp. 1012–1019, 2004.

[Ahme 06] M. M. R. Ahmed, G. Putrus, R. Li, and e. al. "Development of a prototype solid-state fault-current limiting and interrupting device for low-voltage distribution networks". *IEEE Transactions on Power Delivery*, Vol. 21, No. 4, pp. 1997–2005, 2006.

[Alci 06] A. F. Alcidas, M. Saint Paul, and E. Calixte. "Evaluation of Position of a Fault Current Limiter with Regard to the Circuit Breaker". In: *Power Symposium, 2006. NAPS 2006.*, pp. 475–480, 2006.

[Alme 09] M. E. Almeida, C. S. Rocha, J. A. Dente, and e. al. "Enhancement of power system transient stability and power quality using superconducting fault current limiters". In: *Power Engineering, Energy and Electrical Drives, 2009. POWERENG '09.*, pp. 425–430, 2009.

[Ansy] Ansys. "Ansys help files".

[Bern 03] S. Bernet. "Function, Technology and Features of IGCTs and High Voltage IGBTs". 2003.

[Bhal 08] P. Bhalerao. *Characterization of Gate Controlled Diodes for IGCT Applica-*

tions. PhD thesis, Berlin University of Technology, 2008.

[Bin 03a] Z. Bin, L. Yunfeng, Z. Xigen, and e. al. “The high power and high frequency operation of the emitter turn-off (ETO) thyristor”. In: *Industrial Electronics Society, 2003. IECON ’03.*, pp. 1167–1172 Vol.2, 2003.

[Bin 03b] Z. Bin, A. Q. Huang, Z. Xigen, and e. al. “The built-in current sensor and over-current protection of the emitter turn-off (ETO) thyristor”. In: *Industry Applications Conference, 2003. 38th IAS Annual Meeting.*, pp. 1264–1269, 2003.

[Bin 06] C. Bin, A. Q. Huang, M. Baran, and e. al. “Operation characteristics of emitter turn-off thyristor (ETO) for solid-state circuit breaker and fault current limiter”. In: *Applied Power Electronics Conference and Exposition, 2006. APEC ’06. Twenty-First Annual IEEE*, p. 5, 2006.

[Bock 05] J. Bock, F. Breuer, H. Walter, and e. al. “CURL 10: development and field-test of a 10 kV/10 MVA resistive current limiter based on bulk MCP-BSCCO 2212”. *IEEE Transactions on Applied Superconductivity*, Vol. 15, No. 2, pp. 1955–1960, 2005.

[Boen 02] H. J. Boenig, C. H. Mielke, B. L. Burley, and e. al. “The bridge-type fault current controller - a new FACTS controller”. In: *Power Engineering Society Summer Meeting, 2002 IEEE*, pp. 455–460, 2002.

[Boll 03] M. Bollen. “Voltage Dips - A major Power Quality Issue”. 2003.

[Boon 08] P. Boonchiam and N. Mithulananthan. “Diode-clamped Multilevel Voltage Source Converter Based on Medium Voltage DVR”. 2008.

[Boss 02] A. Van den Bossche, V. Valchev, and T. Filchev. “Improved approximation for fringing permeances in gapped inductors”. In: *Industry Applications Conference, 2002. 37th IAS Annual Meeting.*, pp. 932–938, 2002.

[Brac 07] V. Braccini, D. Nardelli, R. Penco, and e. al. “Development of ex situ processed MgB_2 wires and their applications to magnets”. 2007.

[Bram 08] R. Brambilla, F. Grilli, and e. al. “Integral equations for the current density in thin conductors and their solution by the finite-element method”. 2008.

[Busc 01] K. H. J. Buschow. “The encyclopedia of materials science and technology”. 2001.

[Cali 02] E. Calixte, Y. Yokomizu, H. Shimizu, and e. al. “Reduction effect of semiconductor type fault current limiter on interrupting duty of a circuit breaker”. In: *Power Conversion Conference, 2002. PCC Osaka 2002.*, pp. 1423–1428, 2002.

[Cali 04] E. Calixte, Y. Yokomizu, H. Shimizu, and e. al. “Reduction of rating required for circuit breakers by employing series-connected fault current limiters". *Generation, Transmission and Distribution, IEE Proceedings*, Vol. 151, No. 1, pp. 36–42, 2004.

[Chan 00] C. S. Chang and P. C. Loh. "Designs synthesis of resonant fault current limiter for voltage sag mitigation and current limitation". In: *Power Engineering Society Winter Meeting, 2000. IEEE*, pp. 2482–2487, 2000.

[Chan 01] C. S. Change and P. C. Loh. "Integration of fault current limiters on power systems for voltage quality improvement". 2001.

[Chen 02] M. Chen, W. Paul, M. Lakner, and e. al. "6.4 MVA resistive fault current limiter based on Bi-2212 superconductor". 2002.

[Chen 04] M. Chen, W. Paul, M. Decroux, and e. al. "Superconducting fault current limiter". 2004.

[Chen 05] B. Chen, A. Q. Huang, S. Atcitty, and e. al. "Emitter turn-off (ETO) thyristor: an emerging, lower cost power semiconductor switch with improved performance for converter-based transmission controllers". In: *Industrial Electronics Society, 2005. IECON 2005. 31st Annual Conference of IEEE*, p. 6, 2005.

[Chen 97] M. Chen, T. Baumann, P. Unternahrer, and e. al. "Fabrication and Characterisation of Superconducting Rings for Fault Current Limiter Application". 1997.

[Chon] E. Chong, L. Rasolonjanahary, and e. al. "A Novel Concept for a Fault Current Limiter".

[CIGR 03] CIGRE. "Fault Current Limiters in Electrical Medium and High Voltage Systems". 2003.

[CIGR 07] CIGRE. "Guideline on the impact of fault current limiting devices on protection system". 2007.

[Cost 08] E. J. Coster, J. M. A. Myrzik, and W. L. Kling. "Transient stability of distributed generation in MV-Ring networks". In: *Transmission and Distribution Conference and Exposition, 2008. IEEE/PES*, pp. 1–7, 2008.

[Cred 03] R. Credo. "McGraw-Hill dictionary of scientific and technical terms". 2003.

[Cvor 08a] D. Cvoric, S. W. H. de Haan, and J. A. Ferreira. "CB Stress Reduction and Comparison of Energy Dissipation for Two Types of FCLs". In: *Transmission and Distribution Conference and Exposition, 2008. IEEE/PES*, pp. 1–7, 2008.

[Cvor 08b] D. Cvoric, S. W. H. de Haan, and J. A. Ferreira. "Improved Configuration of the Inductive Core-Saturation Fault Current Limiter with the Magnetic Decoupling". In: *Industry Applications Society Annual Meeting, 2008. IAS*

'08. IEEE, pp. 1–7, 2008.

[Cvor 09] D. Cvoric, S. W. H. de Haan, and J. A. Ferreira. "New saturable-core Fault Current Limiter topology with reduced core size". In: *Power Electronics and Motion Control Conference, 2009. IPEMC '09. IEEE 6th International*, pp. 920–926, 2009.

[Dale 07] R. B. Dalessandro, M. Bocchi, V. Rossi, and e. al. "Test Results on 500 kVA-Class MgB_2-Based Fault Current Limiter Prototypes". *IEEE Transactions on Applied Superconductivity*, Vol. 17, No. 2, pp. 1776–1779, 2007.

[Darm 04] F. A. Darmann and T. P. Beales. "Superconducting Fault Current Limiter". 2004.

[De G 04] H. De Gersem and T. Weiland. "Field-circuit coupling for time-harmonic models discretized by the finite integration technique". *IEEE Transactions on Magnetics*, Vol. 40, No. 2, pp. 1334–1337, 2004.

[Decr 03] M. Decroux, L. Antognazza, S. Reymond, and e. al. "Studies of YBCO strip lines under voltage pulses: optimization of the design of fault current limiters". *IEEE Transactions on Applied Superconductivity*, Vol. 13, No. 2, pp. 1988–1991, 2003.

[Deve 09] Y. Developpment. "How SiC will impact electronics: A 10 year projection...". 2009.

[Domm 10] R. Dommerque and e. al. "First Commercial Medium Voltage Superconducting Fault-Current Limiters Production, Test and Installation". 2010.

[Dula 04] P. Dular and J. Gyselinck. "Modeling of 3-D stranded inductors with the magnetic vector potential formulation and spatially dependent turn voltages of reduced support". *IEEE Transactions on Magnetics*, Vol. 40, No. 2, pp. 1298–1301, 2004.

[Eckr 05] S. Eckroad. "Survey of Fault Current Limiter (FCL) Technologies". Technical Update, 2005.

[Eich 96] S. Eicher. *The Transparent Anode GTO (TGTO): A New Low-Loss Power Switch.* PhD thesis, Swiss Federal Institute of Technology Zurich, 1996.

[Elsc 03] S. Elschner, F. Breuer, M. Noe, and e. al. "Manufacturing and testing of MCP 2212 bifilar coils for a 10 MVA fault current limiter". *IEEE Transactions on Applied Superconductivity*, Vol. 13, No. 2, pp. 1980–1983, 2003.

[Elsc 06] S. Elschner, F. Breuer, and e. al. "Magnetic Field Assisted Quench Propagation as a New Concept for Resistive Current Limiting Devices". 2006.

[Emhe 09] A. S. Emhemed, R. M. Tumilty, N. K. Singh, and e. al. "Analysis of Transient Stability Enhancement of LV-Connected Induction Microgenerators by

Using Resistive-Type Fault Current Limiters". *IEEE Transactions on Power Systems*, Vol. PP, No. 99, pp. 1–1, 2009.

[Ener] U. D. o. Energy.

[EPCO 02] EPCOS. "Varistor - general technical information". 2002.

[Fles 09] S. Fleshler, D. Roy, M. W. Rupich, and e. al. "Reducing the Price-Performance Ratio of 2G Wire". 2009.

[Gang 04] C. Gang, J. Daozhuo, L. Zhengyu, and e. al. "A new proposal for solid state fault current limiter and its control strategies". In: *Power Engineering Society General Meeting, 2004. IEEE*, pp. 1468–1473, 2004.

[Geor 79] A. O. George, E. S. William, and W. S. Andrew. "Saturable reactor limiter for current". 1979.

[Gers 98] J. M. Gers and E. J. Holmes. *Protection of electricity distribution networks*. Institution of Electrical Engineers, London, 1998.

[Grai 94] J. J. Grainger and W. D. Stevenson. *Power system analysis*. McGraw-Hill, New York, 1994.

[Gras 05] G. Grasso. "Cost considerations for MgB_2 conductors". 2005.

[Gril 05] F. Grilli, L. Martini, S. Stavrev, and e. al. "Analysis of magnetic field and geometry effects for the design of HTS devices for AC power applications". *IEEE Transactions on Applied Superconductivity*, Vol. 15, No. 2, pp. 2074–2077, 2005.

[Gril 09] F. Grilli, R. Brambilla, L. F. Martini, and e. al. "Current Density Distribution in Multiple YBCO Coated Conductors by Coupled Integral Equations". *IEEE Transactions on Applied Superconductivity*, Vol. 19, No. 3, pp. 2859–2862, 2009.

[Grom 99] B. Gromoll, G. Ries, W. Schmidt, and e. al. "Resistive fault current limiters with YBCO films 100 kVA functional model". *IEEE Transactions on Applied Superconductivity*, Vol. 9, No. 2, pp. 656–659, 1999.

[Grun 96] H. Gruning, J. Rees, A. Weber, and e. al. "High-Power Hard-Driven GTO Module for 4.5 kV/3 kA Snubberless Operation". 1996.

[Hann 03] M. A. Hannan and A. Mohamed. "Performance Evaluation of Solid State Fault Current Limiters in Electric Distribution System". 2003.

[Hass 04] W. V. Hassenzahl, D. W. Hazelton, B. K. Johnson, and e. al. "Electric power applications of superconductivity". *Proceedings of the IEEE*, Vol. 92, No. 10, pp. 1655–1674, 2004.

[Henr 03] S. Henry, T. Baldwin, and M. Steurer. "The effects of a fast switching fault current limiter on distance protection". In: *Proceedings of the 35th South-*

eastern Symposium on System Theory, 2003., pp. 264–268, 2003.

[Ho M 04] K. Ho Min, J. Jankowski, L. Haigun, and e. al. “Stability of bare and copper-laminated YBCO samples: experimental and simulation results”. *IEEE Transactions on Applied Superconductivity*, Vol. 14, No. 2, pp. 1290–1293, 2004.

[Hong 09] H. Hong, Z. Cao, J. Zhang, and e. al. “DC Magnetization System for a 35 kV/90 MVA Superconducting Saturated Iron-Core Fault Current Limiter”. *IEEE Transactions on Applied Superconductivity*, Vol. 19, No. 3, pp. 1851–1854, 2009.

[Hosh 01] T. Hoshino, K. Mohammad Salim, M. Nishikawa, and e. al. “DC reactor effect on bridge type superconducting fault current limiter during load increasing”. *IEEE Transactions on Applied Superconductivity*, Vol. 11, No. 1, pp. 1944–1947, 2001.

[Huan 99] A. Q. Huang, K. Motto, and Y. Li. “Development and Comparison of High-Power Semiconductor Switches”. 1999.

[Hui 06] D. Hui, Z. K. Wang, J. Y. Zhang, and e. al. “Development and Test of 10.5 kV/1.5 kA HTS Fault Current Limiter”. *IEEE Transactions on Applied Superconductivity*, Vol. 16, No. 2, pp. 687–690, 2006.

[Hye 02] K. Hye-Rim, C. Hyo-Sang, L. Hae-Ryoung, and e. al. “Resistance of superconducting fault current limiters based on YBa2Cu3O7 thin films after quench completion”. 2002.

[Hyo 01] C. Hyo-Sang, H. Ok-Bae, and K. Hye-Rim. “Quench characteristics of resistive supercondcuting fault current limiters based on YBCO films”. 2001.

[Hyou 08] K. Hyoungku, L. Chanjoo, N. Kwanwoo, and e. al. “Development of a 13.2 kV/630 A (8.3 MVA) High Temperature Superconducting Fault Current Limiter”. *IEEE Transactions on Applied Superconductivity*, Vol. 18, No. 2, pp. 628–631, 2008.

[Ichi 03a] M. Ichikawa, H. Kado, M. Shibuya, and e. al. “Inductive type fault current limiter with Bi-2223 thick film on a MgO cylinder”. *IEEE Transactions on Applied Superconductivity*, Vol. 13, No. 2, pp. 2004–2007, 2003.

[Ichi 03b] M. Ichikawa, H. Kado, M. Shibuya, and e. al. “Properties of Bi-2223 thick films on a MgO substrate prepared by a coating method”. *IEEE Transactions on Applied Superconductivity*, Vol. 13, No. 2, pp. 3691–3694, 2003.

[Ichi 95] M. Ichikawa and M. Okazaki. “A magnetic shielding type superconducting fault current limiter using a Bi2212 thick film cylinder”. *IEEE Transactions on Applied Superconductivity*, Vol. 5, No. 2, pp. 1067–1070, 1995.

[Juan 08] H. L. Juan-Carlos, S. W. Charles, and W. H. Drew. "Testing and Demonstration Results for the Transmission-Level (138kV) 2G Superconducting Fault Current Limiter at SuperPower". 2008.

[Juen 03] K. P. Juengst and G. Kuperman. "Current Limiter with Electric Valves for Limiting the Short-Cicruit Current in an Electric Power Circuit". 2003.

[Juen 08] K. P. Juengst, M. Noe, and G. Kuperman. "Current Limiter for Limiting Current in Case of a Fault". 2008.

[Junz 99] K. Junzo, A. Hiroshi, F. Chihiro, and e. al. "Fault Current Limiting System for 500-kV Power Systems". 1999.

[Kado 05] H. Kado, M. Ichikawa, M. Shibuya, and e. al. "Inductive type fault current limiter using Bi-2223 thick film on MgO cylinder with Bi-2212 buffer Layer". *IEEE Transactions on Applied Superconductivity*, Vol. 15, No. 2, pp. 2051–2054, 2005.

[Kado 97] H. Kado and M. Ickikawa. "Performance of a high-Tc superconducting fault current limiter-design of a 6.6 kV magnetic shielding type superconducting fault current limiter". *IEEE Transactions on Applied Superconductivity*, Vol. 7, No. 2, pp. 993–996, 1997.

[Kang 06] R. Kang-Sik, J. young Sik, and P. Minwon. "Overview of the development of the advanced power system by the applied superconductivity technologies programme in Korea". 2006.

[Kim 07] H. M. Kim, K. B. Park, B. W. Lee, and e. al. "Theoretical Prediction of the Quench Behavior of a SFCL Module Having a BSCCO-2212 Bulk Coil and a Shunt Coil". *IEEE Transactions on Applied Superconductivity*, Vol. 17, No. 2, pp. 1871–1874, 2007.

[Kind 97] H. Kinder, P. Berberich, and e. al. "YBCO Film Deposition on Very Large Areas Up to 20 by 20 cm2". 1997.

[Koya 04] H. Koyama, M. Hanai, M. Sakai, and e. al. "Dielectric characteristics of 66 kV/750 A high-Tc superconducting fault current limiter coil". *IEEE Transactions on Applied Superconductivity*, Vol. 14, No. 2, pp. 1181–1184, 2004.

[Koya 08] K. Koyanagi, T. Yazawa, M. Takahashi, and e. al. "Design and Test Results of a Fault Current Limiter Coil Wound With Stacked YBCO Tapes". *IEEE Transactions on Applied Superconductivity*, Vol. 18, No. 2, pp. 676–679, 2008.

[Koza] J. Kozak and T. Janowski. "Applications of HTS Fault Current Limiters in Power Network".

[Krae 03] H. P. Kraemer, W. Schmidt, B. Utz, and e. al. "Switching behavior of YBCO thin film conductors in resistive fault current limiters". *IEEE Transactions* *on Applied Superconductivity*, Vol. 13, No. 2, pp. 2044–2047, 2003.

[Krae 05] H. P. Kraemer, W. Schmidt, B. Utz, and e. al. "Test of a 1 kA superconducting fault current limiter for DC applications". *IEEE Transactions on Applied Superconductivity*, Vol. 15, No. 2, pp. 1986–1989, 2005.

[Kreu 05] R. Kreutz, J. Bock, F. Breuer, and e. al. "System technology and test of CURL 10, a 10 kV, 10 MVA resistive high-Tc superconducting fault current limiter". *IEEE Transactions on Applied Superconductivity*, Vol. 15, No. 2, pp. 1961–1964, 2005.

[Kuma 06] J. R. S. S. Kumara, A. Atputharajah, J. B. Ekanayake, and e. al. "Over current protection coordination of distribution networks with fault current limiters". In: *Power Engineering Society General Meeting, 2006. IEEE*, p. 8, 2006.

[Kund 03] K. Kunde, M. Kleimaier, and L. Klingbeil. "Integration of fast acting electronic fault current limiters (EFCL) in medium-voltage systems". 2003.

[Lang 02] T. Lang and H. S. Zeller. "Short-circuit-resistante IGBT module". 2002.

[Lee 08] B. W. Lee, K. B. Park, J. Sim, and e. al. "Design and Experiments of Novel Hybrid Type Superconducting Fault Current Limiters". *IEEE Transactions on Applied Superconductivity*, Vol. 18, No. 2, pp. 624–627, 2008.

[Leht 04] J. Lehtonen, H. C. Freyhardt, A. Usoskin, and e. al. "Design and demonstration of superconducting power link". *Generation, Transmission and Distribution, IEE Proceedings.*, Vol. 151, No. 6, pp. 755–760, 2004.

[Leun 00] E. M. Leung. "Superconducting Fault Current Limiters". 2000.

[Leun 97] E. M. Leung, I. Rodriguez, G. W. Albert, and e. al. "High temperature superconducting fault current limiter development". *IEEE Transactions on Applied Superconductivity*, Vol. 7, No. 2, pp. 985–988, 1997.

[Li 09] X. Li, M. W. Rupich, C. L. H. Thieme, and e. al. "The Development of Second Generation HTS Wire at American Superconductor". *IEEE Transactions on Applied Superconductivity*, Vol. 19, No. 3, pp. 3231–3235, 2009.

[Libr] Library.

[Lin 07] Y. Lin, M. Majoros, A. M. Campbell, and e. al. "MgB2 Sample Tests for Possible Applications of Superconducting Fault Current Limiters". *IEEE Transactions on Applied Superconductivity*, Vol. 17, No. 2, pp. 2826–2829, 2007.

[Maed 88] H. Maeda, Y. Tanaka, M. Fukutomi, and e. al. "A New High-Tc Oxide Superconductor without a Rare Earth Element". *Japanese Journal of Applied Physics*, Vol. 27, p. 2, 1988.

[maga 09] M. T. d. s. t. magazine. 2009.

[Majo 07] M. Majoros, L. Ye, A. M. Campbell, and e. al. "Fault Current Limiting Properties of MgB_2 Superconducting Wires". *IEEE Transactions on Applied Superconductivity*, Vol. 17, No. 2, pp. 1764–1767, 2007.

[Marc 09] B. Marchionini, N. K. Fall, and M. Steurer. "An Assessment of Fault Current Limiter Testing Requirements". 2009.

[Mari 09] F. Mariconi and e. al. "FY2009 Superconductivity for Electric Systems Peer Review Project Summary Form". 2009.

[Mart 05] L. Martini, M. Bocchi, M. Levati, and e. al. "Simulations and electrical testing of superconducting fault current limiter prototypes". *IEEE Transactions on Applied Superconductivity*, Vol. 15, No. 2, pp. 2067–2070, 2005.

[Mart 06] L. Martini, I. Arcos, and e. al. "Resistive Fault Current Limiter Prototypes: Mechanical and Electrical Analyses". 2006.

[Mart 07] L. Martini, M. Bocchi, and e. al. "Electrical Testing of 1 MVA-class Three-Phase Superconducting Fault Current Limiter Prototypes". 2007.

[Mart 09] L. Martini, M. Bocchi, R. Brambilla, and e. al. "Design and Development of 15 MVA Class Fault Current Limiter for Distribution Systems". *IEEE Transactions on Applied Superconductivity*, Vol. 19, No. 3, pp. 1855–1858, 2009.

[Maru 07] M. Maruyama, D. Iioka, Y. Yokomizu, and e. al. "Inductance Ratio of Flat Type Fault Current Limiter With High Tc Superconducting Disks". *IEEE Transactions on Applied Superconductivity*, Vol. 17, No. 2, pp. 1819–1822, 2007.

[Mati 06] V. Matias. "Overview of CC program in South Corea". 2006.

[Mats 05] T. Matsumura, M. Sugimura, Y. Yokomizu, and e. al. "Generating performance of limiting impedance in flat type of fault current limiter with high Tc superconducting plate". *IEEE Transactions on Applied Superconductivity*, Vol. 15, No. 2, pp. 2015–2018, 2005.

[Meye 04a] C. Meyer, P. Kollensperger, and R. W. De Doncker. "Design of a novel low loss fault current limiter for medium-voltage systems". In: *Applied Power Electronics Conference and Exposition, 2004. APEC '04.*, pp. 1825–1831, 2004.

[Meye 04b] C. Meyer, S. Schroder, and R. W. De Doncker. "Solid-state circuit breakers and current limiters for medium-voltage systems having distributed power systems". *IEEE Transactions on Power Electronics*, Vol. 19, No. 5, pp. 1333–1340, 2004.

[Min 04] A. Min Cheol, L. Seungje, K. Hyoungku, and e. al. "Design, fabrication, and test of high-Tc superconducting DC reactor for inductive superconducting fault current limiter". *IEEE Transactions on Applied Superconductivity*, Vol. 14, No. 2, pp. 827–830, 2004.

[Min 05] A. Min Cheol, H. Kang, B. Duck Kweon, and e. al. "The short-circuit characteristics of a DC reactor type superconducting fault current limiter with fault detection and signal control of the power converter". *IEEE Transactions on Applied Superconductivity*, Vol. 15, No. 2, pp. 2102–2105, 2005.

[Min 06] A. Min Cheol, B. Duck Kweon, Y. Seong Eun, and e. al. "Manufacture and Test of Small-Scale Superconducting Fault Current Limiter by Using the Bifilar Winding of Coated Conductor". *IEEE Transactions on Applied Superconductivity*, Vol. 16, No. 2, pp. 646–649, 2006.

[Min 07] A. Min Cheol, P. Dong Keun, Y. Seong Eun, and e. al. "Recovery Characteristics of Resistive SFCL Wound With YBCO Coated Conductor in a Power System". *IEEE Transactions on Applied Superconductivity*, Vol. 17, No. 2, pp. 1859–1862, 2007.

[Mott 00] K. Motto, Y. Li, and A. Q. Huang. "Comparison of the state-of-the-art high power IGBTs, GCTs and ETOs". In: *Applied Power Electronics Conference and Exposition, 2000. APEC 2000.*, pp. 1129–1136, 2000.

[Mult 08] C. Multiphysics. "Comsol Multiphysics - Reference Guide". 2008.

[Muta 04] I. Muta, T. Hoshino, K. M. Salim, and e. al. "Proposal of dc shield reactor type superconducting fault current limiter". 2004.

[Naka 95] T. Nakagawa, F. Tokunoh, M. Yamamoto, and e. al. "A new high power low loss GTO". In: *Power Semiconductor Devices and ICs, 1995. ISPSD '95.*, pp. 84–88, 1995.

[Nard 07] D. Nardelli, R. Marabotto, G. Grasso, and e. al. "Test Results on MgB_2 Windings for AC Applications". *IEEE Transactions on Applied Superconductivity*, Vol. 17, No. 2, pp. 2742–2745, 2007.

[Neum 06] C. Neumann. "Superconducting fault current limiter (SFCL) in the medium and high voltage grid". In: *Power Engineering Society General Meeting, 2006. IEEE*, p. 6, 2006.

[Neum 07] H. W. Neumueller, H. P. Kraemer, W. Schmidt, and e. al. "Economically Viable Fault Current Limiters using YBCO coated conductors". In: *Power Engineering Society General Meeting, 2007. IEEE*, pp. 1–5, 2007.

[Niay 04] K. Niayesh, J. Tepper, and F. Konig. "On the arcless commutation of currents higher than 1 kA". In: *Proceedings of the 50th IEEE Holm Conference on Electrical Contacts and the 22nd International Conference on Electrical*

Contacts, pp. 388–394, 2004.

[Niay 06] K. Niayesh, J. Tepper, and F. Konig. “A novel current limitation principle basedon application of liquid metals”. *IEEE Transactions on Components and Packaging Technologies*, Vol. 29, No. 2, pp. 303–309, 2006.

[Noe 07a] M. Noe, A. Kudymow, S. Fink, and e. al. “Conceptual Design of a 110 kV Resistive Superconducting Fault Current Limiter Using MCP-BSCCO 2212 Bulk Material”. *IEEE Transactions on Applied Superconductivity*, Vol. 17, No. 2, pp. 1784–1787, 2007.

[Noe 07b] M. Noe and M. Steurer. “High-temperature superconductor fault current limiters: concepts applications and development status”. Tech. Rep., 2007.

[Noe 08] M. Noe, M. Steurer, S. Eckroad, and e. al. “Progress on the RD of Fault Current Limiters (FCLs) for Utility Applications”. 2008.

[Noe 09] M. Noe. “Summary on Field Test Results of Superconducting Power Equipment”. 2009.

[Oh 09] S. S. Oh. “RD Status of HTS Coated Conductors in Korea”. 2009.

[Ohta 04] Y. Ohtani, T. Yazawa, T. Kurita, and e. al. “Cryostat for 66 kV/750 A high-Tc superconducting fault current limiter magnet”. *IEEE Transactions on Applied Superconductivity*, Vol. 14, No. 2, pp. 855–858, 2004.

[Ok B 03] H. Ok-Bae, C. Sang-Do, K. Hye-Rim, and e. al. “Shunt-assisted simultaneous quenches in series-connected resistive SFCL components”. *IEEE Transactions on Applied Superconductivity*, Vol. 13, No. 2, pp. 2060–2063, 2003.

[Ok B 05] H. Ok-Bae, K. Hye-Rim, S. Jungwook, and e. al. “6.6 kV resistive superconducting fault current limiter based on YBCO films”. *IEEE Transactions on Applied Superconductivity*, Vol. 15, No. 2, pp. 2027–2030, 2005.

[Onne 11] H. K. Onnes. “The superconductivity of mercury”. *Comm. Phys. Lab. Univ. Leiden, Nos. 122 and 124*, 1911.

[Otet 04] A. Otete. *A novel fault current limiter*. PhD thesis, The Floriday State University, 2004.

[Pait] Y. Paithankar and S. Bhide. *Fundamentals of Power System Protection.*

[Pan 08] Y. Pan, M. Steurer, T. L. Baldwin, and e. al. “Impact of Waveform Distorting Fault Current Limiters on Previously Installed Overcurrent Relays”. *IEEE Transactions on Power Delivery*, Vol. 23, No. 3, pp. 1310–1318, 2008.

[Park 03] K. B. Park, J. S. Kang, B. W. Lee, and e. al. “Quench behavior of YBaCuO films for fault current limiters under magnetic field”. *IEEE Transactions on Applied Superconductivity*, Vol. 13, No. 2, pp. 2092–2095, 2003.

[Paul 01] W. Paul, M. Chen, M. Lakner, and e. al. “Fault current limiter based on high temperature superconductors - different concepts, test results, simulations, applications". 2001.

[Paul 98] W. Paul and M. Chen. "Superconducting control for surge currents". 1998.

[Peel 96] D. F. Peelo, G. S. Polovick, J. H. Sawada, and e. al. "Mitigation of circuit breaker transient recovery voltages associated with current limiting reactors". *IEEE Transactions on Power Delivery*, Vol. 11, No. 2, pp. 865–871, 1996.

[Phas 04] "Phase I Results and Phase II Plans of DAPAS". 2004.

[Powe] Powerex. "CM600HG-130H, HV IGBT module Datasheet".

[Qing 08] L. Qingmin, L. Hongshun, L. Jie, and e. al. "Impact Research of Inductive FCL on the Rate of Rise of Recovery Voltage With Circuit Breakers". *IEEE Transactions on Power Delivery*, Vol. 23, No. 4, pp. 1978–1985, 2008.

[Raju 82] B. P. Raju, K. C. Parton, and T. C. Bartram. "A Current Limiting Device Using Superconducting D.C. Bias Applications and Prospects". *IEEE Transactions on Power Apparatus and Systems*, Vol. PAS-101, No. 9, pp. 3173–3177, 1982.

[Raso 06] J. L. Rasolonjanahary, J. P. Sturgess, E. F. H. Chong, and e. al. "Design and construction of a magnetic fauft current limiter". In: *Power Electronics, Machines and Drives, 2006. PEMD 2006.*, pp. 681–685, 2006.

[Rost 07] L. J. Rostila, J. R. Lehtonen, M. J. Masti, and e. al. "AC Losses and Current Sharing in an YBCO Cable". *IEEE Transactions on Applied Superconductivity*, Vol. 17, No. 2, pp. 1688–1691, 2007.

[Roze 07] V. Rozenshtein, A. Friedman, Y. Wolfus, and e. al. "Saturated Cores FCL: A New Approach". *IEEE Transactions on Applied Superconductivity*, Vol. 17, No. 2, pp. 1756–1759, 2007.

[Rube 07a] H. Rubenbauer and G. Herold. "Determination of the Firing Angle for a Dynamic Fault Current Delimiter (DFCL) in Case without a Fault". 2007.

[Rube 07b] H. Rubenbauer and G. Herold. "A Dynamic Fault Current Limiter (DFCL)". In: *Power Engineering Society Conference and Exposition in Africa, 2007. PowerAfrica '07. IEEE*, pp. 1–7, 2007.

[Rube 08] H. Rubenbauer. *Dynamische Kurzschlustrombegrenzung auf Basis eines sechspulsigen Thyristorgleichrichters*. PhD thesis, 2008.

[Saka 06] M. Sakai, H. Kaneiwa, H. Koyama, and e. al. "Dielectric Characteristics of EPR for 66 kV-Class Power Leads of High-Tc Superconducting Fault Current Limiter". *IEEE Transactions on Applied Superconductivity*, Vol. 16, No. 2, pp. 1790–1793, 2006.

[Sali 04] K. M. Salim, I. Muta, and e. al. "Proposal of rectifier type superconducting fault current limiter with non-inductive reactor (SFCL)". 2004.

[Sati 02] G. Satish. "Press pack power semiconductor module". 2002.

[Schm 06] H. Schmitt. "Fault current limiters report on the activities of CIGRE WG A3.16". In: *Power Engineering Society General Meeting, 2006. IEEE*, p. 5, 2006.

[Schm 07] W. Schmidt, H. P. Kraemer, H. W. Neumueller, and e. al. "Investigation of YBCO Coated Conductors for Fault Current Limiter Applications". *IEEE Transactions on Applied Superconductivity*, Vol. 17, No. 2, pp. 3471–3474, 2007.

[Scho] S. Schoft, J. Tepper, and K. Niayesh. "Short circuit current limitation by means of liquid metal technology".

[Seun 01] L. Seungje, L. Chanjoo, K. Tae Kuk, and e. al. "Stability analysis of a power system with superconducting fault current limiter installed". *IEEE Transactions on Applied Superconductivity*, Vol. 11, No. 1, pp. 2098–2101, 2001.

[Seun 04] L. Seung, K. Hyoung, B. Duck Kwoen, and e. al. "Development of 6.6 kV-200 A DC reactor type superconducting fault current limiter". *IEEE Transactions on Applied Superconductivity*, Vol. 14, No. 2, pp. 867–870, 2004.

[Shim 02] K. Shimohata, S. Yokoyama, K. Inaguchi, and e. al. "Design of a large current-type fault current limiter with YBCO films". 2002.

[Shim 92] S. Shimizu, H. Kado, Y. Uriu, and e. al. "Single-line-to-ground fault test of a 3-phase superconducting fault current limiting reactor". *IEEE Transactions on Magnetics*, Vol. 28, No. 1, pp. 442–445, 1992.

[Shir 08] Y. Shirai, K. Furushiba, Y. Shouno, and e. al. "Improvement of Power System Stability by Use of Superconducting Fault Current Limiter With ZnO Device and Resistor in Parallel". *IEEE Transactions on Applied Superconductivity*, Vol. 18, No. 2, pp. 680–683, 2008.

[Shuk 07] W. Shuki, A. Friedman, J. Yeshurun, and e. al. "Fault Current Limiters (FCLs) with the Cores Saturated by the Superconducting Coils". 2007.

[Sim 07] J. Sim, K. B. Park, H. R. Kim, and e. al. "14 kV single-phase superconducting fault current limiter based on YBCO films". 2007.

[Slui 01] L. Van der Sluis. *Transients in Power Systems*. John Wiley and Sons Ltd, 2001.

[Soko] V. Sokolovsky, V. Meerovich, and I. Vajda. "Transient stability of a power system with superconducting fault current limiters".

[Soko 04] V. Sokolovsky, V. Meerovich, I. Vajda, and e. al. "Superconducting FCL:

design and application". *IEEE Transactions on Applied Superconductivity*, Vol. 14, No. 3, pp. 1990–2000, 2004.

[Suga 04] Y. Sugawara, D. Takayama, K. Asano, and e. al. "12.7 kV ultra high voltage SiC commutated gate turn-off thyristor: SICGT". In: *Power Semiconductor Devices and ICs, ISPSD '04.*, pp. 365–368, 2004.

[Supe] A. Superconductor. "HTS Magnets vs. LTS Magnets".

[Supe 08] "Superconductor week, November 3, 2008.". 2008.

[Taka 01] M. Takasaki, S. Torii, H. Taniguchi, and e. al. "Performance verification of a practical fault current limiter using YBCO thin film". *IEEE Transactions on Applied Superconductivity*, Vol. 11, No. 1, pp. 2499–2502, 2001.

[Tayl 05] T. Taylor, A. Hanson, D. Lubkeman, and e. al. "Fault Current Review Study". Tech. Rep., ABB, 2005.

[Tekl 99] K. Tekletsadik, M. P. Saravolac, and A. Rowley. "Development of a 7.5 MVA superconducting fault current limiter". *IEEE Transactions on Applied Superconductivity*, Vol. 9, No. 2, pp. 672–675, 1999.

[Tixa 07] P. Tixador, Y. Cointe, C. Villard, and e. al. "Limiting Experiments With Coated Conductors". *IEEE Transactions on Applied Superconductivity*, Vol. 17, No. 2, pp. 3467–3470, 2007.

[Tosa 01] F. Tosato and S. Quaia. "Reducing voltage sags through fault current limitation". *IEEE Transactions on Power Delivery*, Vol. 16, No. 1, pp. 12–17, 2001.

[Tsud 01] M. Tsuda, Y. Mitani, K. Tsuji, and e. al. "Application of resistor based superconducting fault current limiter to enhancement of power system transient stability". *IEEE Transactions on Applied Superconductivity*, Vol. 11, No. 1, pp. 2122–2125, 2001.

[Ueda 03] K. Ueda, K. Yasuda, K. Inoue, and e. al. "RD of HTS power cable and fault current limiter in Super-ACE project". 2003.

[Usos 03] A. Usoskin, H. C. Freyhardt, A. Issaev, and e. al. "SUPERPOLI fault-current limiters based on YBCO-coated stainless steel tapes". *IEEE Transactions on Applied Superconductivity*, Vol. 13, No. 2, pp. 1972–1975, 2003.

[Usos 07] A. Usoskin, L. Kirchhoff, J. Knoke, and e. al. "Processing of Long-Length YBCO Coated Conductors Based on Stainless Steel Tapes". *IEEE Transactions on Applied Superconductivity*, Vol. 17, No. 2, pp. 3235–3238, 2007.

[Utz 97] B. Utz, S. Rieder-Zecha, and H. Kinder. "Continuous YBCO film deposition by optically controlled reactive thermal co-evaporation". *IEEE Transactions on Applied Superconductivity*, Vol. 7, No. 2, pp. 1181–1184, 1997.

[Verh 99] T. Verhaege, P. F. Herrmann, J. Bock, and e. al. "European project on a self-limiting superconducting power link". 1999.

[Wake 05] F. Wakeman, G. Li, and A. Golland. "New family of 4.5kV Press-pack IGBTs". 2005.

[Wang 06] Z. K. Wang, J. Y. Zhang, D. Zhang, and e. al. "Design and Test of High-Tc Superconducting Coils for a Three-Phase 10.5 kV/1.5 kA Fault Current Limiter". *IEEE Transactions on Applied Superconductivity*, Vol. 16, No. 2, pp. 658–661, 2006.

[Wayn 03] J. A. Waynert, H. J. Boenig, C. H. Mielke, and e. al. "Restoration and testing of an HTS fault current controller". *IEEE Transactions on Applied Superconductivity*, Vol. 13, No. 2, pp. 1984–1987, 2003.

[Webe 08] C. Weber. "Transmission Level HTS Fault Current Limiter". Tech. Rep., 2008. DOE Annual Peer Review.

[Wiki] Wikipedia.

[Wrig 93] A. Wright and C. Christopoulos. *Electrical power system protection*. Chapman and Hall, London ; New York, 1st Ed., 1993.

[Wtec] Wtec.

[Wu 87] M. K. Wu, J. R. Ashburn, and C. J. Torng. "Superconductivity at 93K in a New Mixed-Phase YBCO Compound System at Ambient Pressure". 1987.

[Xiao 05] Z. Xiaoqing and L. Ming. "Using the Fault Current Limiter with Transformer Type Reactor to Reduce Short Circuit Currents". In: *Transmission and Distribution Conference and Exhibition: Asia and Pacific, 2005 IEEE/PES*, pp. 1–4, 2005.

[Xie 07] Y. Y. Xie, K. Tekletsadik, D. Hazelton, and e. al. "Second Generation High-Temperature Superconducting Wires for Fault Current Limiter Applications". *IEEE Transactions on Applied Superconductivity*, Vol. 17, No. 2, pp. 1981–1985, 2007.

[Xin 07] Y. Xin, W. Gong, and e. al. "Development of Saturated Iron Core HTS Fault Current Limiters". *IEEE Transactions on Applied Superconductivity*, Vol. 17, No. 2, 2007.

[Xin 09] Y. Xin, W. Z. Gong, X. Y. Niu, and e. al. "Manufacturing and Test of a 35 kV/90 MVA Saturated Iron-Core Type Superconductive Fault Current Limiter for Live-Grid Operation". *IEEE Transactions on Applied Superconductivity*, Vol. 19, No. 3, pp. 1934–1937, 2009.

[Xing 02] L. Xingyuan, Z. Min, and L. Hongchao. "A novel fault current limiter with series compensation". In: *Power System Technology, 2002. Proceedings. Pow-*

erCon 2002., pp. 1467–1471, 2002.

[Xing 05] Y. Xing, K. Tekletsadik, L. Kovalsky, and e. al. "Proof-of-concept prototype test results of a superconducting fault current limiter for transmission-level applications". *IEEE Transactions on Applied Superconductivity*, Vol. 15, No. 2, pp. 1982–1985, 2005.

[Yasu 05] K. Yasuda, A. Ichinose, A. Kimura, and e. al. "Research and development of superconducting fault current limiter in Japan". *IEEE Transactions on Applied Superconductivity*, Vol. 15, No. 2, pp. 1978–1981, 2005.

[Yaza 01] T. Yazawa, E. Yoneda, J. Matsuzaki, and e. al. "Design and test results of 6.6 kV high-Tc superconducting fault current limiter". *IEEE Transactions on Applied Superconductivity*, Vol. 11, No. 1, pp. 2511–2514, 2001.

[Yaza 03] T. Yazawa, H. Koyama, K. Tasaki, and e. al. "66 kV-class high-Tc superconducting fault current limiter magnet model coil experiment". *IEEE Transactions on Applied Superconductivity*, Vol. 13, No. 2, pp. 2040–2043, 2003.

[Yaza 04a] T. Yazawa, Y. Ootani, M. Sakai, and e. al. "Development of 66 kV/750 A High-Tc superconducting fault current limiter magnet". *IEEE Transactions on Applied Superconductivity*, Vol. 14, No. 2, pp. 786–790, 2004.

[Yaza 04b] T. Yazawa, T. Tosaka, T. Kuriyama, and e. al. "Fatigue tests of HTS coils". *IEEE Transactions on Applied Superconductivity*, Vol. 14, No. 2, pp. 1214–1217, 2004.

[Yaza 05] T. Yazawa, Y. Ootani, M. Sakai, and e. al. "66 kV/1 kA high-Tc superconducting fault current limiter magnet". *IEEE Transactions on Applied Superconductivity*, Vol. 15, No. 2, pp. 2059–2062, 2005.

[Yaza 06] T. Yazawa, Y. Ootani, M. Sakai, and e. al. "Design and Test Results of 66 kV High-Tc Superconducting Fault Current Limiter Magnet". *IEEE Transactions on Applied Superconductivity*, Vol. 16, No. 2, pp. 683–686, 2006.

[Yaza 09] T. Yazawa, K. Koyanagi, M. Takahashi, and e. al. "Design and Experimental Results of Three-Phase Superconducting Fault Current Limiter Using Highly-Resistive YBCO Tapes". *IEEE Transactions on Applied Superconductivity*, Vol. 19, No. 3, pp. 1956–1959, 2009.

[Youn 06] J. Young-Sik, R. Kang-Sik, and M. Park. "1st Phase Results and Future Plan of DAPAS Program". *IEEE Transactions on Applied Superconductivity*, Vol. 16, No. 2, pp. 678–682, 2006.

[Yuan 07] Z. Yuan, S. W. H. de Haan, and J. A. Ferreira. "A New FACTS component - Distributed Power Flow Controller (DPFC)". In: *Power Electronics and Applications, 2007 European Conference*, pp. 1–4, 2007.

[Yuji 01] Z. Yuji and A. Jun. "Discovery of the new superconductor MgB_2 and its recent development". 2001.

[Zhan 04] B. Zhang, A. Q. Huang, B. Chen, and e. al. "SPETO: a superior power switch for high power, high frequency, low cost converters". In: *Industry Applications Conference, 2004. 39th IAS Annual Meeting.*, pp. 1940–1946, 2004.

[Zhen 03] L. Zhengyu, J. Daozhuo, and W. Zhaolin. "A new topology of fault-current limiter and its parameters optimization". In: *Power Electronics Specialist Conference, 2003. PESC '03. 2003 IEEE 34th Annual*, pp. 462–465, 2003.

[Zou 02] J. Zou, J. Chen, and E. Dong. "Study of fast-closing switch based fault current limiter with series compensation". 2002.

LIST OF PUBLICATIONS

Journals

1. **Cvoric, D.**; de Haan, S. W. H.; Ferreira, J. A.; Yuan, Z.; van Riet, M.; Bozelie, J.: "New Three-Phase Inductive FCL with Common Core and Trifilar Windings", *IEEE Transaction on Power Delivery*, August 2010, Volume: 25, Issue: 4, ISSN: 0885-8977.
2. Yuan, Z.; de Haan, S. W. H.; Ferreira, J. A.; **Cvoric, D.**: "A FACTS Device - Distributed Power Flow Controller (DPFC)", *IEEE Transaction on Power Electronics* October 2010, Volume: 25, Issue: 10, ISSN: 0885-8993.
3. **Cvoric, D.**; de Haan, S. W. H.; Ferreira, J. A.: "New Saturable-Core FCL Topology with Reduced Core Size", *Transaction on Electrical and Electronic Engineering* (TEEE) 2009, *To be published.*
4. **Cvoric, D.**; de Haan, S. W. H.; Ferreira, J. A.; van Riet, M.; Bozelie, J.: "Three-phase non-superconductive fault current limiter based on the core-saturation effect - challenges and ideas", *Transaction in VGB PowerTech Journal*, October 2010, Volume: 90, ISSN: 1435-3199.

Conference proceedings

1. **Cvoric, D.**; de Haan, S. W. H.; Ferreira, J. A.: "Comparison of the Two Concepts of the Inductive Fault Current Limiter", *IEEE Benelux Young Researcher Symposium* (YRS) 2008, pp. 1-6.
2. **Cvoric, D.**; de Haan, S. W. H.; Ferreira, J. A.: "CB Stress Reduction and Comparison of Energy Dissipation for Two Types of FCLs", *IEEE Transmission and Distribution Conference and Exposition* (PES) 2008, pp. 1-7.

3. **Cvoric, D.**; de Haan, S. W. H.; Ferreira, J. A.: "Comparison of the Four Configurations of the Inductive Fault Current Limiter", *IEEE Power Electronics Specialist Conference* (PESC) 2008, pp. 1-7.
4. **Cvoric, D.**; de Haan, S. W. H.; Ferreira, J. A.: "Improved Configuration of the Inductive Core-Saturation Fault Current Limiter with the Magnetic Decoupling", *IEEE Industry Application Society Annual Meeting* (IAS) 2008, pp. 1-7.
5. Lahaye, D.; **Cvoric, D.**; de Haan, S. W. H.; Ferreira, J. A.: "Field-Circuit Coupling Applied to Inductive Fault Current Limiters", *Comsol User Conference* (CUC) 2008, pp. 1-7.
6. **Cvoric, D.**; de Haan, S.W. H.; Ferreira, J. A.: "New Saturable-Core Fault Current Limiter Topology with Reduced Core Size", *IEEE Power Electronics and Motion Control Conference* (IPEMC) 2009, pp. 1-6.
7. **Cvoric, D.**; de Haan, S. W. H.; Ferreira, J. A.: "Guidelines for 2D/3D FE Transient Modeling of Inductive Saturable-Core Fault Current Limiters", *IEEE International Conference on Electric Power and Energy Conversion Systems* (EPECS) 2009, pp. 1-6.
8. Yuan, Z.; **Cvoric, D.**; de Haan, S. W. H.; Ferreira, J. A.: "Utilize Distributed Power Flow Controller (DPFC) to Compensate Unbalanced 3-phase Currents in Transmissions Systems", *IEEE International Conference on Electric Power and Energy Conversion Systems* (EPECS) 2009, pp. 1-5.
9. **Cvoric, D.**; Lahaye, D.; de Haan, S. W. H.; Ferreira, J. A.: "3D Nonlinear Transient Field-Circuit Modeling of Inductive Fault Current Limiters", *IEEE Compumag* 2009, pp. 1-4.
10. **Cvoric, D.**; Lahaye, D.; de Haan, S. W. H.; Ferreira, J. A.: "3D Transient Field-Circuit Modeling of Inductive Fault Current Limiters", *Compumag* 2009, pp. 1-4.

Patent

1. **Cvoric, D.**; van Riet, M.; Ferreira, J. A.; de Haan, S. W. H.: "Fault Current Limiter", International Patent, 2009, number 2002216.

BIOGRAPHY

Dalibor Čvorić was born in Zvornik, in Bosnia and Herzegovina in 1982. He finished primary school 'Vuk Karadžić' in 1997 and Grammar high school 'Milorad Vlačić' in 2001 in his home town Vlasenica.

He graduated at University of Novi Sad, Faculty of Technical Sciences on the department of Power, Electronics and Telecommunication Engineering in Serbia in 2006. He was awarded diploma of Graduate Electrical and Computer Science Engineer with major in Microcomputer Electronics.

In 2010, he attained a Ph.D. degree at Delft University of Technology, Department for Electrical Engineering, Mathematics and Computer Sciences in the group for Electrical Power Processing (EPP). His Ph.D. research was in the field of fault current limiting in utility grids.